Synthesis, Structure and Properties of Sodium and Lithium All-Solid-State Electrolytes for All-Solid-State Battery Applications

by

Erika Ramos

A thesis
presented to the University of Waterloo
in fulfillment of the
thesis requirement for the degree of
Doctor of Philosophy
in
Chemistry (Nanotechnology)

Waterloo, Ontario, Canada, 2020

Examining Committee Membership

The following served on the Examining Committee for this thesis. The decision of the Examining Committee is by majority vote.

External Examiner:	Venkataraman Thangadurai Professor
Supervisor(s):	Linda F. Nazar Professor
Internal Member:	Holger Kleinke Professor Pavle Radovanovic Professor
Internal-External Member:	Michael Pope Assistant Professor
Other Member(s):	German Sciaini Assistant Professor

Author's Declaration

I hereby declare that I am the sole author of this thesis. This is a true copy of the thesis, including any required final revisions, as accepted by my examiners.

I understand that my thesis may be made electronically available to the public.

Abstract

All-solid-state batteries have received a keen interest as emerging attractive alternatives to conventional liquid electrolyte cells, because of their potential in improving battery safety and electrochemical properties. The discovery and development of high-performance solid-state electrolytes -which lie at the heart of the solid-state battery concept- is critical for the realization of all-solid-state battery technology. Among the variety of different solid electrolyte chemistries, sodium and lithium thiophosphates are of great interest for all-solid-state batteries because of their high ion conductivity, ductility and processability.

Herein, the synthesis, structure and properties of new sodium and lithium-ion conductors, namely $Na_{11}Sn_2PnQ_{12}$ with Pn=P and Sb; Q=S and Se, $Li_{4.29}P_{0.71}Si_{0.29}S_4I$ and $Li_{3.3}P_{0.85}Al_{0.15}S_4$ are presented. Detailed structure analysis of each solid electrolyte was obtained by a combination of powder neutron diffraction, single crystal and powder X-ray diffraction techniques. The mobile ion dynamics of the synthesized solid electrolytes was studied by electrochemical impedance spectroscopy and direct current polarizability techniques, whereas their thermal stability was investigated by differential scanning calorimetry. Computational chemistry was carried out to obtain the topology of the potential ion-migration pathways in the different crystal structure frameworks.

For solid state synthesis, the heat treatment parameters including, temperature and holding time strongly influence the phase purity, relative density and ionic conductivity of the final product. By optimizing the synthesis conditions of the Na-ion conductor $Na_{11}Sn_2PS_{12}$, its ionic transport properties were successfully enhanced, from 0.5 $mS{\cdot}cm^{-1}$ to 1.39 $mS{\cdot}cm^{-1}$. The enhanced conductivity was attributed to a reduction of the grain boundary resistance.

The structure analysis of the Sb-analogue, $Na_{11}Sn_2SbS_{12}$, enabled a further understanding the dynamics of ion transport in this structure type. The findings addressed the role of interstitial site occupation in fast-ion conduction for $Na_{11}Sn_2PnS_{12}$ with Pn=Sb and P. Single crystal X-ray diffraction studies of the isostructural Na-ion conductors, $Na_{11}Sn_2PnS_{12}$ with Pn=Sb and P, allowed the identification of the reasons responsible for the difference in their ionic conductivity. The Se version of $Na_{11}Sn_2SbS_{12}$ was studied by isovalent Se-substitution within the $Na_{11}Sn_2SbS_{12-x}Se_x$ with x=1, 6 and 12; where for each composition, the structure-property relations were identified through single crystal and powder X-ray diffraction studies. The homogeneous distribution of Se on all three available lattice sites, *32g* Wyckoff positions, indicates no site preference and the absence of a solubility limit for selenium within $Na_{11}Sn_2SbS_{12-x}Se_x$.

Examination of the series $Li_{4+x}P_{1-x}Si_xS_4I$ with x=0, 0.12, 0.29 and 0.4 led to the discovery of the fast-ion conductor, $Li_{4.29}P_{0.81}Si_{0.29}S_4I$. The aliovalent substitution in

$Li_{4+x}P_{1-x}Si_xS_4I$, (Li^+ + Si^{4+}) for P^{5+}, induced a highly defected Li sublattice. This structural change significantly improved the ionic transport properties of the pristine Li_4PS_4I poor ion conductor by lowering the energy barrier for Li^+ diffusion. This work shows a promising strategy towards the design and development of fast-ion conductors by inducing mobile-cation site disorder using elemental substitution; besides, it highlights the role of point defects on ion transport mechanism in crystalline solid electrolytes.

A version of the β-Li_3PS_4 structure, a high-temperature phase, with a more disordered Li sublattice was stabilized at room temperature by Al substitution in $Li_{3+2x}P_{1-x}Al_xS_4$. The solubility of Al in the lattice was determined by the analysis of the series $Li_{3+2x}P_{1-x}Al_xS_4$ with x=0.15, 0.2 and 0.33. Single crystal X-ray diffraction revealed that Al substitution led to structural splitting of one of the Li sites, effectively creating a disorder Li^+ distribution, which resulted in an increase in the ionic conductivity versus that of the bulk β-Li_3PS_4 solid electrolyte. The findings obtained in this study shed light on the predicted via first principle calculations, $Li_{11}AlP_2S_{12}$ fast-ion conductor, by elucidating the greater thermodynamic stability of the $Li_{9.9}Al_{0.45}P_{2.55}S_{12}$ phase and the limited solubility of Al in this thio-LISICON structure. All the data presented in this thesis were obtained during my studies, unless attributed in-text to another researcher.

Acknowledgements

I wish to express my sincere appreciation to my supervisor, Professor Linda Nazar for providing guidance and feedback throughout this project. I would like to thank my Ph.D. committee members Dr. Holger Kleinke, Dr. Pavle Radovanovic and Dr. German Sciaini for taking the time to give me suggestions about my research during the committee meetings. I would also like to thank my internal-external member Dr. Michael Pope and my external examiner Dr. Venkataraman Thangadurai for being able to participate in my thesis defence. I also want to thank Dr. Abdeljalil Assoud for his help during all these years of research.

With many thanks to the rest of the group, especially to Kavish Kaup, Se Young and C. Y. Kwok for the great office environment.

Dedication

I dedicate this thesis to my lovely family and husband for their support.

Table of Contents

List of Figures xii

List of Tables xxii

List of Abbreviations xxix

1 Introduction 1

1.1 Energy . . . 1

1.1.1 Energy storage . . . 2

1.2 Batteries . . . 3

1.3 Working principles of Batteries . . . 3

1.4 All-Solid-State Batteries . . . 5

1.5 All-Solid-State Electrolytes . . . 7

1.5.1 Sodium Solid Electrolytes . . . 11

1.5.2 Lithium Solid Electrolytes . . . 13

2 Background 16

2.1 Diffraction Techniques . . . 16

2.1.1 X-ray diffraction . . . 16

2.1.2 Powder X-ray Diffraction . . . 18

2.1.3 Single Crystal X-ray Diffraction . . . 19

2.1.4 Time-of-Flight Neutron Diffraction . . . 21
2.2 Rietveld Refinement . . . 22
2.3 Electrochemical Impedance Spectroscopy . . . 25
2.3.1 Impedance . . . 25
2.3.2 Equivalent Circuit Elements . . . 27
2.3.3 Nyquist plots and equivalent circuit models . . . 30
2.4 DC polarization . . . 32
2.5 Thermal Analysis . . . 32
2.6 Vibrational spectroscopy:Raman . . . 33

3 Experimental Methods 35
3.1 Introduction . . . 35
3.2 Sample Preparation . . . 35
3.2.1 Mechanochemical route . . . 36
3.2.2 High-temperature . . . 37
3.3 Diffraction Techniques . . . 38
3.3.1 Powder and Single-crystal X-ray diffraction . . . 38
3.3.2 Time-of-Flight neutron diffraction . . . 38
3.4 Impedance Spectroscopy Measurements . . . 39
3.5 Differential scanning calorimetry measurements . . . 40
3.6 Raman Measurements . . . 40

4 Analysis of the structural and transport properties of $Na_{11}Sn_2PnS_{12}$ with Pn=P and Sb 41
4.1 Introduction . . . 41
4.2 $Na_{11}Sn_2PS_{12}$ . . . 42
4.2.1 Introduction . . . 42
4.2.2 Synthesis of $Na_{11}Sn_2PS_{12}$ . . . 44

4.2.3 Crystal structure of $Na_{11}Sn_2PS_{12}$ . . . 45
4.2.4 Ionic properties of $Na_{11}Sn_2PS_{12}$ . . . 46
4.3 $Na_{11}Sn_2SbS_{12}$ . . . 48
4.3.1 Introduction . . . 48
4.3.2 Synthesis of $Na_{11}Sn_2SbS_{12}$ . . . 48
4.3.3 Crystal structure of $Na_{11}Sn_2SbS_{12}$ . . . 49
4.3.4 Ionic and electronic properties of $Na_{11}Sn_2SbS_{12}$ . . . 54
4.4 Comparison between $Na_{11}Sn_2PnS_{12}$ with Pn=Sb and P . . . 56
4.5 Vacancies formation in $Na_{11}Sn_2PnS_{12}$ with Pn=Sb and P . . . 65
4.6 Air stability of $Na_{11}Sn_2PnS_{12}$ with Pn=Sb and P . . . 70
4.7 Summary . . . 72

5 Elucidating the structure-property relations in $Na_{11}Sn_2SbS_{12-x}Se_x$ 74
5.1 Introduction . . . 74
5.2 Synthesis . . . 75
5.3 Crystal structure . . . 75
5.4 Ionic and electronic properties . . . 82
5.5 Summary and Future Prospects . . . 90

6 Triggering fast lithium ion conduction in $Li_{4+x}P_{x-1}Si_xS_4I$ 92
6.1 Introduction . . . 92
6.2 Synthesis . . . 93
6.3 Crystal structure . . . 93
6.4 Ionic and electronic properties . . . 105
6.5 Summary and Future Prospects . . . 113

7 Revealing the effects of Al substitution on the structural and transport properties of $Li_{3+2x}P_{1-x}Al_xS_4$ **116**

7.1 Introduction 116

7.2 Synthesis 117

7.3 Crystal structure 117

7.4 Ionic and electronic properties 126

7.5 Summary 131

8 Final Thoughts **133**

References **135**

APPENDICES **151**

A Chapter 4 **152**

B Chapter 5 **163**

C Chapter 6 **174**

D Chapter 7 **185**

List of Figures

1.1 Schematic diagrams of the charge and discharge processes in a battery. Reproduced with permission of Dr. Lalere. 5

1.2 Schematic diagrams of two cell designs of ***Left:*** LIBs with cells connected in series; ***Right:*** ASSBs in a bipolar configuration. Reproduced from Ref. [10] with permission from the journal of Solid State Electrochemistry. . . . 6

1.3 Total ionic conductivity of various classes of Li-ion SEs. Reproduced from Ref. [35] with permission of The American Chemical Society. 8

1.4 Schematic diagram of point defects in a crystal. Reproduced from Ref. [40] with permission of Chinese Physics B journal. 9

1.5 Potential energy profile of mobile ions in crystalline SEs. Reproduced from Ref. [35] with permission of The American Chemical Society. 10

1.6 **a.** Na-ion diffusion in different compounds. Reproduced from Ref. [56] with permission of The Journal of Materials Science. **b.** Temperature-dependent ionic conductivities of various Na-ion SEs, including oxides and sulfides. Reproduced from Ref. [57] with permission of Royal Society of Chemistry. 13

1.7 Unit cell of $Li_{10}GeP_2S_{12}$: **a.** Data obtained from powder neutron diffraction (PND); **b.** Data obtained from single crystal XRD. Reproduced from Ref. [72] with permission of The Royal Society of Chemistry. 15

2.1 Schematic diagram of Bragg's law. 17

2.2 Schematic diagrams of PXRD geometries. 18

2.3 ***Left:*** XRD pattern of single crystal; **Right:** single crystal XRD technique summary. Reproduced from Ref. [80] with permission from the Rigaku Journal. 20

2.4 Schematic diagram of the different stages of structure determination from powder diffraction data. Reproduced from Ref. [74] with permission from The Angewandte Chemie International Edition. 24

2.5 The impedance Z plotted as a planar vector. Reproduced with permissions from Ref. [89]. Copyright 2001 John Wiley & Sons Ltd. 26

2.6 Diagram of the measurement and characterization of a material-electrode system. Reproduced from Re. [92] with permission from The Journal of Electroanalytical Chemistry and Interfacial Electrochemistry. 27

2.7 **a.** Equivalent circuit of the impedance spectrum; **b.** Nyquist plot exhibiting the bulk and grain boundary contributions to the impedance data as long with the diffusion line. Reproduced from Ref. [93] with the permission from The Chemical Physics Letters. 31

2.8 Nyquist plot exhibiting one arc at high-frequency. The total circuit is shown in black, while the individual components of the circuit are shown in blue and red. 31

2.9 Representation of a typical DSC curve. 33

3.1 **a.** The inside of a milling jar with ZrO_2 balls (grey) and sample powder (yellow). Reproduced from Ref. [100] with permission of Dr. Lalere; **b.** A pellet; **c.** A furnace used to perform the heat-treatments. Reproduced from Ref. [100] of Dr. Lalere. 36

3.2 **a.** A agate mortar used to hand grind the powder precursors. Reproduced from Ref. [100] with permission of Dr. Lalere; **b.** A pellet; **c.** A furnace used to perform the heat-treatments. Reproduced from Ref. [100] with permission of Dr. Lalere. 37

3.3 Schematic diagram of the impedance cell used for EIS measurements. Reproduced from Ref. [101] with permission of MS Houtarde. 39

4.1 View of the structure of $Na_{11}SnP_2S_{12}$ from single crystal XRD along two directions: **a.** [100]; **b.** [001]. The LGPS tetragonal unit cell is shown in dotted lines. Color code: SnS_4: blue; PS_4: light blue; S: yellow; Na(1) and Na(2): rose; Na(3), Na(4) and Na(5): red. 43

4.2 Comparison of the XRD patterns of different heat-treatments conducted on the targeted composition $Na_{11}Sn_2PS_{12}$, Bragg-Brentano geometry. 44

4.3 Pawley fit of single-phase polycrystalline $Na_{11}Sn_2PS_{12}$ (Bragg-Brentano geometry). The black points correspond to the data, and the red lines to the calculated pattern. The difference map is shown in blue. The calculated positions for Bragg reflections are marked by dark green vertical ticks. . . . 45

4.4 Nyquist plot of $Na_{11}Sn_2PS_{12}$ at 30°C showing the impedance data and the fit with the corresponding equivalent circuit (inset). 46

4.5 Arrhenius conductivity plot of $Na_{11}Sn_2PS_{12}$ from 20°C to 50°C. The inset displays the Nyquist impedance plot from 20°C to 50°C. 47

4.6 View of the structure of $Na_{11}Sn_2SbS_{12}$ along, **a.** [010], **b.** [100]; **c.** [001]. Thermal ellipsoids are drawn at 50% probability. Color code: Na(1) and Na(2): light-rose; Na(3), Na(4), and Na(5): red; Na(6): pink; Sn: blue; Sb: purple; S: yellow. SnS_4 and SbS_4 polyhedra are shown in blue and purple respectively. Reproduced from Ref. [114] with the permission of The American Chemical Society. 52

4.7 Rietveld refinement fit of $Na_{11}Sn_2SbS_{12}$ (Debye-Scherrer geometry). The black circles correspond to the data points, the red line denotes the calculated pattern and the difference map is shown in blue. Olive vertical ticks correspond to Bragg reflections. Two unknown tiny impurity peaks (at 15° and 30°) were excluded from the refinement. Reproduced from Ref. [114] with the permission of The American Chemical Society. 53

4.8 View of the diffusion channels: **a.** Formed by Na(4)-Na(3)-Na(1) sites along the *c*-axis; **b.** Along the *a,b*- plane formed by Na(4)-Na(2)-Na(4) or Na(3)-Na(2)-Na(3) at z=0; View of the interconnection points created by the Na(6): **c.** At z=0.87 between the diffusion channels formed by Na(1)-Na(5)-Na(1) chains; **d.** Along the *c*-axis between the diffusion channels that run along the *a,b*- plane. Color code: Na(1), Na(2): light-rose; Na(3), Na(4), Na(5): red; Na(6): pink. Reproduced from Ref. [114] with the permission of The American Chemical Society. 54

4.9 Nyquist plot of $Na_{11}Sn_2SbS_{12}$ at 30°C showing the impedance data and the fit with the corresponding equivalent circuit (inset). Reproduced from Ref. [114] with the permission of The American Chemical Society. 55

4.10 **a.** Arrhenius conductivity plot of $Na_{11}Sn_2SbS_{12}$ from 10°C to 60°C. The inset displays the Nyquist impedance plot from 10°C to 60°C. Reproduced from Ref. [114] with the permission of The American Chemical Society; **b.** DC polarization of $Na_{11}Sn_2SbS_{12}$ with an applied voltage of 0.35 V. 56

4.11 **a.** View of the structure of $Na_{11}Sn_2SbS_{12}$ based on single crystal data. Color code: Na(1) and Na(2): light-rose; Na(6): pink; Sn: blue; Sb: purple; S: yellow. SnS_4, SbS_4 polyhedra are shown in blue and purple respectively. **b.** View of the structure of $Na_{11}Sn_2PS_{12}$ based on single crystal data. PS_4 tetrahedra are shown in light blue. 57

4.12 Rietveld refinement fit of $Na_{11}Sn_2PS_{12}$ (Debye-Scherrer geometry). The black circles correspond to the data points, the red line denotes the calculated pattern, and the difference map is shown in blue. Olive vertical ticks correspond to Bragg reflections. 61

4.13 **a.** View of the interconnection between Na(1)-Na(6)-Na(2) sites. Transport bottlenecks in $Na_{11}Sn_2PnS_{12}$ with Pn=Sb and P: **b.** ***Top.*** Na(1)-Na(6) where the dotted S^{2-} anion lies just below the trigonal plane spanned by the other sulfur anions; ***Bottom.*** Na(2)-Na(6). The distance shown is for Sb-phase and the value in brackets is for P-phase. Reproduced from Ref. [114] with the permission of The American Chemical Society. 62

4.14 View of the interconnection points in $Na_{11}Sn_2SbS_{12}$ created by the Na(6) site along the *c*-axis between the diffusion channels that run along the *a,b*-plane (composed of Na(4)-Na(2)-Na(4) or Na(3)-Na(2)-Na(3)). Color code: Na(2): light-rose; Na(3), Na(4): red; Na(6): pink; SbS_4: purple. 64

4.15 Comparison of the XRD patterns of $Na_{11-x}Sn_{2-x}Sb_{1+x}S_{12}$ with x=0, 0.20, 0.25 and 0.5 (Bragg-Brentano geometry). The black vertical ticks correspond to the Bragg-reflections of Na_3SbS_4, unknown reflections are marked with an asterisk. Reproduced from Ref. [114] with the permission of The American Chemical Society. 66

4.16 **a.** Rietveld refinement fit of $Na_{10.8}Sn_{1.5}Sb_{0.5}PS_{12}$ (Debye-Scherrer geometry). The black circles correspond to the data points, the red line denotes the calculated pattern and the difference map is shown in blue. Gold vertical ticks correspond to the Bragg reflections of $Na_{11}Sn_2SbS_{12}$ and the black ticks to Na_3SbS_4; **b.** RT ionic conductivities of $Na_{11-x}Sn_{2-x}Sb_{1+x}S_{12}$ (x=0.20, 0.25 and 0.50). The inset displays the Nyquist impedance plot and fit with the respective equivalent circuit. Reproduced from Ref. [114] with the permission of The American Chemical Society. 67

4.17 Comparison of the XRD patterns of $Na_{11-x}Sn_{2-x}Sb_xPS_{12}$ with x=0, 0.3 and 0.5 (Bragg-Brentano geometry). The black vertical ticks correspond to the Bragg-reflections of Na_3Sb_4. 68

4.18 **a.** Rietveld refinement fit of $Na_{10.5}Sn_{1.5}Sb_{0.5}PS_{12}$ (Debye-Scherrer geometry). The black circles correspond to the data points, the red line denotes the calculated pattern and the difference map is shown in blue. Gold vertical ticks correspond to the Bragg reflections of $Na_{11}Sn_2PS_{12}$ and the black ticks to Na_3SbS_4; **b.** RT ionic conductivities as a function of composition of $Na_{11-x}Sn_{2-x}Sb_xPS_{12}$ (x=0, 0.30 and 0.50). The inset displays the Nyquist impedance plot and fit with the respective equivalent circuit. 69

4.19 **a.** XRD patterns of $Na_{11}Sn_2PnS_{12}$ with Pn=Sb and P before dry air exposure, after 24 h and 36 h (Bragg-Brentano geometry); **b.** Variation on the ionic conductivity versus exposure time. Reproduced from Ref. [114] with the permission of The American Chemical Society. 71

4.20 Comparative schematic diagram of the Na sites in $Na_{11}Sn_2PnS_{12}$ with Pn=Sb and P crystal structures illustrating the proposed role of the interstitial Na(6) site on the Na^+ ion transport mechanism. Reproduced from Ref. [114] with the permission of The American Chemical Society. 72

5.1 PXRD patterns of the as-milled $Na_{11}Sn_2SbS_{12-x}Se_x$ with x=1, 6 and 12 (Bragg-Brentano geometry). 76

5.2 ***Left:*** RT PXRD patterns of $Na_{11}Sn_2SbS_{12-x}Se_x$ (x=0, 1, 6 and 12) with unknown, Na_3SbS_4 and $NaSbSe_2$ impurities as labelled (Debye-Scherrer geometry); ***Right:*** Expanded view on the right showing the peak shift in the (408) reflection toward lower angles. 77

5.3 Unit cell parameters, a (Å) and c (Å), of $Na_{11}Sn_2SbS_{12-x}Se_x$ with x=0, 1, 6 and 12 obtained from single crystal XRD at 280 K. 77

5.4 **a.** and **b.** Q=S and Se occupancies on two *32g* Wyckoff sites as a function of Se content in $Na_{11}Sn_2SbS_{12-x}Se_x$ with x=0, 1, 6 and 12; **c.** $Sn(Q)_4^{3-}$ and $Sb(Q)_4^{3-}$ tetrahedral volume calculated with VESTA© using the data obtained from single crystal XRD at 280 K. 78

5.5 Rietveld refinement fit of $Na_{11}Sn_2SbS_{12-x}Se_x$ (Debye-Scherrer geometry): **a.** x=1, two unknown peaks at 15° and 30° were excluded from the refinement; **b.** x=6, with 4.75 wt% of Na_3SbS_4 phase; **c.** x=12, with 12.48 wt% of $NaSbSe_2$ phase. The black circles correspond to the data points, the red line denotes the calculated pattern, and the difference map is shown in blue. **d.** View of the structure of $Na_{11}Sn_2SbSe_{12}$ along the [100] and [001] directions. Thermal ellipsoids are drawn at 50% probability. Color code: Na(1) and Na(2): light-rose; Na(3), Na(4) and Na(5):red; Na(6): pink; Sn: grey; Sb: purple; Se: orange. SnS_4 and SbS_4 polyhedral are shown in grey and purple respectively. 80

5.6 Coordination environment of NaS_6 polyhedra in $Na_{11}Sn_2SbSe_{12}$. The dot circles denote Na sites. 81

5.7 View of the $Na_{11}Sn_2SbQ_{12}$ with Q=S and Se crystal structures along the *c*-axis displaying the difference in Na occupancy arrangement. 82

5.8 Arrhenius plots of the total conductivity of: **a.** $Na_{11}Sn_2SbS_6Se_6$ from 30°C to 65°C. The inset displays the Nyquist impedance plot from 30°C to 60°C; **b.** $Na_{11}Sn_2SbSe_{12}$ from 30°C to 60°C, the inset displays the Nyquist impedance plot from 30°C to 60°C. 83

5.9 RT Nyquist impedance plot and fit of $Na_{11}Sn_2SbS_{12-x}Se_x$ with x=1, 6 and 12 samples with the respective equivalent circuit. 84

5.10 **a.** RT ionic conductivity as a function of Se content in $Na_{11}Sn_2SbS_{12-x}Se_x$ with x=0, 1, 6 and 12; **b.** Activation energy; **c.** Sodium channel volume calculated with VESTA© using the data obtained from single crystal XRD at 280 K. 85

5.11 Bond lengths of $(SbQ)_4$ and $(SnQ)_4$ polyhedral as a function of Se content in $Na_{11}Sn_2SbS_{12-x}Se_x$ with x=0, 1, 6 and 12 obtained from single crystal XRD data at 280 K. The coordination environment of Sn corresponds to one of the three S/Se sites, S2/Se2. 86

5.12 **a.** DC polarization curves for electronic conductivity determination of $Na_{11}Sn_2SbSe_{12}$ with an applied voltage of 0.25 (orange), 0.50 (purple) and 0.75 V (grey); **b.** Linear fit of the voltage versus current. 88

5.13 **a.** BVSE model of Na^+ ion migration pathways visualized as isosurfaces of constant bond valence site energy along the *a,b*- plane; **b.** *c*-axis; **c.** View of the diffusion channels interconnecting Na(4)-Na(2)-Na(4) and Na(2)-Na(3)-Na(2) along the *a,b*- plane; **d.** Na(4)-Na(3)-Na(1)-Na(4) sites along the *c*-axis. Color code: Na(1), Na(3), Na(5): red; Na(4): light-rose. 89

5.14 DSC curve of $Na_{11}Sn_2SbSe_{12}$ and at a heating rate of $10°C \cdot min^{-1}$ up to 500°C. 90

6.1 **a.** View of the structure of $Li_{4.29}P_{0.71}Si_{0.29}S_4I$ along [001] from single crystal data; **b.** Environment of the Li(1) and Li(3) sites in $Li_{4.29}P_{0.71}Si_{0.29}S_4I$. Color code: Li(1), Li(2), Li(3) and Li(4): light rose; S: yellow, I:purple; $(P/Si)S_4$ polyhedra are shown in blue. 97

6.2 Raman spectra of $Li_{4.29}P_{0.71}Si_{0.29}S_4I$. 98

6.3 Environment of the Li(1) and Li(2) sites in Li_4PS_4I. Li(1) is 5-fold coordinated by four sulfurs and one iodine atom, Li(2) is 6-fold coordinated by four sulfurs and two iodine atoms. Color code: Li(1): light-rose; Li(2): dark rose; S: yellow, I: purple. 100

6.4 TOF neutron diffraction patterns and the corresponding Rietveld refinement fits of **a.** Li_4PS_4I, olive vertical ticks correspond to Li_4PS_4I and blue ticks to Li_2S (8.16wt%) Bragg reflections; **b.** $Li_{4.29}P_{0.71}Si_{0.29}S_4I$, blue vertical ticks correspond to Li_2S (9.6wt%) and green ticks to $Li_{4.29}P_{0.71}Si_{0.29}S_4I$ Bragg reflections. Two unknown diffraction peaks around 3.9 Å were excluded for the refinement. The black circles correspond to the data points, the red line denotes the calculated pattern, and the difference map is shown in blue. . . 101

6.5 Rietveld refinement fits of **a.** Li_4PS_4I, olive vertical ticks correspond to Li_4PS_4I Bragg reflections; **b.** $Li_{4.29}P_{0.71}Si_{0.29}S_4I$, purple vertical ticks correspond to LiI (3.8 wt%), blue to Li_2S (4.29 wt%), and green to $Li_{4.29}P_{0.71}Si_{0.29}S_4I$ Bragg reflections; **c.** $Li_{4.12}P_{0.88}Si_{0.12}S_4I$, purple vertical ticks correspond to LiI (2.32%), blue to Li_2S (1.47%), and orange to $Li_{4.12}P_{0.88}Si_{0.12}S_4I$ Bragg reflections. Two small reflections were omitted (17° and 27°). The black circles correspond to the data points, the red line denotes the calculated pattern, and the difference map is shown in blue (Debye-Scherrer geometry was used for **a-c**); **d.** PXRD pattern of the targeted $Li_{4.4}P_{0.6}Si_{0.4}S_4$ composition (Bragg-Brentano geometry), XRD pattern of Li_4SiS_4 shown in green, $Li_{4.29}P_{0.71}Si_{0.29}S_4I$ (olive vertical ticks), LiI (pink ticks), and Li_2S (blue ticks). 102

6.6 **a.** Li^+ vacancy concentration and Li content concentration as a function of Si content in $Li_{4+x}P_{1-x}Si_xS_4I$; **b.** Polyhedral volume of $(P/Si)S_4$ as a function of Si content in $Li_{4+x}P_{1-x}Si_xS_4I$. 103

6.7 Comparison between: **a.** Disordered small cell model; **b.** Highly ordered model as a function of Si content in $Li_{4+x}P_{1-x}Si_xS_4I$. The inset labels correspond to the lattice parameters:**a.** *a* (brown color) and *c* (blue color) ; **b.** Unit cell volume (pink color) and polyhedral $(P/Si)S_4$ volume (grey color); **c.** Li^+ vacancy (green color) and Li content (orange color) concentrations. 104

6.8 Nyquist impedance plot and fit of $Li_{4+x}P_{1-x}Si_xS_4I$ with x=0, 0.12, 0.29 and 0.40 with the respective equivalent circuit. 106

6.9 **a.** RT ionic conductivities as a function of composition in $Li_{4+x}P_{1-x}Si_xS_4I$ with x=0, 0.12, 0.29 and 0.40 (green color), and activation energies of x=0, 12, and 0.29 (blue color). Arrhenius conductivity plots, with the insets displaying the corresponding Nyquist impedance plots of: **b.** Li_4PS_4I from 30°C to 60°C; **c.** $Li_{4.29}P_{0.71}Si_{0.29}S_4I$ from 30°C to 60°C; **d.** $Li_{4.12}P_{0.88}Si_{0.12}S_4I$ from 30°C to 65°C. 107

6.10 DC polarization curves for electronic conductivity determination with an applied voltage of 0.25 (orange), 0.50 (purple) and 0.75 V (grey) of $Li_{4+x}P_{1-x}Si_xS_4I$: **a.** x=0; **b.** x=0.29. Linear fit of the voltage versus current of $Li_{4+x}P_{1-x}Si_xS_4I$: **c.** x=0; **d.** x=0.29. 108

6.11 Negative nuclear density distribution (of Li ions) in $Li_{4.29}P_{0.71}Si_{0.29}S_4I$ calculated using the MEM along **a.** [100]; **b.** [001]; **c.** [010] with the structure in the polyhedral motif along the *ac*-, plane showing the lithium diffusion along the *c*-axis through the chain formed by Li(4)-Li(3)-Li(3)-Li(4) sites and interatomic distances. 110

6.12 **a.** BVSE model of Li^+-ion migration pathways in $Li_{4.29}P_{0.71}Si_{0.29}S_4I$ along the [001], [010] and [100] directions visualized as isosurfaces of constant BVSE using the small cell model. The orange isosurface corresponds to a site energy characteristic of local hopping paths, while the yellow range isosurface corresponds to the long-range migration involving the i1 interstitial site; **b.** View of the structure of $Li_{4.29}P_{0.71}Si_{0.29}S_4I$ along the [001] direction, [010] and [100] directions, showing the Li(4)-Li(4) and Li(4)-i1 interatomic distances. 111

6.13 BVSE models of migration barriers of $Li_{4.29}P_{0.71}Si_{0.29}S_4I$. 112

6.14 Differential scanning calorimetry curves of $Li_{4.29}P_{0.71}Si_{0.29}S_4I$ and Li_4PS_4I at a heating rate of 10°C·min^{-1} up to 400°C. 113

6.15 Ionic conductivity as a function of Si content in $Li_{4+x}P_{1-x}Si_xS_4I$. View of the Li-ion sublattice of Li_4PS_4I (bottom left), and $Li_{4.29}P_{0.71}Si_{0.29}S_4I$ (top right), ... 114

7.1 PXRD patterns of $Li_{3+2x}P_{1-x}Al_xS4$ with x=0, 0.15, 0.20 and 0.33 (Debye-Scherrer geometry). The Li_5AlS_4 impurity is indicated by circle markers. . 118

7.2 Magnified view of the XRD patterns of **a.** $Li_{3.3}P_{0.85}Al_{0.15}S_4$ and β-Li_3PS_4 compounds of the 2θ=17.2° - 18.6° and 2θ=28.2° - 30.5° range; **b.** $Li_{3+2x}P_{1-x}Al_xS_4$ with x=0.15, 0.20 and 0.33. compounds of the 2θ =17.2° - 18.6° and 2θ = 28.2° - 30.5° range. 119

7.3 View of the structure of $Li_{3.3}P_{0.85}Al_{0.15}S_4$ from single crystal data along **a.** [100]; **b.** [010]. Color code: Li(1), Li(2), and Li(3): light rose; S: yellow, P:blue; (P/Al)S_4 polyhedra are shown in blue. Using the model obtained by single crystal data. 122

7.4 Rietveld refinement fits of $Li_{3+2x}P_{1-x}Al_xS_4$ (Debye-Scherrer geometry) and TOF neutron diffraction pattern shown in the inset: **a.** x=0.15, olive vertical ticks correspond to $Li_{3.3}P_{0.85}Al_{0.15}S_4$ Bragg reflections; **b.** x=0.20, purple vertical ticks correspond to Li_5AlS_4, and black to BN impurity coming from the BN crucible; **c.** x=0.33. The black circles correspond to the data points, the red line denotes the calculated pattern and the difference map is shown in blue; **d.** View of the $Li_{3.3}P_{0.85}Al_{0.15}S_4$ structure along the [001] direction obtained from TOF neutron data. 123

7.5 RT Nyquist impedance plot of $Li_{3+2x}P_{1-x}Al_xS_4$ with x=0.15, 0.20 and 0.33 with the respective equivalent circuit. 127

7.6 **a.** Arrhenius conductivity plot of $Li_{3.3}P_{0.85}Al_{0.15}S_4$ from 30°C to 70°C. The top inset displays the Nyquist impedance plot from 30°C to 70°C. The low inset shows the Arrhenius conductivity plot of another sample for x=0.15 from 30°C to 65°C, with the inset showing the Nyquist impedance plot from 30°C to 65°C; **b.** DC polarization curves for electronic conductivity determination of $Li_{3.3}P_{0.85}Al_{0.15}S_4$ with an applied voltage of 0.25 (orange), 0.50 (purple), and 0.75 V (grey). 128

7.7 Rietveld refinement fits of **a.** $Li_{3.3}P_{0.85}Al_{0.15}S_4$ (8.3 wt% amorphous content) mixed with 12 - 13 wt% of Si, which was used as an internal standard; **b.** Targeted $Li_{3.67}P_{0.67}Al_{0.33}S_4$ mixed with 15 - 17 wt% of Si (Debye-Scherrer geometry). 129

7.8 View of the structure of $Li_{3.3}P_{0.85}Al_{0.15}S_4$ along the [001] direction, and bond valence map of Li^+ ion migration pathways visualized as isosurfaces of constant bond valence site energy. The orange isosurface corresponds to a site energy characteristic of local hopping paths, while the yellow range isosurface corresponds to the long-range migration. 130

7.9 BVSE models of migration barriers of $Li_{3.3}P_{0.85}Al_{0.15}S_4$ along; **a.** *b*-axis. The Li(2) split site energies are referenced to zero as the lowest energy which is a relative, not absolute value. 131

7.10 Schematic diagram showing the higher ionic conductivity of $Li_{3.3}P_{0.85}Al_{0.15}S_4$ vs. bulk β-Li_3PS_4. View of the Li^+-ion diffusion pathway along the *b*-axis for each phase. 132

B.1 Temperature dependence of the bulk and grain boundary conductivity of $Na_{11}Sn_2SbSe_{12}$. 173

D.1 ^{31}P MAS-NMR spectrum of crystalline $Li_{3.3}P_{0.85}Al_{0.15}S_4$ at 850 MHz and 30 kHz MAS rate. The primary signal is at 81.5 ppm, with a shoulder centred at 84 ppm and a secondary signal at 89.3 ppm. 188

D.2 Linear fit of the voltage vs current of $Li_{3.3}P_{0.85}Al_{0.15}S_4$. 188

List of Tables

1.1 Conductivity of thio-LISICON electrolytes and other sulfide-based ionic conductors. . . . 14

4.1 Parameters of the fit for the impedance data of $Na_{11}Sn_2PS_{12}$ at RT. . . . 46

4.2 Experimental and predicted ionic conductivity and activation energy data of $Na_{11}Sn_2PS_{12}$ compared to other Na-ion thiophosphate conductors. . . . 47

4.3 Atomic coordinates, site occupation factors and equivalent isotropic displacement parameters of $Na_{11.08(8)}Sn_2SbS_{12}$ obtained from single crystal XRD at 280 K. . . . 49

4.4 Anisotropic displacement parameters ($Å^2$) of $Na_{11.08(8)}Sn_2SbS_{12}$ obtained from single crystal XRD at 280 K. . . . 50

4.5 Interatomic distances of $Na_{11.08(8)}Sn_2SbS_{12}$ obtained from single crystal XRD at 280 K. . . . 51

4.6 Parameters of the fit for the impedance data of $Na_{11}Sn_2SbS_{12}$ at RT. . . . 55

4.7 Site occupation factors and equivalent isotropic displacement parameters of ***Left***: $Na_{11.08(8)}Sn_2SbS_{12}$; ***Right***: $Na_{10.8(11)}Sn_2PS_{12}$ obtained from single crystal XRD at 280 K. . . . 58

4.8 Atomic coordinates, site occupation factors and equivalent isotropic displacement parameters of $Na_{11.08(10)}Sn_2PS_{12}$ obtained from single crystal XRD at 280 K. . . . 59

4.9 Anisotropic displacement parameters ($Å^2$) of $Na_{11.08(10)}Sn_2PS_{12}$ obtained from single crystal XRD at 280 K. . . . 59

4.10 Interatomic distances of $Na_{11.08(10)}Sn_2PS_{12}$ obtained from single crystal XRD at 280 K. . . . 60

4.11 Bottlenecks for Na^+-ion transport in $Na_{11}Sn_2PnS_{12}$ with P=Sb and P obtained from single crystal XRD data at 280 K. 63

4.12 Volume of the NaS_6 polyhedra in $Na_{11}Sn_2PnS_{12}$ with Pn=Sb and P obtained from single crystal XRD data at 280 K, calculated using VESTA©. 64

4.13 Parameters of the fit for the impedance data of $Na_{11+1}Sn_{2-x}Sb_{1+x}S_{12}$ with x=0.2, 0.25 and 0.5 at RT. 68

4.14 Parameters of the fit for the impedance data of $Na_{11-x}Sn_{2-x}Sb_xPS_{12}$ with x=0.3 and 0.5 at RT. 69

5.1 Atomic coordinates, site occupation factors and equivalent isotropic displacement parameters of $Na_{11.15(7)}Sn_2SbSe_{12}$ obtained from single crystal XRD at 280 K. 79

5.2 Anisotropic displacement parameters ($Å^2$) of $Na_{11.15(7)}Sn_2SbSe_{12}$ obtained from single crystal XRD at 280 K. 79

5.3 Volume of the $(Na6)S_6$ polyhedra in $Na_{11}Sn_2SbS_{12-x}Se_x$ with x=0, 1, 6 and 12 obtained from single crystal XRD data at 280 K, calculated using VESTA©. 81

5.4 Parameters of the fit for the impedance data of $Na_{11}Sn_2SbS_{12-x}Se_x$ with x=0, 1 and 6 at RT. 84

5.5 Weight fractions of phases present in $Na_{11}Sn_2SbS_{12-x}Se_x$ with x=1, 6 and 12 samples from the Rietveld refinement results. 87

6.1 Atomic coordinates, site occupation factors and equivalent isotropic displacement parameters of $Li_{4.14(10)}P_{0.88(6)}Si_{0.12(6)}S_4I$ obtained from single crystal XRD at 280 K. 94

6.2 Anisotropic displacement parameters ($Å^2$) of $Li_{4.14(10)}P_{0.88(6)}Si_{0.12(6)}S_4I$ obtained from single crystal XRD at 280 K. 94

6.3 Interatomic distances of $Li_{4.14(10)}P_{0.88(6)}Si_{0.12(6)}S_4I$ obtained from single crystal XRD at 280 K. 95

6.4 Atomic coordinates, site occupation factors and equivalent isotropic displacement parameters of $Li_{4.31(3)}P_{0.71(11)}Si_{0.29(11)}S_4I$ obtained from single crystal XRD at 280 K. 95

6.5 Anisotropic displacement parameters ($Å^2$) of $Li_{4.31(3)}P_{0.71(11)}Si_{0.29(11)}S_4I$ obtained from single crystal XRD at 280 K. 96

6.6 Interatomic distances of $Li_{4.31(3)}P_{0.71(11)}Si_{0.29(11)}S_4I$ obtained from single crystal XRD at 280 K. 96

6.7 Atomic coordinates, site occupation factors and equivalent isotropic displacement parameters of Li_4PS_4I obtained from single crystal XRD at 280 K. 99

6.8 Anisotropic displacement parameters ($Å^2$) of Li_4PS_4I obtained from single crystal XRD at 280 K. 99

6.9 Interatomic distances of Li_4S_4I obtained from single crystal XRD at 280 K. 100

6.10 Parameters of the fit for the impedance data of $Li_{4+x}P_{1-x}Si_xS_4I$ with x=0, 0.12, 0.29 and 0.4 at RT. 106

6.11 Conductivity and activation energy of $Li_{4.29}P_{0.71}Si_{0.29}S_4I$, Li_4PS_4I and other sulfide-based ion conductors. *ssr*:solid-state route, *scr*:soft chemistry route. 109

7.1 Atomic coordinates, site occupation factors and equivalent isotropic displacement parameters of $Li_{3.11(2)}P_{0.85}Al_{0.15}S_4$ obtained from single crystal XRD at 280 K. 120

7.2 Anisotropic displacement parameters ($Å^2$) of $Li_{3.11(2)}P_{0.85}Al_{0.15}S_4$ obtained from single crystal XRD at 280 K. Li3 site was refined isotropically. 120

7.3 Interatomic distances of $Li_{3.11(2)}P_{0.85}Al_{0.15}S_4$ obtained from single crystal XRD at 280 K. 121

7.4 Atomic coordinates, site occupation factors and equivalent isotropic displacement parameters of $Li_{3.33(2)}P_{0.85}Al_{0.15}S_4$ obtained from TOF neutron diffraction at 300°K. With lattice parameters a=12.9598(19) Å, b=8.0689(12) Å, c=6.1392(9) Å, and V=641.99(17) $Å^3$. 124

7.5 Unit cell parameters of $Li_{3.3}P_{0.85}Al_{0.15}S_4$ obtained from single crystal XRD at 280 K and of β-Li_3PS_4 obtained at 364 K. 125

7.6 Volumes of the LiS_x (x=4 and 6) and (P/Al)S_4 polyhedra for $Li_{3.3}P_{0.85}Al_{0.15}S_4$ and β-Li_3PS_4 compounds. The values for x=0.15 were taken from the single crystal X-ray diffraction data using VESTA. 125

7.7 RT ionic conductivity values of $Li_{3+2x}P_{1-x}Al_xS_4$ with x=0.15, 0.20 and 0.33 taken from **Table** D.2. 127

7.8 Parameters of the fit for the impedance data of $Li_{3+2x}P_{1-x}Al_xS_4$ with x=0.15, 0.20 and 0.33 at RT. 127

A.1 Crystallographic data for $Na_{11.01(11)}Sn_2SbS_{12}$ obtained from single crystal XRD at 200 K. . . . 153

A.2 Atomic coordinates, site occupation factors and equivalent isotropic displacement parameters of $Na_{11.01(11)}Sn_2SbS_{12}$ obtained from single crystal XRD at 200 K. . . . 154

A.3 Anisotropic displacement parameters ($Å^2$) of $Na_{11.01(11)}Sn_2SbS_{12}$ obtained from single crystal XRD at 200 K. . . . 154

A.4 Interatomic distances of $Na_{11.01(11)}Sn_2SbS_{12}$ obtained from single crystal XRD at 200 K. . . . 155

A.5 Crystallographic data for $Na_{11.09(9)}Sn_2SbS_{12}$ obtained from single crystal XRD at 273 K. . . . 156

A.6 Atomic coordinates, site occupation factors and equivalent isotropic displacement parameters of $Na_{11.09(9)}Sn_2SbS_{12}$ obtained from single crystal XRD at 273 K. . . . 157

A.7 Anisotropic displacement parameters ($Å^2$) of $Na_{11.09(9)}Sn_2SbS_{12}$ obtained from single crystal XRD at 273 K. . . . 157

A.8 Interatomic distances of $Na_{11.09(9)}Sn_2SbS_{12}$ obtained from single crystal XRD at 273 K. . . . 158

A.9 Crystallographic data for $Na_{11.08(8)}Sn_2SbS_{12}$ obtained from single crystal XRD at 280 K. . . . 159

A.10 Crystallographic data for $Na_{11.08(10)}Sn_2PS_{12}$ obtained from single crystal XRD at 280 K. . . . 160

A.11 Room temperature ionic conductivity values of $Na_{11}Sn_2PnS_{12}$ with Pn=Sb and P obtained by EIS of the pressed at 2 tons and 1.0 cm diameter pellets. The relative density of $Na_{11}Sn_2PnS_{12}$ was calculated using **Equations** A.1 and A.2. The SD and SE were calculated using **Equations** 2.29 and 2.30, respectively. . . . 162

B.1 Crystallographic data for $Na_{11.15(7}Sn_2SbSe_{12}$ obtained from single crystal XRD at 280 K. . . . 164

B.2 Crystallographic data for $Na_{11.09(10)}Sn_2SbS_{10.9(3)}Se_{1.1(3)}$ obtained from single crystal XRD at 280 K. . . . 165

B.3 Atomic coordinates, site occupation factors and equivalent isotropic displacement parameters of $Na_{11.09(10)}Sn_2SbS_{10.9(3)}Se_{1.1(3)}$ obtained from single crystal XRD at 280 K. . . . 166

B.4 Anisotropic displacement parameters ($Å^2$) of $Na_{11.09(10)}Sn_2SbS_{10.9(3)}Se_{1.1(3)}$ obtained from single crystal XRD at 280 K. . . . 166

B.5 Interatomic distances of $Na_{11.09(10)}Sn_2SbS_{10.9(3)}Se_{1.1(3)}$ obtained from single crystal XRD at 280 K. . . . 167

B.6 Crystallographic data for $Na_{11.12(10)}Sn_2SbS_{6.25(3)}Se_{5.75(3)}$ obtained from single crystal XRD at 280 K. . . . 168

B.7 Atomic coordinates, occupation factor and equivalent isotropic displacement parameters of $Na_{11.12(10)}Sn_2SbS_{6.25(3)}Se_{5.75(3)}$ obtained from single crystal XRD at 280 K. . . . 169

B.8 Anisotropic displacement parameters ($Å^2$) of $Na_{11.12(10)}Sn_2SbS_{6.25(3)}Se_{5.75(3)}$ obtained from single crystal XRD at 280 K. . . . 169

B.9 Interatomic distances of $Na_{11.12(10)}Sn_2SbS_{6.25(3)}Se_{5.75(3)}$ obtained from single crystal XRD at 280 K. . . . 170

B.10 Interatomic distances of $Na_{11.12(10)}Sn_2SbS_{6.25(3)}Se_{5.75(3)}$ obtained from single crystal XRD at 280 K. . . . 171

B.11 Room temperature ionic conductivity values of $Na_{11}Sn_2SbS_{12-x}Se_x$ with x= 1, 6 and 12 obtained by EIS of the pressed at 2 tons and 1.0 cm diameter pellets. The SD and SE were calculated using **Equations** 2.29 and 2.30, respectively. The relative density of $Na_{11}Sn_2SbS_6Se_6$ was calculated using **Equations** A.1 and A.2. . . . 172

C.1 Crystallographic data for $Li_{4.14(10)}P_{0.88(6)}Si_{0.12(6)}S_4I$ obtained from single crystal XRD at 280 K. . . . 175

C.2 Crystallographic data for $Li_{4.31(3)}P_{0.71(11)}Si_{0.29(11)}S_4I$ obtained from single crystal XRD at 280 K. . . . 176

C.3 Crystallographic data for Li_4PS_4I obtained from single crystal XRD at 280 K. 177

C.4 Atomic coordinates, site occupation factors and equivalent isotropic displacement parameters of $Li_{4.3(7)}P_{0.71}Si_{0.29}S_4I$ obtained from TOF neutron diffraction at 300 K. With lattice parameters a=8.5086(15) Å, c=5.9490(2) Å, Z=2 and V=430.69(2) Å^3. Due to the similar neutron scattering factors of Si and P (4.14 versus 5.13 fm), the Si/P ratio was fixed to the single crystal value, and the other parameters were freely refined except for a constrain on total Li occupancy for charge balance. 178

C.5 Atomic coordinates, site occupation factors and equivalent isotropic displacement parameters of Li_4PS_4I obtained from TOF neutron diffraction at 300 K. With lattice parameters a=8.47019(5) Å, c=11.84157(15) Å, Z=4 and V=849.562(15)Å^3. 178

C.6 Room temperature ionic conductivity values of $Li_{4+x}P_{1-x}Si_xS_4I$ with x=0, 0.12, 0.29 and 0.4 obtained by EIS of the pressed at 2 tons and 1.0 cm diameter pellets. The SD and SE were calculated using **Equations** 2.29 and 2.30, respectively. The relative density of $Li_{4.29}P_{0.71}Si_{0.29}S_4I$ was calculated using **Equations** A.1 and A.2. 179

C.7 Atomic coordinates, site occupation factors and equivalent isotropic displacement parameters of $Li_{4.09(16)}P_{0.89(5)}Si_{0.11(5)}S_4I$ -$Li_{4.12}P_{0.88}Si_{0.12}S_4I$- obtained from single crystal XRD at 280 K using the highly ordered model. . 180

C.8 Anisotropic displacement parameters (Å^2) of $Li_{4.09(16)}P_{0.89(5)}Si_{0.11(5)}S_4I$ obtained from single crystal XRD at 280 K using the highly ordered model. . 180

C.9 Interatomic distances of $Li_{4.09(16)}P_{0.89(5)}Si_{0.11(5)}S_4I$ obtained from single crystal XRD at 280 K using the highly ordered model. 181

C.10 Atomic coordinates, site occupation factors and equivalent isotropic displacement parameters of $Li_{3.81(1)}P_{0.71}Si_{0.29}S_4I$ -$Li_{4.29}P_{0.71}Si_{0.29}S_4I$- obtained from single crystal XRD at 280 K using the highly ordered model. An underestimation of Li content is observed (3.81 f.u.(Li) versus the targeted 4.29 f.u.(Li)) 181

C.11 Anisotropic displacement parameters (Å^2) of $Li_{3.81(1)}P_{0.71}Si_{0.29}S_4I$ obtained from single crystal XRD at 280 K using the highly ordered model. 182

C.12 Interatomic distances of $Li_{3.81(1)}P_{0.71}Si_{0.29}S_4I$ obtained from single crystal XRD at 280 K using the highly ordered model. 182

C.13 Atomic coordinates, site occupation factors and equivalent isotropic displacement parameters of $Li_{4.08(9)}PS_4I$ -Li_4PS_4I- obtained from single crystal XRD at 280 K suing the small cell model. 183

C.14 Anisotropic displacement parameters (Å^2) of $Li_{4.08(9)}PS_4I$ obtained from single crystal XRD at 280 K using the small cell model. 183

C.15 Interatomic distances of $Li_{4.08(9)}PS_4I$ obtained from single crystal XRD at 280 K using the small cell model. 184

C.16 Interatomic distances of the vacant site i1 at 0.75, 0.073, 0.903 in $Li_{4.29}P_{0.71}Si_{0.29}S_4I$ obtained from bond valence site calculations using the small cell model. 184

D.1 Crystallographic data for $Li_{3.11(9)}P_{0.85}Al_{0.15}S_4$ obtained from single crystal X-ray diffraction at 280 K. 186

D.2 Room temperature ionic conductivity values of $Li_{3+x}P_{1-x}Al_xS_4$ with x= 0.15, 0.20 and 0.33 obtained by EIS of the pressed at 2 tons and 1.0 cm diameter pellets. The SD and SE were calculated using **Equations** 2.29 and 2.30, respectively. 187

List of Abbreviations

EVs	Electric Vehicles
LIBs	Lithium Ion Batteries
ASSBs	All-Solid-State Batteries
SEs	Solid Electrolytes
RT	Room Temperature
1D, 2D, 3D	One, Two, Three Dimensional
AIMD	*ab initio* Molecular Dynamic
XRD	X-ray Diffraction
HSAB	Hard and Soft Acid and Base
SOF	Site Occupancy Fraction
PXRD	Powder X-ray Diffraction
TOF	Time-of-flight
PND	Powder Neutron Diffraction
EIS	Electrochemical Impedance Spectroscopy
AC	Alternating Current
DC	Direct Current
R	Resistance
C	Capacitance
CPE	Constant-Phase Element
DSC	Differential Scanning Calorimetry
f.u.	Formula Unit
ADPs	Atomic Displacement Parameters
E_a	Activation Energy
BVSE	Bond Valence Site Energy
MEM	Maximum-Entropy Method
SEM	Scanning Electron Microscopy

Chapter 1

Introduction

1.1 Energy

World energy demand and consumption continue increasing due to global progress in industry and technology. Accessible technology plays a critical role in our daily life as a way of improving social and economic development [1] [2] [3] [4]. To enhance energy needs considering not only the economics of energy resources, but also the impact on the environment, society is slowly moving towards seeking sustainable energy production methods [3] [5]. Energy generation, reduced air pollution from vehicles and reduction of greenhouse gas emissions are some of the aspects that must be considered when promoting alternatives to meet the developing world's growing energy needs [5].

Energy resources are split into two categories: nonrenewable and renewable. Nonrenewable energy comes from sources that cannot be replenished, i.e. fossil fuels such as coal, oil and natural gas [5]. Conventional energy sources based on fossil fuels have proven to be highly effective drivers of economic progress [6]. Thus, the economic growth of industrialized modern societies depends mostly on energy obtained from fossil fuels. As fossil fuels can be stored and transported easily, they are considered as an efficient fuel use to power commercial-industrial sectors, heat production and domestic electricity [5]. In the transportation sector mostly petroleum products i.e. gasoline, diesel and oil are preferred.

Excessive use of fossil fuels causes environmental issues that have negative effects on human activities all over the world [7]. Humankind is contributing through its economic and other activities to the increase in the atmospheric concentrations of various greenhouse gases. For example, CO_2 releases from fossil fuel combustion, methane emissions

from increased human activity and deforestation all contribute to the greenhouse effect [7]. Advanced technologies that promote environmental sustainability are thus critically important for achieving sustainable development and securing our common future [8]. Renewable energy technologies are considered a potential solution to the current environmental problems associated with harmful pollutant emissions [9].

Electric energy is one of the most important elements to meet the essential needs of modern life. The effect of a 24-h cut in electricity supplies to a city shows our dependence on this particularly useful form of energy. New advances in the extraction, conversion and storage of electricity may be the key to making renewable energy sources competitive with fossil fuels and improving environmental sustainability [5]. Electrochemical energy storage in the form of rechargeable batteries are believed to be the most efficient and feasible solution for different energy sectors such as transportation and stationary storage [10]. Batteries can solve power supply concerns with their mobile charge/discharge capabilities [11].

1.1.1 Energy storage

Since the discovery of electricity, effective approaches to store that energy for use on demand have been sought [12]. In traditional electrical power generation, energy produced must be consumed immediately otherwise it will be wasted. Additionally, the places where the electricity is generated are usually located far from the locations where it is consumed [7]. Generators are connected through power grids forming a power system. Since power lines are always needed, if a failure on a line occurs, the supply of electricity will be interrupted [13]. Moreover, intermittent renewable energy such as wind and solar cannot be stockpiled in the absence of energy storage systems and must also be used when available [13]. Therefore, there is a need for electrical energy storage systems which are to be charged at a time of less energy demand and discharged during high demand [13] [3].

Currently, batteries are the most widely used among the different energy storage technologies [14]. Battery energy storage solutions are designed for facilitating the transition to new ways of generating and distributing electricity. Batteries are not only used to power almost all portable electronic devices (laptops, cell phones, etc.), but also have been successfully implemented in transport applications [10]. The potential of battery technologies is represented in the case of electric vehicles (EVs), which are already commercialized. Battery performance has improved significantly in order to meet the challenges of practical EVs and utility applications (mobile devices) [15]. Each application will require distinct battery features; for large-scale storage the price of batteries plays an important role, while mobile

applications require small batteries (Wh/L), for transport applications weight (Wh/kg) will be an important factor. Other factors like safety, life-time and efficiency also are considered in deciding the type of battery that is suitable for a certain application demand [14] [16].

1.2 Batteries

In the 1800s Alessandro Volta discovered the first practical method of generating electricity; he developed the first electrochemical cell consisting of zinc and copper plates, between which an acid solution was added [10]. The movement of the zinc-ions between the two plates allows the transfer of electrons through an external circuit, generating electricity. Faraday was who identified the passage of charge through an electrolyte with motion of mobile ions [10].

Michel Faraday was also the first to discover solid electrolytes (1834) [17]; he recorded the transitions of two solids into highly ion-conducting states (Ag_2S at 177°C and PbF_2 near 500°C) [18]. Unaware of the difference between solids with mixed ionic/electronic conductivity, such as silver sulfide, and ionic conductors such as lead fluoride; Faraday discovered the first two members of the two classes [17]. In 1976 Michel O'Keeffe pointed out that Faraday's experiments appear to be the first observations of conduction materials that we now call solid electrolytes [10].

Following these discoveries, hundreds of combinations of materials were tested for battery applications [10]. Lithium-ion battery (LIB) technology was first commercialized in 1991 by Sony Corporation, comprising of a non-aqueous electrolyte, $LiCoO_2$ and graphite as cathode and anode materials, respectively [10]. LIBs facilitated a remarkable advance in portable electronics technology; however, the increasing energy demand requires further improvements of novel technologies such as LIB to ensure sustainable long-term energy generation, conversion and storage [10]. As the demand for high energy density electrochemical storage devices will most likely continue to increase, research and development of novel materials for battery technology applications are strongly needed.

1.3 Working principles of Batteries

A battery is a device consisting of one or more electrochemical cells that convert stored chemical energy into electrical energy. Each cell contains a positive electrode, or cathode, a

negative electrode, or anode and an electrolyte. The electrochemical roles of the electrodes reverse between cathode and anode depending on the direction of current flow through the cell. During discharge, the electrons flow from the anode through the external load to the cathode, where the electrons are accepted (**Figure** 1.1a). Thus, the role of the three primary functional components are summarized:

- *The cathode*: It is the electrode in a cell at which reduction reaction occurs. It takes up electrons from an external circuit.
- *The anode*: It is the electrode at which oxidation reaction occurs. It gives up electrons to the external circuit.
- *Electrolyte*: It is the medium that provides the conduction of ions between the anode and cathode electrodes; it is thus an ionic conductor and electronic insulator.

In rechargeable batteries, by applying an electrical source using an external circuit the ions and electrons will flow towards the anode. Therefore, during charge the current flow is reversed and oxidation takes place at the positive electrode and reduction at the negative electrode (**Figure** 1.1b). The transfer of electrons from anode to the cathode is driven by the electrical potential difference, also known as cell potential, between the two electrodes.

Conventional LIBs rely on an organic electrolyte composed of a lithium salt in an organic solvent, a graphite anode and a metal oxide cathode. At elevated temperatures the cathode decomposes and releases O_2 that can ignite the highly flammable organic liquid electrolyte, creating hazardous conditions including fire and explosion [19]. Hence, worldwide research efforts are focused toward the replacement of the currently used liquid electrolytes, with materials having higher performance in terms of safety, energy, power and cost [20]. Despite significant LIB advances, future progress may rely on a successor technology, i.e., all-solid-state batteries (ASSBs) [16].

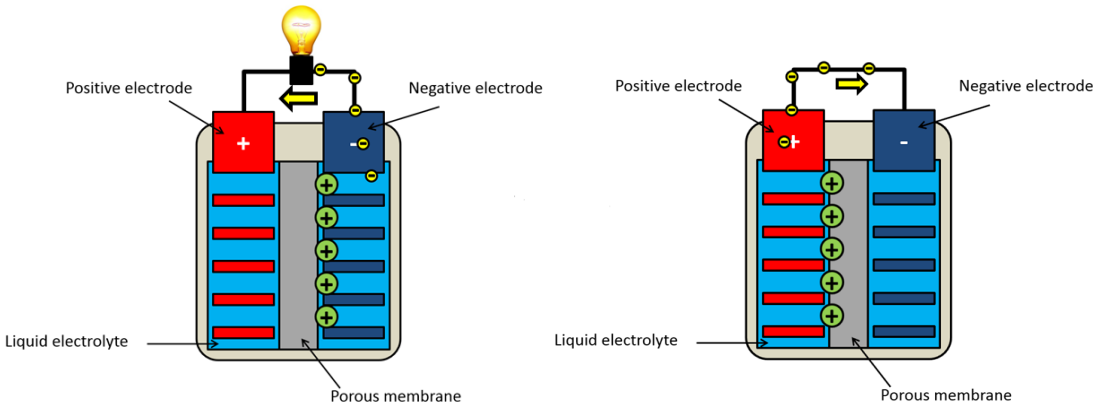

(a) Discharge **(b)** Charge

Figure 1.1: Schematic diagrams of the charge and discharge processes in a battery. Reproduced with permission of Dr. Lalere.

1.4 All-Solid-State Batteries

Among various electrochemical energy storage devices ASSBs have been proposed as a potential candidate for the next-generation technologies. The main proposed benefit of ASSBs is their increased safety, which stems from the absence of flammable liquid electrolytes [21] [22] [23] [16]. The use of inorganic solid-state electrolytes (SEs) rather than the flammable organic liquid electrolytes can potentially not only improve the safety, but also the performance of currently used LIBs due to the possibility of enabling the use of lithium metal as an anode [23] [24].

SEs are usually able to withstand high temperatures (80°C) [25]; as a result, in principle the maximum operating temperature of a solid-state cell is only limited by that of lithium, which melts at 180°C [26]. Moreover, ASSBs can be stacked within a single package by a bipolar configuration where the electrode materials (cathode and anode) are coated on the two sides of the current collector as shown in **Figure** 1.2 [10]. The bipolar stacking reduces the weight and volume of the battery package, increasing the energy density compared to a series connection of conventional LIBs (**Figure** 1.2) [27]. The packing configuration of ASSBs is thus suitable for applications requiring a high voltage and limited space, such as vehicle power sources [28].

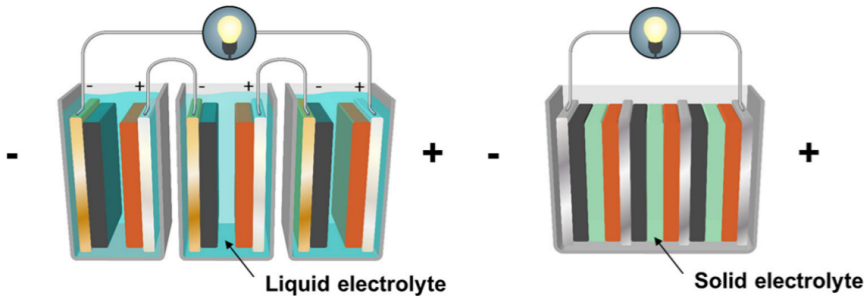

Figure 1.2: Schematic diagrams of two cell designs of ***Left:*** LIBs with cells connected in series; ***Right:*** ASSBs in a bipolar configuration. Reproduced from Ref. [10] with permission from the journal of Solid State Electrochemistry.

Despite fast growing interest in ASSBs, many challenges remain unsolved in both manufacturing and fundamental understanding of the technology. ASSBs typically show low capacities at high (dis)charge rates, which is attributed to the electrode-electrolyte interface. The poor rate and cycle performance of ASSBs are ascribed to high internal resistance for ion transfer over electrode-electrolyte interfaces (solid-solid) [29] [30]. Possible causes for the poor ionic diffusion over the interface are suggested to be a small effective contact area for charge transfer caused by the volume change of the electrode materials during dis(charge) and the formation of poorly conducting decomposition products [31]. Several strategies have been developed in order to form favorable solid-solid interfaces; and example of which includes coating of sulfide electrolytes via gas-phase or liquid-phase process on $LiCoO_2$ or graphite particles [32].

SEs play a crucial role in the realization of ASSBs, high ionic conductivity through the SE is another vital prerequisite for ASSBs with high electrochemical performances [30] [31]. Practical SEs should exhibit the following desired physical and chemical properties to be used in advanced ASSBs:

- High ionic conductivity (10^{-2} S·cm^{-1}) with negligibly electronic conductivity (10^{-9} S·cm^{-1}) [32].
- Chemically compatibility with both anode and cathode electrodes [32].
- Good mechanical stability. As an example, the Young's modulus, hardness and fracture toughness of glassy Li_2S-P_2S_5 solid electrolyte of 70:30 composition were reported to be 18.5(9) GPa, 1.9(2) GPa and 0.23(4) MPa·m$^{1/2}$, respectively [33].

- Wide range of an electrochemical potential window (5 V redox potentail) [21].
- Low interfacial resistance at the SE/electrode interface. The area specific resistance (ASR) of LIPON is as low as 10 $\Omega \cdot cm^{-2}$ with a thickness below 1 μm [34].
- Easy to scale up the synthesis, amiable for cost effective fabrication method, environmentally safe, and chemically stable under ambient condition [32].

1.5 All-Solid-State Electrolytes

The potential of SEs to improve battery safety as well as battery performance has led to the development of a wide range of solid ion conductors. As summarized in **Figure** 1.3 [35], several materials have been reported to show high ionic conductivities (10^{-3}-10^{-2} $S \cdot cm^{-1}$) at room temperature (RT), ionic conductivities comparable to those in currently used liquid electrolytes [36].

SEs can be divided in two major groups: inorganic solids -crystalline, glass and glass-ceramics- and organic solid polymers. Crystalline SEs consist of mobile-ions and metal/nonmetal ions that form the framework structure involving polyhedral units [37]. In an ideal crystal all constituent ions are stacked in a close-packed form; however, at non-zero temperature imperfections in the regular geometrical arrangement of ions exist. The degree of disorder can vary from one material to another or even from one temperature to another in the same material [38] [39]. As the temperature of the system increases, the contributions to the free energy from the entropy becomes more prominent. Entropy, as it is often described, is a measure of the degree of disorder of a system. Thus, the origin of the crystal defect arises from the system trying to minimize the free energy through an increase in the entropy [38].

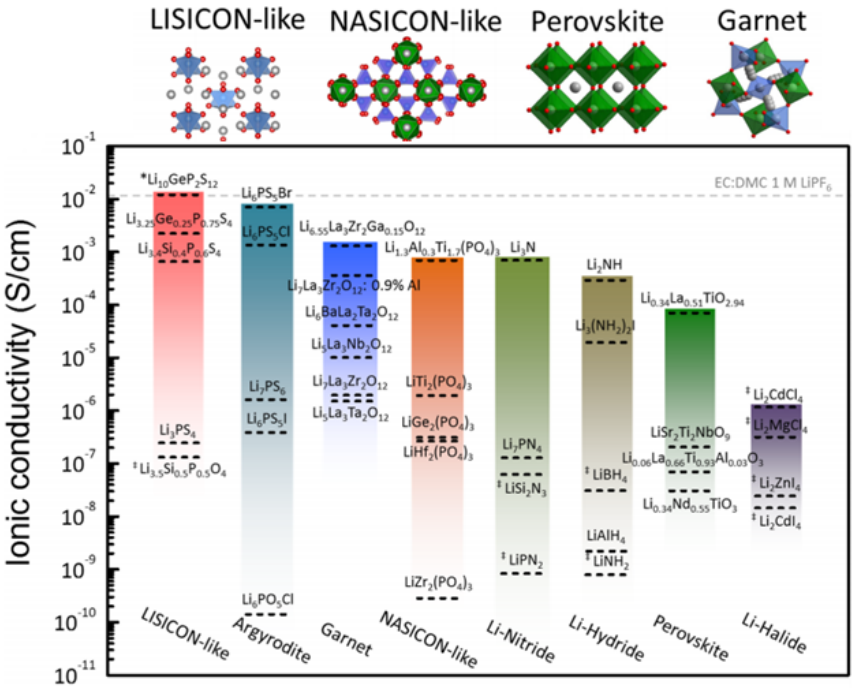

Figure 1.3: Total ionic conductivity of various classes of Li-ion SEs. Reproduced from Ref. [35] with permission of The American Chemical Society.

Generally two types of defects facilitate ion transport in the crystalline materials: Schottky and Frenkel defects (**Figure** 1.4 [40]). In the Schottky defect, two ions of opposite charge leave the lattice, resulting in the formation of vacant sites, which are the absence of ions from points that would normally be occupied in the crystal (**Figure** 1.4a) [40]. Any ion in the immediate vicinity of the vacancies can jump to one of the vacant sites, leaving the previous site vacant which could host another ion. This process is referred to as vacancy migration and leads to the transport of ions across the solid giving rise to conductivity [38]. In the Frenkel defect, an atom moves to a new position between other atoms of the solid, resulting in the formation of an interstitial site, which is the displacement of an ion from its normal lattice point to a nearby interstice (**Figure** 1.4b) [40]. The mechanism of which the ion moves through interstitial sites is termed as interstitial migration [38].

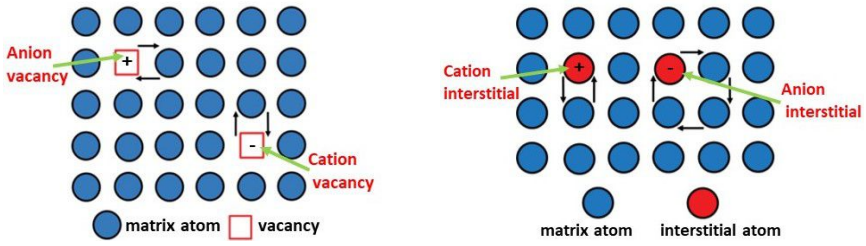

(a) Schottky defect **(b)** Frenkel defect

Figure 1.4: Schematic diagram of point defects in a crystal. Reproduced from Ref. [40] with permission of Chinese Physics B journal.

Current understanding of ion transport in solid materials is based on the classical diffusion model which describes ion diffusion as the hopping of an individual ion from one lattice site to another through inter-connected channels in the crystal framework [41]. The ion conduction is governed by the following equation:

$$\sigma = nq\mu \tag{1.1}$$

$$\mu \alpha e^{E_a/k_B T}, \tag{1.2}$$

where σ is the conductivity, n is the charge carrier concentration, q is the charge of the mobile ion, μ is the mobility, k_B is the Boltzmann's constant and E_a is the activation energy or energy barrier. The factors that influence the conductivity in solid state are the concentration of carriers, the availability of vacant-accessible sites which is controlled by the density of defects, and the ease with which an ion can jump to another site, which is controlled by the activation energy [38].The energy barrier greatly influences the ionic mobility and conductivity, where low energy barriers lead to high ionic mobility and conductivity. Ion diffusion is the migration of the mobile ion between stable sites (local minima) through a higher energy environment. The activation energy for migration is the highest energy along this path, which in good ionic conductors is the main component to the activation energy for long-range diffusion (**Figure** 1.5) [42] [35].

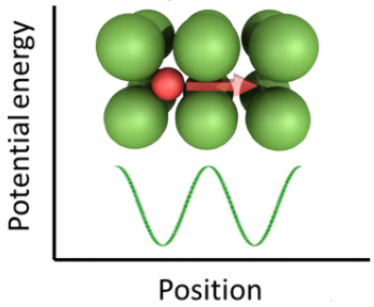

Figure 1.5: Potential energy profile of mobile ions in crystalline SEs. Reproduced from Ref. [35] with permission of The American Chemical Society.

The ionic conductivity of crystalline solids depends on the amount of defects, vacancies or interstitials, which is determined by the defect formation in stoichiometric ion conductors (intrinsic regime). In addition, vacancies or interstitials can also be created by aliovalent substitution. Although, the ionic conductivity can increase with larger concentrations of mobile-ions, the conductivity often reaches a maximum and starts to decrease as more mobile-ions are added, where it is suggested that their mobility is not independent of their concentration. Above the optimal concentration of substitution, the migration barrier surpasses the effect of high mobile-ion concentration and the conductivity decreases [35].

A crystalline SE in general should have the following characteristics [36]:

- High ionic conductivity $\geq 10^{-3}$ S·cm^{-1} or higher with negligibly electronic conductivity 10^{-9} S·cm^{-1} [32].
- High mobile ion transfer number (t_i close to unity).
- Low activation energy (<0.4 eV) for easy ion diffusion.
- Lager number of mobile ions as well as vacant sites.
- Vacant sites as well as occupied sites should have similar potential energies with low activation barrier for hopping between neighboring sites.
- High polarizability of the anion sublattice is beneficial for good cation mobility.

While oxide and sulfide compounds have both been extensively studied as inorganic electrolytes, sulfide-based solid electrolytes are particularly promising candidates [43] [24].

Sulfide electrolytes usually exhibit higher ionic conductivity (i.e., $\geq 10^{-3}$ S·cm^{-1}) than that of oxides. The lower electronegativity of sulfur versus oxygen (2.44 versus 3.5, Allred-Rochow scale) leads to a smaller electrostatic force between the mobile-ion and sulfur in the framework [37]; whereas the larger atomic radius of sulfur (1.84 Å versus 1.35 Å, Shannon-Prewitt radii) is beneficial for creating larger ion transport channels, meeting the primary requirements for fast ion migration [37].

Sulfides have the advantage of being ductile and often form glass-ceramic phases [44]. Thus, by cold-pressing, grain-boundary resistance can be greatly decreased, and even glassy grain-boundary free materials may be obtained [43]. The excellent mechanical properties for intimate contact between electrode and electrolyte and simpler manufacturing operations for processing into a film at low temperature, make them appealing for ASSB applications [24] [45] [46]. Moreover, sulfides-based SEs are synthesized at lower temperatures than oxide-based SEs, reducing the production cost [47]. A shortcoming of sulfide electrolytes is their lower chemical stability in air atmosphere. Sulfides tend to be decomposed by hydrolysis generating harmful H_2S gas. Suppression of hydrolysis of sulfides is thus an important task for developing sulfide electrolytes [47] [43].

1.5.1 Sodium Solid Electrolytes

The production of Li-ion ASSBs depends on the accessibility and abundance of lithium sources. The rising demand for lithium and limited supplies from selected regions (mainly in South America) could potentially compromise the market of Li-ion ASSBs batteries [37]. One of the promising alternatives is sodium due to its vast abundance versus lithium, making it a cheap viable option. Though Li-ion ASSBs are keenly sought for automotive batteries, sodium-ion ASSBs are more suitable for stationary low-cost energy storage systems [45] [37]. As a result, rechargeable sodium batteries have attracted extensive interest as low-cost sustainable alternatives to lithium batteries [45] [48].

Na-based SEs have been commercialized in high-temperature batteries such as β-alumina for Na-S batteries. However, the synthesis of this material involves multiple ball-milling and calcination steps with a final sintering treatment above 1600°C, in order to reduce the grain boundary resistance [22]. NASICON-type oxide materials have been reported with ionic conductivities over 1 mS·cm^{-1}, but the processing also requires high sintering temperatures [49]. Therefore, new SEs should be developed, as they are the key point in the realization of safe Na-ion ASSBs.

In 2012, a milestone in the development of Na-ion conductors was the stabilization of the high-temperature cubic phase (c-Na_3PS_4, $I4_3m$) by crystallization from the $Na_2S - P_2S_5$

glass system, which exhibited a high Na^+-ion conductivity and a low activation energy (0.2 mS·cm^{-1}, 0.28 eV) [45]. The tetragonal Na_3PS_4 phase was also synthesized ($P42_1c$, a=6.9520(4) Å and c=7.0757(5) Å) showing a conductivity one order of magnitude lower [50]. In contrast to the tetragonal phase, the cubic phase contains a three dimensional (3D) Na-ion conduction pathway, which is believed to be responsible for its higher conductivity.

The conductivity of c-Na_3PS_4 was subsequently improved by the partial substitution of Si for P, where the highest ionic conductivity was obtained at x=6 in (100-x)Na_3PS_4 ·xNa_4SiS_4 (0.74 mS·cm^{-1} at RT) [51]. Although, the reason behind the increase in ionic conductivity was not fully elucidated until Ong *et al.* successfully explained this phenomenon using *ab initio* molecular dynamic (AIMD) simulations [52]. Based on the study, the excess of Na ions creates a Na-ion disorder in the crystal framework, where the creation of an interstitial site is thus responsible for the increase in ionic conductivity of the c-Na_3PS_4 [53]. Moreover, Ong *et al.* predicted the effect of other M^{4+} doping (M= Ge and Sn) on the ionic conductivity of Na_3PS_4, $Na_{3.0625}Sn_{0.625}P_{0.9375}S_4$ was predicted to exhibit an ionic conductivity of 10.8 mS·cm^{-1} [52]. These studies proved that the presence of defects is essential to enable fast Na-ion diffusion in Na_3PS_4. Yu *et al.* reported partial substitution of P for As in $Na_3P_{1-x}As_xS_4$, with the highest ionic conductivity obtained at x=0.38 (1.46 mS·cm^{-1} at RT). $Na_3P_{0.62}As_{0.38}S_4$ was exposed to air with 15% humidity for 100 h in order to study its moisture stability. Based on the diffraction data, As substitution not only improved the ionic conductivity of Na_3PS_4 but also its stability under ambient conditions [53].

Anion substitution of S^{2-} with Se^{2-} is another strategy to improve conductivity. Zhang *et al.* experimentally demonstrated that Se-substitution on c-Na_3PS_4 leads to a high ionic conductivity of 1.16 mS·cm^{-1} and a low activation energy of 0.21 eV [54]. The larger ionic radius of selenium versus sulfur, 1.98 Å versus 1.84 Å (Shannon-Prewitt radii), causes the anion sublattice to increase in size, inducing a higher conductivity due to the generally enlarged size of the ion-migration channels [54]. The larger polarizability of Se weakens the binding energy between the mobile cation and the anion framework, leading to a more rapid ionic conduction [54]. Yoon Seok Jung *et al.* reported the substitution of P^{5+} for Sb^{5+} in the tetragonal Na_3PS_4 with a very high conductivity of 3 mS·cm^{-1} and stability in dry air, explained by the faster and stronger reactivity of P with O than Sb with O, based on the hard and soft acid and base theory (HSAB) [55]. Zhang's group successfully reported the synthesis of Sb and Se substituted Na_3SbSe_4 with a high ionic conductivity of 3.7 mS·cm^{-1} and low activation energy of 0.19 eV [56]. The schematic illustration of anion and cation size on Na-ion transport is shown in **Figure** 1.6a [56].

A wide variety of sodium oxides, selenides, and sulfides have been summarized in **Figure** 1.6b [57]. Despite considerable breakthroughs achieved on both theoretical and experi-

mental for sulfide-based Na-ion SEs, their RT ionic conductivities remain low. Nonetheless, sulfide-analogous Na-SEs are far less developed than Li-SEs motivating the development of Na-ion SEs, which could not only address this challenge but also improve their moisture stability [53].

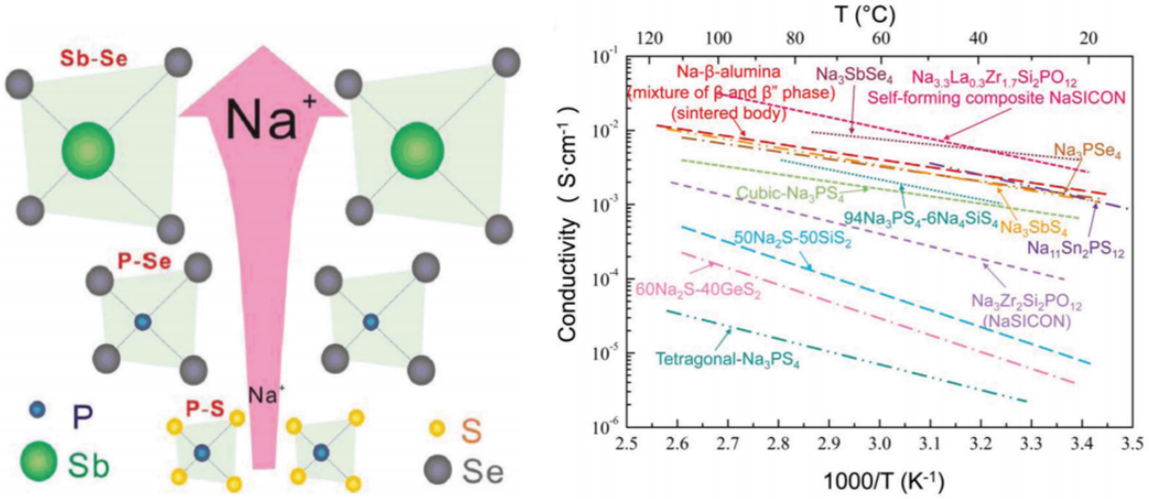

(a) Na-ion diffusion in different compounds

(b) Total ionic conductivity of various Na-ion SEs

Figure 1.6: a. Na-ion diffusion in different compounds. Reproduced from Ref. [56] with permission of The Journal of Materials Science. **b.** Temperature-dependent ionic conductivities of various Na-ion SEs, including oxides and sulfides. Reproduced from Ref. [57] with permission of Royal Society of Chemistry.

1.5.2 Lithium Solid Electrolytes

Lithium-ion-conducting SEs are currently most widely studied in the field primarily due to the importance of LIBs in industry since their commercialization in 1990. In both sodium and lithium systems, thiophosphate materials have inspired growing interest as SEs materials because of their high ionic conductivity and ductility, making them relatively easy to process without requiring high-temperature sintering. The thio-LISICON family of materials with the general formula $Li_xM_{1-y}M'_yS_4$ (M= Si, Ge; M'=P, Al, Zn, Ga, Sb) first developed by Kanno *et al.* exhibits ionic conductivities that go from 10^{-2} to 10^{-4} S·cm^{-1} [58] [59] [60]. These materials are closely related to the LISICON-type solid electrolyte γ-Li_3PS_4 with S^{2-} replacing O^{2-} [61], where the sulfide-type SEs show higher Li^+-ion

mobility and conductivities than the oxide-type counterparts [57]. The conductivities of thio-LISICON electrolytes and other sulfide crystalline materials are shown in **Table** 1.1.

Composition	**Conductivity S·cm^{-1}**	**Temperature (°C)**	**Ref.**
$\mathbf{Li_4GeS_4}$	2.0 x 10 $^{-7}$	25	[58]
$\mathbf{Li_{3.9}Zn_{0.05}S_4}$	3.0 x 10^{-7}	25	[58]
$\mathbf{Li_{4.275}Ge_{0.61}Ga_{0.25}S_4}$	6.5 x 10^{-5}	25	[58]
$\mathbf{Li_{3.25}Ge_{0.25}P_{0.75}S_4}$	2.2 x 10^{-3}	25	[62]
$\mathbf{Li_{4.8}Si_{0.2}Al_{0.8}S_4}$	2.0 x 10^{-7}	25	[59]
$\mathbf{Li_{4.8}Si_{0.2}Al_{0.8}S_4}$	2.0 x 10^{-7}	25	[59]
$\mathbf{Li_{2.2}Zn_{0.1}Zr_{0.9}S_3}$	1.2 x 10^{-4}	30	[63]
γ-$\mathbf{Li_3PS_4}$(crystal)	3.0 x 10 $^{-7}$	25	[61]
β-$\mathbf{Li_3PS_4}$ (nanoporous)	1.6 x 10^{-4}	25	[60]
$\mathbf{Li_2SiS_3}$	2.0 x 10^{-6}	25	[64]
$\mathbf{Li_4SiS_4}$	5.0 x 10^{-8}	25	[64]
$\mathbf{Li_6P_2S_4}$	1.6 x 10^{-10}	25	[65]
$\mathbf{Li_7PS_{11}}$	3.2 x 10^{-3}	25	[66]
$\mathbf{Li_4SnS_4}$	7.0 x 10^{-5}	20	[67]
$\mathbf{Li_{10}GeP_2S_{12}}$	1.2 x 10^{-2}	27	[68]
$\mathbf{Li_{10}SnP_2S_{12}}$	4.0 x 10^{-3}	25	[69]
$\mathbf{Li_{10}SiP_2S_{12}}$	2.3 x 10^{-3}	27	[70]
$\mathbf{Li_{10}Ge_{0.95}Si_{0.05}P_2S_{12}}$	8.6 x 10^{-3}	25	[28]
$\mathbf{Li_{9.54}Si_{1.74}P_{1.44}S_{11.7}Cl_{0.3}}$	2.5 x 10^{-2}	25	[71]

Table 1.1: Conductivity of thio-LISICON electrolytes and other sulfide-based ionic conductors.

Structural and chemical tuning via isovalent/aliovalent substitution of cations in the thio-LISICON family has led to steady increase in the lithium ion conductivity, as well as the discovery of new superionic lithium ion conductors. In 2011, Kamaya *et al.* reported the synthesis and crystal structure of $Li_{10}GeP_2S_{12}$ (LGPS) with a remarkable high ion conductivity of 12 mS·cm^{-1} at RT [68]. The structure of the electrolyte was determined by Rietveld refinement against the powder diffraction data, consisting of PS_4 and $(Ge/P)S_4$ tetrahedra surrounded by LiS_4 tetrahedrons and LiS_6 octahedra, with unit cell parameters a=8.71771(5) Å, c=12.63452(10) Å and $P4_2/nmc$ space group (see **Figure** 1.7a). The $(Ge/P)S_4$ tetrahedrons are connected to LiS_6 octahedra forming 1-dimensional (1D) chains along the c-axis, which are connected by PS_4 tetrahedrons. The tetrahedrally coordinated Li(1) and Li(3) sites form channels for facile Li-ion diffusion along the c-axis while it is

assumed that the octahedrally coordinated Li(2) position is inactive for diffusion [68].

In 2013, Lotsch *et al.* reported the first single structure analysis of the tetragonal LGPS structure, revealing significant differences concerning the Li positions (**Figure** 1.7b) [72]. An extra Li site was identified (Li(4)) with a site occupancy factor (SOF) of 0.77(6). As a result, the occupancies of the Li sites were significantly different from those obtained by the first reported structure data. Based on the single crystal diffraction data, it was suggested that the Li(4) site lies between the 1D Li channels (formed by Li(1) and Li(3) sites), thus forming diffusion pathways connecting the channels along the *c*-axis. [72].

Powder and single crystal XRD are robust methods for the determination of crystal structures of materials. Single crystal diffraction is regarded to be the most powerful technique for determining crystal structures [73] [74]; although, since not all materials can be prepared in the from of single crystals of suitable size and quality, powder diffraction techniques have become essential to study the structural properties of these materials [73]. Remarkable improvements in the determination of crystal structures by powder diffraction techniques have been achieved through advancements in instrumentation and algorithm development [74].

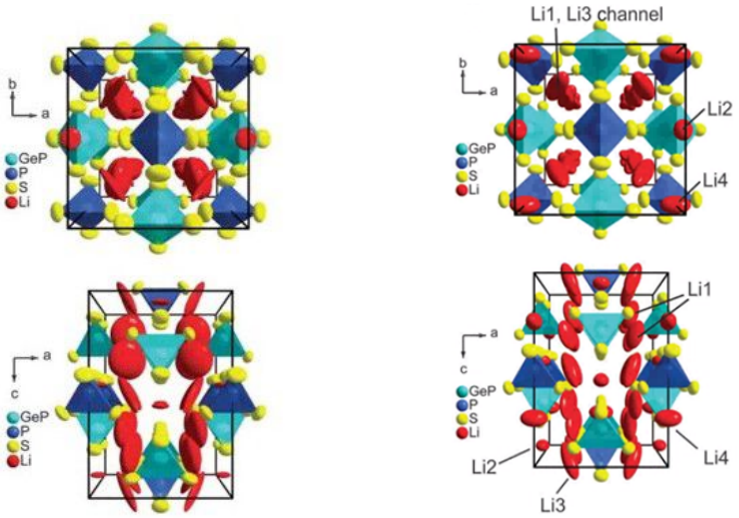

(a) Neutron powder **(b)** Single crystal XRD

Figure 1.7: Unit cell of $Li_{10}GeP_2S_{12}$: **a.** Data obtained from powder neutron diffraction (PND); **b.** Data obtained from single crystal XRD. Reproduced from Ref. [72] with permission of The Royal Society of Chemistry.

Chapter 2

Background

2.1 Diffraction Techniques

2.1.1 X-ray diffraction

A crystal structure consists of an ordered arrangement of atoms in a pattern that repeats periodically in 3D space. Knowledge of how atoms are arranged into crystals structures is the foundation on which we build our understanding of the properties of materials [75]. XRD is an important technique in solid state chemistry used for the fingerprint characterization of crystalline materials and for the determination of their crystal structures [75]. X-rays are electromagnetic radiation with energy $E=hc/\lambda$, for which the wavelength is on the order of magnitude of $\sim$1 Å (10^{-10} m). The fact that crystals with their regular repeating structures are made of atoms with an interatomic separation also on the order of $\sim$1 Å explains why XRD is a powerful technique for crystal structure determination [75].

Bragg approach has been used to treat diffraction by crystals and it regards crystals as built up in layers or planes. Diffraction occurs as a result of the interaction between X-rays and atoms; precisely, between the electron clouds around the atoms and the X-rays. The incident X-ray beam sets each electron of an atom into vibration, and the vibrating electron emits radiation that can interfere constructively or destructively [75]. Constructive interference takes place when the diffracted beams are in-phase with each other, whereas destructive interference or cancellation occurs when diffracted beams are out-of-phase, at angles of incidence different that the Bragg angle. As illustrated in **Figure** 2.1 [76] a constructive interference requires the crystal plane spacing d, wavelength λ and beam angle θ to satisfy the following Bragg's law relationship:

$$2d_{hkl}sin\theta_{hkl} = n\lambda \tag{2.1}$$

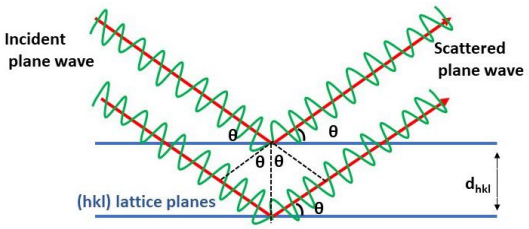

Figure 2.1: Schematic diagram of Bragg's law.

Coherent scattering can be elastic where the wave is deflected by the electron without loss of energy and, therefore, without change of wavelength, and inelastic where a loss of energy and a longer wavelength are observed. The inelastic interaction between X-rays with electrons gives Compton scattering, which provides a background intensity in XRD patterns. The more loosely held valence electrons of an atom are the ones that can participate in Compton scattering.

Intensities of XRD contain important information about the crystal structure of materials. Since scattered X-rays are the resultant of the waves scattered by each electron in the atom, the scattered intensity is then the sum of the individual intensities [75]. The scattering factor (scattering power) of an atom is proportional to its atomic number Z, the number of electrons possessed by that atom [77]. The dependence on the position of the atoms in the unit cell and the scattering power is giving by the structure factor of a reflection, which can be obtained by:

$$F_{hkl} = \Sigma f_j exp[2\pi i(hx_j + ky_j + lz_j)], \tag{2.2}$$

where f is the atomic scattering factor (which dependents on the atom type and the scattering angle), (hkl) is the Miller index of the plane, (x,y,z) is the fractional coordinates of the atom [77]. The intensity of the peak is related to the structure factor via the following equation:

$$I = AF^2, \tag{2.3}$$

where A includes other factors such as polarization (angular dependence of intensity scattered by electrons), absorption and temperature.

2.1.2 Powder X-ray Diffraction

PXRD provides accurate information about the structure of materials. The fact that different structural features of a material have different effects on various parameters of its powder diffraction pattern makes this technique so powerful [78]. In the PXRD method a beam of X-rays is focused on the powdered samples (polycrystalline materials) that, ideally, have crystals randomly arranged in all orientations [75]. The same way, the different lattice planes are also present in every possible orientation. For each set of planes, some crystals are thus oriented at the Bragg angle, θ, to the incident beam and thus, constrictive scattering occurs [77]. However, if the sample has some preferred orientation, the diffraction of some planes will be favored and the intensity of these reflections will be larger than expected [75]. Therefore, in order to ensure to avoid preferred orientation effects, the Debye-Scherrer method has been developed.

Debye-Scherrer geometry employs a parallel beam and the sample has a roughly cylindrical symmetry (**Figure** 2.2a). The sample is contained in a glass capillary which rotates while the X-ray source and detector move $-\theta$ and θ degrees. The main advantage of this geometry is that it is easy to rotate the sample around its axis, thereby eliminating preferred orientation effects. Moreover, this method enables the study of air sensitive materials by sealing the powder in a capillary under the inner atmosphere. In Debye-Scherrer geometry, X-rays penetrate the sample, therefore, this geometry is sensitive to the effect originating from the absorption of the sample. In contrast, Bragg-Brentano geometry which works on reflection is the method of choice for strongly absorbing samples.

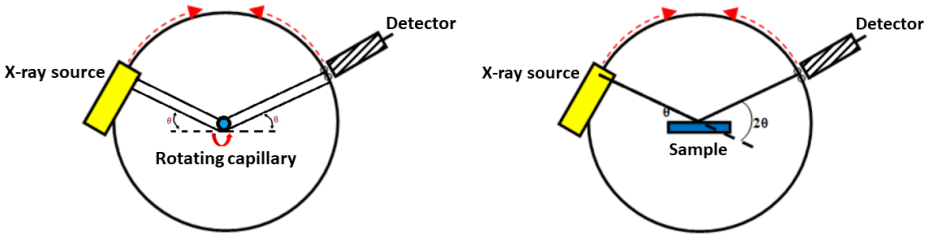

(a) Debye-Scherrer **(b)** Bragg-Brentano

Figure 2.2: Schematic diagrams of PXRD geometries.

In Bragg-Brentano geometry the powder sample is mounted on a flat holder (**Figure** 2.2b), with the X-ray source and detector moving $-\theta$ and θ degrees with respect to the sample stage plane. Although this geometry is the method of choice for strongly absorbing samples, it is sensitive to preferred orientation effects as mentioned above. Both diffraction

geometries were used in the development of the present work (**Figure** 2.2). In the case of Bragg-Brentano geometry, the holders were covered with kapton film in order to prevent air exposure of the sensitive samples. Measurements were performed with a PANalytical Empyrean diffractometer with Cu-Kα radiation. In both diffraction geometries d and θ are the variables at a fixed λ.

The two variables in a powder diffraction pattern are peak position and intensity A diffraction pattern from a material typically contains many distinct peaks, each corresponding to a different d-spacing [75]. As a result of Bragg's law, the position of the diffraction peaks are governed by the values of the unit cell parameters (a, b, c, α, β and γ); while the diffraction peak intensities are directly related to the electron density of the atoms. In an ideal PXRD pattern, obtained from perfect crystals, the Bragg peaks will be extremely sharp, although in practice such perfection is not realized and typically the peaks in powder diffraction patterns are broad [75].

Processing of the data by fitting peak shapes to a suitable peak function is required to obtain both peak positions and intensities. The observed peaks are well described by a peak shape function that considers instrumental and sample contributions, since the peak broadening comes from these two sources [78]. The instrumental broadening depends on geometrical parameters such as geometry and location of the source, slits, etc., the wavelength dispersion accounts for the distribution for the wavelength in the source, and the specimen contribution originates from the crystallite size. A crystal lattice consists of a set of arranged points related to each other by translational symmetry. The lattice sites represent the locations of the atoms or ions, which are connected to the nearest equivalent atoms by vectors. There are fourteen types of lattices, Bravais lattices, used to describe the arrangement of atoms in a crystal; these lattices are a combination of the seven crystal systems: triclinic, monoclinic, orthorhombic, tetragonal, trigonal, cubic and hexagonal, and lattice centering. Each crystalline phase has a characteristic powder pattern which is used to solve the 3D crystal structure(s) of the phase(s) present in the powder. Each phase corresponds to one of the seven crystal systems, which describes the symmetry of the crystal. The details of the Rietveld method for crystal structure determination are presented below.

2.1.3 Single Crystal X-ray Diffraction

Single crystal XRD is an analytical technique which provides the exact atomic positions, and thus bond lengths and angles of crystalline materials [79]. X-ray diffractometers consist of three components, X-ray source, a sample holder and an X-ray detector. When the

geometry of the incident X-rays directed onto the sample satisfies Bragg's law, constructive diffraction occurs [79]. Samples are mounted on thin glass fibers which are attached to brass pins and mounted onto goniometer heads. Adjustment of the X,Y,Z orthogonal directions is required in order to center the crystal within the X-ray beam, as shown in [79]. The intensity of the diffracted X-rays is recorded by rotating the crystal. A crystal is illuminated with an X-ray beam, producing diffracted spots (black dots shown in the left side of **Figure** 2.3). From the position and intensity of these diffraction spots, electron density distributions in crystals can be obtained [80]. With the electron density and chemical composition data of the sample a crystal structure model is constructed (**Figure** 2.3 [80]).

Crystal twinning is a major concern in single crystal diffraction studies; many crystals grow intrinsically in a twinned manner [74]. It is thus important to optimize crystal-growth strategies in order to obtain crystals of appropriate size and quality. By obtaining a well diffracting crystal good results can be assured; in contrast, low quality crystals often lead to the difficulties in solving structure structures [80]. This requirement imposes a limitation on the types of materials that may be investigated by this technique; some crystalline materials give rise to good quality PXRD data but are not suitable for single crystal diffraction studies [74].

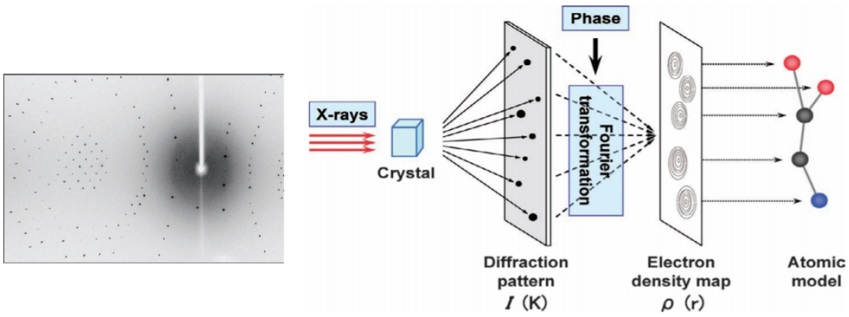

Figure 2.3: ***Left:*** XRD pattern of single crystal; **Right:** single crystal XRD technique summary. Reproduced from Ref. [80] with permission from the Rigaku Journal.

Since single crystal XRD is a powerful technique for accurate elucidation of crystal structures [74], the synthesis protocols conducted in the present work for the development of the Na and Li SEs were designed to favor single crystal growth. Each sample synthesized in the present work resulted in agglomerates of crystals that were gently selected from the reaction product for single crystal studies.

Bond valence site energy (BVSE) calculations are widely used to identify the potential migration pathways of mobile-ion in the crystal structures of SEs. The regions of low bond valence site energy that connect to form migration pathways for mobile-ions are identified by E_{BVSE}(mobile-ion). In the present work, the single crystal data of the $Na_{11}Sn_2SbSe_{12}$, $Li_{4.29}P_{0.71}Si_{0.29}S_4I$, and $Li_{3.3}P_{0.85}Al_{0.15}S_4$ SEs were used as a input for the BVSE calculations utilizing the SoftBV program with the bond valence parameter set developed by S. Adams *et al.* [81] [82]. BVSE calculations were performed in order to analyze the potential Na^+/Li^+ migration pathways in these SEs. Mobile-cation diffusion pathways were visualized as isosurfaces of constant bond valence site energy, where local hopping paths and long-range migration with isosurface levels of 0.8 eV and 0.4 eV, respectively, for $Na_{11}Sn_2SbSe_{12}$, 1.7 eV and 1.9 eV for $Li_{4.29}P_{0.71}Si_{0.29}S_4I$, and 1.8 eV and 2.3 eV for $Li_{3.3}P_{0.85}Al_{0.15}S_4$ SEs were used.

2.1.4 Time-of-Flight Neutron Diffraction

Time-of-flight (TOF) is a valuable technique that can provide information that is not available with other techniques. Neutron beams are usually of low intensity and therefore the sample size required for characterization is relatively large 1 mm^3. Since crystals of this size are often difficult to grow, the crystallographic studies are conducted on polycrystalline samples. Due to the wave-particle duality of elementary particles, giving the de Broglie relation:

$$\lambda = \frac{h}{mv}, \tag{2.4}$$

where m is the mass of the neutron (1.675×10^{-27} kg), and h is Planck's constant, combining this equation with Bragg's law:

$$\frac{h}{mv} = \frac{ht}{mL} = 2dsin\theta, \tag{2.5}$$

The energy and wavelength of the neutrons depend on their velocity which make it possible to select a specific wavelength. The neutrons that are used for diffraction referred as "thermal" (neutron type) have a wavelength of the order of 0.5 Å to 3 Å and an energy of the order of 5-100 meV. In order to have monochromatic neutrons for conventional diffraction techniques, it is necessary to select a particular wavelength and filter out the reminder, resulting in a waste of most of the available neutron energy. In order to overcome this drawback, an advance has been developed which uses pulsed neutron sources coupled

with time-of flight analysis. Neutrons are obtained using particles accelerators to bombard a heavy metal target with high-energy particles such as protons, giving a high neutron flux suitable for diffraction experiments [75]. Instead of changing the diffraction angle θ and fixing λ as in XRD, the entire neutron spectrum (variable wavelength) is used with a fixed θ. Since neutron wavelength depends on velocity, the diffracted radiation arriving at the detector is separated according to its time of flight and wavelength [83].

The scattering powers of atoms towards neutrons are different from those towards X-rays. Unlike X-rays, neutrons interact with the atomic nuclei instead of the electrons of the atom, resulting in different scattering factors [75]. The neutron scattering is equivalent to the effective area presented by the nucleus to the passing neutron [83]. Because in X-rays the scattering power is a function of atomic number, light atoms such as hydrogen diffract X-rays weakly; in contrast hydrogen is a strong scatter of neutrons. Neutron diffraction is also used to distinguish atoms that have similar atomic numbers, since the scattering powers of those atoms may be different [75].

2.2 Rietveld Refinement

Rietveld refinement method was developed in the 1960s by Hugo Rietveld and first reported at the seventh congress of the International Union of crystallography in 1969 [84] [85]. Since then, it has been a widely used method for structure refinement from X-ray and neutron diffraction data. Rietveld refinement uses a least squares approach for modelling a full diffraction profile based on structural parameters of the crystalline sample and instrument effects [86]. While the least square method minimizes the difference between experimental and calculated data, the Rietveld method optimizes the crystal structure model so it has a closer resemblance to the observed data [86].

A powder diffraction pattern is a set of peaks superimposed on a varying background, the contribution of each of the Bragg reflections (Y_h h=hkl) and the background (Y_b) to the observed intensity at every step in the diffraction pattern is expressed by the following equation [86]:

$$Y_c = Y_b + \Sigma Y_h, \tag{2.6}$$

where Y_c is the calculated fit. The Bragg contributions are described by a certain peak shape, i.e. Gaussian or Lorentzian shape, while the background is normally described by a polynomial function. The aim is to match the positions and the intensities of the peaks in the observed diffraction pattern to a calculated diffraction pattern (which is based on the

structural model). Parameters are varied by a least-squares minimization of the weighted differences between the experimental and calculated powder diffraction pattern. The least squares minimization function is described as [86]:

$$M = \Sigma w(Y_o - Y_c)^2, \tag{2.7}$$

where w is a weight factor which depends on variance of the observed data (Y_o) and Y_c. To assess the agreement between the calculated and experimental diffraction data, meaning, the quality of the least squares refinement is indicated by some residual functions: [86]:

$$R_p = \frac{\Sigma \mid Y_o - Y_c \mid}{\Sigma Y_o} \tag{2.8}$$

$$R_{wp} = \sqrt{\frac{M}{\Sigma w(Y_o)^2}} \tag{2.9}$$

The weighted residual, R_{wp}, contains the minimisation function M.

$$R_{exp} = \sqrt{\frac{N_{obs} - N_{var}}{\Sigma w(Y_o)^2}} = \frac{R_{wp}}{\sqrt{X^2}}, \tag{2.10}$$

where N_{obs} is the number of observations (data points), and N_{var} is the number of variables in the model. The "goodness of fit" X^2 is defined [86]:

$$X^2 = \frac{M}{N_{obs} - N_{var}} = (\frac{R_{wp}}{R_{exp}})^2 \tag{2.11}$$

The X^2 will be approximately unity for an optimal refinement [86].

Structure refinement is the last stage in crystal structure determination from diffraction data, number one is determination of the unit cell dimensions (indexing), number two is symmetry determination (space group assignment) and number three is structure solution. The position of the peaks of the diffraction pattern is required for determining the unit cell (a,b, c, α, β and γ), whereas consideration of the relative peak intensities is required for space group assignment, structure solution and structure refinement. During structure solution the aim is to derive an approximate structural model; if this approximate model is a good representation of the actual structure, a good quality structural model can be obtained by refining it against the diffraction data (structure refinement) [74]. A schematic representation to illustrate the different stages of structure determination from powder diffraction data is shown in **Figure** 2.4 [74].

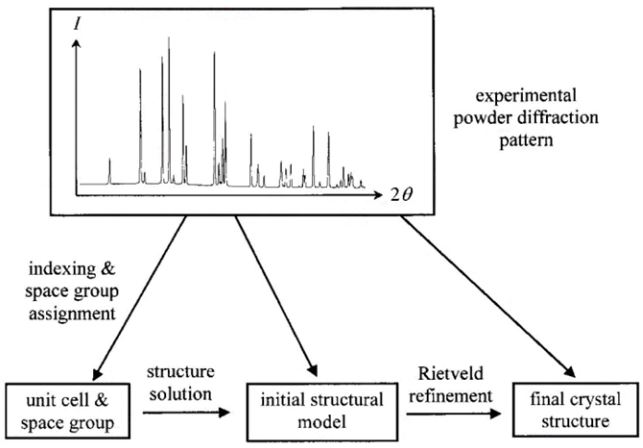

Figure 2.4: Schematic diagram of the different stages of structure determination from powder diffraction data. Reproduced from Ref. [74] with permission from The Angewandte Chemie International Edition.

Programs for indexing diffraction data consider the measured positions of peak maxima for the selected peaks, normally 20, and trial unit cells are generated where the quality of each trial is determined by a whole-profile fitting procedure [74]. Analysis of the diffraction profile before structure solution is important; it is thus suitable to apply a Le Bail fit on the pattern first. This technique involves fitting the complete diffraction profile to assign intensities to each peak in order to obtain the best fit. The fitting includes refinement of the unit cell parameters, background, peak-width and peak-shape parameters, while the atomic information is not considered.

Once a suitable fit is obtained by using the correct structural model, all parameters are relaxed to perform a complete refinement. For successful Rietveld refinement, the structural model obtained at the structure solution stage must be a sufficiently good representation of the correct structure [74]. The refinements conducted in this thesis were performed with TOPAS academic version 6, while VESTA was used to create all crystal structure images.

When needed, the amorphous content of the synthesized polycrystalline SEs in this work was determined using the following equation:

$$A(\%) = (\frac{1 - \frac{W_s}{R_s}}{100 - W_S}) x 10^4 \%, \tag{2.12}$$

where W_S (%) is the weighted concentration of the internal standard (Si) and R_s(%) is the Rietveld analyzed concentration of the internal standard.

All the electronegativity values mentioned in this work were taken from the Allred-Rochow scale, while the given ionic radii values were taken from Shannon-Prewitt radii.

2.3 Electrochemical Impedance Spectroscopy

2.3.1 Impedance

Electrochemical impedance spectroscopy (EIS) is a powerful method for characterizing many of the electrical properties of materials and their interfaces with electronically conducting electrodes [87]. The general approach is to apply a sine-wave electrical stimulation, voltage, to the electrodes and observe the response, the resulting current. The resistance obtained for a system with a phase shift is called impedance and consists of two components, the phase shift between the voltage and the current, and their ratio (V/I) [88]. Impedance is thus a more general form of resistance because unlike resistance, which has only magnitude, impedance takes phase differences into account [89]. Impedance consisting of two components can be expressed as a vector:

In polar form, Z may be written as:

$$Z =\mid Z \mid e^{i(\theta)}, \tag{2.13}$$

The phase angle of the impedance is conveniently the angle of the vector, while $\mid Z \mid$ is the length of the vector [88]. In the Cartesian form:

$$Z = R + iX \tag{2.14}$$

Impedance is defined as a complex number, whose magnitude and direction can be expressed by Z' and $Z"$ components. The following Argand diagram shows a representation of the impedance **Figure** 2.5 [89]. The x coordinate is considered the real part of the complex number, Z', and the y component is the imaginary component, $Z"$. Where the real part R corresponds to the resistance and the imaginary part accounts for the phase difference defined as:

$$Re(Z) = Z' =\mid Z \mid cos(\theta) \tag{2.15}$$

$$Im(Z) = Z" =\mid Z \mid sin(\theta) \tag{2.16}$$

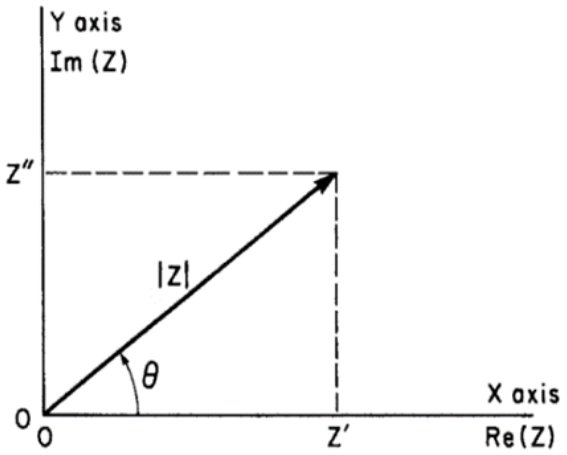

Figure 2.5: The impedance Z plotted as a planar vector. Reproduced with permissions from Ref. [89]. Copyright 2001 John Wiley & Sons Ltd.

Impedance is real when θ=0 and thus $Z = Z'$, that is, for purely resistive behavior -case in which the impedance is frequency independent-. The modulus and the phase angle are given by:

$$| Z | = [(Z')^2 + (Z")^2]^{1/2} \tag{2.17}$$

$$\theta = tang^{-1}(\frac{Z"}{Z'}) \tag{2.18}$$

In alternating current (AC) the resistance is not fixed like in direct current (DC) but depends on the frequency of the applied electric signal [90]. Therefore, EIS measurements can be performed by applying a single-frequency voltage (U) to a sample and measure the resulting amplitude and phase shift of the current (I). The excitation signal or AC single-frequency voltage expressed as a function of time is given by:

$$u(t) = Usin(wt), \tag{2.19}$$

where U is the magnitude of the voltage, and $\omega = 2\pi f$ corresponds to the relationship between radial frequency ω (expressed in radians/second) and frequency f (expressed in hertz). The sinusoidal current or response signal is represented as a complex function:

$$i(t) = Isin(wt + \phi), \tag{2.20}$$

where ϕ denotes the phase shift between the input and output signal. An expression analogous to Ohm's Law allows us to calculate the impedance of the system as:

$$Z(\omega) = \frac{V}{I} = \frac{u(t)}{i(t)} = Z_o \frac{sin(\omega t)}{sin(\omega t + \phi)} \tag{2.21}$$

The impedance is therefore expressed in terms of a magnitude, Z_o, and a phase shift ϕ. The expression for $Z(\omega)$ is composed of a real part -associated with the resistive properties of a sample- and an imaginary part, associated with the capacitive properties of a sample.

If the real part Z'= Re(Z) is plotted on the x-axis and the imaginary part Z''= Im(Z) is plotted on the y-axis of a chart, a Nyquist plot is obtained [91].

The AC response to a test system only defines the relationship between the applied voltage and the current through the test system, as a function of frequency. The physical nature of the test system i.e., single crystal, polycrystalline, blocking or non-blocking electrodes, etc., and its electrical properties such as ionic, electronic, or mix conductor must be considered. Therefore, equivalent circuits are needed in order to represent these properties of the system and model the collected data [91]. **Figure** 2.6 shows a flow diagram for the measurement and characterization of a material-electrode system [92]. The degree of success of an AC analysis depends on how well the experimental data fit the predicted by an appropriate equivalent circuit [89].

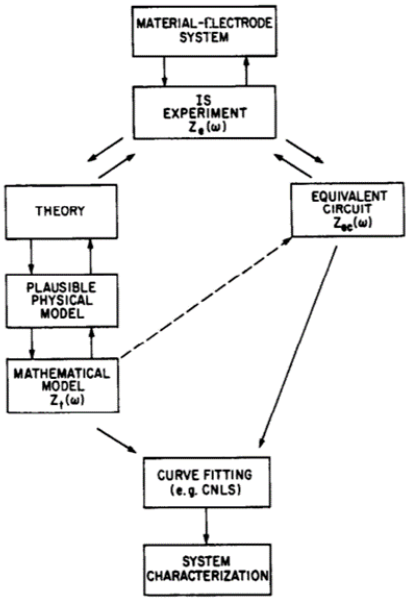

Figure 2.6: Diagram of the measurement and characterization of a material-electrode system. Reproduced from Re. [92] with permission from The Journal of Electroanalytical Chemistry and Interfacial Electrochemistry.

2.3.2 Equivalent Circuit Elements

Electrochemical systems generally consist of elements described by different combinations of resistors and capacitors that can be linked to structural and chemical features of the

system [88]. In order to show that the experimental impedance data Z_e may be well approximated by the impedance Z_{ec} of an equivalent circuit, impedance spectra are commonly analyzed by fitting it to an equivalent electrical circuit model. The different regions of a test system are normally characterized by a resistance (R), capacitance (C) and distributed circuit elements such as constant-phase element (CPE). From an impedance spectrum, it is possible to identify RC elements based on the capacitance value, and assign them to the correct regions of the test system [89] [91]. Distributed circuit elements are essential in understanding and interpreting most impedance spectra. For example, the electrode-solid electrolyte interface on the microscopic level contains many surface defects such as kinks and variations in composition; the CPE is thus introduced to represent a non-ideal diffusion due to the interfacial heterogeneities [93].

Resistance:

Resistance is the real part of impedance. Impedance is defined as the opposition that a circuit presents to a current when a voltage is applied. In a purely resistive behavior in which the impedance is equal to the resistance R (phase shift $\theta = 0$), the ratio between the voltage and the current is described by:

$$Z(R) = \frac{V}{I} = \frac{u(t)}{i(t)} = \frac{Usin(\omega t)}{Isin(\omega t)} = R \tag{2.22}$$

Capacitance:

In a pure capacitive behavior, the capacitance is given by $C{=}q/u(t)$, where C is the capacitance and q is the electric charge, which gives the voltage/current relationship:

$$i_c(t) = \frac{dq}{dt} = C\frac{du_c(t)}{dt} \tag{2.23}$$

Considering the voltage signal to be:

$$u_c(t) = e^{i\omega t} \tag{2.24}$$

Then it follows that:

$$\frac{du_c(t)}{dt} = i\omega C e^{i\omega t} \tag{2.25}$$

And thus, the ratio between the voltage and current for a purely capacitive behavior is:

$$Z_c(\omega) = \frac{V\omega}{I\omega} = \frac{u_c(t)}{i_c(t)} = \frac{1}{i\omega C} \tag{2.26}$$

As expressed in the frequency domain. This expression is imaginary and corresponds to the phase shift.

Constant-Phase-Element:

There are materials whose electrical behaviour is such that ideal resistive and capacitive circuit elements (frequency-independent parameters) are not accurate to describe the AC response [89]; this has caused the introduction of distributed impedance elements such as Q. Hugo Fricke presented the earliest account of the *CPE* in 1932, under the statement that the capacitance was frequency dependent, and that it could be expressed as a function of the frequency [94]. The *CPE* its given by:

$$Z_Q(\omega) = \frac{1}{Q(i\omega)^n}, \tag{2.27}$$

where $Q = 1/\mid Z \mid$ at $\omega = 1$ rad/s, and $n \in [0,1]$. When n=1 this is the same as that for the impedance of capacitor $\mathrm{Z_C}(\omega)$ (**Equation** 2.26) in which $Q \rightarrow C$ and $\mathrm{Z_{CPE}} \rightarrow \mathrm{Z_C}$. In that case, the Nyquist plot forms a perfect, non-depressed semi-circle. For many solid electrodes, n usually takes a value close to 1.0. [95].

The conductivity of a material is an extensive quantity that depends on the dimensions of the test system and its electrical resistance by:

$$\sigma = \frac{L}{AR}, \tag{2.28}$$

where L is the thickness of the material and A is the area.

The standard deviation (SD) and standard error (SE) in the obtained conductivities of each SE were determined from the span in the measurements for various samples of the same composition, acquired values of the impedance analyses are presented in the appendix of each chapter. The SD and SE were calculated using the following equations:

$$SD = \sigma = \sqrt{\frac{\mid x - x_o \mid^2}{n-1}}, \tag{2.29}$$

where x is the first number of the data set, x_0 is the average and n is the number of data points.

$$SE = \frac{SD}{\sqrt{n}}, \tag{2.30}$$

where n is the number of data points.

2.3.3 Nyquist plots and equivalent circuit models

Polycrystalline materials contain 2D defects, grain boundaries, which form the interfaces of grains. The ion transport across the grain boundaries plays an important role in the performance of SEs and therefore the realization of ASSBs [96]. A high grain boundary ionic conductivity will not hinder long-range ion dynamics; low resistive paths through the grain boundaries and/or low impedance boundaries will lead to conduction between the bulk (grains). The equivalent circuit of a Nyquist plot exhibiting the bulk and grain boundary contributions to the impedance data is shown in **Figure** 2.7a. For an impedance spectrum exhibiting the bulk and grain boundary components two arcs are observed, the arc at high frequency is associated to the bulk whereas the small arc at low frequency is attributed to the grain boundary impedance (**Figure** 2.7b [93])

In some impedance spectra the bulk and grain boundary contributions cannot be deconvoluted, and the obtained ionic conductivity is the overall sample conductivity. In this case, the Nyquist plot will exhibit only one semicircle and a straight line at the low-frequency region, which is a typical phenomenon resulting from the diffusion of ions from the bulk electrolyte to the electrode interface (**Figure** 2.8). Often, there are multiple equivalent circuits that may fit the data, which complicates the interpretation of impedance spectra; however, usually the equivalent circuit is chosen based on the following [89]:

- Knowledge of what kind of impedances are expected to be present in the system.
- Examination of the impedance data to determine whether the response is consistent with the proposed circuit.
- Inspection of the obtained R and C values.

Herein, the ionic conductivity of the samples was determined using **Equation** 2.28. While the obtained impedance spectra were fitted in EC-Lab and Z software using the circuit shown in **Figure** 2.8. For the impedance spectrum with one arc, the RQ arc was attributed to the combined bulk and grain boundary impedances, and the resistance of each SE was assumed to be $R{=}R_1$ of the RQ circuit.

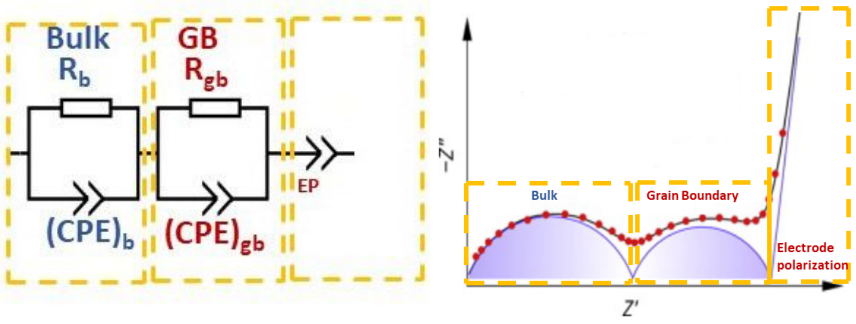

(a) Equivalent circuit **(b)** Nyquist plot.

Figure 2.7: a. Equivalent circuit of the impedance spectrum; **b.** Nyquist plot exhibiting the bulk and grain boundary contributions to the impedance data as long with the diffusion line. Reproduced from Ref. [93] with the permission from The Chemical Physics Letters.

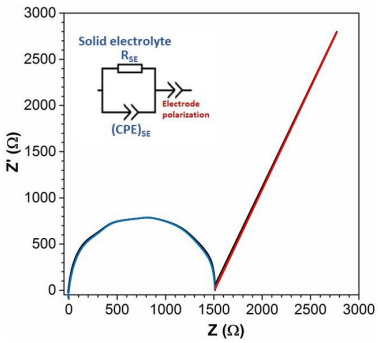

Figure 2.8: Nyquist plot exhibiting one arc at high-frequency. The total circuit is shown in black, while the individual components of the circuit are shown in blue and red.

Temperature-dependent impedance spectroscopy was performed to assess the changes in ionic conductivity of the synthesized SEs. EIS measurements were thus carried out at different temperatures to determine the activation barrier for ion diffusion in the SEs. The temperature dependence of ionic conductivity is given by the Arrhenius equation [77]:

$$\sigma(T) = Aexp(\frac{-E_a}{k_B T}), \qquad (2.31)$$

Where E_a is the activation energy, k_B is the Boltzmann constant, and A is the pre-exponential factor that contains several constants, including the vibrational frequency of the mobile ions [77].

2.4 DC polarization

DC polarization technique has been widely used to evaluate the ionic/electronic contribution to the total ionic conductivity in SEs and ionic/mixed conductors. In this technique a DC voltage is applied to a sample and the resulting current is monitored with respect to time. In this work, the electronic conductivities of the materials were measured by a DC polarization measurement of the Stainless Steel/SE/Stainless Steel symmetric cells at RT. The small potential applied to each SE material between the two SS blocking electrodes led to a decrease in the current until a steady-state value was reached. The obtained DC polarization data were fitted with a decay function and the steady-state current was extrapolated for each set of data.

2.5 Thermal Analysis

Thermal analysis can be defined as the measurement of changes in chemical and physical properties as a function of temperature. Thermal analysis has been widely used in the study of thermal decompositions and phase transitions in materials [77]. One of the main thermal analysis techniques is the differential scanning calorimetry (DSC), which measures the enthalpy changes that occur in a sample as a function of temperature or time [97]. Due to the simplicity, speed and amount of sample needed to perform a DSC analysis, it is the most often used thermal analysis method [77].

For the DSC analysis a reference pan is used, typically an empty sample pan, and throughout the experiment, the sample and the reference pans are maintained at nearly the same temperature ($\Delta T = T_s - T_r = 0$); thus, the extra heat input to the sample, if the sample undergoes an endothermic reaction, or to the reference, if the sample undergoes an exothermic reaction, required to maintain the same temperature is measured. By observing the difference in heat flow between the sample and reference, DSC is able to record the amount of heat absorbed or released during these thermal events [97].

A heat flux DSC instrument was used in the present work, where the difference in heat flow between the sample and reference is measured while the sample temperature is changed at the constant rate. The instrument is comprised of a silver block with an attached disk, which has two raised platforms for where the sample and reference pans are placed, while the thermocouple junctions are connected underneath each platform [98]. Another thermocouple embedded in the silver block is used as a temperature controller.

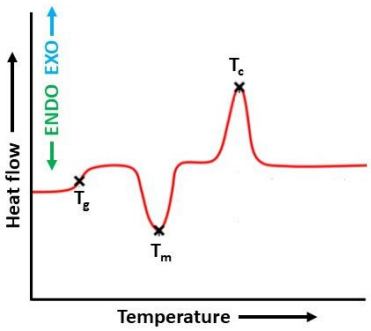

Figure 2.9: Representation of a typical DSC curve.

The result of a DSC analysis is a curve of heat flow versus temperature as shown in **Figure** 2.9. In the present work, the endothermic events are represented as being negative i.e. downward peaks, with respect to the baseline, which corresponds to a decrease transfer of heat to the reference with respect to the sample [98]. Two main factors that affect the obtained DSC curve are: the instrumental factors, i.e, furnace heating rate, furnace atmosphere and instrument's sensitivity, and sample's characteristics i.e. amount of sample.

2.6 Vibrational spectroscopy:Raman

Spectroscopy is one of the three main categories of physical characterization techniques of solids, the other two being diffraction and microscopic. Spectroscopy gives information on local order, while diffraction is concerned with long range order; therefore, spectroscopic studies on solids complement the results obtained from diffraction techniques. There are different spectroscopy techniques and they all work based on the principle that materials are capable of absorbing and emitting energy [77]. The spectra obtained from the experimental results consist of intensity of absorption or emission (y-axis) as a function of energy (x-axis), which can be expressed in terms of frequency f or wavelength λ by the classic equation:

$$E = hf = hc\lambda^{-1} \tag{2.32}$$

Where h is Planck's constant, c is the velocity of light, f is frequency and λ is the wavelength. At high frequencies and short wavelengths, atoms in a solid vibrate at a certain frequency (around 10^{12} Hz), which can be excited to other energy states by the absorption or emission of radiation of appropriate frequency [77]. In the Raman technique, the sample is illuminated with a monochromatic light, laser in the visible range of 514 nm, where two types of scattering are produced by the sample: Raman and Rayleigh. Raman scatter is usually less intense than Rayleigh and emerges either at longer or shorter wavelength than the incident light. In contrast, the Rayleigh scatter emerges with the same energy

and therefore wavelength as the incident light. The elastic scattered radiation, Rayleigh scattering, is filtered out while the rest of the collected light is dispersed onto a detector [77].

Photons of light from the laser of frequency v_o, interact with molecular vibrations, phonons or other excitations in the sample and as a consequence the photons lose or gain energy. After the scattering event, the sample is in a different rotational or vibrational state. Therefore, the collection of this change in energy gives information about the vibrational modes in the sample. Raman shifts in the spectra are normally given in wavenumbers (the number of wavelengths per unit distance, cm^{-1}) [77].

Chapter 3

Experimental Methods

3.1 Introduction

This chapter describes the experimental methods I used in the development and characterization of the herein synthesized Na and Li SE materials. There are four main aspects that need to be considered in planning a solid state reaction: choice of starting materials, mixing method, container and heat treatment parameters. In this chapter the experimental procedures used in this work such as single crystal and powder XRD, TOF neutron diffraction, EIS, DSC and RAMAN are presented. All constituents and synthesized samples were air sensitive, therefore, synthesis and characterization procedures required special handling protocols in order to prevent the samples from decomposition.

3.2 Sample Preparation

I performed all the synthesis of the SEs by either mechanochemical route or classical high-temperature route. During the development of each fast-ion conductor considerable research was conducted to optimize and determine the suitable reaction conditions to obtain products with high chemical homogeneity, which often leads to improved properties (pure materials).

3.2.1 Mechanochemical route

The synthesis of SEs through mechanochemical route encompasses the combination of mechanical alloying and heat treatment (**Figure** 3.1). This mechanical milling technique has attracted much attention as a successful procedure for preparing inorganic amorphous materials because it is carried out at RT [99]. The amorphization via mechanical milling involves deformation, fracture and cold welding of the powder precursors **Figure** 3.1a [100]. The major functions of mechanical milling are to reduce the size and mix the constituents at a molecular level, and enhance the atomic diffusivity through creating abundant structural defects. Several milling parameters such as number and size of the milling balls, jars and balls material, and rotation speed of the apparatus have to be considered when using this approach.

For the present work, I used a Pulverisette 7 Premium Line (Fritsch) planetary ball with two ZrO_2 grinding bowls (jars) of 45 mL volume and a total of 600 ZrO_2 balls of 5 mm diameter milling balls (300 in each jar). The precursors were weighted and mixed together according to the respective molar ratios of the targeted compositions inside of a glove-box under argon atmosphere. 1 g of each mixture was placed in each jar, which were tightly sealed before taking them out of the glove-box.

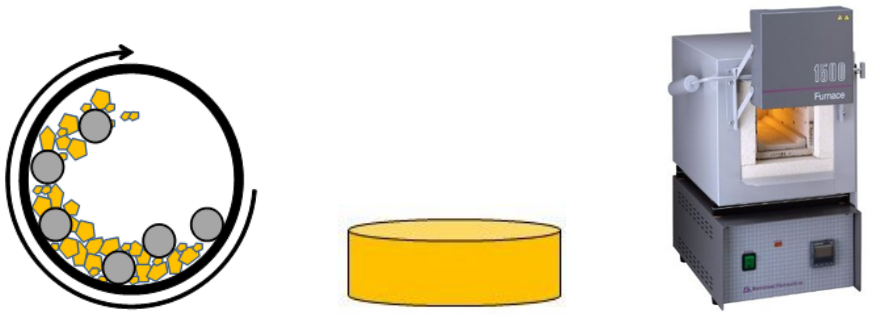

(a) Amorphization **(b)** Pelletization **(c)** Crystallization

Figure 3.1: a. The inside of a milling jar with ZrO_2 balls (grey) and sample powder (yellow). Reproduced from Ref. [100] with permission of Dr. Lalere; **b.** A pellet; **c.** A furnace used to perform the heat-treatments. Reproduced from Ref. [100] of Dr. Lalere.

In the second step, the milled powders were subjected to a densification process where contact between the particles was established by pelletizing under 3 metric tons into 10-13 mm diameter pellets.(**Figure** 3.1b). During the last step, the powders were heat-treated in order for the precursors to react (**Figure** 3.1c [100]). The heat-treatments were conducted

several times varying the parameters in order to find the more suitable parameters for each sample.

3.2.2 High-temperature

The oldest and simplest and still most widely used method is to mix together the powdered reactants, press them into pellets and heat them in a furnace for a specific time. This synthesis process involves the direct reaction of the constituents at high temperatures. Although, the reactants may be well-mixed at the level of individual particles (μm scale), on the atomic level they are very inhomogeneous (**Figure** 3.2a [100]). The precursors were thus hand ground for a long time, between 40 min to 1 h, in order to obtain an intimate mixture of the reactants, followed by palletization (3 metric tons into 10-13 mm diameter pellets) and heat treatment. Different heat-treatments were performed until the optimum parameters for each sample were determined (**Figures** 3.2b and 3.2c [100]).

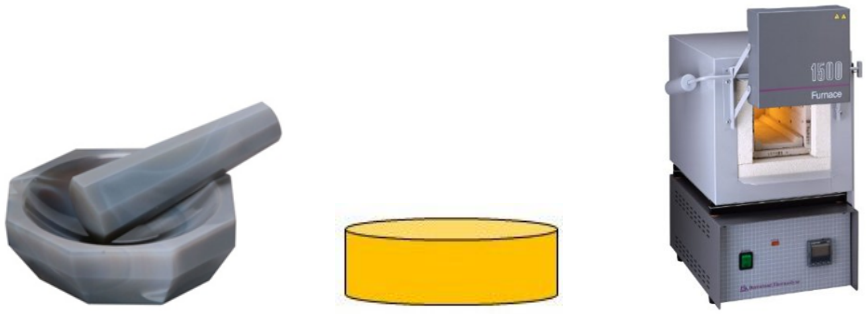

(a) Mixing **(b)** Pelletization **(c)** Crystallization

Figure 3.2: a. A agate mortar used to hand grind the powder precursors. Reproduced from Ref. [100] with permission of Dr. Lalere; **b.** A pellet; **c.** A furnace used to perform the heat-treatments. Reproduced from Ref. [100] with permission of Dr. Lalere.

The first stage of a solid-state reaction process is the nucleation of small crystals; for nuclei to be stable and not to disintegrate as soon as they form, they have to be larger than a single unit cell and therefore contain many tens of atoms [77]. Subsequently, growth and thickening of the product takes place, which is possible due to the diffusion process of the ions to form the targeted product. High temperatures are required so that ions have enough thermal energy for diffusion [77].

3.3 Diffraction Techniques

3.3.1 Powder and Single-crystal X-ray diffraction

All the ball-milled samples as well as the synthesized materials were characterized using powder XRD. On a daily basis, the Bragg-Brentano geometry was used for structural characterization of each sample. A thin layer of powder was placed on a zero-background holder, which was then covered with a kaptom film to avoid exposing the sample to air. The Debye-Scherrer geometry was also used to obtain high quality data and perform a full Rietveld refinement of the different sample diffraction patterns. The microcrystalline samples were loaded into glass capillaries with 0.3 diameter and 0.01 mm wall thickness, and scanned for 20 h. Measurements were performed with a PANalytical Empyrean instrument using Cu-Kα radiations outfitted with a PIXcel bidimensional detector.

All the PXRD patterns of the synthesized materials were first analyzed using HighScore Plus program, a software package that does a complete full powder pattern examination. The search-match algorithm searches and automatically carries out the phase identification using the ICDD PDF4 reference database.

Once the analysis of the PXRD patterns was completed, and if single-crystals were obtained from the conducted heat-treatment of the sample; selected single-crystals from the reaction product were taken for single-crystal studies. In this case, the samples were placed on glass slides, covered with Paratone-N oil and placed in sealed centrifuge tubes in order to prevent air exposure. Single-crystal measurements were performed by Dr. Abdeljalil Assoud at the University of Waterloo with a BRUKER KAPPA diffractometer equipped with a SMART APEX II CCD, with graphite-monochromated Mo-Kα radiation. In order to protect the crystals from decomposition, they were covered by Paratone-N oil and liquid nitrogen flow using an OXFORD Cryostream controller 700.

3.3.2 Time-of-Flight neutron diffraction

TOF neutron diffraction was particularly used to locate light atoms, i.e. Li, in Li SEs. Crystal structures of the Li-ion conductors were initially solved by single crystal method, and neutron diffraction technique was subsequently used. Between 1 g to 2 g were synthesized for PND measurements, the microcrystalline samples were loaded into vanadium cans under argon atmosphere and sealed with a copper gasket and aluminum lid. Data collection was performed on POWGEN at the Spallation Neutron Source (SNS) at the Oak Ridge National Laboratory by Dr. Ashfia Huq.

3.4 Impedance Spectroscopy Measurements

The EIS measurements were performed inside of a glove-box under argon atmosphere, ensuring that the samples were not exposed to air. Each powder sample was placed between two SS rods or pistons of a 10 mm diameter and pressed at 2 metric tons obtaining a cylindrical pellet of 10 mm diameter. A polycarbonate insulator die with a 10 mm diameter was placed in between the two rods (**Figure** 3.3 [101]).

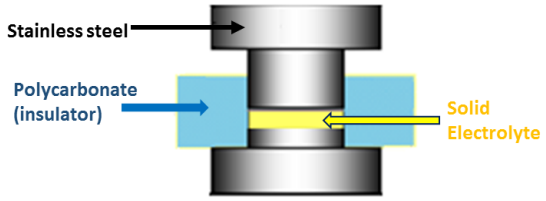

Figure 3.3: Schematic diagram of the impedance cell used for EIS measurements. Reproduced from Ref. [101] with permission of MS Houtarde.

All the EIS measurements in this work were performed using an impedance analyzer MTZ-35 impedance analyzer (Bio-Logic) controlled by the software MT-LAB (Bio-Logic). A constant voltage of 100 mV was applied and the frequency range of the AC signal was typically set from 100 mHz to 1 MHz. To obtain the activation energy of the SE materials, impedance spectroscopy measurements were performed at different temperatures, typically from 30°C to 70°C in steps of either 5°C or 10°C. The samples were equilibrated at each temperature for at least 90 min prior to each measurement. Since the oven was placed outside of the glove-box, the sealed impedance cell was exposed to air. The insulator die of 10 mm diameter used for this measurement was polyetheretherketone (PEEK). Indium foil of 50 μm thickness (from Sigma Aldrich Co.) was placed between the two faces of the pellets to achieve good contact between the SE pellet and the SS electrodes, indium was chosen due to its inherent softness [39].

For DC polarization measurements were conducted inside of a glove-box. The synthesized samples were placed between two SS rods of 10 mm diameter and pressed at 2 metric tons. Applied voltages of 0.25, 0.50 and 0.75 V for 30 min each. The measurements were carried out using the same cell described above (**Figure** 3.3).

3.5 Differential scanning calorimetry measurements

Between 5 to 10 mg of each sample was used for the DSC measurements performed for this work. The measurements were conducted using a TA Instruments DSC Q2000 under constant nitrogen flow. The air-sensitive samples, as well as the reference (Ar) were sealed beforehand in hermetic aluminium pans with a Tzero sample press placed in a glove-box.

3.6 Raman Measurements

Raman spectra was obtained using a 514 nm laser in a Raman HORIBA HR800 equipment. The samples prepared in a glove-box were pelletized and placed on a microscope slide, covered by a glass cover slip and sealed with epoxy glue.

Chapter 4

Analysis of the structural and transport properties of $Na_{11}Sn_2PnS_{12}$ with Pn=P and Sb

4.1 Introduction

In 2015 Kandagal *et al.* computationally predicted a new sodium-ion electrolyte with composition $Na_{10}GeP_2S_{12}$, the Na version of the LGPS-type, with an estimated RT ionic conductivity of 4.7 mS·cm^{-1} [102]. In 2016 Richards *et al.* predicted an increase in the Na^+ diffusivity and a decrease in the activation energy in the series Si, Ge and Sn for $Na_{10}MP_2S_{12}$ with M=Si, Ge and Sn [42]. The synthesis of the sodium-ion electrolyte $Na_{10}SnP_2S_{12}$ with an experimental conductivity of 0.4 mS·cm^{-1} and an activation energy of 0.35 eV was also included in their work. The $Na_{10}SnP_2S_{12}$ material contained amounts of P_2S_5, Na_3PS_4 and Na_2S impurities that were not formed when a faster cooling rate was used for its synthesis; however, the conductivity of the more pure material resulted to be surprisingly lower. The science behind this behaviour remains unclear since the crystal structure was not resolved [42]. Their AIMD simulations showed that $Na_{10}SnP_2S_{12}$ is a 1D ion conductor with chains of NaS_4 tetrahedra connected along the *c*-axis for ion mobility [42]. Later in 2017 Hayashi *et al.* reported the glass-ceramic $Na_{10}GeP_2S_{12}$ with an ionic conductivity of 0.012 mS·cm^{-1}, and an XRD pattern similar to that of the simulated $Na_{10}SnP_2S_{12}$; however, the crystal structure was not resolved [103].

This chapter describes the synthesis and transport properties of the new Na-ion conductor, $Na_{11}Sn_2PS_{12}$, that crystallizes in a unique 3D structure type and exhibits a high

ionic conductivity, with a very low activation energy barrier for Na-ion mobility. The solid electrolyte, $Na_{11}Sn_2SbS_{12}$, that is isostructural with $Na_{11}Sn_2PS_{12}$ and exhibits a very good, albeit lower ion conductivity is also presented in this chapter. Using high quality single crystal XRD data, the reasons responsible for the difference in conductivity between $Na_{11}Sn_2PnS_{12}$ with Pn=P and Sb are identified.

4.2 $Na_{11}Sn_2PS_{12}$

4.2.1 Introduction

In 2017, Dr. Fabien Lalere (postdoc at Nazar's lab) explored the Na-Sn-P-S phase diagram, being able to synthesize for the first time the stoichiometric $Na_{11}Sn_2PS_{12}$ (P-phase) material. The structure of this new sodium ion conductor was successfully solved from single crystal XRD. The unit cell was indexed in the tetragonal space group $I4_1/acd$ with a=13.6148(3) Å and c=27.2244(7) Å. In contrast to the LGPS structure, Na^+- ions occupy only octahedral sites while Sn and P occupy two independent crystallographic sites in $Na_{11}Sn_2PS_{12}$, *16e* and *8a* Wyckoff sites, respectively, resulting in a unit cell five times larger compared to that one of the LGPS (i.e., 5046.4(3) $Å^3$ versus 965.47(9) $Å^3$). The replacement of Li^+ by Na^+ widens the channels resulting in an increase of the unit cell volume. The relationship between the two structures is shown in **Figures** 4.1a and 4.1b [104].

In $Na_{11}Sn_2PS_{12}$, the Na^+ ions are distributed over five Wyckoff positions (*32g, 16d, 16e, 16c* and *16f*). The alternating arrangement of two partially occupied sodium sites (Na(1), SOF=0.868(18) and Na(2), SOF=0.78(3)) with three almost-fully occupied sodium sites (Na(3), SOF=0.965(19); Na(4), SOF=0.97(2); and Na(5), SOF=0.95(3)) is expanded in all crystallographic directions [104]. The ordered Sn/P tetrahedra and the Na^+-ion diffusion channels along the c-axis and a,b- plane presented the first example of a totally 3D face-sharing octahedral site pathway in a solid-state sulfide-based conductor [104].

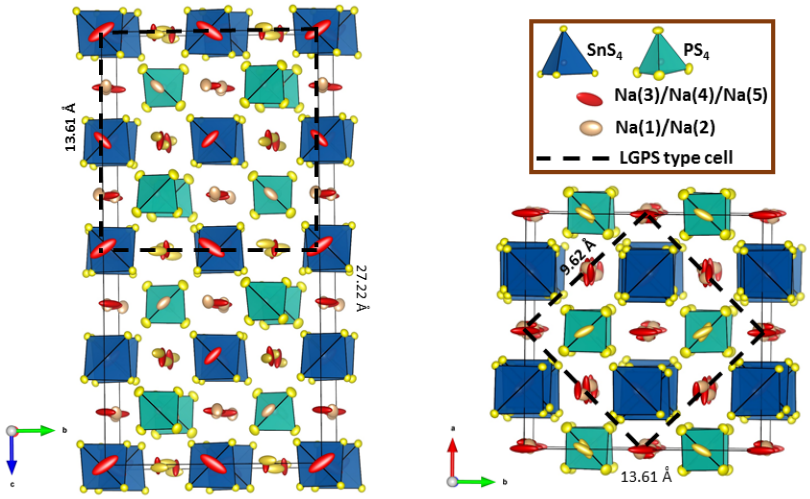

(a) [100] **(b)** [001]

Figure 4.1: View of the structure of $Na_{11}SnP_2S_{12}$ from single crystal XRD along two directions: **a.** [100]; **b.** [001]. The LGPS tetragonal unit cell is shown in dotted lines. Color code: SnS_4: blue; PS_4: light blue; S: yellow; Na(1) and Na(2): rose; Na(3), Na(4) and Na(5): red.

When $Na_{11}Sn_2PS_{12}$ was first synthesized, its ionic conductivity was 0.51 $mS{\cdot}cm^{-1}$ at RT. Since I was working with Dr. Lalere before the $Na_{11}Sn_2PS_{12}$ material was discovered, I was involved in the synthesis and characterization of this SE in order to improve its conductivity properties. For solid-state synthesis, the heat treatment parameters including, temperature and time influence the phase purity, relative density and ionic conductivity of the final product [105]. Thus, I carefully performed different heat treatments with distinct parameters, such as heating-cooling rates, temperature and holding time to enhance the ionic conductivity of $Na_{11}Sn_2PS_{12}$. **Figure** 4.2 shows the XRD patterns of $Na_{11}Sn_2PS_{12}$ synthesized using three different heat-treatment procedures: 1) the $Na_{11}Sn_2PS_{12}$ mixture was grounded for 15 min and heated at $2°C{\cdot}min^{-1}$ to 700°C, kept at that temperature for 5 h followed by a cooling rate of $5°C{\cdot}min^{-1}$. Based on the diffraction data (**Figure** 4.2), the highest intensity peaks are not symmetric (∼12.9°, 18° and 37.4°), pointing to the formation of an impurity phase. 2) the $Na_{11}Sn_2PS_{12}$ mixture was grounded for 20 min and heated at $2°C{\cdot}min^{-1}$ to 700°C kept at that temperature for 24 h followed by a cooling rate of $2.3°C{\cdot}min^{-1}$. The diffraction data of this heat-treatment shows the formation of an unknown secondary phase. 3) a highly crystallized and pure sample with symmetric peaks was synthesized. This heat-treatment will be described in the next section.

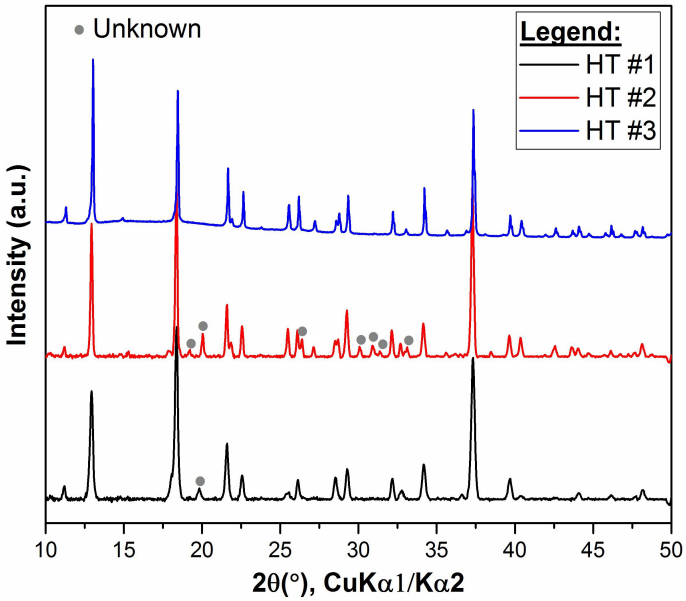

Figure 4.2: Comparison of the XRD patterns of different heat-treatments conducted on the targeted composition $Na_{11}Sn_2PS_{12}$, Bragg-Brentano geometry.

4.2.2 Synthesis of $Na_{11}Sn_2PS_{12}$

After the conduction of different heat treatments, the optimum parameters for the synthesis of $Na_{11}Sn_2PS_{12}$ were determined, heat-treatment number three in **Figure** 4.2. 0.5 g of the precursors Na_2S (99%, Sigma-Aldrich), P_2S_5 (98%, Sigma-Aldrich) and SnS_2 (99%, Kojundo) were mixed at a molar ratio 5.5:0.5:2 in an agate mortar between half an hour and forty minutes. The mixture was grounded for that long in order to obtain a well-mixed of the constituents at the level of individual particles (35-40 min). The mixture was heated at $2°C{\cdot}min^{-1}$ to 700°C; high temperature was needed in order to achieve atomic scale mixing of the reactants. The mixture was kept at that temperature for 5 h followed by two cooling steps: at $0.2°C{\cdot}min^{-1}$ from 700-400°C; the slow cooling rate was chosen in order to obtain large single crystals, less grain boundaries, and at $2°C{\cdot}min^{-1}$ from 400°C to RT. A faster cooling rate was used to avoid the crystallization of secondary phases such as Na_3PS_4.

4.2.3 Crystal structure of $Na_{11}Sn_2PS_{12}$

Figure 4.3 shows the XRD pattern of the synthesized $Na_{11}Sn_2PS_{12}$ material, the lattice parameters were obtained by full profile fitting.

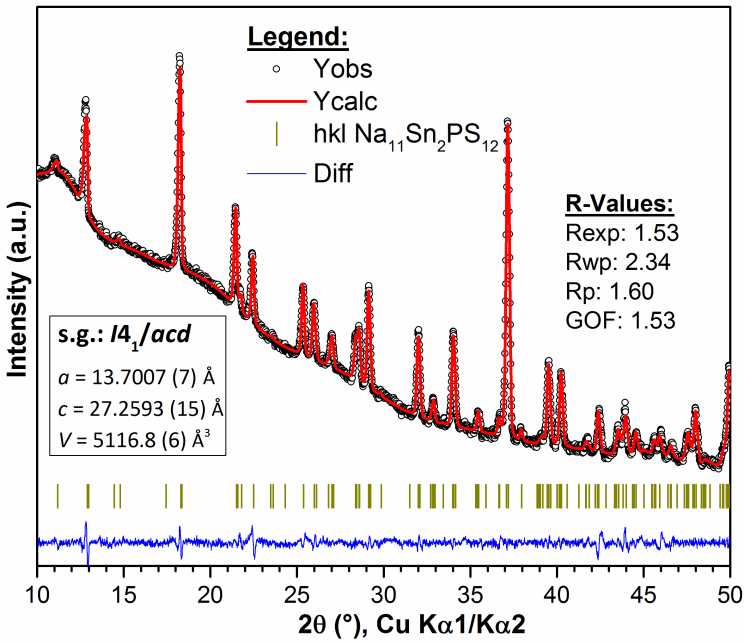

Figure 4.3: Pawley fit of single-phase polycrystalline $Na_{11}Sn_2PS_{12}$ (Bragg-Brentano geometry). The black points correspond to the data, and the red lines to the calculated pattern. The difference map is shown in blue. The calculated positions for Bragg reflections are marked by dark green vertical ticks.

The heat treatment procedure provided a pure phase material with an overall RT ionic conductivity of 1.39±0.21 mS·cm^{-1} (**Table** A.11). The increased in ionic conductivity from 0.51 mS·cm^{-1} to 1.39 mS·cm^{-1} is likely due to a decrease in the grain boundary contribution -by growing larger crystals- to the overall ionic conductivity. Dr. Lalere used a faster cooling rate (2 h from 700°C to RT) during the synthesis of $Na_{11}Sn_2PS_{12}$; likewise, I initially used fast cooling rates (2.5 and 5 h, **Figure** 4.2), likely obtaining smaller crystals and thus more crystal interfaces; high concentration of grain boundaries may hinder the Na^+-ion diffusion in the structure.

Moreover, the area of contact between the reacting solids and hence their surface areas are important factors that influence the rate of reaction between solids [77]. Therefore,

in order to obtain a homogeneous mixture with small crystal size a long grinding time of 30-40 min was used for the synthesis of $Na_{11}Sn_2PS_{12}$. Increasing the surface area with decreasing the particle size may facilitate the formation of larger $Na_{11}Sn_2PS_{12}$ crystals.

4.2.4 Ionic properties of $Na_{11}Sn_2PS_{12}$

Figure 4.4 shows the Nyquist impedance plot of $Na_{11}Sn_2PS_{12}$ at RT and the corresponding equivalent circuit (**Table 4.1**).

Table 4.1: Parameters of the fit for the impedance data of $Na_{11}Sn_2PS_{12}$ at RT.

Element	Value
$\mathbf{R_1}$ (Ω)	141.8
$\mathbf{CPE_1}$ ($\mathbf{F\ s^{a-1}}$)	5.647 x 10^{-9}
$\mathbf{a_1}$	0.854
$\mathbf{CPE_2}$ ($\mathbf{F\ s^{a-1}}$)	8.066 x 10^{-6}
$\mathbf{a_2}$	0.747

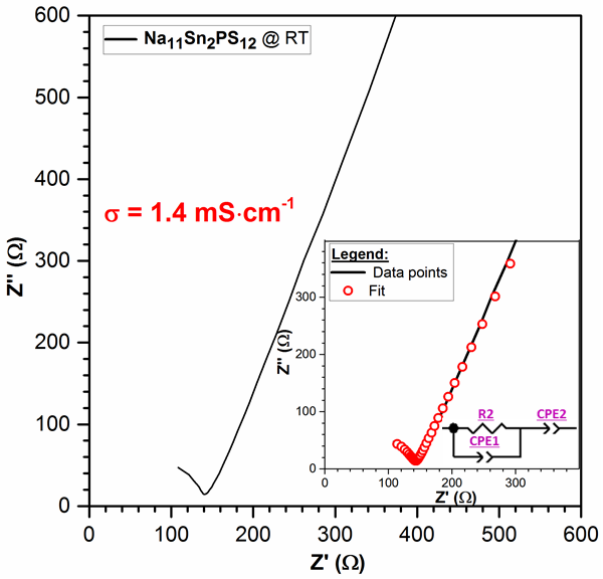

Figure 4.4: Nyquist plot of $Na_{11}Sn_2PS_{12}$ at 30°C showing the impedance data and the fit with the corresponding equivalent circuit (inset).

The synthesis conditions affected the structural properties that influence the Na^+-ion conductivity; changes in the synthesis parameters i.e. cooling rate resulted in the crystalline phase, $Na_{11}Sn_2PS_{12}$, with a likely lower grain boundary impedance. Determining the precise synthesis conditions for $Na_{11}Sn_2PS_{12}$ was critical in order to obtain the optimal properties to achieve a higher Na^+-ion conductivity (> 0.51 mS·cm^{-1}). To determine the migration barrier of $Na_{11}Sn_2PS_{12}$ impedance measurements were conducted every 5°C from 20°C to 50°C. The overall activation energy for Na^+-ion hopping determined from the Arrhenius plot shown in **Figure** 4.5 corresponded to 0.25 eV.

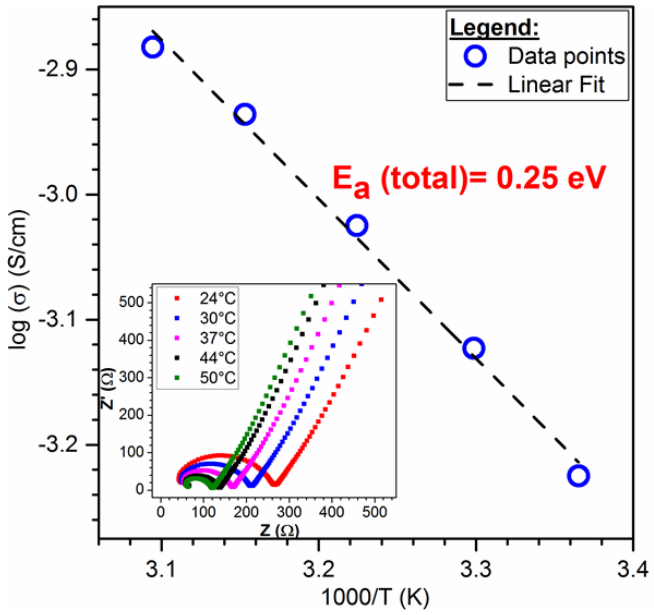

Figure 4.5: Arrhenius conductivity plot of $Na_{11}Sn_2PS_{12}$ from 20°C to 50°C. The inset displays the Nyquist impedance plot from 20°C to 50°C.

The obtained ionic conductivity was amongst the highest reported for sodium ion conductors. The ionic conductivity and activation energy data of $Na_{11}Sn_2PS_{12}$ are compared to other Na^+-ion thiophosphate conductors in **Table** 4.2. Comparison with other compounds was difficult since only few other ionic conductors had been reported for RT sodium-based battery applications [104].

Formula	σ mS·cm^{-1}	E_a (eV)	Reference
$Na_{11}Sn_2PS_{12}$	1.4	0.25	[104]
$Na_{10}SnP_2S_{12}$	0.4	0.36	[42]
$Na_{10}GeP_2S_{12}$(glass-ceramic)	0.012	0.46	[103]
Na_3PS_4 tetragonal	0.004	0.42	[106]
Na_3PS_4 cubic (glass-ceramic)	0.2	0.28	[107]
Na_3PSe_4	0.11	0.28	[108]

Table 4.2: Experimental and predicted ionic conductivity and activation energy data of $Na_{11}Sn_2PS_{12}$ compared to other Na-ion thiophosphate conductors.

After improving the conductivity properties of the new sodium ion conductor, the con-

ductivity of the $Na_{11}Sn_2PS_{12}$ was confirmed to be dominated by the grain conductivity. By fitting the impedance spectroscopy data with the appropriate circuit, Dr. Zhizhen Zhang (postdoc at Nazar's lab) determined the activation energy for ion hopping within the grains to be 0.24 eV (overall activation energy 0.25 eV) [104], confirming the low contribution of the grain boundary component to the total ionic conductivity of $Na_{11}Sn_2PS_{12}$ [104].

4.3 $Na_{11}Sn_2SbS_{12}$

4.3.1 Introduction

The new sodium conductor, $Na_{11}Sn_2PS_{12}$, like other sulfide-based solid electrolytes exhibit fast ion conductivity at RT (i.e., $\geq 10^{-3}$ S·cm^{-1}) [109]. However, it is well established that most alkali thiophosphate superionic conductors have a drawback of being sensitive to oxygen and moisture in air. Chengdu Liang *et al.* explored the synthesis of $Li_{3.833}Sn_{0.833}As_{0.166}S_4$, and suggested that the stability of sulfides follows the rules of the HSAB theory; stating that thiophosphate-based ionic conductors are chemical unstable in the presence of oxygen because oxygen (hard base) reacts preferentially with the phosphorous (hard acid) to replace sulfur (soft base) [110]. Therefore, the utilization of a soft acid could mitigate the reactivity to a certain extent. Researchers have been thus prompted to investigate other soft acid sulfides that could exhibit suitable stability under ambient conditions, such as those based on antimony [111] [56] [112]. Antimony-based sulfides are even reported to be solution processable using water or methanol [55] [113]. In the present work, the single crystal structure and properties of the antimony-based Na^+-ion conductor, $Na_{11}Sn_2SbS_{12}$, have been investigated.

4.3.2 Synthesis of $Na_{11}Sn_2SbS_{12}$

Na_2S (99%, Sigma-Aldrich), SnS_2 (99%, Kojundo), Sb_2S_3 (99%, Sigma-Aldrich) and S powder (99%, Sigma-Aldrich) were mixed together according to the molar ratio of 5.5:2:0.5:1. 0.5 g of mixture was grounded in an agate mortar for 30 to 40 min. The mixture was heated at 700°C with a heating rate of 1°C /min, kept for 5 h, followed by a slow cooling step of 99 h from 700°C to RT. The refinement details from the single crystal diffraction data collected at 200 K, 273 K and 280 K are presented in **Appendix** A.

4.3.3 Crystal structure of $Na_{11}Sn_2SbS_{12}$

Tetragonal $Na_{11}Sn_2SbS_{12}$ crystallizes in the $I4_1/acd$ space group with a=13.7973(8) Å, c=27.5026(19) Å, Z=8 and V=5235.5(19) Å^3 (**Table** A.8). The crystal structure contains isolated SbS_4 and SnS_4 tetrahedra separated by Na^+-ions occupying six different crystallographic sites [114].

Table 4.3 shows the atomic coordinates, occupation factor and isotropic displacement parameters of $Na_{11}Sn_2SbS_{12}$ obtained from single crystal XRD. Two sodium sites are partially vacant (Na(1) and Na(2)), three sites are nearly fully occupied (Na(3), Na(4) and Na(5)), while one site is almost vacant (Na(6)); Sn and Sb occupy two different Wyckoff sites, *16e* and *8a*, respectively [114].

Atom	Wyckoff site	x	y	z	SOF	U_{eq}/Å^2
Sn1	*16e*	0.28897(2)	0	1/4	1	0.01857(7)
Sb1	*8a*	0	1/4	3/8	1	0.01874(8)
S1	*32g*	0.14847(5)	0.36222(5)	0.05012(2)	1	0.02592(13)
S2	*32g*	0.15358(4)	0.06164(5)	0.05191(2)	1	0.02281(13)
S3	*32g*	0.10524(6)	0.15944(6)	0.32646(3)	1	0.03656(16)
Na1	*32g*	0.01935(14)	0.01507(12)	0.12706(5)	0.894(6)	0.0565(7)
Na2	*16d*	0	1/4	0.00718(10)	0.839(11)	0.0907(18)
Na3	*16e*	0.04019(14)	0	1/4	0.977(8)	0.0533(8)
Na4	*16c*	0	0	0	0.927(9)	0.0983(16)
Na5	*16f*	0.23052(12)	0.4805(12)	1/8	0.972(10)	0.0784(13)
Na6	*8b*	0	1/4	1/8	0.076(9)	0.019(8)

Table 4.3: Atomic coordinates, site occupation factors and equivalent isotropic displacement parameters of $Na_{11.08(8)}Sn_2SbS_{12}$ obtained from single crystal XRD at 280 K.

Atom	U_{11}	U_{22}	U_{33}	U_{23}	U_{13}	U_{12}
Sn1	0.018(1)	0.018(1)	0.020(1)	0.001(1)	0	0
Sb1	0.019(1)	0.019(1)	0.019(1)	0	0	0
S1	0.027(1)	0.024(1)	0.027(1)	0.001(1)	0.003(1)	-0.005(1)
S2	0.021(1)	0.026(1)	0.022(1)	0.000(1)	0.005(1)	0.001(1)
S3	0.034(1)	0.034(1)	0.038(1)	-0.011(1)	0.010(1)	0.004(1)
Na1	0.070(1)	0.045(1)	0.054(1)	-0.007(1)	0.035(1)	-0.012(1)
Na2	0.062(2)	0.169(4)	0.040(2)	0	0	-0.072(2)
Na3	0.022(1)	0.069(2)	0.069(2)	0.032(1)	0	0
Na4	0.025(1)	0.206(4)	0.064(2)	-0.040(1)	-0.011(1)	-0.009(2)
Na5	0.104(2)	0.104(2)	0.027(1)	-0.018(1)	0.018(1)	-0.059(2)
Na6	0.019(10)	0.019(10)	0.018(11)	0	0	0.004(10)

Table 4.4: Anisotropic displacement parameters (Å^2) of $Na_{11.08(8)}Sn_2SbS_{12}$ obtained from single crystal XRD at 280 K.

Views of the $Na_{11}Sn_2SbS_{12}$ crystal structure along the [010], [001] and [100] directions are shown in **Figure** 4.6a, 4.6b and 4.6c, respectively. Perfectly ordered Sn/Sb tetrahedra are observed. Five sodium sites form irregular NaS_6 octahedra with interatomic distances between 2.8 Å and 3.6 Å, while one site is loosely bounded to eight sulfur neighbors to from a quasi-cubic environment with interatomic distances between 3.3 Å and 3.9 Å. All Na^+-Na^+ interatomic distances are in the range of 3.2 Å to 3.5 Å as shown in **Table** 4.5, this narrow range of distances facilitates the Na^+-ion transport through the $Na_{11}Sn_2SbS_{12}$ lattice. **Figure** 4.7 shows the PXRD pattern of $Na_{11}Sn_2SbS_{12}$. The XRD data refined using the model initially derived from single crystal diffraction (**Table** 4.3) confirmed the formation of almost pure single phase $Na_{11}Sn_2SbS_{12}$.

Atom1	Atom2	Interatomic distance (Å)
Sn1	**S1**	2.3919(7) × 2
Sn1	**S2**	2.3947(6) × 2
Sb1	**S3**	2.3349(7) × 4
Na1	**S1**	2.9546(16)
Na1	**S1**	3.5647(19)
Na1	**S2**	2.8485(15)
Na1	**S2**	3.242(2)
Na1	**S3**	2.972(2)
Na1	**S3**	3.0165(19)
Na2	**S1**	2.8264(13) × 2
Na2	**S2**	3.5719(12) × 2
Na2	**S3**	2.993(2) × 2
Na3	**S1**	2.8782(16) × 2
Na3	**S2**	2.8262(15) × 2
Na3	**S3**	3.1728(9) × 2
Na4	**S1**	3.1161(7) × 2
Na4	**S2**	2.6929(6) × 2
Na4	**S3**	3.1580(8) × 2
Na5	**S1**	2.8613(18) × 2
Na5	**S2**	2.8018(18) × 2
Na5	**S3**	3.2628(9) × 2
Na6	**S1**	3.2917(6) × 4
Na6	**S2**	3.9096(3) × 4
Na1	**Na6**	3.2529(17) × 2
Na1	**Na3**	3.3998(16) × 2
Na1	**Na4**	3.5107(15) × 2
Na1	**Na5**	3.449(2), 3.484(3)
Na2	**Na6**	3.240(3) × 2
Na2	**Na3**	3.4992(4), 3.4992(4)
Na2	**Na4**	3.4550(3), 3.4550(3)

Table 4.5: Interatomic distances of $Na_{11.08(8)}Sn_2SbS_{12}$ obtained from single crystal XRD at 280 K.

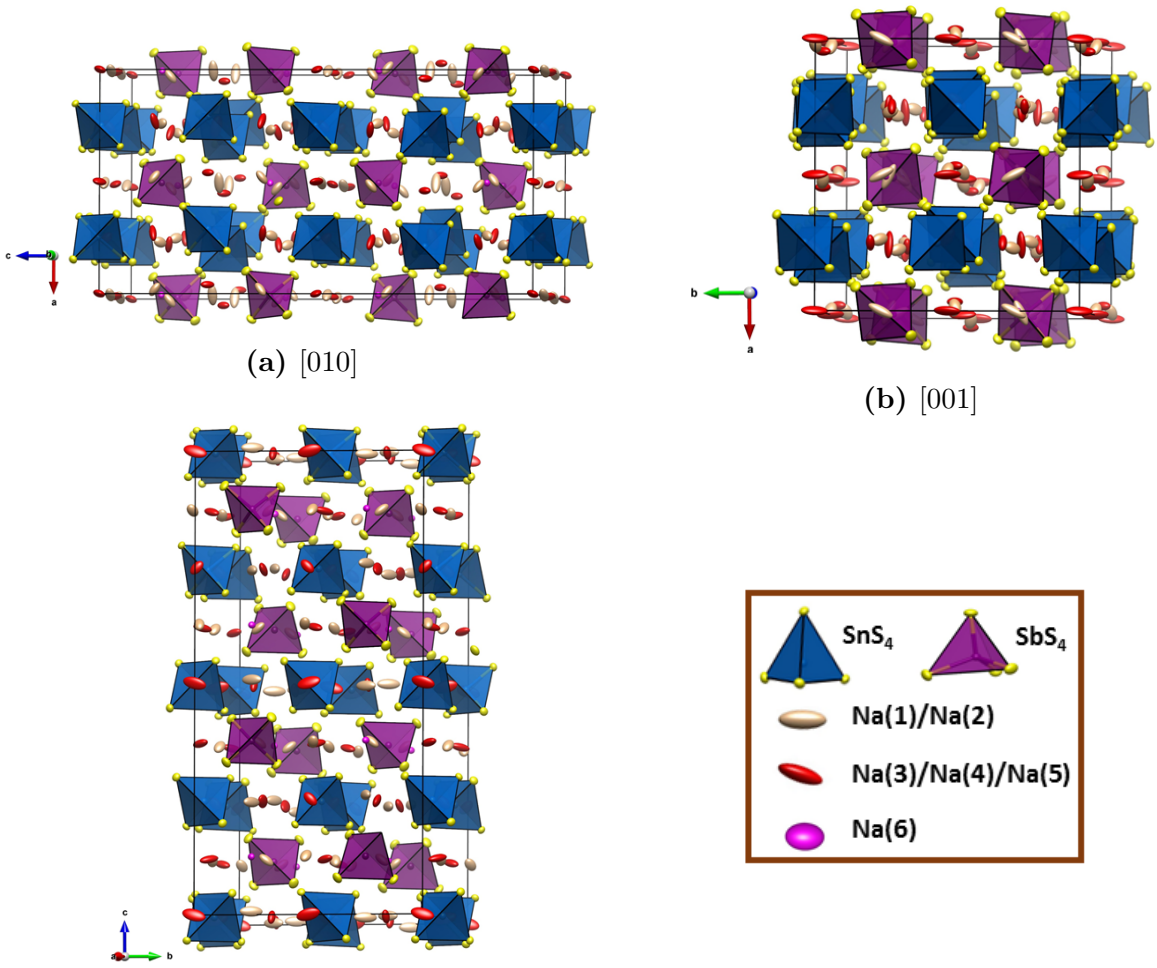

(a) [010]

(b) [001]

(c) [100]

Figure 4.6: View of the structure of $Na_{11}Sn_2SbS_{12}$ along, **a.** [010], **b.** [100]; **c.** [001]. Thermal ellipsoids are drawn at 50% probability. Color code: Na(1) and Na(2): light-rose; Na(3), Na(4), and Na(5): red; Na(6): pink; Sn: blue; Sb: purple; S: yellow. SnS_4 and SbS_4 polyhedra are shown in blue and purple respectively. Reproduced from Ref. [114] with the permission of The American Chemical Society.

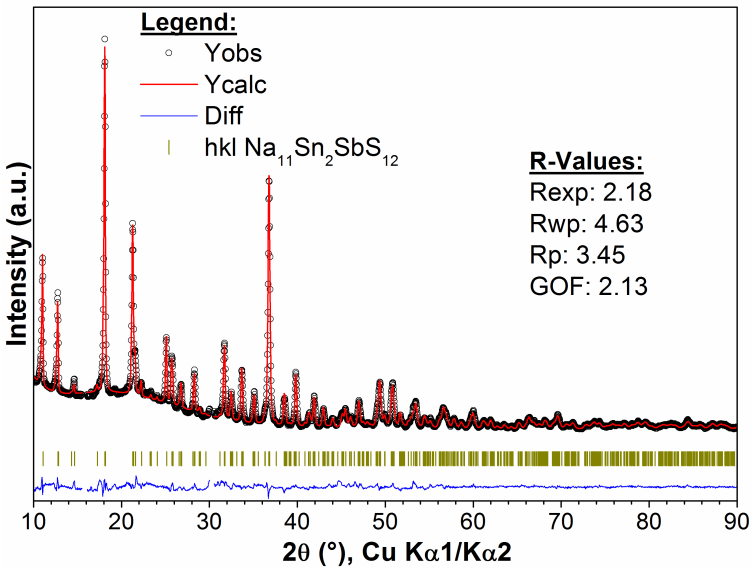

Figure 4.7: Rietveld refinement fit of $Na_{11}Sn_2SbS_{12}$ (Debye-Scherrer geometry). The black circles correspond to the data points, the red line denotes the calculated pattern and the difference map is shown in blue. Olive vertical ticks correspond to Bragg reflections. Two unknown tiny impurity peaks (at 15° and 30°) were excluded from the refinement. Reproduced from Ref. [114] with the permission of The American Chemical Society.

$Na_{11}Sn_2SbS_{12}$ reveals chains of Na-ions running along the *c*-axis and the *a,b*- plane, as depicted in **Figure** 4.8 [114]. As **Table** 4.3 shows, two sodium sites are 84% and 89% occupied (Na(1) and Na(2)), and three sites are nearly fully occupied (Na(3), Na(4) and Na(5)). The Na^+-ion flow is established by the Na(4)-Na(1)-Na(3)-Na(1) chains along the *c*-axis (**Figure** 4.8a), the Na(4)-Na(2)-Na(4) or Na(3)-Na(2)-Na(3) chains in the *a,b*- plane at z=0 (**Figure** 4.8b), and by Na(5)-Na(1)-Na(5) in the *a,b*- plane at z=0.875 (**Figure** 4.8c). These diffusion channels created by face-sharing Na octahedra form a network that spans all three crystallographic directions. The vacancy-rich sodium sites (Na(1) and Na(2)) alternate with each of the almost fully occupied sodium sites (Na(3), Na(4) and Na(5)), providing vital crossover sites for ion transport. The almost vacant Na(6) interstitial site creates additional interconnection points, in the *a,b*- plane between the diffusion channels formed by Na(1)-Na(5)-Na(1) chains (**Figure** 4.8c), and along the *c*-axis that joins the diffusion channels running in the *a,b*- plane, i.e., the Na(4)-Na(2)-Na(4) chains and Na(3)-Na(2)-Na(3) chains (**Figure** 4.8d) [114]. The Na(6) site also connects the Na(1) and Na(2) sites as discussed below.

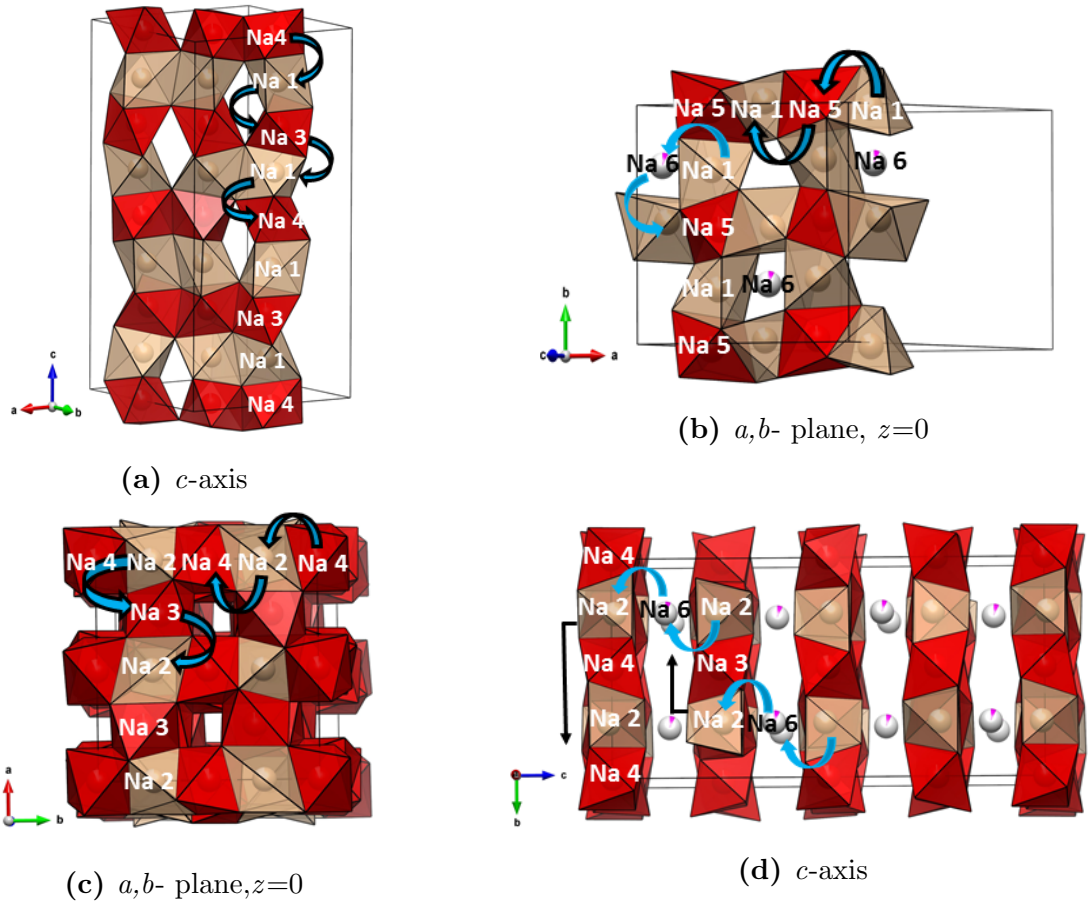

(a) *c*-axis

(b) *a,b*- plane, *z*=0

(c) *a,b*- plane,*z*=0

(d) *c*-axis

Figure 4.8: View of the diffusion channels: **a.** Formed by Na(4)-Na(3)-Na(1) sites along the *c*-axis; **b.** Along the *a,b*- plane formed by Na(4)-Na(2)-Na(4) or Na(3)-Na(2)-Na(3) at *z*=0; View of the interconnection points created by the Na(6): **c.** At *z*=0.87 between the diffusion channels formed by Na(1)-Na(5)-Na(1) chains; **d.** Along the *c*-axis between the diffusion channels that run along the *a,b*- plane. Color code: Na(1), Na(2): light-rose; Na(3), Na(4), Na(5): red; Na(6): pink. Reproduced from Ref. [114] with the permission of The American Chemical Society.

4.3.4 Ionic and electronic properties of $Na_{11}Sn_2SbS_{12}$

$Na_{11}Sn_2SbS_{12}$ shows an ionic conductivity of 0.57±0.06 mS·cm^{-1} at RT (**Table** A.11). **Figure** 4.9 depicts the Nyquist plot of $Na_{11}Sn_2SbS_{12}$ and the corresponding equivalent circuit (**Table** 4.6 [114]).

Table 4.6: Parameters of the fit for the impedance data of $Na_{11}Sn_2SbS_{12}$ at RT.

Element	Value
$\mathbf{R_1}$ (Ω)	237.1
$\mathbf{CPE_1}$ ($\mathbf{F\ s^{a-1}}$)	60.16 x 10^{-9}
$\mathbf{a_1}$	0.678
$\mathbf{CPE_2}$ ($\mathbf{F\ s^{a-1}}$)	7.327 x 10^{-6}
$\mathbf{a_2}$	0.577

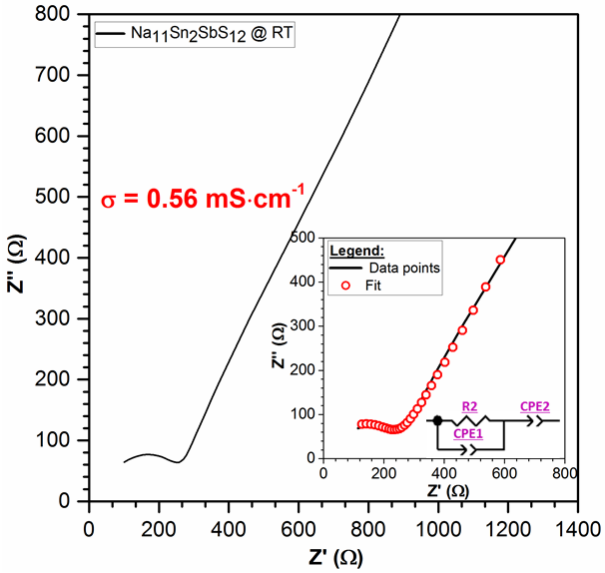

Figure 4.9: Nyquist plot of $Na_{11}Sn_2SbS_{12}$ at 30°C showing the impedance data and the fit with the corresponding equivalent circuit (inset). Reproduced from Ref. [114] with the permission of The American Chemical Society.

The linear dependence of $\log \cdot \sigma$ versus $1/T$ following the Arrhenius law over the temperature range (10°C to 60°C) for $Na_{11}Sn_2SbS_{12}$ is shown in **Figure** 4.10a. The activation energy for Na^+-ion diffusion determined from the slope of the plot is 0.34 eV, much higher than that in the $Na_{11}Sn_2PS_{12}$ phase (0.25 eV). **Figure** 4.10b shows the DC polarization curve of $Na_{11}Sn_2SbS_{12}$ at 0.35 V. The DC electronic conductivity of $Na_{11}Sn_2SbS_{12}$ is estimated to be 7.23 x 10^{-6} mS·cm^{-1}.

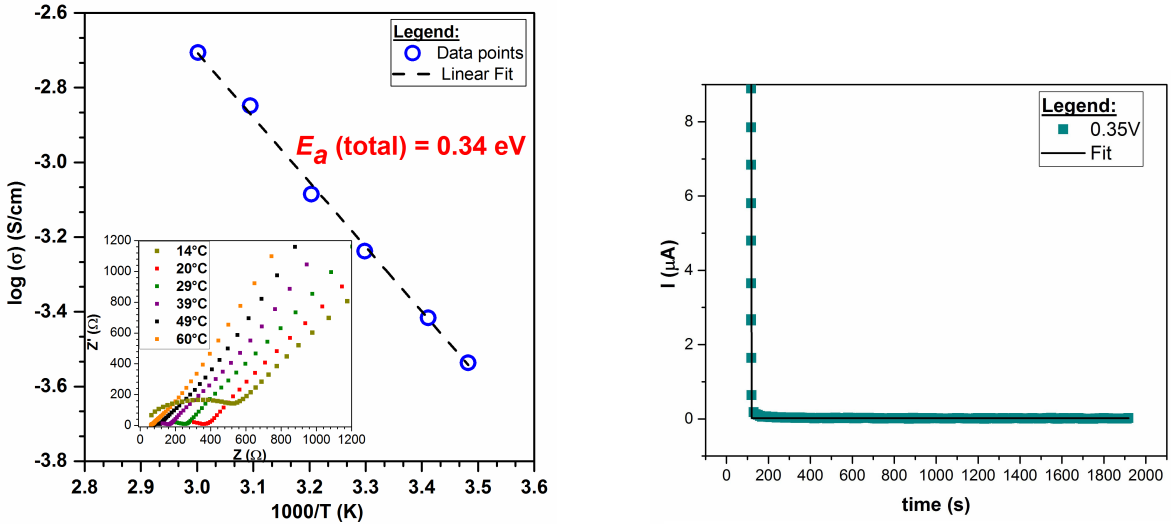

(a) (b)

Figure 4.10: a. Arrhenius conductivity plot of $Na_{11}Sn_2SbS_{12}$ from 10°C to 60°C. The inset displays the Nyquist impedance plot from 10°C to 60°C. Reproduced from Ref. [114] with the permission of The American Chemical Society; **b.** DC polarization of $Na_{11}Sn_2SbS_{12}$ with an applied voltage of 0.35 V.

4.4 Comparison between $Na_{11}Sn_2PnS_{12}$ with Pn=Sb and P

According to the single crystal and powder XRD data, $Na_{11}Sn_2SbS_{12}$ crystallizes in the same crystal system and space group as the P-phase; albeit, significant differences concerning the Na sublattice were identified in their structural details: (i) most importantly, an additional Na position (Na(6)) was clearly identified in $Na_{11}Sn_2SbS_{12}$ [114]. **Figure** 4.11 shows a comparison of the crystal structures of both compounds $Na_{11}Sn_2PnS_{12}$ with Pn=Sb and P. (ii) The sodium distribution over the available crystallographic sites is different as shown in **Table** 4.7. The sodium atoms distributed over the five Wyckoff positions account for a Na content of 10.8(11) in $Na_{11}Sn_2PS_{12}$, while the Na content in the Sb-based material is 11.08(8).

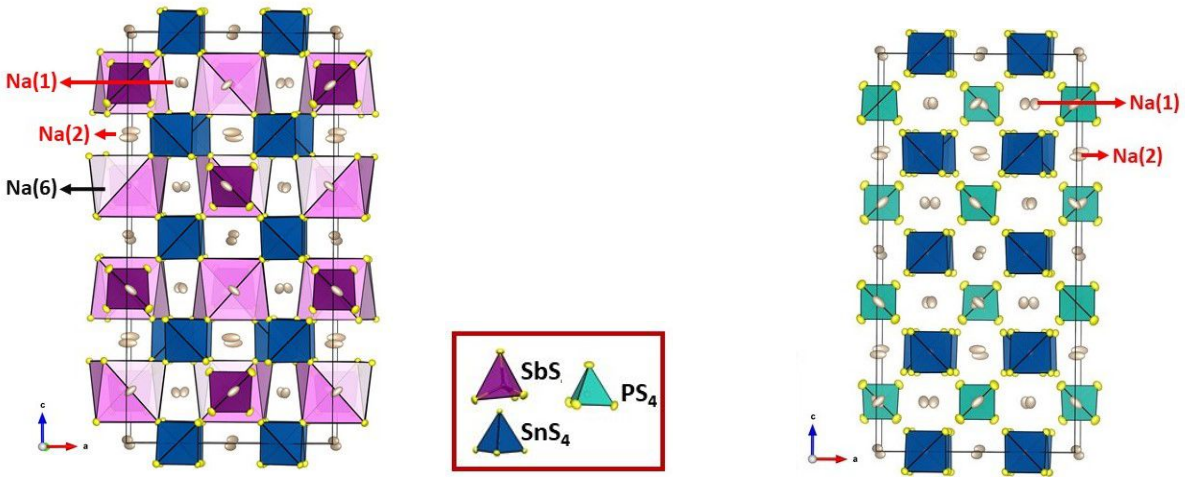

(a) $Na_{11}Sn_2SbS_{12}$ **(b)** $Na_{11}Sn_2PS_{12}$

Figure 4.11: a. View of the structure of $Na_{11}Sn_2SbS_{12}$ based on single crystal data. Color code: Na(1) and Na(2): light-rose; Na(6): pink; Sn: blue; Sb: purple; S: yellow. SnS_4, SbS_4 polyhedra are shown in blue and purple respectively. **b.** View of the structure of $Na_{11}Sn_2PS_{12}$ based on single crystal data. PS_4 tetrahedra are shown in light blue.

The crystal structure of the thioantimonate (Sb-phase) was solved as follows: first, the three sodium ions Na(1), Na(2) and Na(3) were initially identified, then their atomic positions were refined. Then two other Na atoms (Na(4) and Na(5)) were located in the remainder of the electron density. After refining the atomic positions and the thermal displacements of the Sb, Sn, the three sulfur atoms and the five sodium atoms, the site occupancy fraction of these five sodium atoms were freely refined: R1 and wR2 converged to 0.0269 and 0.0946 respectively. A strong peak in the remainder of the electron density of 2.25 e·Å^{-3} situated near Na(1), Na(2) and S(1) with interatomic distances of 3.25, 3.24 and 3.29 Å respectively, was added as Na(6) and its atomic positions, thermal displacements and occupancy were refined. This resulted in a drop in the R-values to R1=0.0221 and wR2=0.0507 and a drop in the remaining electron density to 1.12 e·Å^{-3}. The crystals of the P-phase showed pseudo-merohedral twinning -poorer quality crystals than those of the Sb-phase-, and therefore we were unable to accurately identify the Na(6) site in $Na_{11}Sn_2PS_{12}$ (**Figure** 4.11b). Due to the potential role of the N(6) site on the Na-ion transport dynamics in $Na_{11}Sn_2SbS_{12}$ (**Figures** 4.8b and 4.8d), we revisited the crystallography of $Na_{11}Sn_2PS_{12}$ (**Table** A.9).

Atom Wyckoff site	SOF	U_{eq}/Å^2
Sn1 *16e*	1	0.01857(7)
Sb1 *8a*	1	0.01874(8)
S1 *32g*	1	0.02592(13)
S2 *32g*	1	0.02281(13)
S3 *32g*	1	0.03656(16)
Na1 *32g*	0.894(6)	0.0565(7)
Na2 *16d*	0.839(11)	0.0907(18)
Na3 *16e*	0.977(8)	0.0533(8)
Na4 *16c*	0.927(9)	0.0983(16)
Na5 *16f*	0.972(10)	0.0784(13)
Na6 *8b*	0.076(9)	0.019(8)

Atom Wyckoff site	SOF	U_{eq}/Å^2
Sn1 *16e*	1	0.02195(15)
Sb1 *8a*	1	0.0242(6)
S1 *32g*	1	0.019964(5)
S2 *32g*	1	0.030119(5)
S3 *32g*	1	0.041812(7)
Na1 *32g*	0.868(18)	0.073(2)
Na2 *16d*	0.78(3)	0.082(4)
Na3 *16e*	0.965(19)	0.092(3)
Na4 *16c*	0.97(2)	0.092(3)
Na5 *16f*	0.95(3)	0.136(6)

Table 4.7: Site occupation factors and equivalent isotropic displacement parameters of ***Left***: $Na_{11.08(8)}Sn_2SbS_{12}$; ***Right***: $Na_{10.8(11)}Sn_2PS_{12}$ obtained from single crystal XRD at 280 K.

Table 4.8 shows the new crystallographic data, i.e., atomic coordinates, occupation factor and isotropic displacement parameters of $Na_{11}Sn_2PS_{12}$. The unit cell parameters correspond to a=13.6148(3) Å, c=27.2244(7) Å, V=5046.4(3) Å^3 and Z=8. **Figure** 4.12 shows the powder diffraction pattern of $Na_{11}Sn_2PS_{12}$, the refinement was performed using the model derived from single crystal diffraction, confirming the formation of $Na_{11}Sn_2PS_{12}$ phase. The revisited crystallographic data of $Na_{11}Sn_2PS_{12}$ also explicitly shows occupation of the Na(6) site with a SOF of 0.22(3), an occupation which greatly exceeds that in the antimony phase (SOF=0.076(9)). Duchardt *et al.* also identified a possible low-energy

interstitial "i1" site in $Na_{11}Sn_2PS_{12}$ (Na(6) *8b* site in our nomenclature). They estimated an occupancy of 20% for this site, however it was neglected in the final refinement due to limitations of PXRD data.

Atom	Wyckoff site	x	y	z	SOF	U_{eq}/Å^2
Sn1	*16e*	0.27463(5)	0	1/4	1	0.02204(14)
P1	*8a*	0.14789(10)	0.37559(11)	0.05036(5)	1	0.0234(5)
S1	*32g*	0.15089(10)	0.07664(11)	0.05119(5)	1	0.0282(3)
S2	*32g*	0.08891(13)	0.16558(14)	0.33188(7)	1	0.0263(17)
S3	*32g*	0	1/4	3/8	1	0.0475(4)
Na1	*32g*	0.0099(3)	0.0185(4)	0.12519(14)	0.866(17)	0.0727(19)
Na2	*16d*	0	1/4	0.0071(2)	0.79(3)	0.085(4)
Na3	*16e*	0.0248(4)	0	1/4	0.969(18)	0.092(3)
Na4	*16c*	0	0	0	0.97(2)	0.162(6)
Na5	*16f*	0.2383(3)	0.4883(3)	1/8	0.97(3)	0.137(5)
Na6	*8b*	0.27463(5)	0	1/4	0.22(3)	0.10(2)

Table 4.8: Atomic coordinates, site occupation factors and equivalent isotropic displacement parameters of $Na_{11.08(10)}Sn_2PS_{12}$ obtained from single crystal XRD at 280 K.

Atom	U_{11}	U_{22}	U_{33}	U_{23}	U_{13}	U_{12}
Sn1	0.022(1)	0.020(1)	0.025(1)	-0.001(1)	0	0
P1	0.020(1)	0.020(1)	0.030(1)	0	0	0
S1	0.028(1)	0.026(1)	0.031(1)	0.001(1)	0.004(1)	-0.003(1)
S2	0.023(1)	0.028(1)	0.027(1)	0.000(1)	0.003(1)	0.001(1)
S3	0.045(1)	0.046(1)	0.051(1)	-0.013(1)	0.0011(1)	0.006(1)
Na1	0.088 (4)	0.055(3)	0.075(3)	-0.003(2)	0.042(2)	-0.009(2)
Na2	0.065(5)	0.147(8)	0.042(4)	0	0	-0.063(5)
Na3	0.020(1)	0.131(5)	0.124(5)	0.89(4)	0	0
Na4	0.026(3)	0.296(13)	0.163(7)	-0.156(8)	-0.007(3)	-0.001(4)
Na5	0.193(8)	0.193(8)	0.024(2)	-0.009(3)	0.009(3)	-0.142(8)
Na6	0.110(30)	0.110(30)	0.60(30)	0	0	-0.030(20)

Table 4.9: Anisotropic displacement parameters (Å^2) of $Na_{11.08(10)}Sn_2PS_{12}$ obtained from single crystal XRD at 280 K.

Atom1	Atom2	Interatomic distance (Å)
Sn1	**S1**	2.3787(12) × 2
Sn1	**S2**	2.3796(12) × 2
P1	**S3**	2.0416(14) × 4
Na1	**S1**	2.969(5)
Na1	**S1**	3.006(5)
Na1	**S2**	2.891(4)
Na1	**S2**	3.1885(5)
Na1	**S3**	2.969(5)
Na1	**S3**	3.006(5)
Na2	**S1**	2.899(3) × 2
Na2	**S2**	3.358(2) × 2
Na2	**S3**	2.928(5) × 2
Na3	**S1**	2.829(4) × 2
Na3	**S2**	2.803(4) × 2
Na3	**S3**	3.288(2) × 2
Na4	**S1**	2.9668(14) × 2
Na4	**S2**	2.6919(14) × 2
Na4	**S3**	3.3313(16) × 2
Na5	**S1**	2.832(4) × 2
Na5	**S2**	2.783(4) × 2
Na5	**S3**	3.361(2) × 2
Na6	**S1**	3.3328(12) × 4
Na6	**S2**	3.7196(10) × 4
Na1	**Na6**	3.152(5) × 2
Na1	**Na3**	3.3998(16) × 2
Na1	**Na4**	3.5107(15) × 2
Na1	**Na5**	3.385(6), 3.448(6)
Na2	**Na6**	3.227(6) × 2
Na2	**Na3**	3.4249(6), 3.4249(6)
Na2	**Na4**	3.4082(3) × 2

Table 4.10: Interatomic distances of $Na_{11.08(10)}Sn_2PS_{12}$ obtained from single crystal XRD at 280 K.

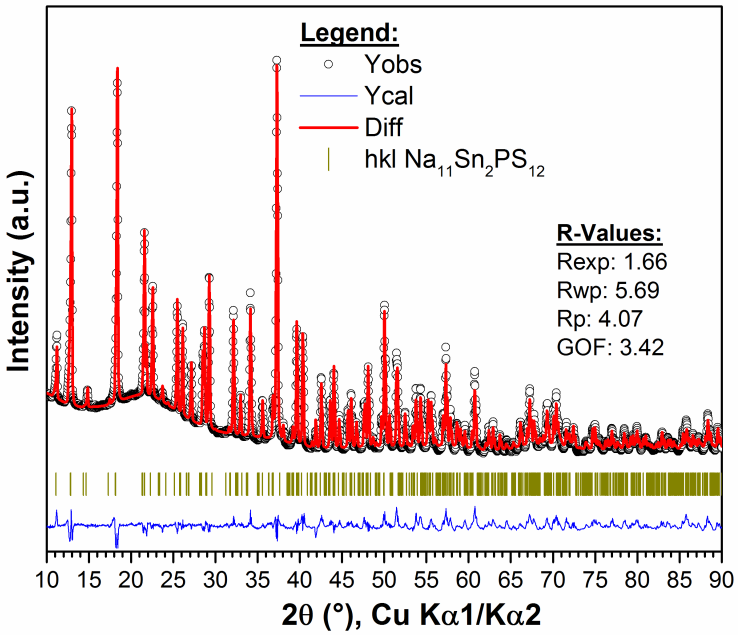

Figure 4.12: Rietveld refinement fit of $Na_{11}Sn_2PS_{12}$ (Debye-Scherrer geometry). The black circles correspond to the data points, the red line denotes the calculated pattern, and the difference map is shown in blue. Olive vertical ticks correspond to Bragg reflections.

Both $Na_{11}Sn_2PnS_{12}$ with Pn=Sb and P structures have the same Na content (11.08(8) (Sb) and 11.08(10) (P) **Tables** A.8 and A.9); however, the distribution of sodium vacancies over the six available sites are different, particularly on the crossover Na(1) and Na(2) sites [Na(1): SOF=0.894(6) (Sb) versus SOF=0.866(17) (P); Na(2): SOF=0.839(11) (Sb) versus SOF=0.79(3) (P), **Tables** 4.3 and 4.8]. Likely, the existence of the Na(6) site opens up other paths for ion hopping, since it directly connects Na(1) in the *32g* site and Na(2) in the *16d* site. **Figure** 4.13a exhibits an excised portion of structure showing the Na(6) site located between two Na(1) or Na(2) octahedra and depiction of the size of the bottleneck across the quasi four-sided face illustrating the short dimension across the sulfur atoms [114]. Although the position of Na(6) in the *8b* Wyckoff site in $Na_{11}Sn_2PS_{12}$ could not be refined in prior studies [104] [115], a path through this site was suggested by BVSE calculations in the P-phase; suggesting that the position plays a role in its ion conduction process [115].

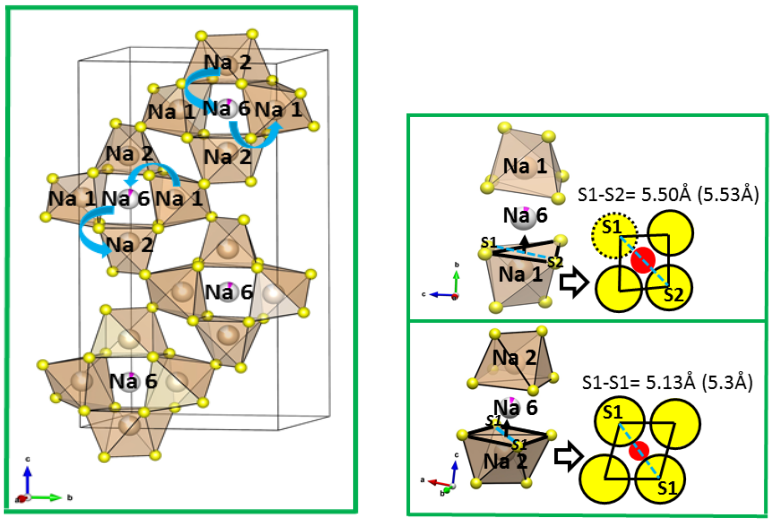

(a) **(b)**

Figure 4.13: a. View of the interconnection between Na(1)-Na(6)-Na(2) sites. Transport bottlenecks in $Na_{11}Sn_2PnS_{12}$ with Pn=Sb and P: **b.** ***Top.*** Na(1)-Na(6) where the dotted S^{2-} anion lies just below the trigonal plane spanned by the other sulfur anions; ***Bottom.*** Na(2)-Na(6). The distance shown is for Sb-phase and the value in brackets is for P-phase. Reproduced from Ref. [114] with the permission of The American Chemical Society.

Additional mobility in the *a,b*- plane (via the Na(1)-Na(6)-Na(1) path), and along the *c*-axis (via the Na(2)-Na(6)-Na(2) path) may be enabled as was shown in **Figure** 4.7. These hops would occur through a quasi-four-sided sulfide window in either case, where the shortest S^{2-}-S^{2-} distance across the window determines the void space for the passage of the sodium cation (**Figure** 4.13b). The bottlenecks for Na^+-ion transport in $Na_{11}Sn_2PnS_{12}$ with Pn= Sb and P are shown for comparison in **Table** 4.11 (calculated by Dr. Zhizhen Zhang). The values shown correspond to the radius of the circumscribed circle of the triangle spanned by the centres of the three S^{2-} anions on the triangular faces of the NaS_6 octahedra (Na1-Na3, 4, 5, 6; Na2-Na3, 4, 5, 6); or the shortest sulfide anion distance across the quasi four-sided window for Na1-Na6 or Na2-Na6 (see **Figure** 4.13). The bottleneck radius can be calculated by subtracting the radius of the sulfide anion (1.84 Å). The distance across the window is not only fairly spacious, but similar for $Na_{11}Sn_2PnS_{12}$ with Pn=Sb and P especially for the Na(1)-Na(6)-Na(1) path, and therefore it is not a bottleneck for Na^+-ion transport.

Na^+-Na^+	Bottleneck size (Å)	
	Sb	**P**
Na1-Na3	2.47	2.47
Na1-Na4	2.47	2.48
Na1-Na5	2.42, 2.54	2.45, 2.53
Na1-Na6	5.50	5.53
Na2-Na3	2.46	2.47
Na2-Na4	2.52	2.51
Na2-Na6	5.13	5.30

Table 4.11: Bottlenecks for Na^+-ion transport in $Na_{11}Sn_2PnS_{12}$ with P=Sb and P obtained from single crystal XRD data at 280 K.

The bottleneck sizes for Na^+ transport are similar in $Na_{11}Sn_2SbS_{12}$ and $Na_{11}Sn_2PS_{12}$ compounds, indicating that ion migration through the interstitial (Na(6)) site does not govern their difference in ion conductivity. In accord, we note that for long range transport, hops through Na(6) must be accompanied by ion migration through the triangular faces of the $Na(2)S_6$ octahedra as shown in **Figures** 4.14 and 4.8d. Such a tortuous zig-zag path is dictated by the presence of the $(Sn/Sb)S_4$ tetrahedra in the lattice that would block a continuous path along the *c*-axis. A comparison of the volumes of the NaS_6 polyhedra for $Na_{11}Sn_2PnS_{12}$ with Pn=Sb and P is shown in **Table** 4.12.

Very similar values are obtained for the $(Na1\text{-}Na5)S_6$ polyhedra for both phases, while $Na(6)S_6$ shows a significantly larger volume for the Sb phase (75 $Å^3$ versus 70 $Å^3$). This destabilizes the site (i.e. it lies at a higher energy) and thus occupation of the site is less favorable. This leads us to propose that the primary cause of the Na(6) site occupation difference in the two cases is based on the subtle structural difference that results in a larger volume of the Na(6) site in the Sb phase [114].

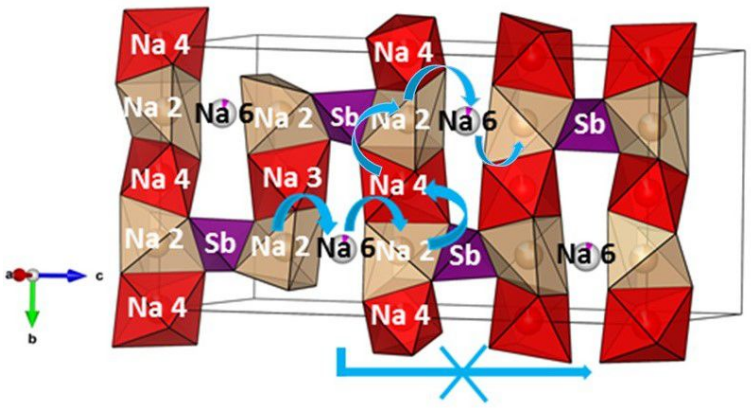

Figure 4.14: View of the interconnection points in $Na_{11}Sn_2SbS_{12}$ created by the Na(6) site along the *c*-axis between the diffusion channels that run along the *a,b*- plane (composed of Na(4)-Na(2)-Na(4) or Na(3)-Na(2)-Na(3)). Color code: Na(2): light-rose; Na(3), Na(4): red; Na(6): pink; SbS_4: purple.

Polyhedral	**Polyhedral Volume(Å^3)**	
	Sb	**P**
Na1$_{oct}$	34.02	32.10
Na2$_{oct}$	31.81	30.59
Na3$_{oct}$	32.95	33.47
Na4$_{oct}$	34.31	34.43
Na5$_{oct}$	33.61	34.13
Na6$_{distoredcubic}$	75.18	70.09

Table 4.12: Volume of the NaS_6 polyhedra in $Na_{11}Sn_2PnS_{12}$ with Pn=Sb and P obtained from single crystal XRD data at 280 K, calculated using VESTA©.

The higher Na occupancies on the sites that form the mayor conduction pathways in $Na_{11}Sn_2SbS_{12}$ are a consequence of the redistribution of sodium ions from the interstitial site (Na(6)) onto the two crossover sites (Na(1) and Na(2)), which implies that Na(6) is less favorable in the Sb lattice (SOF=0.076(9) (Sb) versus SOF=0.22(3) (P)); **Tables** 4.3 and 4.8). Implying that the vacancy concentration and distribution play a critical role in dictating sodium ion conductivity in this structure type [114]. The transport possibility is likely higher along the main NaS_6 octahedral site pathways (i.e. Na1-Na3-Na4-Na1), than

through the interstitial Na(6) site. Expecting the latter path to be even more minor for Sb because of its higher interstitial site energy (lower population). Thus, hopping through this interstitial site likely constitutes a less important, albeit non-negligible contribution to Na^+-ion diffusivity in both cases.

The properties of $Na_{11}Sn_2SbS_{12}$ stem from its structural framework, which allows Na^+-ions to diffuse in 3D pathways as described above. However, its ion conductivity is lower than isostructural $Na_{11}Sn_2PS_{12}$ (σ=1.39 mS·cm^{-1}) despite having a larger unit cell volume (5235.5(19) Å^3 versus 5046.4(3) Å^3) [104]. This may be partly explained by effects of the local bonding (P-S versus Sb-S) interactions on ion transport. The substitution of Sb for P within the tetrahedral PnS_4 units results in longer Sb-S bonds (**Tables** and 4.5 and 4.10), as expected since Sb^{5+} is a larger cation than P^{5+}. The lower electronegativity of Sb^{5+} versus P^{5+} (1.8 versus 2.1) will lead to higher electron density on S^{2-}, and hence stronger Na^+-S^{2-} Coulombic attractions in $Na_{11}Sn_2SbS_{12}$ that would bind the Na^+-ions more tightly. Such an inductive effect was invoked in explaining the lower Li^+ ion conductivity in $Li_{10}(Ge_{1-x}Sn_x)_2PS_{12}$, with Sn^{4+} substitution for the more electronegative Ge^{4+} [116]. This can explain the two-fold lower atomic displacement parameters (ADPs) of the Na(3), Na(4) and Na(5) sites in the major conduction pathways of the Sb phase (0.0533(8), 0.0983(16) and 0.0784(13), respectively, for (Sb) versus 0.092(3), 0.162(6) and 0.137(5), respectively, for (P)), which indicates these Na^+-ions are less mobile on the site (**Table** 4.3) [114].

4.5 Vacancies formation in $Na_{11}Sn_2PnS_{12}$ with Pn=Sb and P

Introduction

The existence of defects and a high concentration of mobile carriers, as well as a low energy barrier for mobile ion migration are prerequisites to obtain high diffusivity in solids [117]. Theoretical studies revealed that stoichiometry Na_3PSe_4 and c-Na_3PS_4 present negligible Na^+-ion diffusivity [108] [52], but the introduction of either Na interstitials or Na vacancies improve their conductivity. Indeed, defects are believed to play a more crucial role than the framework structure in governing ion diffusion [111].

The Na vacancy concentration plays a critical role in dictating sodium ion conductivity in $Na_{11}Sn_2PnS_{12}$ structure type. Therefore, attempts to introduce additional Na vacancies by decreasing the Sn/Sb ratio in $Na_{11}Sn_2SbS_{12}$ to form $Na_{11-x}Sn_{2-x}Sb_{1+x}S_{12}$ with x=0.2,

0.25 and 0.5, and by substitution of Sn by Sb in $Na_{11-x}Sn_{2-x}Sb_xPS_{12}$ with x=0.3 and 0.5 were carried out.

$Na_{11-x}Sn_{2-x}Sb_{1+x}S_{12}$ with x=0.2, 0.25 and 0.5

The non-stoichiometry materials were synthesized following the same procedure employed in the synthesis of compound $Na_{11}Sn_2SbS_{12}$. **Figure** 4.15 exhibits the PXRD patterns of $Na_{11-x}Sn_{2-x}Sb_{1+x}S_{12}$ with x=0, 0.2, 0.25 and 0.5.

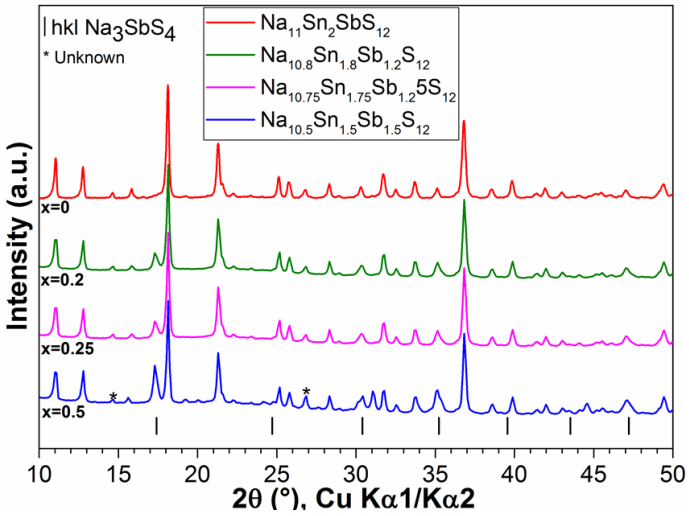

Figure 4.15: Comparison of the XRD patterns of $Na_{11-x}Sn_{2-x}Sb_{1+x}S_{12}$ with x=0, 0.20, 0.25 and 0.5 (Bragg-Brentano geometry). The black vertical ticks correspond to the Bragg-reflections of Na_3SbS_4, unknown reflections are marked with an asterisk. Reproduced from Ref. [114] with the permission of The American Chemical Society.

Based on the XRD patterns, the as-prepared powders consist primarily of the $Na_{11}Sn_2SbS_{12}$ phase, with c-Na_3SbS_4 present as a secondary phase whose content increases with x. A refinement of the targeted composition -$Na_{10.8}Sn_{1.8}Sb_{1.2}S_{12}$- was conducted to establish the Na_3SbS_4 content (**Figure** 4.16a [114]).

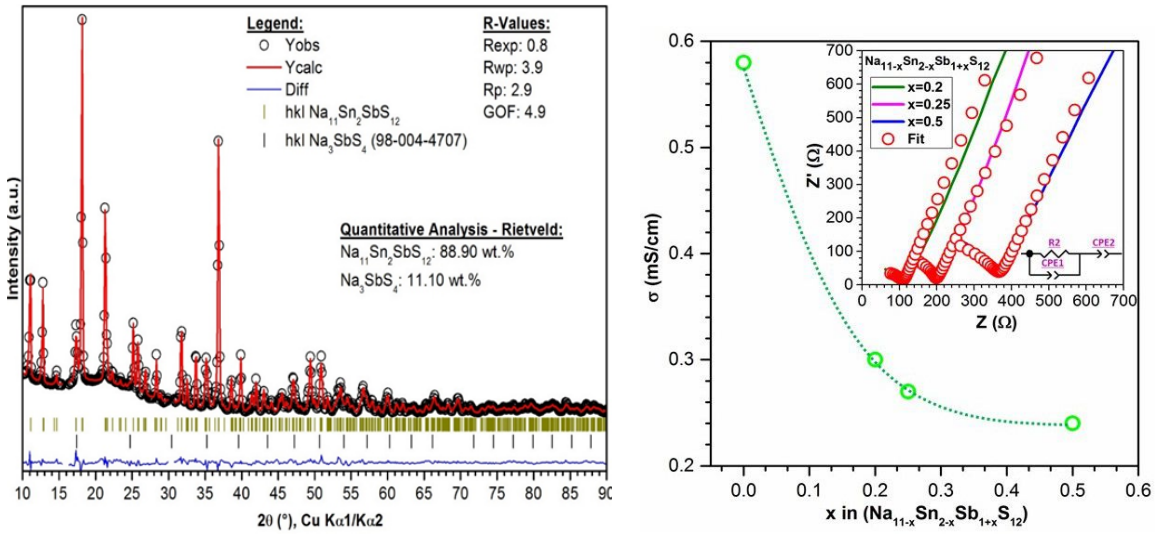

(a) **(b)**

Figure 4.16: a. Rietveld refinement fit of $Na_{10.8}Sn_{1.5}Sb_{0.5}PS_{12}$ (Debye-Scherrer geometry). The black circles correspond to the data points, the red line denotes the calculated pattern and the difference map is shown in blue. Gold vertical ticks correspond to the Bragg reflections of $Na_{11}Sn_2SbS_{12}$ and the black ticks to Na_3SbS_4; **b.** RT ionic conductivities of $Na_{11-x}Sn_{2-x}Sb_{1+x}S_{12}$ (x=0.20, 0.25 and 0.50). The inset displays the Nyquist impedance plot and fit with the respective equivalent circuit. Reproduced from Ref. [114] with the permission of The American Chemical Society.

The refinement of the targeted composition, $Na_{10.8}Sn_{1.8}Sb_{1.2}S_{12}$, was performed using the model initially derived from single crystal diffraction of $Na_{11}Sn_2SbS_{12}$ (**Table** 4.3). Two tiny unknown impurity peaks (at 15° and 30°) were excluded from the refinement. The PXRD shows a fraction of the 11 wt% of the impurity phase, Na_3SbS_4, indicating the strict limit of solubility of Sb in the crystal structure; i.e., x is essentially zero on the Sb-rich side. The RT ion conductivities for x=0.2, 0.25 and 0.5 are also summarized in **Figure** 4.16b. The highest value was obtained for stoichiometry $Na_{11}Sn_2SbS_{12}$ (0.57 mS·cm^{-1}). We conclude that even though Na_3SbS_4 is a good Na-ion conductor (1.7 mS·cm^{-1}) [111], its formation -potentially in the grain boundaries- lowers the overall conductivity of $Na_{11-x}Sn_{2-x}Sb_{1+x}S_{12}$ [114].

Compound	CPE_1 ($F\ s^{a-1}$) (10^{-9})	a_1	CPE_2 ($F\ s^{a-1}$) (10^{-6})	a_2	R_1 (Ω)
$Na_{10.5}Sn_{1.5}Sb1.5S_{12}$	6.347	0.841	7.765	0.723	365.1
$Na_{10.75}Sn_{1.75}Sb1.25S_{12}$	4.119	0.888	6.729	0.758	197
$Na_{10.8}Sn_{1.8}Sb1.2S_{12}$	22.71	0.789	6.841	0.744	111

Table 4.13: Parameters of the fit for the impedance data of $Na_{11+1}Sn_{2-x}Sb_{1+x}S_{12}$ with x=0.2, 0.25 and 0.5 at RT.

$Na_{11-x}Sn_{2-x}Sb_xPS_{12}$ with x=0.3 and 0.5

The non-stoichiometry materials were synthesized following the same procedure employed in the synthesis of $Na_{11}Sn_2PS_{12}$ compound. **Figure** 4.17 exhibits the PXRD patterns of $Na_{11-x}Sn_{2-x}Sb_xPS_{12}$ with x=0, 0.3 and 0.5.

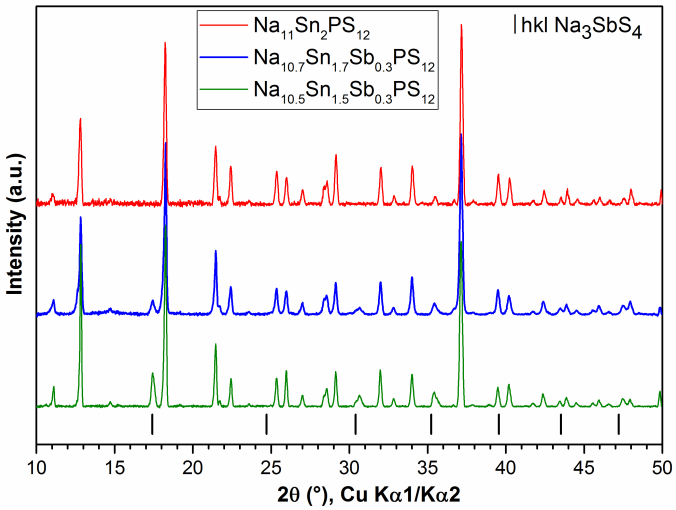

Figure 4.17: Comparison of the XRD patterns of $Na_{11-x}Sn_{2-x}Sb_xPS_{12}$ with x=0, 0.3 and 0.5 (Bragg-Brentano geometry). The black vertical ticks correspond to the Bragg-reflections of Na_3Sb_4.

The XRD patterns show that the as-prepared powders consist primarily of the $Na_{11}Sn_2PS_{12}$ phase, also with c-Na_3SbS_4 present as an impurity phase whose content increases with x. The refinement of the targeted composition, $Na_{10.8}Sn_{1.5}Sb_{0.5}PS_{12}$ (**Figure**

4.18a), was performed using the model initially derived from single crystal diffraction (**Table** 4.8). The PXRD shows a fraction of the 10.44 wt% of Na_3Sb_4 secondary phase. The RT ion conductivities for x=0, 0.30 and 0.50 are summarized in **Figure** 4.18b. The highest ionic conductivity is shown by x=0, $Na_{11}Sn_2PS_{12}$ (1.39 mS·cm^{-1}). The crystallization of Na_3Sb_4 as x increases in $Na_{11-x}Sn_{2-x}Sb_xPS_{12}$ has a detrimental effect on the overall conductivity.

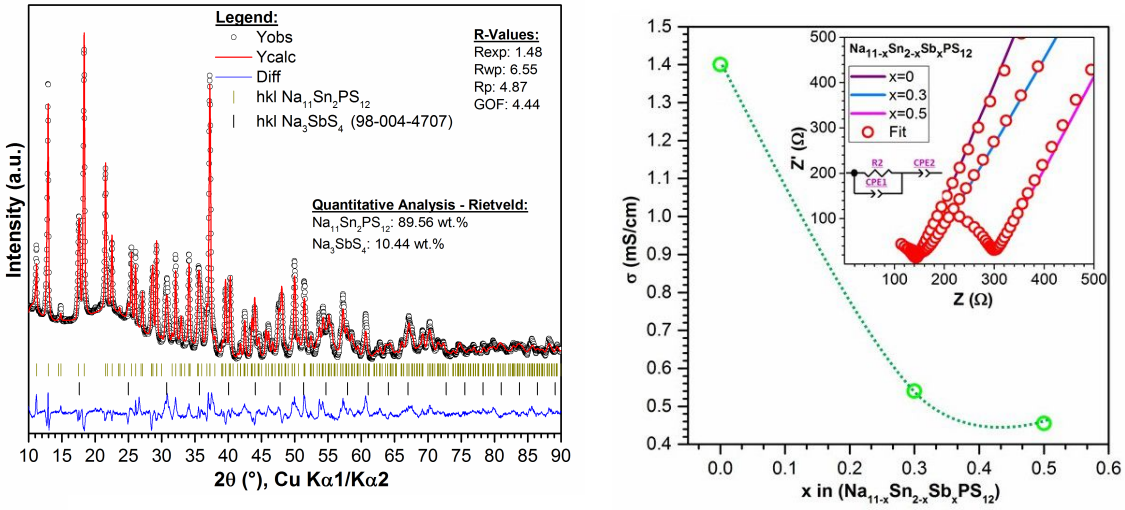

(a) **(b)**

Figure 4.18: a. Rietveld refinement fit of $Na_{10.5}Sn_{1.5}Sb_{0.5}PS_{12}$ (Debye-Scherrer geometry). The black circles correspond to the data points, the red line denotes the calculated pattern and the difference map is shown in blue. Gold vertical ticks correspond to the Bragg reflections of $Na_{11}Sn_2PS_{12}$ and the black ticks to Na_3SbS_4; **b.** RT ionic conductivities as a function of composition of $Na_{11-x}Sn_{2-x}Sb_xPS_{12}$ (x=0, 0.30 and 0.50). The inset displays the Nyquist impedance plot and fit with the respective equivalent circuit.

Compound	**CPE$_1$ (F s^{a-1}) (10^{-9})**	**a$_1$**	**CPE$_2$ (F s^{a-1}) (10^{-6})**	**a$_2$**	**R$_1$ (Ω)**
$Na_{10.7}Sn_{1.7}Sb0.3PS_{12}$	88.61	0.652	5.293	0.687	155.6
$Na_{10.5}Sn_{1.5}Sb0.5PS_{12}$	2.355	0.888	6.778	0.723	295.3

Table 4.14: Parameters of the fit for the impedance data of $Na_{11-x}Sn_{2-x}Sb_xPS_{12}$ with x=0.3 and 0.5 at RT.

4.6 Air stability of $Na_{11}Sn_2PnS_{12}$ with Pn=Sb and P

Solid electrolytes, with a central element acting as a softer acid than phosphorus, have a tolerance against hydrolysis, resulting in better chemical stability than that of Li_3PS_4 [118]. Determination of the air stability of $Na_{11}Sn_2PnS_{12}$ with Pn=Sb and P materials was carried out by exposing samples to a flow of dry air for 36 h, and measuring XRD patterns and conductivity every 12 h (**Figure** 4.19 [114])

XRD patterns of $Na_{11}Sn_2SbS_{12}$ after exposure slightly change (**Figure** 4.19a), and a small decrease in ionic conductivity is observed in **Figure** 4.19b. In contrast, the XRD patterns of $Na_{11}Sn_2PS_{12}$ show significant degradation suggestive of very poor air stability of the thiophosphate phase (**Figure** 4.19a).

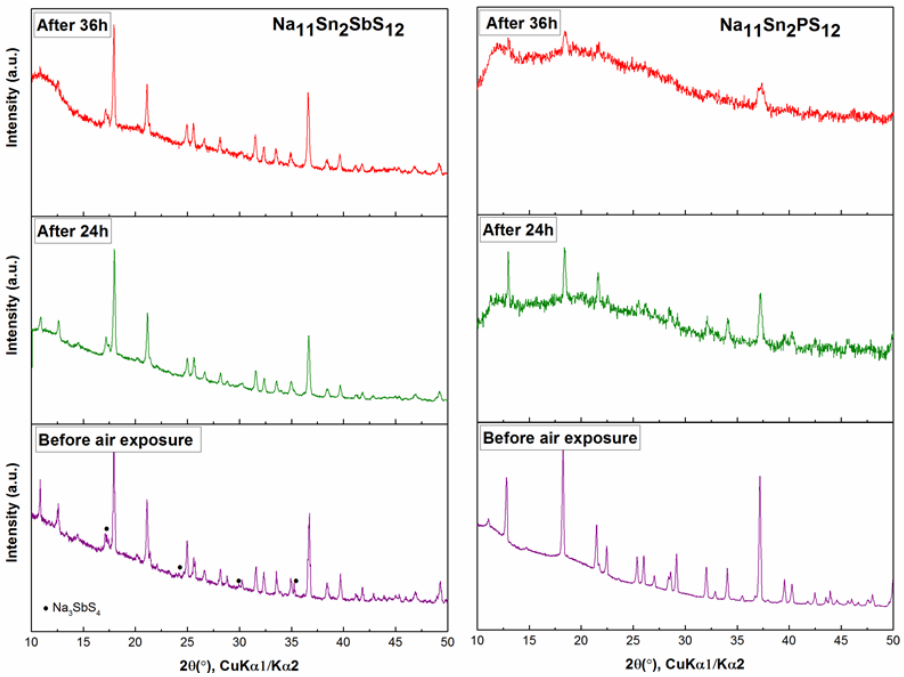

(a)

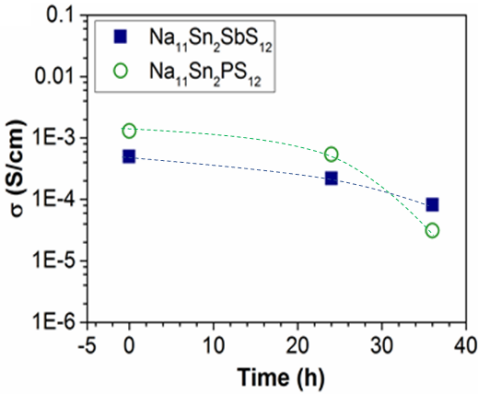

(b)

Figure 4.19: a. XRD patterns of $Na_{11}Sn_2PnS_{12}$ with Pn=Sb and P before dry air exposure, after 24 h and 36 h (Bragg-Brentano geometry); **b.** Variation on the ionic conductivity versus exposure time. Reproduced from Ref. [114] with the permission of The American Chemical Society.

4.7 Summary

Even though $Na_{11}Sn_2SbS_{12}$ is isostructural with the P-based analogue -with very similar 3D pathways for Na-ion transport- it exhibits poorer ion conduction.

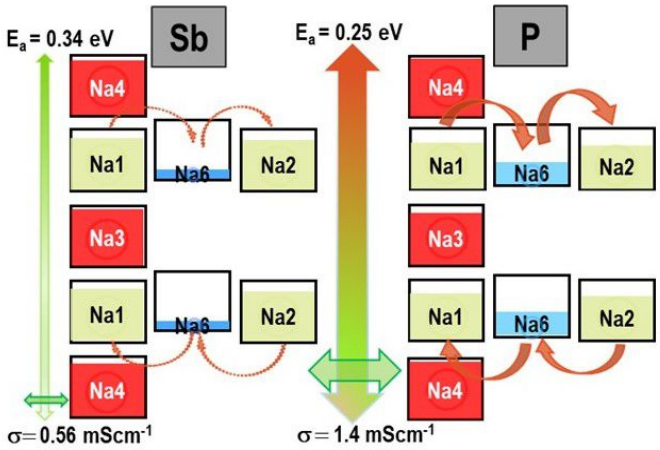

Figure 4.20: Comparative schematic diagram of the Na sites in $Na_{11}Sn_2PnS_{12}$ with Pn=Sb and P crystal structures illustrating the proposed role of the interstitial Na(6) site on the Na^+ ion transport mechanism. Reproduced from Ref. [114] with the permission of The American Chemical Society.

A partially occupied interstitial Na(6) site was unequivocally identified in this structural class. The larger volume of the $Na(6)S_6$ polyhedra along with its lower occupancy in $Na_{11}Sn_2SbS_{12}$ suggests a higher site energy for Na(6) in this phase framework, making its potential role in conduction pathways less favorable. Albeit, transport through this site, while likely non-negligible, does not appear to govern ion conductivity.

These studies suggest that the major role of the interstitial site is to provide an accessible site for some of the Na^+ cations required to balance the charge in the framework, allowing a higher vacancy population in the major conduction pathways, and facilitating ion transport. The much lower ADPs of the Na(3), Na(4) and Na(5) sites in the major conduction pathways of $Na_{11}Sn_2SbS_{12}$ (0.0533(8), 0.0983(16) and 0.0784(13), respectively, for (Sb) versus 0.092(3), 0.162(6) and 0.137(5), respectively, for (P)), indicates these Na^+-ions are less mobile on the site.

Stronger Na^+-S^{2-} Coulombic attractions in the Sb phase, induced by a lower effective anion charge on the SbS_4 tetrahedra, may contribute to its lower conductivity. The subtle

interplay between local structural changes (inductive effect) and the distribution of Na vacancies over the six available crystallographic sites dictate the transport properties in this new class of ion conductors. The discovery of this Sb based sodium ion conductor with a complete structure solution provides valuable understanding for designing future fast ion conductors.

Isoelectronic substitution of sulfur with the larger and more polarizable selenium in $Na_{11}Sn_2SbS_{12}$, will broaden the diffusion pathways and lead to a softer more polarizable lattice, all of which may positively influence ionic conduction in the Se- substituted material. Thus, approaches to engineer the structure to increase conductivity of $Na_{11}Sn_2SbS_{12}$ rely on elemental substitution altering the lattice dynamics through introducing a softer, more polarizable anion without modifying the sodium concentration.

Chapter 5

Elucidating the structure-property relations in $Na_{11}Sn_2SbS_{12-x}Se_x$

5.1 Introduction

Although, RT Na-S batteries have prompted extensive research interest due to the high-charge storage capacity and abundance of both sodium and sulfur [119] [120], the low electronic conductivity of sulfur (0.5×10^{-27} S·cm^{-1}) leads to low utilization of the active material in the electrode [121]. Selenium has been regarded as another promising cathode material for both sodium and lithium-ion batteries [122] [123], due to its considerably higher electrical conductivity (1 mS·cm^{-1} versus 0.5×10^{-27} S·cm^{-1}) [122] [124] [125]. This feature has stimulated the development of Se-based solid electrolytes for Na^+-ion ASSB applications [126] [56] [127].

In 2015, the superionic conductor, c-Na_3PSe_4 (1.16 mS·cm^{-1}), was synthesized for the first time by Long Zhang *et al.* [54], followed by computational and experimental investigations on the same material conducted by Ceder *et al.* [108]. Although the crystal structure of c-Na_3SbSe_4 was first reported in 1989 [128], its ionic conductivity properties, σ=3.7 mS·cm^{-1} and E_a=0.19 eV, were not known until 2017 [56]. In both c-Na_3PSe_4 and c-Na_3SbSe_4 electrolytes, enhancement of ion transport was observed when compared to the S-based analogue electrolytes (0.2 mS·cm^{-1} and 2.8 mS·cm^{-1}, respectively) [45] [111]. The selenium analogue of the new structure-type $Na_{11}Sn_2PS_{12}$ was recently developed by two different groups, with reported ionic conductivities of 1.7 mS·cm^{-1} and 2.15 mS·cm^{-1} at 25°C, respectively. [127][126]. Albeit, the obtained values are slightly lower than the highest reported conductivity for the S-based $Na_{11}Sn_2PS_{12}$ (3.7 mS·cm^{-1}) [115]. Stefan

Adams *et al.* synthesized the $Na_{11}Sn_2PSe_{12}$ by mechanochemical method with a conductivity of 1 mS·cm^{-1} after annealing for 6 h [129]. Remarkable success has been achieved for Se-substituted $Na_{11}Sn_2PS_{12}$, including its application as electrolyte in Na-Se ASSBs [56]. Nerveless, the number of Na-Se ion conductors reported today is still limited; compared to sulfides and oxides, selenides are rather a large field of ionic conductor discovery. Here, following this view, I examined the Se-substitution within $Na_{11}Sn_2SbS_{12-x}Se_x$ with x=1, 6 and 12, which led to the successful synthesis of the new sodium SE, $Na_{11}Sn_2SbSe_{12}$.

5.2 Synthesis

Tetragonal $Na_{11}Sn_2SbS_{12-x}Se_x$ with x=1, 6 and 12 precursors were synthesized by mechanochemical route. Na_2S (99 %, Sigma-Aldrich), Na_2Se synthesized by one of my colleagues Abhinandan Shyamsunder, Sb_2S_3 (99%, Sigma-Aldrich), S powder (99.9%, Sigma-Aldrich), Se powder (99%, Sigma-Aldrich), Sn powder (99%, Sigma-Aldrich) and Sb powder (99%, Sigma-Aldrich) were mixed together according to the respective molar ratios of the targeted compositions. The mixtures were ball milled at 400 rpm for 33 h, then heated at 750°C with a heating rate of 94°C /h, held for 5 h, then cooled by a slow cooling step of 9 h from 750°C to 545°C, flowed by ice quenching. The refinement details from the single crystal diffraction data are presented in **Appendix** B.

5.3 Crystal structure

Figure 5.1 exhibits the RT PXRD patterns of the as-milled series of compositions $Na_{11}Sn_2SbS_{12-x}Se_x$ with x=1, 6 and 12. Halo patterns with no crystalline reflections that could be assigned to the starting materials were observed, indicating the formation of an amorphous phase for each composition. After the mechanochemical process, the resulting amorphous samples were heat-treated, turning into ion-conductive crystalline phases.

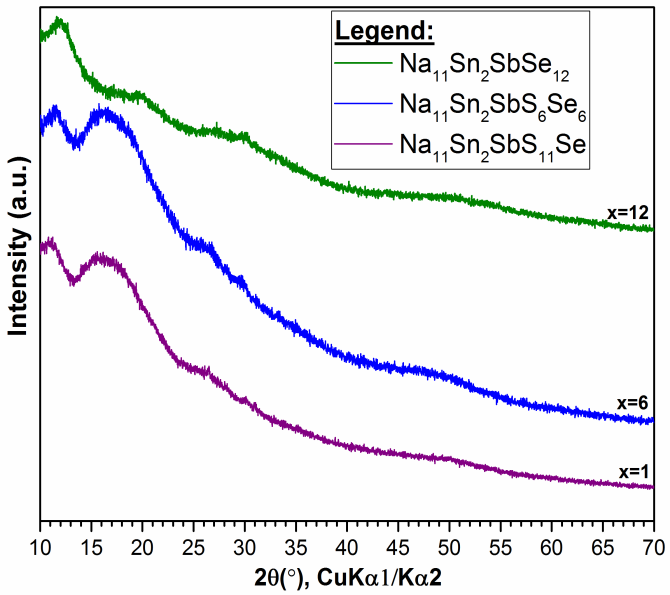

Figure 5.1: PXRD patterns of the as-milled $Na_{11}Sn_2SbS_{12-x}Se_x$ with x=1, 6 and 12 (Bragg-Brentano geometry).

Figure 5.2 presents the RT PXRD patterns of the heat-treated $Na_{11}Sn_2SbS_{12-x}Se_x$ with x=1, 6 and 12samples, with the pattern of $Na_{11}Sn_2SbS_{12}$ shown for comparison. Accordingly, $Na_{11}Sn_2SbS_{12-x}Se_x$ materials show characteristic diffraction peaks to those of $Na_{11}Sn_2SbS_{12}$. As shown in the figure, driven by the larger ionic radius of Se versus S (1.98 Å versus 1.84 Å), as the Se content increases, the Bragg reflections i.e. (408) show a shift toward higher d-spacing relative to $Na_{11}Sn_2SbS_{12}$, indicating the successful synthesis of solid solutions.

The opportunity to establish a detailed structural understanding of each sample relies on the successful synthesis of single crystals of appropriate size and quality for single crystal XRD studies. Based on the single crystal data (**Table** 5.1 and **Appendix** B), the crystal structures of $Na_{11}Sn_2SbS_{12-x}Se_x$ with x=1, 6 and 12 were found to be isostructural to $Na_{11}Sn_2SbS_{12}$ ($I4_1/acd$ with Z=8). A comparison of the unit cell parameters of $Na_{11}Sn_2SbS_{12-x}Se_x$ materials is presented in **Figure** 5.3. The linear expansion of the unit cell volume from 5235.5(19) Å for x=0 to 5932.8(3) Å for x=12 (+13.3% increase of the volume) with increasing Se content, stems for a significant increase in the lattice parameters (+4.3% in a=b and +4.1% in c) thereby obeying Vegard's law in accordance with the results obtained from PXRD.

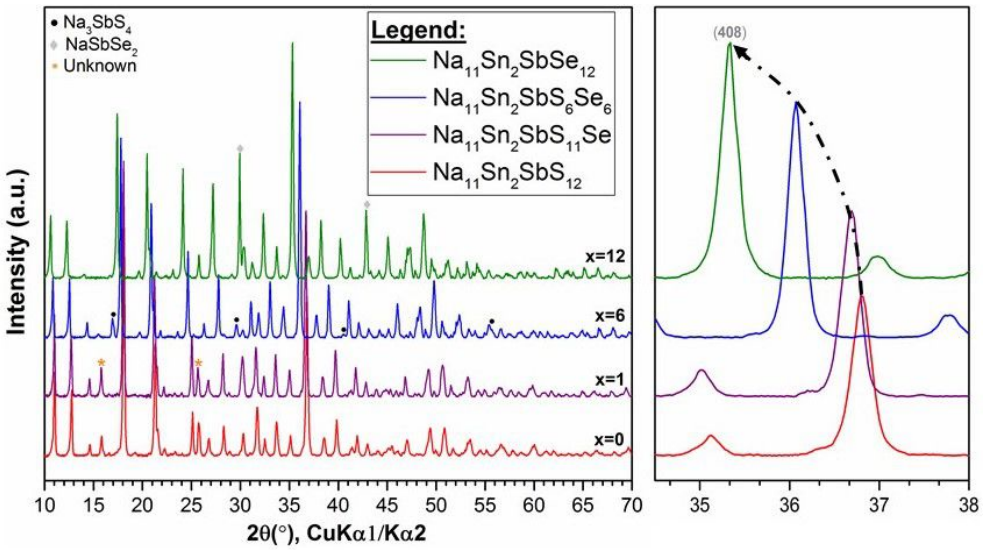

Figure 5.2: ***Left:*** RT PXRD patterns of $Na_{11}Sn_2SbS_{12-x}Se_x$ (x=0, 1, 6 and 12) with unknown, Na_3SbS_4 and $NaSbSe_2$ impurities as labelled (Debye-Scherrer geometry); ***Right:*** Expanded view on the right showing the peak shift in the (408) reflection toward lower angles.

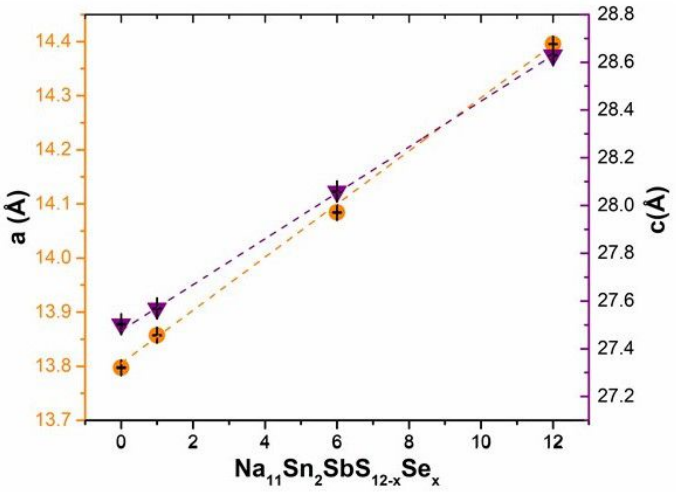

Figure 5.3: Unit cell parameters, a (Å) and c (Å), of $Na_{11}Sn_2SbS_{12-x}Se_x$ with x=0, 1, 6 and 12 obtained from single crystal XRD at 280 K.

Additional structural features such as the increased of Se occupancy on the three *32g* Wyckoff positions in $Na_{11}Sn_2SbS_{12-x}Se_x$ with x=0, 1, 6 and 12 was observed (**Tables** 4.4, 5.1, B.3 and B.7), the Q (Q=S and Se) occupancy on two of the three *32g* Wyckoff sites, and the volume of the $Sn(Q)_4$ and $Sb(Q)_4$ polyhedra are shown in **Figure** 5.4. Similar to the lattice parameters, increasing the degree of selenium substitution leads to an expansion of the $Sn(Q)_4{}^{3-}$ and $Sb(Q)_4{}^{3-}$ tetrahedra **Figure** 5.4**c**. The overall change in the Se occupancy on all three lattice sites suggests a homogeneous distribution of Se between the sites and an absence of site preference and solubility limit within $Na_{11}Sn_2SbS_{12-x}Se_x$.

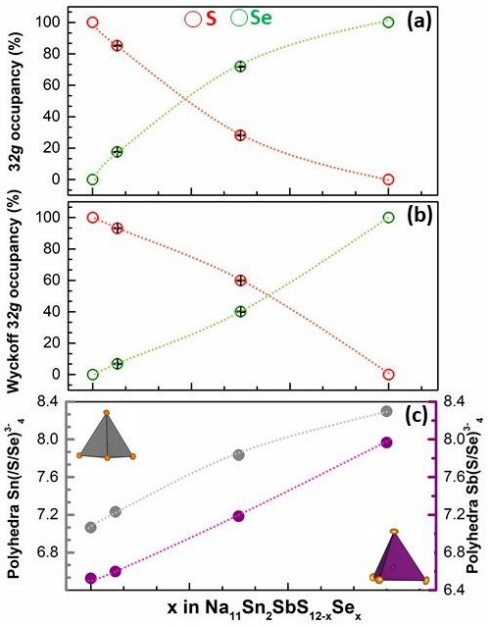

Figure 5.4: a. and **b.** Q=S and Se occupancies on two *32g* Wyckoff sites as a function of Se content in $Na_{11}Sn_2SbS_{12-x}Se_x$ with x=0, 1, 6 and 12; **c.** $Sn(Q)_4{}^{3-}$ and $Sb(Q)_4{}^{3-}$ tetrahedral volume calculated with VESTA© using the data obtained from single crystal XRD at 280 K.

Figure 5.5a, 5.5b and 5.5c show the PXRD patterns and Rietveld refinements of x=1, 6 and 12 in $Na_{11}Sn_2SbS_{12-x}Se_x$, respectively. The refinements were performed using the models initially obtained from single crystal diffraction for each composition, confirming the formation of almost pure phases. **Figure** 5.5d exhibits the crystal structure of $Na_{11}Sn_2SbSe_{12}$ along the [100] and [001] directions. The crystal structure of $Na_{11}Sn_2SbS_{12-x}Se_x$ consists of two crystallography independent *8a* and *16e* Wyckoff positions for $[Sb(Q)_4]^{3-}$ and $[Sn(Q)_4]^{3-}$ anions, respectively. Na^+-ions are distributed over six distinct crystallographic sites, five of which are octahedrally coordinated by $(Q)^{2-}$ ions and connected through face-sharing, while the "interstitial" Na(6) (*8b* Wyckoff position) site is loosely bonded to eight anion neighbors forming a quasi-cubic environment.

Representative single crystal structure data for $Na_{11}Sn_2SbSe_{12}$ is shown in **Table** 5.1. Three of the six sodium sites are almost, but not quite fully, occupied (Na(1), SOF=0.926(6); Na(3), SOF=0.962(7) and Na(5), SOF=0.969(8)); two sites are partially vacant (Na(2), SOF=0.869(8) and Na(4), SOF=0.894(8)), and one site is low-occupied (Na(6), SOF=0.058(10)). In $Na_{11}Sn_2SbS_{12-x}Se_x$ with x=1, 6 and 12, as expected

and confirmed by bond length data (**Tables** B.5, B.9 and B.10), the Na-Q interatomic distance increases as the Se content increases (from 2.7 Å in x=1 to 2.92 Å in x=12) while the the Na^+-Na^+ interatomic distances changed from 3.2 Å- 3.5 Å in x=0 to 3.5 Å- 3.67 Å in x=12.

Atom	**Wyckoff site**	**x**	**y**	**z**	**SOF**	**U_{eq}/Å^2**
Sn1	*16e*	0.20753(2)	1/2	1/4	1	0.01900(6)
Sb1	*8a*	0	1/4	3/8	1	0.01827(7)
Se1	*32g*	0.10799(2)	0.39642(2)	0.19925(2)	1	0.02496(7)
Se2	*32g*	0.31043(2)	0.40368(2)	0.30285(2)	1	0.02182(7)
Se3	*32g*	0.09094(2)	0.35943(2)	0.42474(2)	1	0.03067(8)
Na1	*32g*	0.25640(12)	0.27157(11)	0.37789(5)	0.926(6)	0.0448(6)
Na2	*16d*	0	1/4	0.24718(9)	0.869(8)	0.0605(11)
Na3	*16e*	0.04327(13)	1/2	1/4	0.962(7)	0.0418(7)
Na4	*16c*	1/4	1/4	1/4	0.894(8)	0.0556(10)
Na5	*16f*	0.22792(10)	0.52208(10)	3/8	0.969(8)	0.0515(9)
Na6	*8b*	0	1/4	1/8	0.058(10)	0.020(11)

Table 5.1: Atomic coordinates, site occupation factors and equivalent isotropic displacement parameters of $Na_{11.15(7)}Sn_2SbSe_{12}$ obtained from single crystal XRD at 280 K.

Atom	**U_{11}**	**U_{22}**	**U_{33}**	**U_{23}**	**U_{13}**	**U_{12}**
Sn1	0.018(1)	0.019(1)	0.020(1)	0.001(1)	0	0
Sb1	0.018(1)	0.018(1)	0.018(1)	0	0	0
Se1	0.023(1)	0.025(1)	0.027(1)	-0.001(1)	0.001(1)	-0.005(1)
Se2	0.025(1)	0.019(1)	0.021(1)	0.003(1)	0.001(1)	0.001(1)
Se3	0.029(1)	0.030(1)	0.033(1)	-0.008(1)	-0.009(1)	-0.003(1)
Na1	0.039(1)	0.052(2)	0.043(1)	0.019(1)	-0.004(1)	-0.007(1)
Na2	0.100(3)	0.048(2)	0.034(1)	0	0	-0.037(2)
Na3	0.022(1)	0.057(1)	0.047(1)	-0.021(1)	0	0
Na4	0.094(2)	0.027(1)	0.046(1)	-0.012(1)	-0.010(1)	-0.011(1)
Na5	0.063(1)	0.063(1)	0.028(1)	-0.012(1)	-0.012(1)	0.034(1)
Na6	0.020(14)	0.020(14)	0.020(18)	0	0	0.005(14)

Table 5.2: Anisotropic displacement parameters (Å^2) of $Na_{11.15(7)}Sn_2SbSe_{12}$ obtained from single crystal XRD at 280 K.

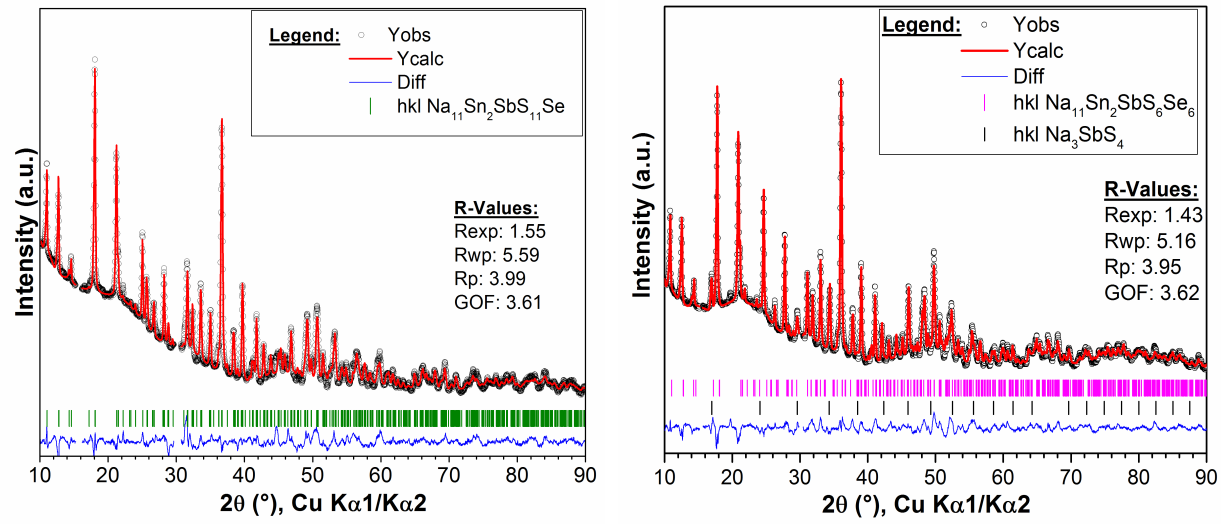

(a) x=1 **(b)** x=6

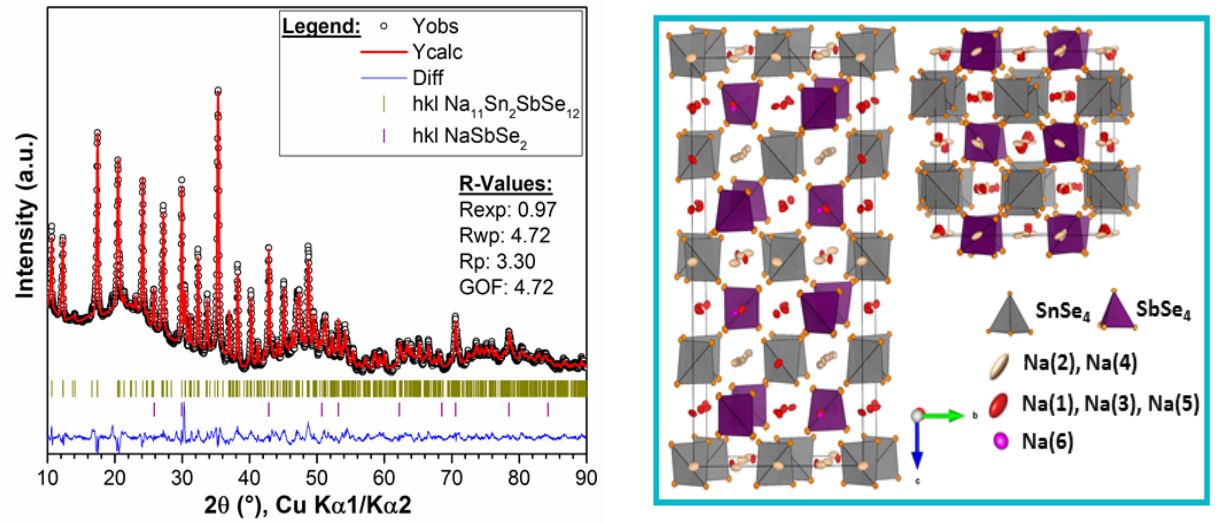

(c) x=12 **(d)** x=12

Figure 5.5: Rietveld refinement fit of $Na_{11}Sn_2SbS_{12-x}Se_x$ (Debye-Scherrer geometry): **a.** x=1, two unknown peaks at 15° and 30° were excluded from the refinement; **b.** x=6, with 4.75 wt% of Na_3SbS_4 phase; **c.** x=12, with 12.48 wt% of $NaSbSe_2$ phase. The black circles correspond to the data points, the red line denotes the calculated pattern, and the difference map is shown in blue. **d.** View of the structure of $Na_{11}Sn_2SbSe_{12}$ along the [100] and [001] directions. Thermal ellipsoids are drawn at 50% probability. Color code: Na(1) and Na(2): light-rose; Na(3), Na(4) and Na(5):red; Na(6): pink; Sn: grey; Sb: purple; Se: orange. SnS_4 and SbS_4 polyhedral are shown in grey and purple respectively.

Based on the single crystal diffraction data of $Na_{11}Sn_2SbS_{12-x}Se_x$ with x=1, 6 and 12 materials, all five sodium sites (Na(1)-Na(5)) are observed to have an occupancy ratio higher than 80%, while the probability that a sodium ion occupies the Na(6) site is rather low (SOF<14%, **Tables** 5.1, B.3 and B.7). Considering the coordination number of Na-ions in the structure, and the ionic radius of Se^{2-} and S^{2-} ions (1.94 Å and 1.84 Å, respectively), the five Na sites, octahedrally coordinated by Q^{2-}, require the occupancy of a cation whose ionic radius is over 0.76 Å and 0.781 Å for Q=S and Se, respectively. In contrast, for the Na(6) site, coordinated by eight Q^{2-} ions, the required radius of the cation is over 1.35 Å and 1.45 Å for Q=S and Se, respectably (**Figure** 5.6). The large size difference between the Na(6) site in Q=S and Se framework and sodium ion (1.35 Å (S), 1.45 Å (Se) versus 1.02 Å), might explain the decrease in SOF as the unit cell increases from S^{2-} to Se^{2-} (SOF= 0.076(9) (S) versus 0.058(10) (Se)) (**Tables** 4.3 and 5.1)

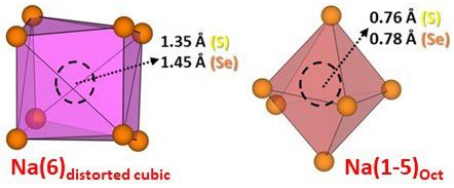

Figure 5.6: Coordination environment of NaS_6 polyhedra in $Na_{11}Sn_2SbSe_{12}$. The dot circles denote Na sites.

$Na_{11}Sn_2SbS_{12-x}Se_x$ x=1 composition shows the smallest volume of the $Na(6)S_6$ polyhedra between the $Na_{11}Sn_2SbS_{12-x}Se_x$ with x=0, 1, 6 and 12 phases (**Table** 5.3), likely making the occupation of the Na(6) site more favorable. In accordance with this, based on the single crystal data, x=1 phase shows the highest occupancy on the Na(6) site when compared to the other Sb phases (SOF=0.133(12), **Table** 5.3). However, $Na_{11}Sn_2SbS_{12}Se$ exhibits poorer ion conduction than the undoped material, as discussed below, which suggests a low contribution from the Na(6) site to the ion transport mechanism of $Na_{11}Sn_2SbS_{12-x}Se_x$.

Compound	**Polyhedral $Na6S_6$ Vol.(Å^3)**	**SOF of Na(6) site**
$Na_{11}Sn_2SbS_{12}$	75.18	0.076 (9)
$Na_{11}Sn_2SbS_{11}Se$	74.49	0.133(12)
$Na_{11}Sn_2SbS_6Se_6$	77.08	0.047(11)
$Na_{11}Sn_2SbSe_{12}$	83.02	0.058(10)

Table 5.3: Volume of the $(Na6)S_6$ polyhedra in $Na_{11}Sn_2SbS_{12-x}Se_x$ with x=0, 1, 6 and 12 obtained from single crystal XRD data at 280 K, calculated using VESTA©.

The alternating "full/vacancy/full" arrangement observed in $Na_{11}Sn_2SbS_{12}$ with P=Sb

and P (**Figure** 5.7, **Tables** 4.3 and 4.8) made by the vacancy-rich sodium sites (Na(1) ∼SOF=85% and Na(2) ∼SOF=81%) alternate with the almost fully occupied sodium sites (Na(3), Na(4) and Na(5)) [104] [114], changes in $Na_{11}Sn_2SbSe_{12}$ framework, where the Na(2) SOF=87% and Na(4) SOF=89% are the vacancy-rich sodium sites, while the Na(1), Na(3) and Na(5) are the almost fully occupied sites (**Figure** 5.7 and **Table** 5.1). The occupancies in the sodium sites are thus subtly different between $Na_{11}Sn_2SbQ_{12}$ with Q=S and Se crystal structures.

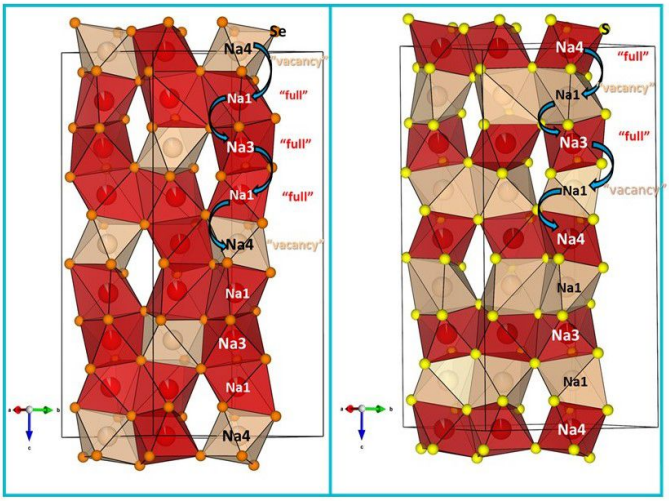

Figure 5.7: View of the $Na_{11}Sn_2SbQ_{12}$ with Q=S and Se crystal structures along the c-axis displaying the difference in Na occupancy arrangement.

5.4 Ionic and electronic properties

Figures 5.8a and 5.8b display the Arrhenius plots of the ionic conductivity of x=6 and 12, respectively. The overall sodium ion conductivity shows an Arrhenius behavior ($\log \sigma \cdot T$ versus $1/T$) for the $Na_{11}Sn_2SbS_{12-x}Se_x$ series that leads to activation energies of E_a 0.36 eV and 0.41 eV for x=6 and 12, respectively. The Nyquist plot of the $Na_{11}Sn_2SbS_{12-x}Se_x$ series is exhibited in **Figure** 5.9 (**Table** 5.4).

A comparison between the RT ionic conductivities and activation energies obtained from impedance spectroscopy for the synthesized $Na_{11}Sn_2SbS_{12-x}Se_x$ with x=0, 1, 6 and 12 samples is shown in **Figures** 5.10**a** and 5.10**b**, respectively (**Table** B.11). The ionic conductivity decreases from 0.56 $mS{\cdot}cm^{-1}$ for x=0 to 0.15±0.04 $mS{\cdot}cm^{-1}$ for x=12, while

the activation energy increases from 0.34 eV to 0.41 eV. Since Se substitution gives rise to an increase in the unit cell dimensions as well as the Na channel volume (5070 Å^3 for (S) versus 5736 Å^3 for (Se), **Figure** 5.10**c** and **Equation** B.1), the Na^+-ion diffusivity in $Na_{11}Sn_2SbS_{12-x}Se_x$ is not solely controlled by the size of the diffusion channels.

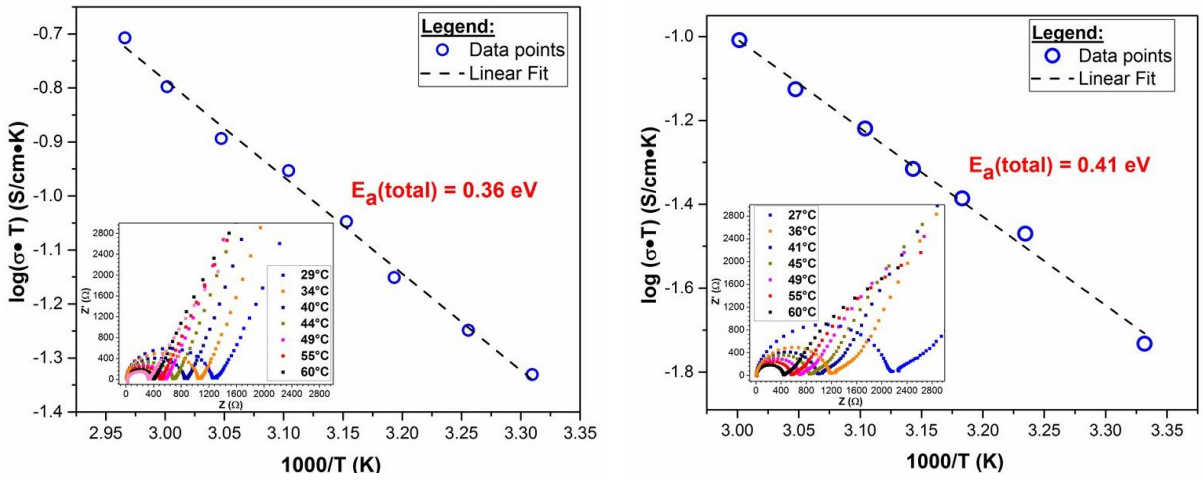

(a) x=0.6 **(b)** x=12

Figure 5.8: Arrhenius plots of the total conductivity of: **a.** $Na_{11}Sn_2SbS_6Se_6$ from 30°C to 65°C. The inset displays the Nyquist impedance plot from 30°C to 60°C; **b.** $Na_{11}Sn_2SbSe_{12}$ from 30°C to 60°C, the inset displays the Nyquist impedance plot from 30°C to 60°C.

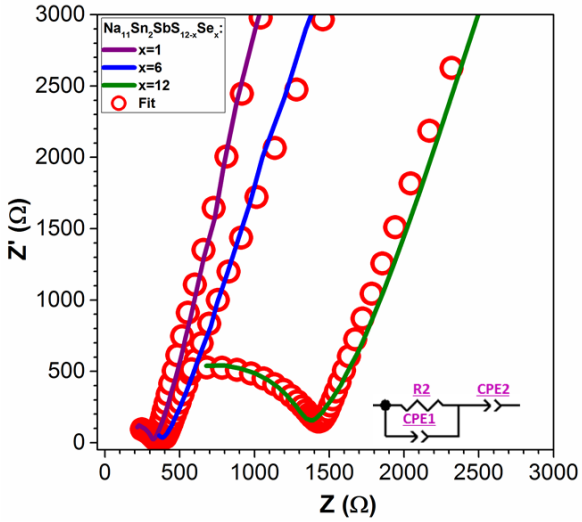

Figure 5.9: RT Nyquist impedance plot and fit of $Na_{11}Sn_2SbS_{12-x}Se_x$ with x=1, 6 and 12 samples with the respective equivalent circuit.

Compound	**CPE$_1$ (F s^{a-1}) (10^{-9})**	**a$_1$**	**CPE$_2$ (F s^{a-1}) (10^{-6})**	**a$_2$**	**R$_1$ (Ω)**
$Na_{11}Sn_2SbS_{11}Se$	31.43	0.725	5.143	0.853	341.8
$Na_{11}Sn_2SbS_6Se_6$	29.25	0.735	8.459	0.782	400.4
$Na_{11}Sn_2SbSe_{12}$	8.082	0.802	2.91	0.793	1435

Table 5.4: Parameters of the fit for the impedance data of $Na_{11}Sn_2SbS_{12-x}Se_x$ with x=0, 1 and 6 at RT.

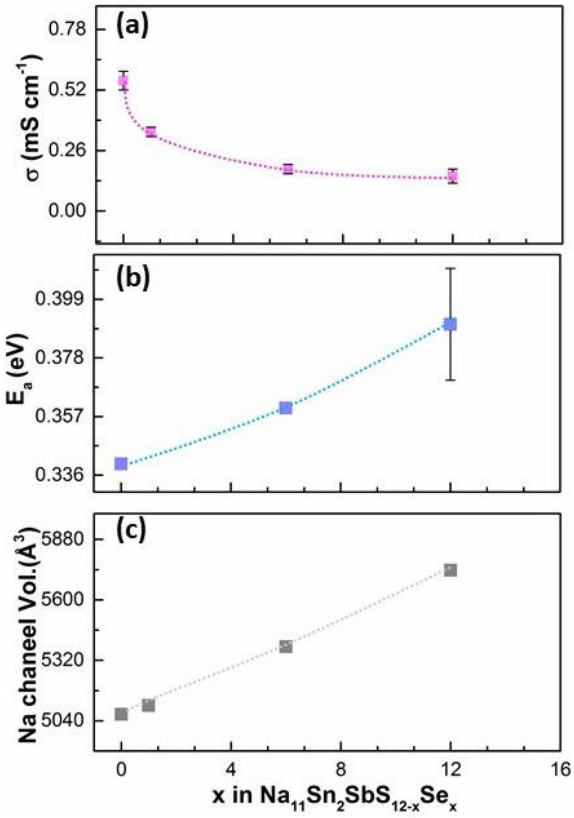

Figure 5.10: a. RT ionic conductivity as a function of Se content in $Na_{11}Sn_2SbS_{12-x}Se_x$ with x=0, 1, 6 and 12; **b.** Activation energy; **c.** Sodium channel volume calculated with VESTA© using the data obtained from single crystal XRD at 280 K.

The increase in the polarizability of the anion framework in $Na_{11}Sn_2SbSe_{12}$ makes the lattice softer, affecting all cation-anion interactions. Se substitution increases the Sn-Q and Sb-Q bond lengths within $(SnQ)_4$ and $(SbQ)_4$ polyhedra (**Figure** 5.11). A longer bond length, together with a weaker bonding, has been confirmed by Bernt K. for SnQ_4 $^{4-}$ with Q=S and Se, and SbS_4 $^{4-}$ corresponding to 2.55 Å, 1.53 N/cm for S, 2.42 Å, 1.75 N/cm for Se, and 2.43 Å, 1.74 N/cm, respectively [130]. A weaker Sb/Sn-Se bonding in $Na_{11}Sn_2SbSe_{12}$, compared to its S-based analogue, along with the slightly higher electronegativity of Se^{2-} versus S^{2-} (2.5 versus 2.4), may lead to a higher electron density on Se^{2-} and hence a stronger Coulombic attraction between Na-Se versus Na-S. This likely results in a higher activation barrier in $Na_{11}Sn_2SbSe_{12}$ for Na^+-ion diffusion (E_a= 0.41 eV versus 0.34 eV). Similar inductive effects have been observed in other materials such as

$Na_{11}Sn_2PnS_{12}$ with Pn=Sb and P, $Na_3P_{1-x}As_xS_4$ [53], and $Li_{10}Ge_{1-x}Sn_xPS_{12}$ [116].

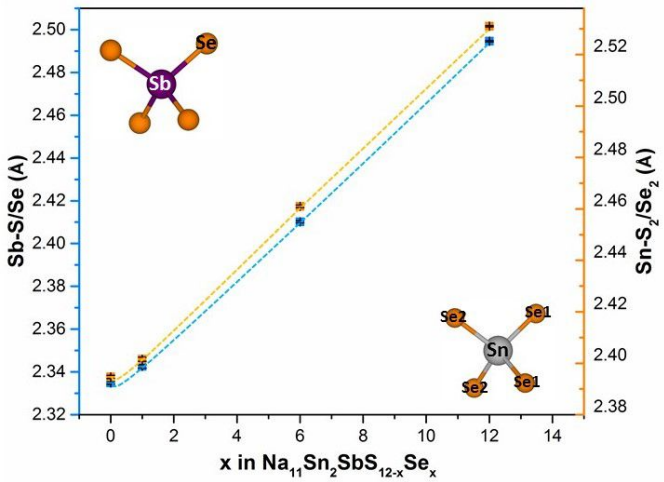

Figure 5.11: Bond lengths of $(SbQ)_4$ and $(SnQ)_4$ polyhedral as a function of Se content in $Na_{11}Sn_2SbS_{12-x}Se_x$ with x=0, 1, 6 and 12 obtained from single crystal XRD data at 280 K. The coordination environment of Sn corresponds to one of the three S/Se sites, S2/Se2.

In addition to the influence of inductive effect in the ion transport mechanism, phase purity affects the ionic conductivity properties of the $Na_{11}Sn_2SbS_{12-x}Se_x$ series. Different amounts of impurity phases are present in these samples (**Table** 5.5). The formation of secondary phases at the grain boundaries of $Na_{11}Sn_2SbS_{12-x}Se_x$ will likely block the ionic transport causing a large resistive barrier and hinder ion migration across the interface, leading to a low-grain boundary conductivity in accordance with the obtained $\sigma_{g.b.}$ value for $Na_{11}Sn_2SbSe_{12}$ (0.0523 mS·cm^{-1}) calculated by Dr. Rettenwander (**Figure** B.1). The difference between the $E_{a.bulk}$ and $E_{a.g.b}$ values in $Na_{11}Sn_2SbSe_{12}$ (0.32 eV versus 0.38 eV, respectively, **Figure** B.1), points to the presence of contaminants in the grain boundary region. The ion migration across the grain boundaries thus becomes the rate-determining step. Hence, the observed conductivity variation are not only be correlated with the compositional factors described above, including crystal structure, size of the Na diffusion channels, lattice softness and bond length, but also the presence of secondary phases.

Compound	Impurity phase fraction (wt%)
$Na_{11}Sn_2SbS_{11}Se$	Two unknown peaks at 39.6 °C and 15.82°C
$Na_{11}Sn_2SbS_6Se_6$	4.75% Na_3SbS_4
$Na_{11}Sn_2SbSe_{12}$	12.48% of $NaSbSe_2$

Table 5.5: Weight fractions of phases present in $Na_{11}Sn_2SbS_{12-x}Se_x$ with x=1, 6 and 12 samples from the Rietveld refinement results.

The RT electronic conductivity of $Na_{11}Sn_2SbSe_{12}$ was measured by DC polarization measurement. **Figure** 5.12a shows the DC polarization curves of $Na_{11}Sn_2SbSe_{12}$ at three different voltages, 0.25 V, 0.50 V and 0.75 V. From a linear fit of voltage versus stabilized current (**Figure** 5.12b), the electronic conductivity for $Na_{11}Sn_2SbSe_{12}$ was estimated to be 4.05 $\times$ 10^{-4} mS·cm^{-1}, which is only three orders of magnitude lower than the ionic conductivity (0.15 mS·cm^{-1}). High electronic conductivities have also been reported for other SE materials, i.e., $Li_7La_3Zr_2O_{12}$ (10^{-5} - 10^{-4} mS·cm^{-1}) [131] [132] and Li_2S-P_2S_5 (10^{-6} - 10^{-5} mS·cm^{-1}) [133] [134]. However, Wang *et al.* recently acknowledged that high electronic conductivities in SEs could potentially be a primary reason for dendrite formation in SEs and thus, electronic conductivities lower than 10^{-10} S·cm^{-1} are desired [135]; thus, the high electronic conductivity of $Na_{11}Sn_2SbSe_{12}$ may limit its utilization as a SE. Albeit, a variety of factors such as impurities on the surface of the electrodes, pore surfaces, presence of secondary phases and grain boundaries might be the origin for the observed high electronic conductivity of $Na_{11}Sn_2SbSe_{12}$ (σ_e=4.05 $\times$ 10^{-4} mS·cm^{-1}) [136]. Indeed, the secondary phase $NaSbSe_2$ observed in the $Na_{11}Sn_2SbSe_{12}$ XRD pattern (**Figure** 5.2), is utilized in solar cells applications because of its low band gap (1.36 eV) [137]. Thus, to accurately determine the intrinsic σ_e of the Se-phase, a pure material needs to be synthesized, and conduct the DC polarization measurement for longer than 30 min in order to ensure that the steady-state current value is reached.

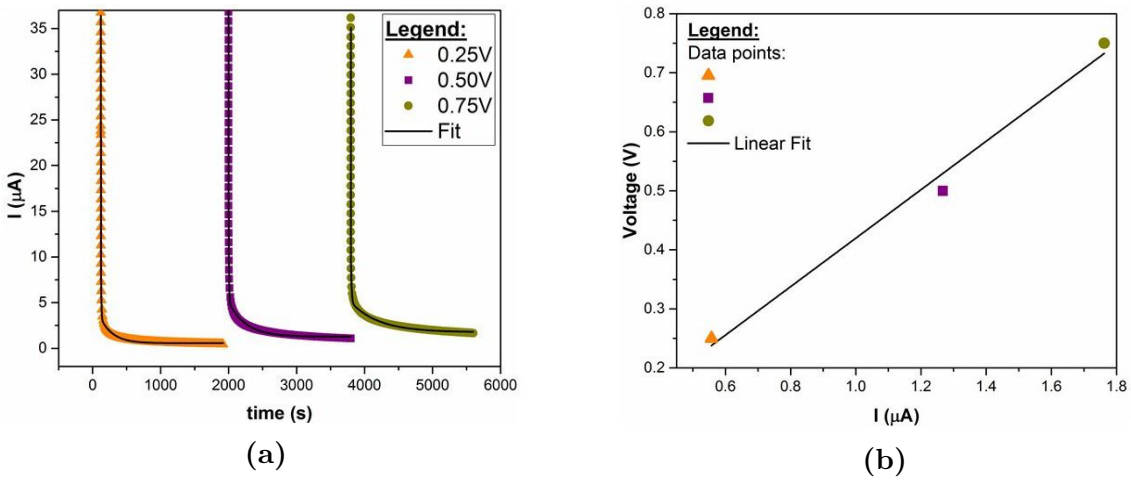

Figure 5.12: **a.** DC polarization curves for electronic conductivity determination of $Na_{11}Sn_2SbSe_{12}$ with an applied voltage of 0.25 (orange), 0.50 (purple) and 0.75 V (grey); **b.** Linear fit of the voltage versus current.

$Na_{11}Sn_2SbSe_{12}$ crystal structure was analyzed by the BVSE calculations to explore the topology of potential ion-migration pathways in the framework [81] [82]. **Figures** 5.13a and 5.13b display the bond valence model of Na^+-ion migration pathways in $Na_{11}Sn_2SbSe_{12}$ along the *a,b*- plane and *c*-axis, respectively, with the structure in the polyhedral motif shown for comparison. The BVSE maps, depicted as isosurfaces of constant bond valence site energy, suggest 3D interconnected network pathways displayed as a light blue isosurfaces likely involving all Na sites that formed the major potential conduction pathways in the framework, for example, Na(4)-Na(2)-Na(4) and Na(2)-Na(3)-Na(2) chains along the *a,b*- plane, and Na(4)-Na(1)-Na(3)-Na(1)-Na(4) chain along the *c*-axis as depicted in **Figures** 5.13c and 5.13d, respectively.

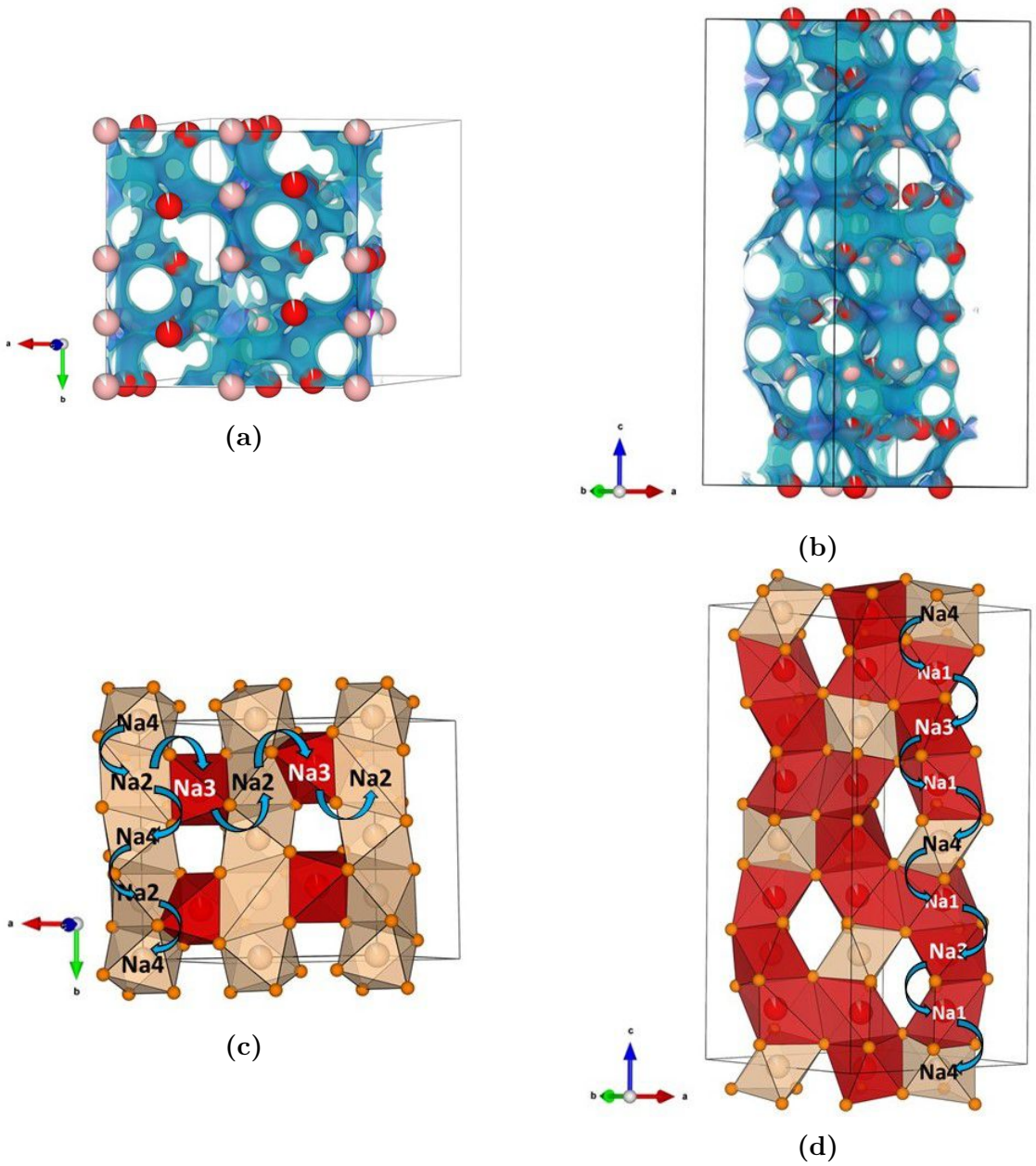

Figure 5.13: a. BVSE model of Na^+ ion migration pathways visualized as isosurfaces of constant bond valence site energy along the *a,b*- plane; **b.** *c*-axis; **c.** View of the diffusion channels interconnecting Na(4)-Na(2)-Na(4) and Na(2)-Na(3)-Na(2) along the *a,b*- plane; **d.** Na(4)-Na(3)-Na(1)-Na(4) sites along the *c*-axis. Color code: Na(1), Na(3), Na(5): red; Na(4): light-rose.

The thermal stability of $Na_{11}Sn_2SbSe_{12}$ was studied by DSC technique. The DSC curve of $Na_{11}Sn_2SbSe_{12}$ exhibited in **Figure** 5.14 shows no large peaks, but minor thermal events, exothermic/endothermic peaks, for example, 175.68°C and 318.49°C, respectively, which may correspond to the crystallization/melting processes of the secondary phase ($NaSbSe_2$).

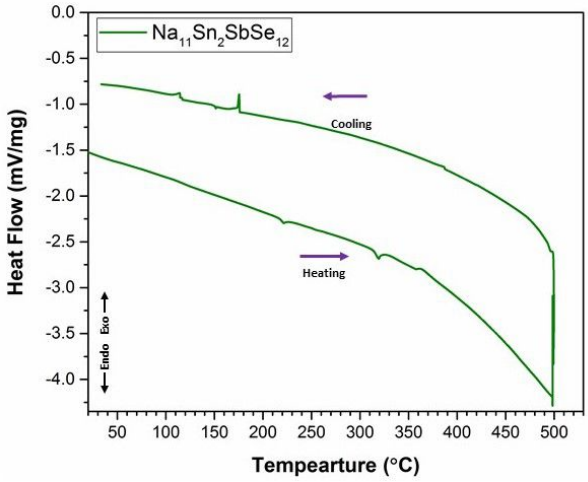

Figure 5.14: DSC curve of $Na_{11}Sn_2SbSe_{12}$ and at a heating rate of 10°C·min^{-1} up to 500°C.

5.5 Summary and Future Prospects

$Na_{11}Sn_2SbSe_{12}$ shows poorer ion transport properties than those of the S-based analogue, σ=0.15 mS·cm^{-1} versus 0.57 mS·cm^{-1} and E_a 0.41 eV versus 0.34 eV.

While the increasing of the Na channel volume with Se^{2-} substitution should be more beneficial for Na^+-ion transport, increasing the Se fraction in $Na_{11}Sn_2SbS_{12-x}Se_x$ wir x=1, 6 and 12 led to an increase in the activation energy and a reduction in the ionic conductivity. This may be explained based on:

- The formation of secondary phases likely at the grain boundaries of $Na_{11}Sn_2SbS_{12-x}Se_x$ with x=1, 6 and 12 blocks the ionic transport causing a large resistive barrier, hindering ion migration across the interface.
- The compositional change, caused by S^{2-} substitution for Se^{2-}, modifies the electrostatic interactions within the lattice likely leading to stronger ionic bonding interac-

tions between Na^+-Se^{2-} versus Na^+-S^{2-}, causing an increase in the activation barrier for Na^+-ion diffusion in $Na_{11}Sn_2SbSe_{12}$ framework.

Future Prospects

Secondary-phase formation has a detrimental effect on the Na-ion conductivity of $Na_{11}Sn_2SbSe_{12}$. Impurity free $Na_{11}Sn_2SbSe_{12}$ powder thus plays an important role in determining its total conductivity. Heat treatment parameters, such as temperature and time influence the ion transport properties of the final product, as observed for the $Na_{11}Sn_2PS_{12}$ material and reported somewhere else [105] [138]. The purity of the polycrystalline $Na_{11}Sn_2SbSe_{12}$ thus could be improved by optimizing the synthesis conditions i.e. lowering the synthesis temperature and increasing the holding time.

Since the Na-ion conductivity through the grain boundaries decreases the total conductivity of the polycrystalline $Na_{11}Sn_2SbSe_{12}$, its ionic conductivity can be further improved by reducing the grain boundary impedance by hot pressing approach; this process generally results in materials with higher relative density, higher grain-to-grain contact, likely lowering the grain boundary resistance that originates from voids in the pellet [139].

Chapter 6

Triggering fast lithium ion conduction in $Li_{4+x}P_{x-1}Si_xS_4I$

6.1 Introduction

The addition of 45 mol% of LiI to $2Li_2S{\cdot}P_2S_5$ glass was reported to improve the conductivity from 10^{-4} S·cm^{-1} to 10^{-3} S·cm^{-1} [140]. In addition to the good ion conduction properties, Tatsumisago *et al.* reported the excellent electrochemical stability of the $80(0.7Li_2S{\cdot}0.3P_2S_5){\cdot}20LiI$ glass with a wide electrochemical window up to 10 V versus Li^+/Li [141]. Ball-milled Li_6PS_5I exhibits an ionic conductivity of 0.22 mS·cm^{-1}, while the crystalline counterpart shows a lower conductivity of 0.46 x 10^{-3} mS·cm^{-1} which has been explained based on its ordered anion framework (S^{2-}/I^-) [142]. Chengdu Lian *et al.* reported the solvent-based synthesis ($Li_3PS_4 \cdot 2CH_3CN$) of the crystalline $Li_7P_2S_8I$ phase with an electrochemical stability up to 10 V versus Li^+/Li, and an ionic conductivity of 0.63 mS·cm^{-1}; however, its crystal structure was not resolved [143]. Janek *et al.* reported the structural information of the crystalline Li_4PS_4I, discovered utilizing a solvent-based synthesis approach ($Li_3PS_4 \cdot C_4H_{10}O_2$). The obtained Li_4PS_4I material shows an ionic conductivity between 0.12 and 0.064 mS·cm^{-1} [144]. Even though excellent electrochemical stabilities and good battery performances have been reported for the Li_2S-P_2S_5-LiI system, only a handful of processable highly conductive iodine-sulfur SEs have been reported (>10^{-4} S·cm^{-1}) [140] [143] [144] [145] [146] [147]. Inspired by this prospective, I explored the aliovalent substitution effects in the Li-ion conductor $Li_{4+x}P_{1-x}Si_xS_4I$ through the examination of the series x=0, 0.12 and 0.29.

6.2 Synthesis

$Li_{4+x}P_{1-x}Si_xS_4I$ with x=0, 0.12 and 0.29 compositions were synthesized by solid state reaction. Li_2S (99%, Sigma-Aldrich), LiI (99%, Sigma-Aldrich), P_2S_5 (99%, Sigma-Aldrich) and Si powder (99%, Sigma-Aldrich) were mixed together according to the molar ratio and grounded in an agate mortar for 40 min to 50 min. The mixtures were heated to 700°C with a heating rate of 63°C/h, held for 5 h, then followed by a slow cooling step (1°C/h) to 621°C, where the samples were ice quenched to RT. The refinement details from the single crystal diffraction data are presented in **Appendix** C.

6.3 Crystal structure

Based on single crystal XRD studies, conducted on a couple of samples for each composition to ensure reproducibility, $Li_{4+x}P_{1-x}Si_xS_4I$ with x=0.12 and 0.29 adopt a structure with a primitive tetragonal unit cell (P_4/nmm and Z=2) and refined lattice parameters a=8.4813(6) Å, c=5.927(4) Å and V=426.34(7) Å^3 for x=0.12, and a=8.5090(7) Å, c=5.9473(5) Å and V=430.6(1) Å^3 for x=0.29 (**Tables** C.1 and C.2).

Tables 6.1-6.6 show the crystal structure data of $Li_{4+x}P_{1-x}Si_xS_4I$ with x=0.12 and 0.29. Their crystal structure is comprised of lithium ions distributed over four distinct partially occupied sites: *2b*, *8j*, *2c* and *4e* Wyckoff positions (the SOFs of all four Li sites were freely refined). While P and Si share the *2b* site, I and S occupied two independent crystallographic sites *2c* and *8i*, respectively (**Tables** 6.1 and 6.4). The larger Si^{4+} (2.20 Å versus 1.84 Å) not only increases the size of the unit cell (426.34(7) Å^3 for x=0.12 versus 430.6(1) Å^3 for x=0.29), but it also increases the Li^+ content and leads to a rising occupancy of Li^+ on the available four Li sites: (Li(1), SOF=0.51(3) for x=0.12 versus SOF=0.58(5) for x=0.29; Li(2), SOF=0.62(2) for x=0.12 versus SOF=0.65(5) for x=0.29; Li(3), SOF=0.527(11) for x=0.12 versus SOF=0.54(2) for x=0.29 and Li(4), SOF=0.449(17) for x=0.12 versus SOF=0.46(3) for x=0.29 (**Tables** 6.1 and 6.4).

Atom	Wyckoff site	x	y	z	SOF	U_{eq}/Å^2)
P	*2b*	3/4	1/4	1/2	0.88(6)	0.0168(3)
Si	*2b*	3/4	1/4	1/2	0.12(6)	0.0168(3)
S	*8i*	1/4	0.55464(3)	0.70368(5)	1	0.01611(7)
I	*2c*	1/4	1/4	0.15774(6)	1	0.01872(6)
Li1	*2c*	1/4	1/4	0.6118(18)	0.51(3)	0.030(4)
Li2	*2a*	3/4	1/4	0	0.62(2)	0.026(3)
Li3	*8j*	0.0444(4)	0.0444(4)	0.4239(9)	0.527(11)	0.0283(15)
Li4	*4d*	0	0	0	0.449(17)	0.042(3)

Table 6.1: Atomic coordinates, site occupation factors and equivalent isotropic displacement parameters of $Li_{4.14(10)}P_{0.88(6)}Si_{0.12(6)}S_4I$ obtained from single crystal XRD at 280 K.

Atom	U_{11}	U_{22}	U_{33}	U_{23}	U_{13}	U_{12}
P	0.0096(3)	0.0096(3)	0.0312(4)	0	0	0
Si	0.0096(3)	0.0096(3)	0.0312(4)	0	0	0
S	0.01643(14)	0.01199(13)	0.01990(15)	0	0	0
I	0.02117(7)	0.02117(7)	0.01382(8)	0	0	0
Li1	0.033(4)	0.033(4)	0.022(6)	0	0	0
Li2	0.030(3)	0.030(3)	0.017(4)	0	0	0
Li3	0.0259(18)	0.0259(18)	0.033(3)	-0.0013(14)	-0.0013(14)	0.0062(18)
Li4	0.048(4)	0.048(4)	0.032(5)	0.005(3)	0.005(3)	-0.017(4)

Table 6.2: Anisotropic displacement parameters (Å^2) of $Li_{4.14(10)}P_{0.88(6)}Si_{0.12(6)}S_4I$ obtained from single crystal XRD at 280 K.

Atom1	Atom2	Bond distance (Å)
P/Si	**S1**	2.0501(3) × 4
Li1	**S1**	2.641(3) × 4
	I	2.702(11), 3.225(11)
Li2	**S2**	2.4145(3) 2.933(5)
Li3	**S1**	2.549(5) ×2, 2.610(4) ×2
	I	2.933(5) × 2
Li4	**S1**	2.7920(2) × 4
	I	3.1378(2) × 2
Li1	**Li3**	2.706(7) × 2, 3.538(5)× 2
Li2	**Li4**	2.9986(2)× 2
Li3	**Li3**	1.396(9)
Li3	**Li4**	2.568(5), 3.456(5)

Table 6.3: Interatomic distances of $Li_{4.14(10)}P_{0.88(6)}Si_{0.12(6)}S_4I$ obtained from single crystal XRD at 280 K.

Atom	Wyckoff site	x	y	z	SOF	U_{eq}/Å^2
P	*2b*	3/4	1/4	1/2	0.71(11)	0.0179(5)
Si	*2b*	3/4	1/4	1/2	0.29(11)	0.0179(5)
S	*8i*	1/4	0.55519(8)	0.70352(11)	1	0.02088(18)
I	*2c*	1/4	1/4	0.15774(6)	1	0.02643(16)
Li1	*2c*	1/4	1/4	0.617(4)	0.58(5)	0.043(8)
Li2	*2a*	3/4	1/4	0	0.65(5)	0.039(4)
Li3	*8j*	0.0438(10)	0.0438(10)	0.4230(19)	0.54(2)	0.04230(19)
Li4	*4d*	0	0	0	0.46(3)	0.064(9)

Table 6.4: Atomic coordinates, site occupation factors and equivalent isotropic displacement parameters of $Li_{4.31(3)}P_{0.71(11)}Si_{0.29(11)}S_4I$ obtained from single crystal XRD at 280 K.

Atom	U_{11}	U_{22}	U_{33}	U_{23}	U_{13}	U_{12}
P	0.0122(6)	0.0122(6)	0.0295(8)	0	0	0
Si	0.0122(6)	0.0122(6)	0.0295(8)	0	0	0
S	0.0234(4)	0.0155(3)	0.0236(3)	0.0001(2)	0	0
I	0.030(1)	0.030(1)	0.01904(19)	0	0	0
Li1	0.042(10)	0.042(10)	0.045(13)	0	0	0
Li2	0.045(9)	0.045(9)	0.026(9)	0	0	0
Li3	0.034(4)	0.034(4)	0.050(7)	-0.001(4)	-0.001(4)	0.013(5)
Li4	0.069(12)	0.069(12)	0.054(13)	0.012(8)	0.012(8)	-0.014(13)

Table 6.5: Anisotropic displacement parameters (Å^2) of $Li_{4.31(3)}P_{0.71(11)}Si_{0.29(11)}S_4I$ obtained from single crystal XRD at 280 K.

Atom1	Atom2	interatomic distance (Å)
P/Si	**S1**	2.0525(7) × 4
Li1	**S1**	2.641(3) × 4
	I	2.73(2), 2.940(12)
Li2	**S2**	2.4201(7) × 4
Li3	**S1**	2.613(9)×2, 2.563(10) ×2
	I	2.940(10), 2.933(5)
Li4	**S1**	2.8026(5) × 4
	I	3.1513(3) × 2
Li1	**Li3**	2.738(15) × 2, 3.538(5)× 2
Li2	**Li4**	3.0084(3)× 2
Li3	**Li3**	1.40(2)
Li3	**Li4**	2.570(11) 3.472(11)

Table 6.6: Interatomic distances of $Li_{4.31(3)}P_{0.71(11)}Si_{0.29(11)}S_4I$ obtained from single crystal XRD at 280 K.

The crystal structures of $Li_{4+x}P_{1-x}Si_xS_4I$ with x=0.12 and 0.29 were solved as follows: first, the positions of P/Si, S and I were located and were anisotropically refined using the least-squares method. Then the Li positions were located in the remaining electron density in the Fourier map. Subsequently, the Li site occupancies were freely and anisotropically refined. The structure models converged to residual factors of 0.0094 and 0.0259 for x=0.12 and 0.29, respectively. Representative view of the $Li_{4.29}P_{0.71}Si_{0.29}S_4I$ crystal structure along

the [001] direction is shown in **Figure** 6.1a. $(P/Si)S_4$ tetrahedra arranged in layers perpendicular to the *c*-axis held apart by I^- ions. The lithium atoms reside in 4-, 5- and 6-fold coordination environments. Li(1) and Li(4) have a 6-fold coordination sphere around four sulfurs and two iodine atoms, Li(2) is 4-fold coordinated by sulfur atoms, and Li(3) is 5-fold coordinated by four sulfurs and one iodine atom (**Figure** 6.1b). The (P/Si)-S bond length is 2.0500(3) Å for x=0.12 and 2.0525(7) Å for x=0.29 (**Tables** 6.3 and 6.6, respectively), which are slightly longer than the P-S bong length in Li_4PS_4I (2.04(1) Å [144] or 2.0415(4) Å **Table** 6.9), β-Li_3PS_4 (2.004(2) Å) [148] and Li_7PS_6 (2.044(1) Å) [149], confirming the successful incorporation of Si^{4+} on the P^{5+} site (*2b*). The Li-S bond length varies from 2.4 Å to 2.8 Å, while the Li-I bond length ranges between 2.73 Å to 3.15 Å in x=0.29 (**Table** 6.3); the Li(1) site is sitting in a distorted octahedron in the framework giving rise to the shortest Li-I bond length in (2.932(4) for x=0.12 and 2.73(2) Å for x=0.29, **Tables** 6.3 and 6.6, respectively).

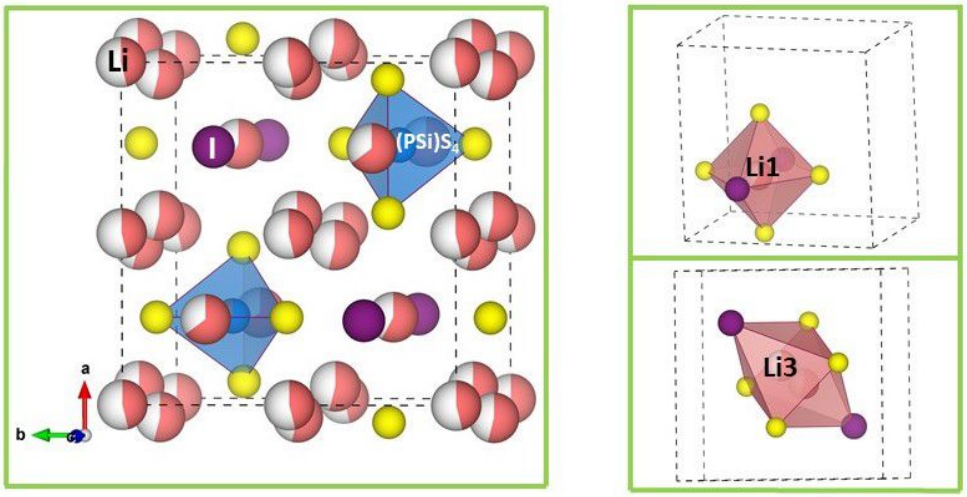

(a) **(b)**

Figure 6.1: a. View of the structure of $Li_{4.29}P_{0.71}Si_{0.29}S_4I$ along [001] from single crystal data; **b.** Environment of the Li(1) and Li(3) sites in $Li_{4.29}P_{0.71}Si_{0.29}S_4I$. Color code: Li(1), Li(2), Li(3) and Li(4): light rose; S: yellow, I:purple; $(P/Si)S_4$ polyhedra are shown in blue.

Figure 6.2 displays the Raman spectra of the new ion conductor $Li_{4.29}P_{0.71}Si_{0.29}S_4I$ in a frequency range from 100 cm^{-1} to 700 cm^{-1}. The band at 420 cm^{-1} has been assigned to symmetric stretching vibration of the P-S bonds in $PS_4{}^{3-}$ units along with two other bands at 270 and 550 cm^{-1} [150] [149] [151] [152]. In $Li_{4.29}P_{0.71}Si_{0.29}S_4I$, these Raman

peaks shift to 426, 278 and 556 cm^{-1}, respectively, confirming the local structural change of the PS_4 $^{3-}$ units due to silicon substitution, in agreement with the single crystal data. The mode at 283 cm^{-1} has been assigned to a SiS_2 structure type i.e., SiS_2 (triangular) [153] [154].

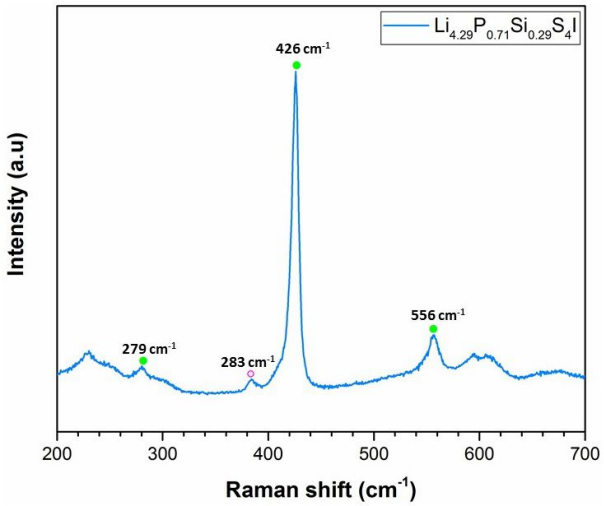

Figure 6.2: Raman spectra of $Li_{4.29}P_{0.71}Si_{0.29}S_4I$.

In $Li_{4+x}P_{1-x}Si_xS_4I$ framework, iodine and sulfur atoms are distributed over two distinct crystallographic sites (*2c* and *8i* Wyckoff sites, respectively). The large I^- is not exchanged for S^{2-} (2.20 Å versus 1.84 Å), resulting in a highly ordered anion framework in the complementary, disordered Li sublattice, which supports a random distribution of Li mobile ions over four likely equipotential sites, based on the proximity of the Li SOFs.

Based on the reported crystal structure obtained from PXRD data of the synthesized by soft chemistry Li_4PS_4I (P_4/nmm, Z=2, a=8.48284(12) Å, c=5.93013(11) Å and V=426.725(15) Å^3), the suggested conduction mechanism in Li_4PS_4I is 3D in nature; however, its conductivity appears to be rather low (between 0.12 and 0.064 $mS{\cdot}cm^{-1}$), where the influence from impurities was assumed (LiI or β-Li_3PS_4) [144]. By contrast, the herein synthesized by solid state reaction and characterized by single crystal XRD, Li_4PS_4I, crystallizes in the tetragonal system (P_4/nmm) with lattice parameters a=8.4789(4) Å, c=11.8499(6) Å, Z=4 and V=851.91(9) Å^3 (**Tables** 6.7- 6.9 and C.3).

Atom	Wyckoff site	x	y	z	SOF	U(eq)(Å^2)
P	*4f*	3/4	1/4	0.23808(5)	1	0.01285(13)
S1	*8i*	1/4	0.55085(5)	0.85705(4)	1	0.01798(11)
S2	*8i*	1/4	0.55964(5)	0.34542(4)	1	0.01769(11)
I1	*2c*	1/4	1/4	0.07640(2)	1	0.02508(9)
I2	*2c*	1/4	1/4	0.57613(2)	1	0.02168(9)
Li1	*2c*	1/4	1/4	0.3040(7)	1	0.0339(18)
Li2	*2b*	3/4	1/4	1/2	1	0.0314(16)
Li3	*8j*	0.0457(3)	0.0457(3)	0.7120(3)	1	0.0319(8)
Li4	*4d*	0	0	0	1	0.0546(17)

Table 6.7: Atomic coordinates, site occupation factors and equivalent isotropic displacement parameters of Li_4PS_4I obtained from single crystal XRD at 280 K.

Atom	U_{11}	U_{22}	U_{33}	U_{23}	U_{13}	U_{12}
P	0.0132(3)	0.0109(3)	0.0144(3)	0	0	0
S1	0.0211(2)	0.0135(2)	0.0194(2)	0.00319(16)	0	0
S2	0.0206(2)	0.0130(2)	0.0194(2)	0.00201(16)	0	0
I1	0.02903(12)	0.02903(12)	0.01718(14)	0	0	0
I2	0.02382(11)	0.02382(11)	0.01741(14)	0	0	0
Li1	0.0275(11)	0.0275(11)	0.041(2)	-0.0013(12)	-0.0013(12)	0.0071(15)
Li2	0.059(3)	0.059(3)	0.046(3)	0.008(2)	0.008(2)	-0.009(4)
Li3	0.038(3)	0.038(3)	0.026(4)	0	0	0
Li4	0.038(3)	0.038(3)	0.018(3)	0	0	0

Table 6.8: Anisotropic displacement parameters (Å^2) of Li_4PS_4I obtained from single crystal XRD at 280 K.

Atom1	Atom2	Bond distance (Å)
P	**S1**	2.0302(6) × 2
	S2	2.0549(6) × 2
Li1	**S1**	2.574(3) × 2
	S2	2.601(3) × 2
	I2	2.932(4)
Li2	**S1**	2.7475(3) × 4
	I1	3.13147(15)
Li3	**S2**	2.6708(15) ×4
	I1	2.697(8)
	I2	3.224(8)
Li4	**S2**	2.4414(5) ×4
Li1	**Li1**	3.464(6)
Li1	**Li2**	3.456(4)

Table 6.9: Interatomic distances of Li_4S_4I obtained from single crystal XRD at 280 K.

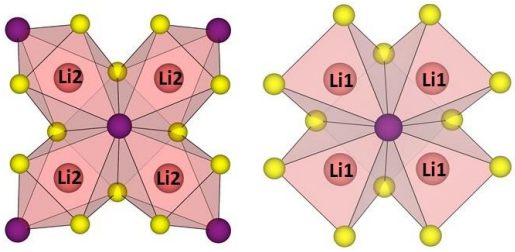

Figure 6.3: Environment of the Li(1) and Li(2) sites in Li_4PS_4I. Li(1) is 5-fold coordinated by four sulfurs and one iodine atom, Li(2) is 6-fold coordinated by four sulfurs and two iodine atoms. Color code: Li(1): light-rose; Li(2): dark rose; S: yellow, I: purple.

Analogous to $Li_{4+x}P_{1-x}Si_xS_4I$, the PS_4^{3-} tetrahedra in Li_4PS_4I are arranged in layers perpendicular to the *c*-axis, I^- anions between the tetrahedra layers and Li^+ cations as illustrated in the inset of **Figures** 6.4a and 6.4b. Lithium ions are likewise distributed over four crystallographic independent sites (Wyckoff *8j*, *4d*, *2c* and *2b* **Table** 6.7): Li(1) is 5-fold coordinated by four sulfurs and one iodine atom, Li(2) and Li(3) are 6-fold coordinated by four sulfurs and two iodine atoms, and Li(4) has a 4-fold coordination sphere around the sulfur atoms (**Figure** 6.3). Although, all four lithium sites are fully occupied in Li_4PS_4I, in contrast with the highly disorder Li sublattice of $Li_{4.29}P_{0.71}Si_{0.29}S_4I$, elucidating for its low RT ionic conductivity as discuss below.

Figures 6.4a and 6.4b display the PND patterns and Rietveld refinement fits of $Li_{4.29}P_{0.71}Si_{0.29}S_4I$ and Li_4PS_4I, respectively. The Rietveld refinement of the neutron TOF data provided results that show disorder of the Li over each of the four sites for

$Li_{4.29}P_{0.71}Si_{0.21}S_4I$, whereas a fully ordered Li sub-lattice for Li_4PS_4I (**Tables** C.4 and C.5 respectively), in excellent accord with the single crystal data described above. PXRD patterns and Rietveld refinement fits of $Li_{4+x}P_{1-x}Si_xS_4I$ with x=0, 0.12 and 0.29 are presented in **Figures** 6.5a-6.5c, respectively, confirming the Si incorporation onto the lattice and thus the obtained crystal structure solutions. Attempts to introduce additional silicon and lithium into $Li_{4+x}P_{1-x}Si_xS_4I$ caused formation of a secondary phase, Li_4SiS_4 at x=0.4, likely due to the thermodynamic instability of the lattice at high lithium content (**Figure** 6.5d).

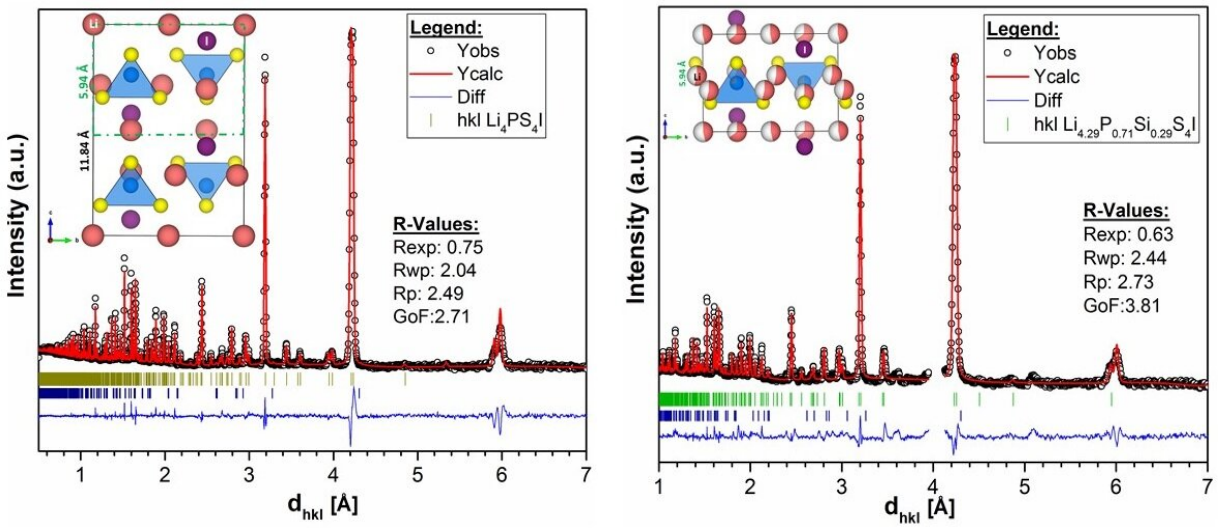

(a) x=0 **(b)** x=0.29

Figure 6.4: TOF neutron diffraction patterns and the corresponding Rietveld refinement fits of **a.** Li_4PS_4I, olive vertical ticks correspond to Li_4PS_4I and blue ticks to Li_2S (8.16wt%) Bragg reflections; **b.** $Li_{4.29}P_{0.71}Si_{0.29}S_4I$, blue vertical ticks correspond to Li_2S (9.6wt%) and green ticks to $Li_{4.29}P_{0.71}Si_{0.29}S_4I$ Bragg reflections. Two unknown diffraction peaks around 3.9 Å were excluded for the refinement. The black circles correspond to the data points, the red line denotes the calculated pattern, and the difference map is shown in blue.

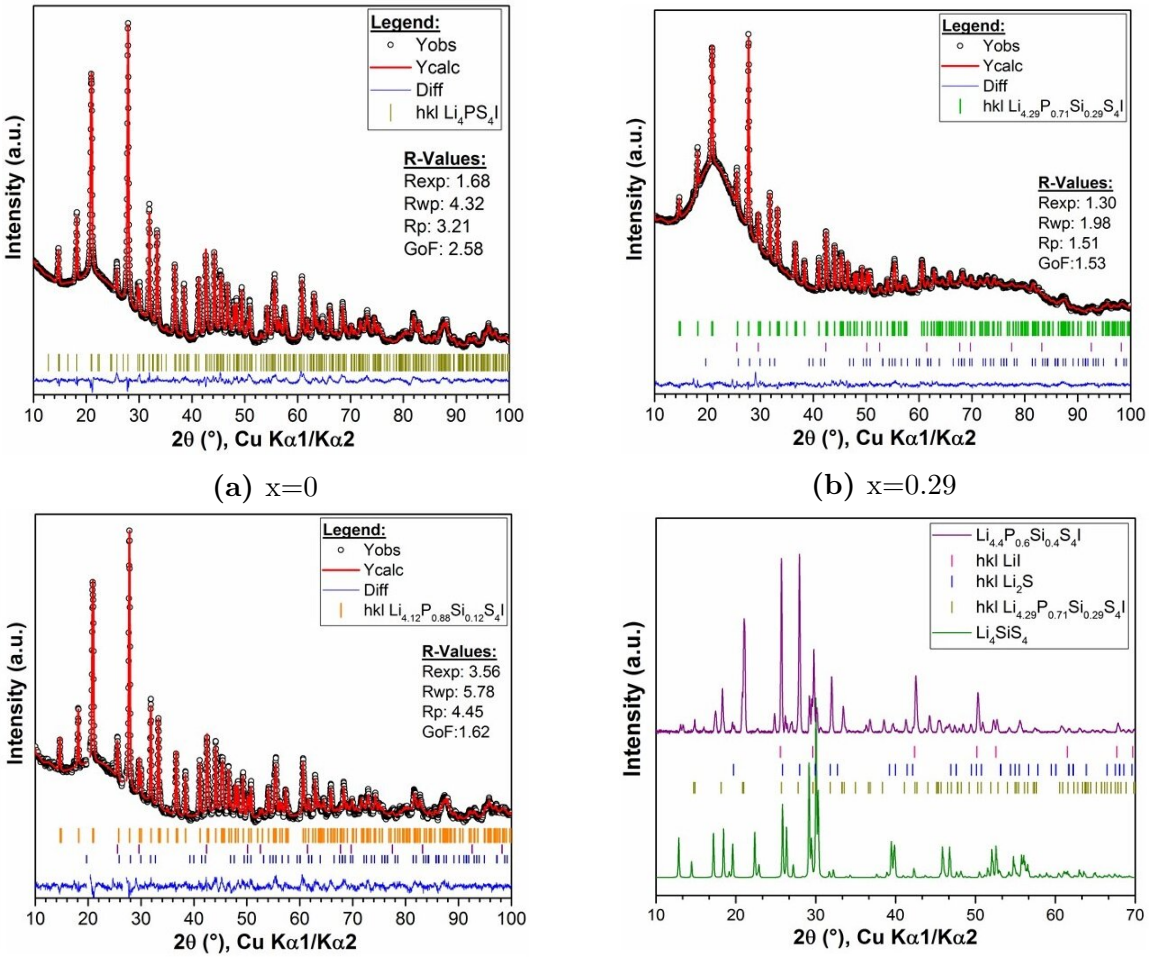

(a) x=0 **(b)** x=0.29

(c) x=0.12 **(d)** x=0.4

Figure 6.5: Rietveld refinement fits of **a.** Li_4PS_4I, olive vertical ticks correspond to Li_4PS_4I Bragg reflections; **b.** $Li_{4.29}P_{0.71}Si_{0.29}S_4I$, purple vertical ticks correspond to LiI (3.8 wt%), blue to Li_2S (4.29 wt%), and green to $Li_{4.29}P_{0.71}Si_{0.29}S_4I$ Bragg reflections; **c.** $Li_{4.12}P_{0.88}Si_{0.12}S_4I$, purple vertical ticks correspond to LiI (2.32%), blue to Li_2S (1.47%), and orange to $Li_{4.12}P_{0.88}Si_{0.12}S_4I$ Bragg reflections. Two small reflections were omitted (17° and 27°). The black circles correspond to the data points, the red line denotes the calculated pattern, and the difference map is shown in blue (Debye-Scherrer geometry was used for **a-c**); **d.** PXRD pattern of the targeted $Li_{4.4}P_{0.6}Si_{0.4}S_4$ composition (Bragg-Brentano geometry), XRD pattern of Li_4SiS_4 shown in green, $Li_{4.29}P_{0.71}Si_{0.29}S_4I$ (olive vertical ticks), LiI (pink ticks), and Li_2S (blue ticks).

With Si substitution, the a lattice parameter increases (8.4789(4) Å for x=0 versus 8.5090(7) Å for x=0.29), whereas the c parameter significantly decreases (11.8499(6) Å for x=0 versus 5.9473(5) Å for x=0.29, **Tables** C.2 and C.3), yet Si^{4+} radius is larger than that of P^{5+} (0.26 Å versus 0.17 Å). The substitution of P^{5+} for Si^{4+} leads to a highly disordered Li sublattice with a large concentration of Li^{+} vacancies in $Li_{4+x}P_{1-x}Si_xS_4I$ framework, ∼48.3% in x=0.12 and slightly lower in x=0.29 due to the increase in Li content concentration (**Figure** 6.5**a**). This results in a reduction of the c-axis and thus a decrease of the equivalent unit cell volume with respect to that of the fully ordered Li_4PS_4I phase (851.91(9) $Å^3$ versus 430.6(1) $Å^3$, **Tables** C.2 and C.3). As the Si content increases in $Li_{4+x}P_{1-x}Si_xS_4I$, Si^{4+} occupancy on the $(P_{1-x}Si_x)S_4$ $^{(3+x)-}$ tetrahedra increases as well as the polyhedral volume (**Figure** 6.5**b** and **Tables** 6.3, 6.6 and 6.9).

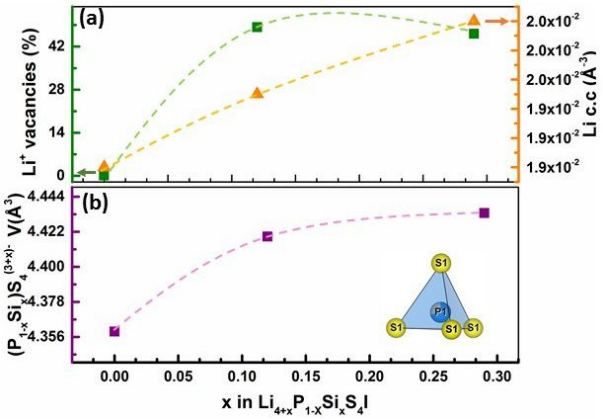

Figure 6.6: a. Li^{+} vacancy concentration and Li content concentration as a function of Si content in $Li_{4+x}P_{1-x}Si_xS_4I$; **b.** Polyhedral volume of $(P/Si)S_4$ as a function of Si content in $Li_{4+x}P_{1-x}Si_xS_4I$.

For comparison purposes the single crystal data of $Li_{4+x}P_{1-x}Si_xS_4I$ with x=0.12 and 0.29 have been also refined using the ordered structural model of Li_4PS_4I (**Table** 6.7 and **Figure** 6.4a), whereas the disorder model was used to refine the Li_4PS_4I data (**Tables** C.6-C.16). The obtained, highly ordered model of $Li_{4+x}P_{1-x}Si_xS_4I$ with x=0.12 and 0.29 is comprised of five distinct Li sites (*8j*, *4d*, *2c*, *2b* and *2a* Wyckoff sites); the extra fifth Li site, *2a* Wyckoff, is occupied due to the increase of Li content with incorporation of Si onto the lattice, (Li^{+} + Si^{+4}) for P^{+5} (**Tables** C.7 and C.10). The Li occupancies in x=0, 0.12 and 0.29 are significantly different between the two models (**Tables** C.7, C.10 and C.13), a defected versus a highly ordered Li sublattice, yet both models confirm the substitution

of P^{5+} for Si^{4+} in the *2b* Wyckoff, by unit cell and $(P/Si)S_4$ tetrahedra volume expansion (**Figures** 6.7**a** and 6.7**b**).

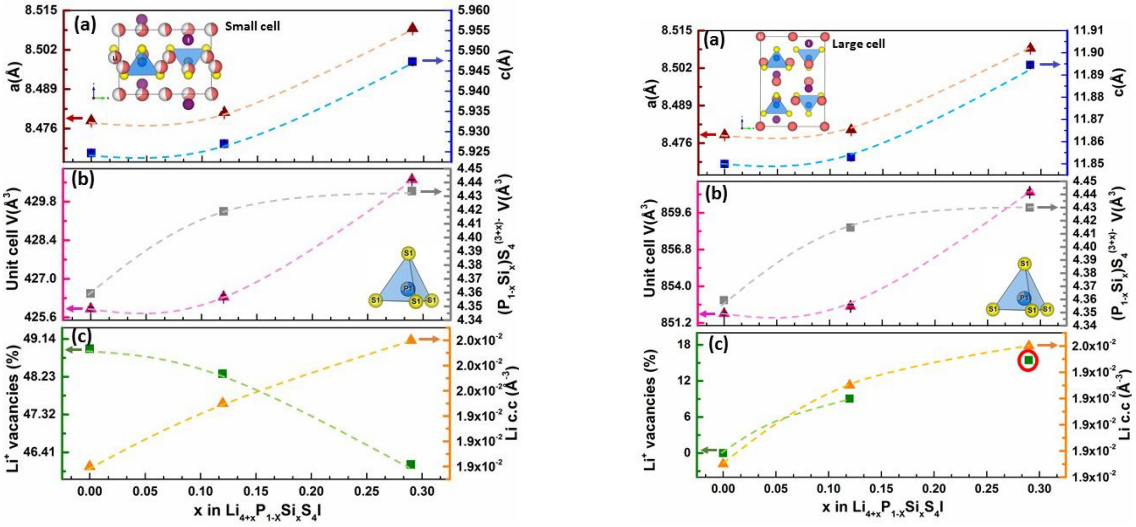

(a) Small cell model **(b)** Highly ordered model

Figure 6.7: Comparison between: **a.** Disordered small cell model; **b.** Highly ordered model as a function of Si content in $Li_{4+x}P_{1-x}Si_xS_4I$. The inset labels correspond to the lattice parameters:**a.** *a* (brown color) and *c* (blue color) ; **b.** Unit cell volume (pink color) and polyhedral $(P/Si)S_4$ volume (grey color); **c.** Li^+ vacancy (green color) and Li content (orange color) concentrations.

For the disorder small lattice model (**Figure** 6.7a), as expected, Li^+ vacancies decrease as the Li content increases in the lattice (**Figure** 6.7**c** inset). The opposite is observed for the highly ordered model (**Figure** 6.7b), in which all four Li sites are fully occupied at x=0, Si substitution induces disorder in the Li substructure, creating a large content of vacancies in x=0.12 and x=0.29 (**Figure** 6.7**c** inset); although, an underestimation of Li content in the latter composition is observed (3.81 versus 4.29 f.u.), and therefore an overestimation of Li vacancies (this data point has been highlighted with a red circle in **Figure** 6.7b).

The striking contrast in crystal structure between the reported structural disordered framework [144] and the herein obtained fully ordered of Li_4PS_4I may relay on the two synthesis approaches. The formation of Li_4PS_4I structure during the removal of the dimethoxyethane solvent may generate a large number of vacancy defects and thus a disor-

dered Li substructure, albeit, with a poor conductivity (between 0.12 and 0.064 mS·cm^{-1}) [144]. By contrast, the herein utilized solid-state reaction method with a slow cooling rate gives more time to the mobile ions to accommodate in the lattice sites resulting in an ordered lithium configuration in Li_4PS_4I, elucidating for its low ionic conductivity. Since all four Li sites are fully occupied, as the Li content increases, due to the incorporation of Si onto the lattice, either a new interstitial Li sites need to be formed (*2a* Wyckoff in the highly ordered model), or an structural change needs to take place (small cell model).

6.4 Ionic and electronic properties

The Nyquist plot of $Li_{4+x}P_{1-x}Si_xS_4I$ with x=0, 0.12, 0.29 and 0.4 series is presented in **Figure** 6.8 (fitted parameters are shown in **Table** 6.10). **Figure** 6.9a shows the RT ionic conductivity of $Li_{4+x}P_{1-x}Si_xS_4I$ (x=0, 0.12, 0.29 and 0.4), as measured by impedance spectroscopy (**Table** C.6). With increasing fraction of Si^{4+} and Li^+, the conductivity increases over two orders of magnitude and reaches a maximum conductivity of $\sigma(Li^+)$= 1.46±0.21 mS·cm^{-1} for $Li_{4.29}P_{0.71}Si_{0.29}S_4I$, at x=0.4 the conductivity drops to 0.39±0.07 mS·cm^{-1}, likely due to the crystallization of the Li_4SiS_4 impurity phase as shown by PXRD data (**Figure** 6.5d).

The lower ionic conductivity of x=0.12 versus x=0.29 (0.42± 0.20 mS·cm^{-1} versus 1.46±0.21 mS·cm^{-1}) is likely due to its lower Li^+ content concentration in the lattice (4.12 f.u. for x=0.12 versus 4.29 f.u. for x=0.29, **Figure** 6.6). The lower ADPs of the Li sites in x=0.12, particularly Li(3) and Li(4) sites (Li(3), SOF=0.0283(15) for x=0.12 versus SOF=0.4230(19) for x=0.29; Li(4), SOF=0.042(3) for x=0.12 versus SOF=0.064(9) for x=0.29, **Tables** 6.1 and 6.4), indicate less mobile Li^+-ions in x=0.12 and therefore lower ionic conductivity. Temperature-dependent impedance spectroscopy was performed to assess the changes in the ionic conductivity of $Li_{4+x}P_{1-x}Si_xS_4I$ with x=0, 0.12 and 0.29 (**Figures** 6.9b, 6.9c and 6.9d, respectively). The activation energy for Li^+-ion diffusion gradually decreases as Si content in the lattice increases, from 0.44 eV for x=0 to 0.32 eV for x=0.29 (**Figure** 6.9).

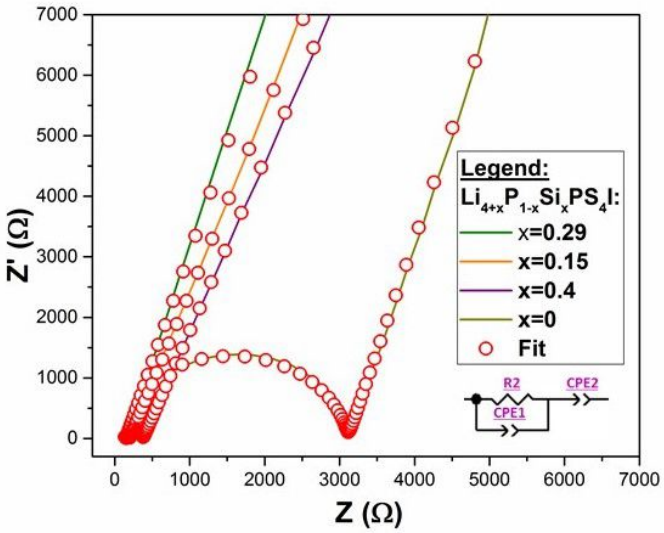

Figure 6.8: Nyquist impedance plot and fit of $Li_{4+x}P_{1-x}Si_xS_4I$ with x=0, 0.12, 0.29 and 0.40 with the respective equivalent circuit.

Compound	**CPE$_1$ (F s^{a-1}) (10^{-9})**	**a$_1$**	**CPE$_2$ (F s^{a-1}) (10^{-6})**	**a$_2$**	**R$_1$ (Ω)**
Li_4PS_4I	1.158	0.915	8.407	0.830	3 108
$Li_{4.12}P_{0.88}Si_{0.12}S_4I$	0.917	0.928	4.833	0.794	197.8
$Li_{4.29}P_{0.71}Si_{0.29}S_4I$	1.68	0.884	10.88	0.797	147.8
$Li_{4.4}P_{0.6}Si_{0.4}S_4I$	1.84	0.898	7.768	0.784	379

Table 6.10: Parameters of the fit for the impedance data of $Li_{4+x}P_{1-x}Si_xS_4I$ with x=0, 0.12, 0.29 and 0.4 at RT.

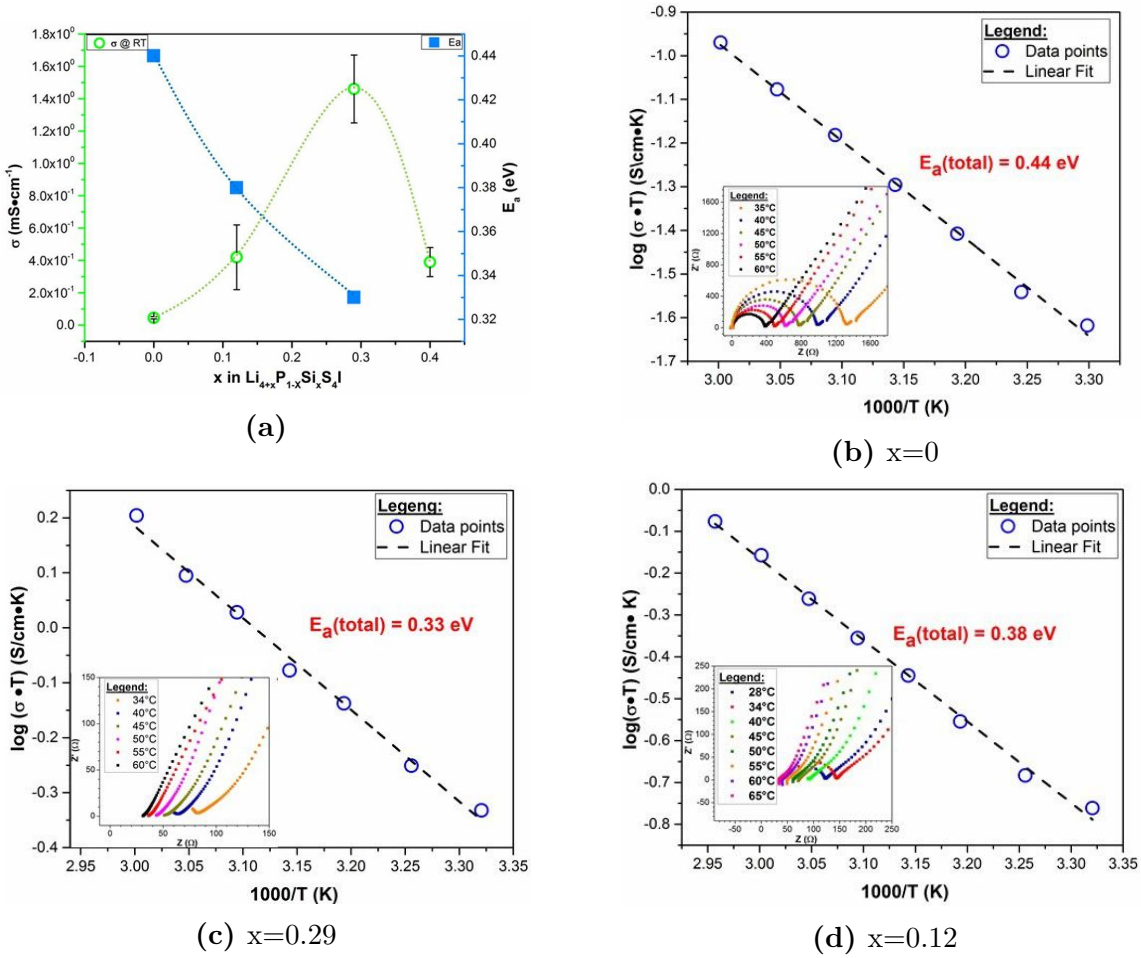

Figure 6.9: a. RT ionic conductivities as a function of composition in $Li_{4+x}P_{1-x}Si_xS_4I$ with x=0, 0.12, 0.29 and 0.40 (green color), and activation energies of x=0, 12, and 0.29 (blue color). Arrhenius conductivity plots, with the insets displaying the corresponding Nyquist impedance plots of: **b.** Li_4PS_4I from 30°C to 60°C; **c.** $Li_{4.29}P_{0.71}Si_{0.29}S_4I$ from 30°C to 60°C; **d.** $Li_{4.12}P_{0.88}Si_{0.12}S_4I$ from 30°C to 65°C.

The electronic conductivities of $Li_{4+x}P_{1-x}Si_xS_4I$ for x=0 and x=0.29 materials were measured by a DC polarization measurement. **Figure** 6.10 shows the DC polarization curves of Li_4PS_4I (**Figure** 6.10a) and $Li_{4.29}P_{0.71}Si_{0.29}S_4I$ (**Figure** 6.10b) at three voltages (0.25 V, 0.50 V and 0.75 V). From a linear fit of DC voltage and stabilized current (**Figures** 6.10c and 6.10d), the DC electronic conductivities are estimated to be 9.72 x 10^{-6} mS·cm^{-1} for Li_4PS_4I, and 1.8 x 10^{-6} mS·cm^{-1} for $Li_{4.29}P_{0.71}Si_{0.29}S_4I$ -with SiS_2 as

one of the impurities (**Figure** 6.2).

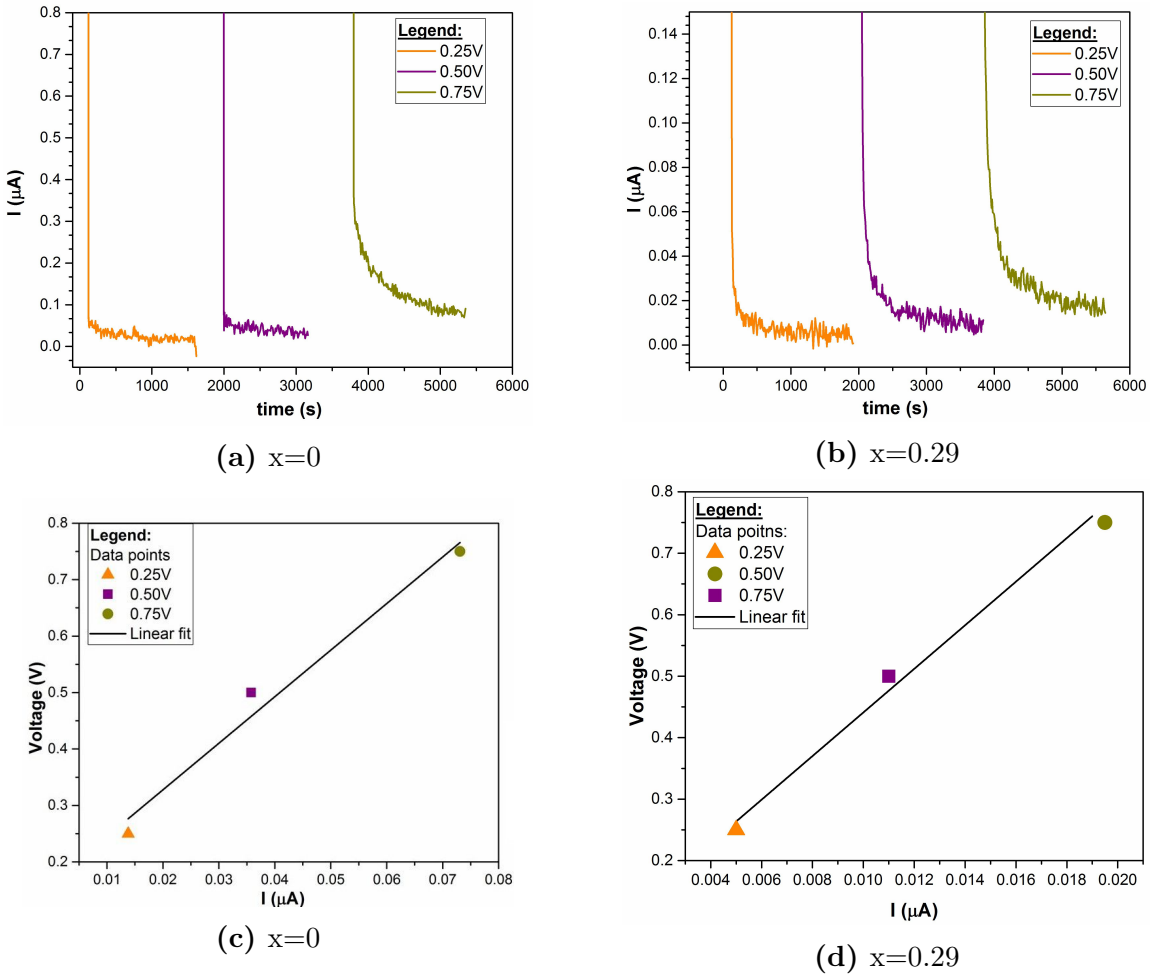

(a) x=0 **(b)** x=0.29

(c) x=0 **(d)** x=0.29

Figure 6.10: DC polarization curves for electronic conductivity determination with an applied voltage of 0.25 (orange), 0.50 (purple) and 0.75 V (grey) of $Li_{4+x}P_{1-x}Si_xS_4I$: **a.** x=0; **b.** x=0.29. Linear fit of the voltage versus current of $Li_{4+x}P_{1-x}Si_xS_4I$: **c.** x=0; **d.** x=0.29.

The large increase in ionic conductivity and decrease in activation energy with Si content shows that aliovalent substitution approach has a remarkable influence on the degree of disorder of the Li substructure and thus on the ion transport properties of SEs, as it has been observed for Ge^{4+} substitution in $Li_{6+x}P_{1-x}Ge_xS_5I$ [152] and recently Si^{+4} substitution

in $Li_{3+x}[Si_xP_{1-x}]S_4$ [155]. The high ionic conductivity of $Li_{4.29}P_{0.71}Si_{0.29}S_4I$ is comparable to other lithium ion conductors in **Table** 6.11. $Li_{4.29}P_{0.71}Si_{0.29}S_4I$ shows an ionic conductivity two and four orders higher than that of Li_4PS_4I and Li_6PS_5I, respectively. The Li^+-ion conductivity of $Li_{4.29}P_{0.71}Si_{0.29}S_4I$ is comparable to those of well-known superionic conductors,*e.g.*, Cl- argyrodite [142], LGPS-type [70], and Li_7PS_{11} [66].

Compound	**Ionic conductivity mS·cm^{-1}**	**Activation energy (eV)**	**Ref.**
$Li_{4.29}P_{0.71}Si_{0.29}S_4I$	1.46	0.32	this work
$Li_4PS_4I_{ssr}$	0.046	0.44	this work
$Li_4PS_4I_{scr}$	0.064-0.12	0.37-0.43	[144]
$Li_7P_2S_8I$	0.63	—-	[143]
Li_6PS_5I	0.000046	0.26	[151]
$Li_{6.6}P_{0.4}Ge_{0.6}S_5I$	5.4	—	[152]
$Li_7P_3S_{11}$	3.2	0.124	[66]
Li_6PS_5X X=Cl, Br	1.9, 6.8	0.2, 0.3	[142]
$Li_{10}SnP_2S_{12}$	4.0	0.27_g, $0.60_{g.b}$	[69]
$Li_{10}SiP_2S_{12}$	2.3	0.196	[70]

Table 6.11: Conductivity and activation energy of $Li_{4.29}P_{0.71}Si_{0.29}S_4I$, Li_4PS_4I and other sulfide-based ion conductors. *ssr*:solid-state route, *scr*:soft chemistry route.

Insights into the potential diffusion pathways in $Li_{4.29}P_{0.71}Si_{0.29}S_4I$ framework are examined by the maximum-entropy method (MEM), the 3D nuclear density map using the MEM was obtained using Dysnomia software [156] which visualizes the Li nuclear density in $Li_{4.29}P_{0.71}Si_{0.29}S_4I$. The obtained structure factors from the Rietveld analysis of the neutron diffraction data were used as an initial input to evaluate the dynamic disorder of lithium in the lattice. The lithium negative nuclear density maps for $Li_{4.29}P_{0.71}Si_{0.29}S_4I$ along the *a,b*-, *b,c*- and *a,c*- planes are shown in **Figures** 6.11a, 6.11b and 6.11c respectively. The structure in the polyhedral motif along the *a,c*- plane is shown for comparison **Figure** 6.11d. The MEM maps suggest a complex 3D character of the lithium conductivity in $Li_{4.29}P_{0.71}Si_{0.29}S_4I$ at RT (**Figures** 6.11a - 6.11c), in which lithium diffusion is observed along the *c*-axis through the chain formed by Li(4)-Li(3)-Li(3)-Li(4) sites with Li(4)-Li(3) and Li(3)-Li(3) interatomic distances of 2.57(12) Å and 1.40(3) Å, respectively (**Figure** 6.11c).

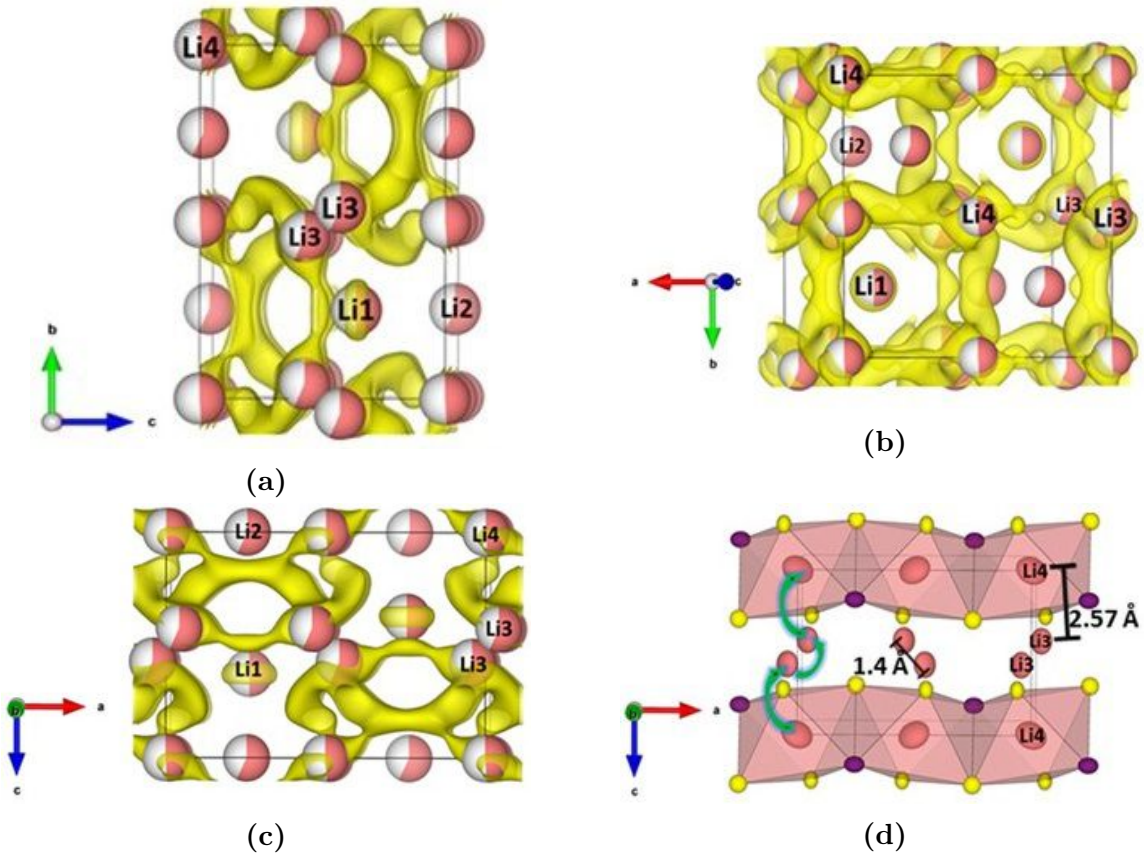

Figure 6.11: Negative nuclear density distribution (of Li ions) in $Li_{4.29}P_{0.71}Si_{0.29}S_4I$ calculated using the MEM along **a.** [100]; **b.** [001]; **c.** [010] with the structure in the polyhedral motif along the *ac*-, plane showing the lithium diffusion along the *c*-axis through the chain formed by Li(4)-Li(3)-Li(3)-Li(4) sites and interatomic distances.

BVSE maps [81] [82] were used to analyze the energetics of probable ion diffusion pathways in the lattice of $Li_{4.29}P_{0.71}Si_{0.29}S_4I$ **Figure** 6.12. **Figure** 6.12a shows the BVSE maps of $Li_{4.29}P_{0.71}Si_{0.29}S_4I$ along the [001], [010] and [100] directions, underneath the depiction of the structure in the polyhedral motif for comparison (**Figure** 6.12b). Analysis of the BVSE maps indicates that Li^+ diffusion follows a well-connected 3D pathway likely involving an interstitial site i1 at 0.75, 0.073, 0.903 (Wyckoff *8i*, depicted as black spheres. The i1 site shortens the Li(4)-Li(4) interatomic distance from 4.25(4) Å to 2.28(18) Å likely allowing ion diffusion along the *a* and *b*-axes (**Table** C.16 and **Figure** 6.12b).

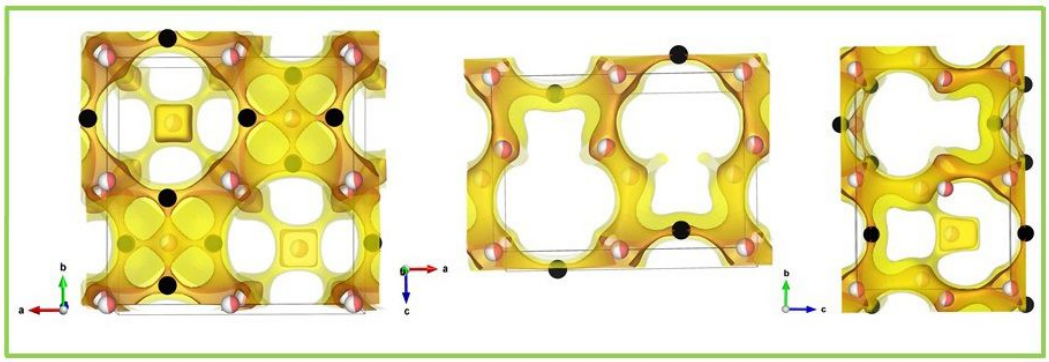

(a)

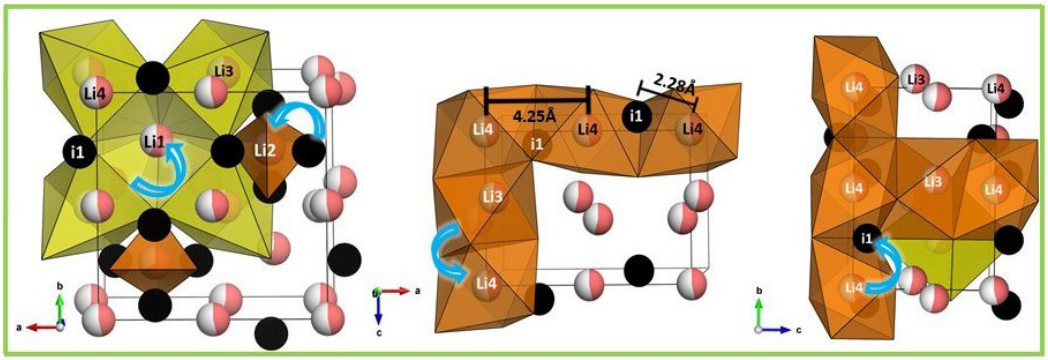

(b)

Figure 6.12: a. BVSE model of Li^+-ion migration pathways in $Li_{4.29}P_{0.71}Si_{0.29}S_4I$ along the [001], [010] and [100] directions visualized as isosurfaces of constant BVSE using the small cell model. The orange isosurface corresponds to a site energy characteristic of local hopping paths, while the yellow range isosurface corresponds to the long-range migration involving the i1 interstitial site; **b.** View of the structure of $Li_{4.29}P_{0.71}Si_{0.29}S_4I$ along the [001] direction, [010] and [100] directions, showing the Li(4)-Li(4) and Li(4)-i1 interatomic distances.

BVSE attempts to predict the energetic environment of Li^+-ions from a static structure model. **Figure** 6.13 shows the BVSE model of migration barriers for Li-ion diffusion in $Li_{4.29}P_{0.71}Si_{0.29}S_4I$. As indicated in **Figure** 6.13, Li-ion diffusion takes place through the Li(4)-i1, Li(4)-Li(3) and Li(2)-i1 sites with activation energy barriers of 0.314 eV, 0.236 eV and 0.219 eV (relatively low ∼0.2), respectively, in accordance with the proposed diffusion pathways in **Figure** 6.12b. In contrast, a large activation energy of 0.731 eV for the Li(1)-Li(4) jump was observed (**Figure** 6.13). Albeit, the BVSE model cannot be expected to

yield activation energies with high exactitude, since by using a static structure model the structural relaxations are not taking into account, leading to an overestimation of migration barriers [157]. Furthermore, recent *ab initio* modeling has reported that unique mobile ion configurations such as mobile ions occupying high-energy sites along with strong mobile ion interactions can trigger concerted migration with a reduced migration energy barrier [41]. The high energy Li(4) and Li(1) sites may activate concerted ion migration to further lower the activation energy.

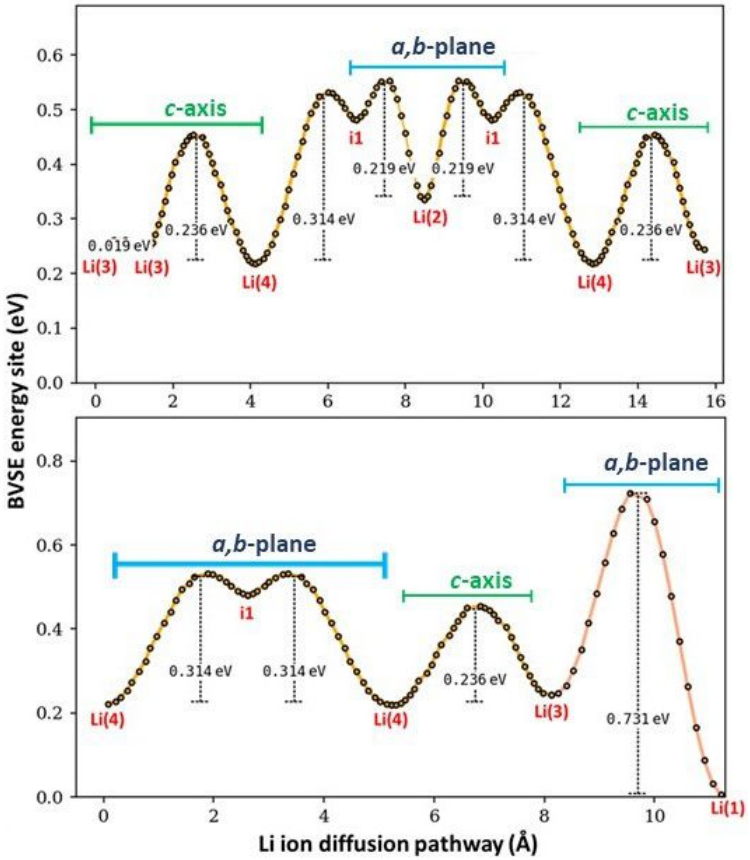

Figure 6.13: BVSE models of migration barriers of $Li_{4.29}P_{0.71}Si_{0.29}S_4I$.

Available sites with similar Li^+-ion adsorption energies result in partial site occupancies, and thus Li^+-ion site configurational disorder; a critical condition for achieving high ionic conductivity [158] [159]. The increase of Li concentration (from 4 f.u. to 4.29 f.u.) in $Li_{4+x}P_{1-x}Si_xS_4I$ leads to a structural disorder in the Li sublattice, which lowers the

activation energy for Li^+-ion diffusion, compared to the ordered Li_4PS_4I framework (0.33 eV versus 0.44 eV). The maximal configurational entropy and high ionic conductivity are achieved when the concentration of mobile ions is equal to that of mobile vacancies [158]. $Li_{4.29}P_{0.71}Si_{0.29}S_4I$ counts with 16 sites available for 8.29 Li^+-ions, leading to a large number of vacancies in the Li sublattice, ∼46.13% (**Figures** 6.6**a** and 6.7**c**).

The thermal stability of $Li_{4+x}P_{1-x}Si_xS_4I$ with x=0 and 0.29 was investigated by DSC technique. **Figure** 6.14 exhibits the DSC curves of $Li_{4.29}P_{0.71}Si_{0.29}S_4I$ and Li_4PS_4I. The DSC traces of Li_4PS_4I in the heating/cooling cycle processes show several exothermic/endothermic peaks, i.e., 229°C, 312°C, 454°C and 456°C. In contrast, $Li_{4.29}P_{0.71}Si_{0.29}S_4I$ shows two peaks (exothermic(412°C)/endothermic(425°C)) in the temperature range, indicating its higher thermal stability.

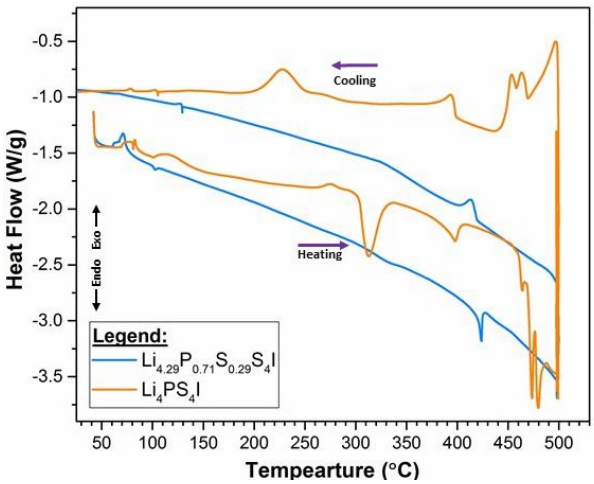

Figure 6.14: Differential scanning calorimetry curves of $Li_{4.29}P_{0.71}Si_{0.29}S_4I$ and Li_4PS_4I at a heating rate of 10°C·min^{-1} up to 400°C.

6.5 Summary and Future Prospects

Li_4PS_4I was synthesized for the first time by solid-state reaction with a RT ionic conductivity four orders of magnitude lower than that of the new Li^+-ion conductor, $Li_{4.29}P_{0.71}Si_{0.29}S_4I$ (0.046 mS·cm^{-1} versus 1.46 mS·cm^{-1}).

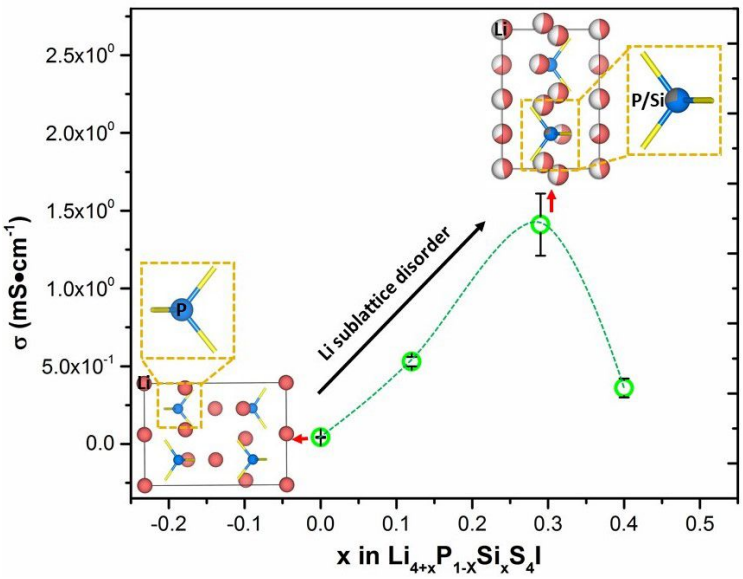

Figure 6.15: Ionic conductivity as a function of Si content in $Li_{4+x}P_{1-x}Si_xS_4I$. View of the Li-ion sublattice of Li_4PS_4I (bottom left), and $Li_{4.29}P_{0.71}Si_{0.29}S_4I$ (top right),

The significantly increased in ionic conductivity showed by $Li_{4.29}P_{0.71}Si_{0.29}S_4I$ may be explained based on:

- The configurational disorder of the Li sublattice -a highly defected mobile Li sublattice- supporting a random Li-ion distribution over four likely equipotential sites.
- Si substitution -0.29(Li^+ + Si^{4+}) for P^{5+}- increases the mobile-cation carrier concentration.

Thus, the conductivity has been improved by increasing the Li^+ concentration, the defect concentration, and by lowering the activation energy for ion diffusion (0.44 eV versus 0.32 eV). Aliovalent substitution can be a promising approach of highly defective Li sublattices in the development of ionic conductivity enhancement strategies.

Future Prospects

This work demonstrated that inducing mobile-cation disorder in Li_4PS_4I by Si substitution, $Li_{4+x}P_{1-x}Si_xS_4I$, is a promising approach to enhance ionic transport properties in

solid electrolytes. Anion site disorder has also been correlated to a decrease in the activation barrier and an increase in the conductivity in Li-argyrodite superionic conductors [152]. The substitution of I for Br in $Li_{4.29}P_{0.71}Si_{0.29}S_4I$ could induce disorder in its anion sublattice -S/Br-. In contrast to the large size mismatch between S^{2-} and I^- (1.84 Å versus 2.20 Å), S/Br anion site disorder can be possible due to the similar ionic radii of Br^- and S^{2-} anions, 1.96 Å and 1.84 Å, respectively.

The possibility of increasing charge carrier density and widening of the diffusion pathways for Li^+ by the incorporation of Ge^{4+} into the Li_4PS_4I framework, $Li_{4+x}P_{1-x}Ge_xS_4I$, is worth exploring. As shown by Ge^{4+} substitution in Li-argyrodite, $Li_{6+x}P_{1-x}Ge_xS_5I$ [152]; an increase in the unit cell after Ge^{4+} substitution due to the larger ionic radius of Ge^{4+} versus P^{5+} (0.17Å versus 0.39 Å) allowed for better mixing of the mismatched anions S/I, enabling anion site disorder in $Li_{4+x}P_{1-x}Ge_xS_4I$ framework.

Chapter 7

Revealing the effects of Al substitution on the structural and transport properties of $Li_{3+2x}P_{1-x}Al_xS_4$

7.1 Introduction

Ceder *et al.* investigated the complete substitution of Ge^{+4} for Al^{+3} in the LGPS structure, leading to the predicted composition $Li_{11}AlP_2S_{12}$ [160]. This material was suggested to be an even better ionic conductor at lower material cost, σ_{Li}=33 mS·cm^{-1} versus 13 mS·cm^{-1} and E_a=0.18 eV versus 0.21 eV. The predicted higher ionic conductivity of the aluminum-based SE compared to that of the germanium-based compound was explained based on its larger channel size for Li-ion diffusion (1.92 Å versus 1.46 Å) [160]. Recently, Chen *et al.* reported the apparent synthesis of $Li_{11}AlP_2S_{12}$ with an RT ionic conductivity of 0.8 mS·cm^{-1} [149]. However, the structure was not resolved by either powder or single crystal methods, and therefore the relationship between the crystal structure and Li-ion conductivity was not elucidated. In this direction, I studied the Al-substitution in $Li_{3+2x}P_{1-x}Al_xS_4$ through the examination of the series x=0.15, 0.20 and 0.33, where the solubility limit of Al in the structure was determined.

7.2 Synthesis

$Li_{3+2x}P_{1-x}Al_xS_4$ with x=0.15, 0.20 and 0.33 compositions were synthesized by solid state reaction. For each of these compositions, Li_2S (99%, Sigma-Aldrich), Al_2S_3 (99%, Sigma-Aldrich) and P_2S_5 (99%, Sigma-Aldrich) were mixed together according to the molar ratios: 1.65:0.425:0.075, 1.7:0.4:0.1 and 1.83:0.335:0.165, respectively. Each mixture was grounded in an agate mortar for 1 h. The mixtures were heated at 700°C with a heating rate of 63°C/h, kept for 5 h, followed by a slow cooling step of 1°C/h from 700°C to 621°C where the samples were ice quenched. The refinement details from the single crystal diffraction data are presented in **Appendix** D.

7.3 Crystal structure

Figure 7.1 shows the RT PXRD patterns of $Li_{3+2x}P_{1-x}Al_xS_4$ with x=0.15, 0.20 and 0.33, with the diffraction pattern of β-Li_3PS_4 shown for comparison [148]. A secondary phase, Li_5AlS_4, whose content increases with x is observed, indicating the low solubility of Al in the crystal structure. The expanded PXRD patterns of $Li_{3.3}P_{0.85}Al_{0.15}S_4$ and β-Li_3PS_4 compounds are shown in **Figure** 7.2a. The (210) and (002) Bragg reflections are shifted toward lower angles, while the (011) and (221) reflections are shifted toward higher angles relative to β-Li_3PS_4 [148]. However, the Bragg reflections are unchanged with attempted increase in Al substitution, i.e., x=0.20 and 0.33, as shown in **Figure** 7.2b, and this -coupled with the crystallization of Li_5AlS_4- indicates not only that the solid solution between Al and P is formed within a narrow concentration range, but also that the limit of Al solubility is reached at about x=0.15. This limit is likely dictated by the availability and lattice energy needed to accommodate the additional lithium in the structure.

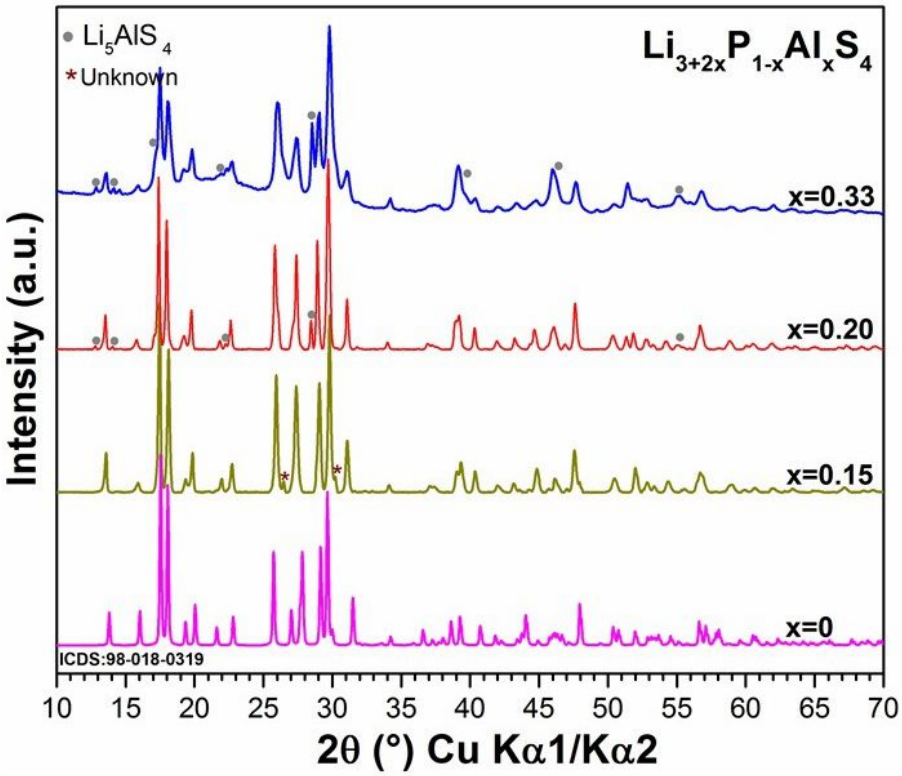

Figure 7.1: PXRD patterns of $Li_{3+2x}P_{1-x}Al_xS4$ with x=0, 0.15, 0.20 and 0.33 (Debye-Scherrer geometry). The Li_5AlS_4 impurity is indicated by circle markers.

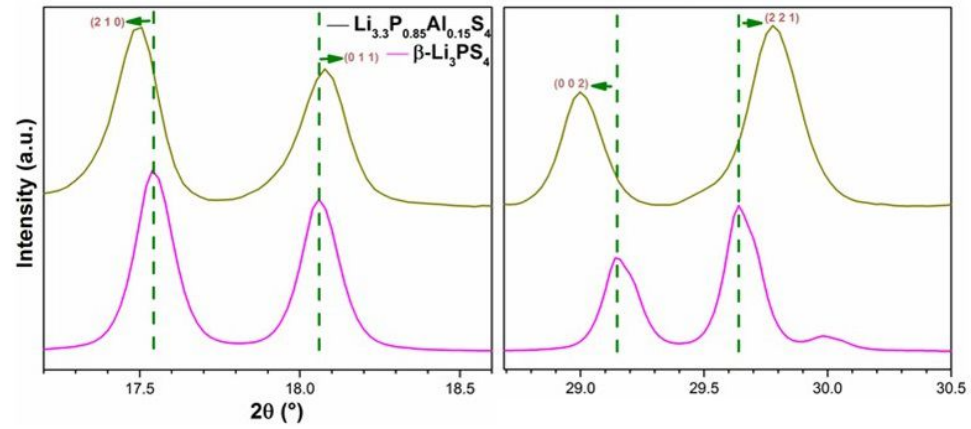

(a)

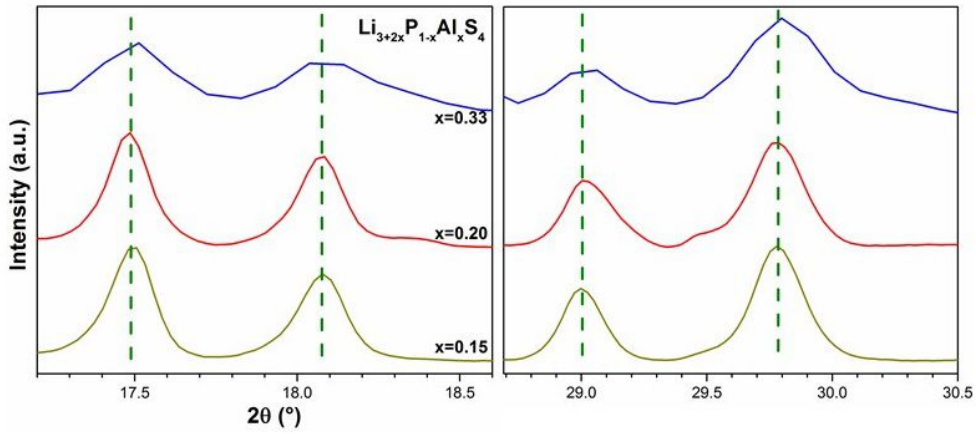

(b)

Figure 7.2: Magnified view of the XRD patterns of **a.** $Li_{3.3}P_{0.85}Al_{0.15}S_4$ and β-Li_3PS_4 compounds of the 2θ=17.2° - 18.6° and 2θ=28.2° - 30.5° range; **b.** $Li_{3+2x}P_{1-x}Al_xS_4$ with x=0.15, 0.20 and 0.33. compounds of the 2θ =17.2° - 18.6° and 2θ = 28.2° - 30.5° range.

Single crystals of $Li_{3.3}P_{0.85}Al_{0.15}S_4$ were successfully obtained contributing to elucidate the crystal structure of this new Li-ion conductor (**Tables** 7.1 - 7.3 and D.1). Based on the single crystal data, orthorhombic $Li_{3.3}P_{0.85}Al_{0.15}S_4$ crystallizes in the space group *Pnma* with a=12.9575(13) Å, b=8.0861(8) Å, c=6.1466(6) Å, Z=4 and V=644.00(11) Å^3. Lithium atoms are distributed over three independent Wyckoff positions (*8d*, *8d* and *4c*) accounting for a Li content of 3.11(9), while Al and P share the *4c* Wyckoff position 4-fold coordinated (**Table** 7.1), while typical Li-S bond length range between 2.4 and 2.7

Å (**Table** 7.3).

Atom	Wyckoff site	x	y	z	SOF	U_{eq}/Å^2
P	*4c*	0.08870(6)	1/4	0.15746(13)	0.85	0.01454(19)
Al	*4c*	0.08870(6)	1/4	0.15746(13)	0.15	0.01454(19)
S1	*8d*	0.15343(4)	0.03863(8)	0.2484(18)	1	0.02484(18)
S2	*4c*	0.43848(6)	1/4	0.22942(13)	1	0.0191(2)
S3	*4c*	0.10279(4)	1/4	0.82802(13)	1	0.0250(2)
Li1	*8d*	0.3323(4)	0.4660(7)	0.3925(10)	1	0.0452(13)
Li2	*8d*	0.0067(9)	0.0438(15)	0.5525(18)	0.45(2)	0.040(4)
Li3	*4c*	0.430(10)	1/4	0.80(2)	0.21(7)	0.15(6)

Table 7.1: Atomic coordinates, site occupation factors and equivalent isotropic displacement parameters of $Li_{3.11(2)}P_{0.85}Al_{0.15}S_4$ obtained from single crystal XRD at 280 K.

Atom	U_{11}	U_{22}	U_{33}	U_{23}	U_{13}	U_{12}
P	0.0141(4)	0.0168(4)	0.0127(4)	0	0.0008(3)	0
Al	0.0141(4)	0.0168(4)	0.0127(4)	0	0.0008(3)	0
S1	0.0206(3)	0.0244(3)	0.0296(3)	0.0069(2)	-0.0001(2)	0.0047(2)
S2	0.0139(3)	0.0218(4)	0.0217(4)	0	-0.0018(3)	0
S3	0.0347(5)	0.0255(4)	0.0149(4)	0	0.0028(3)	0
Li1	0.036(2)	0.039(3)	0.061(3)	-0.018(3)	-0.008(2)	0.000(2)
Li2	0.029(5)	0.049(8)	0.040(8)	0.021(5)	0.005(5)	-0.003(5)

Table 7.2: Anisotropic displacement parameters (Å^2) of $Li_{3.11(2)}P_{0.85}Al_{0.15}S_4$ obtained from single crystal XRD at 280 K. Li3 site was refined isotropically.

Atom1	Atom2	Interatomic distances (Å)
P/Al	**S1**	2.0385(7) × 2
	S2	2.0670(11)
	S3	2.0331(11)
Li1	**S1**	2.427(5), 2.436(6)
	S2	2.438(5)
	S3	2.478(6)
Li2	**S1**	2.421(11), 2.550(11)
	S2	2.562(11) ×2
	S3	2.683(12) ×2
Li3	**S1**	2.58(6) ×2
	S2	2.62(12)
	S3	2.39(13)
Li1	**Li2**	3.019(13)
Li2	**Li3**	2.14(9), 2.95(8)
Li1	**Li3**	3.32(11)
Li1	**Li1**	3.492(11)
Li2	**Li2**	0.97(3)

Table 7.3: Interatomic distances of $Li_{3.11(2)}P_{0.85}Al_{0.15}S_4$ obtained from single crystal XRD at 280 K.

Views of the $Li_{3.3}P_{0.85}Al_{0.15}S_4$ crystal structure along the [100] and [010] directions are shown in **Figures** 7.3a and 7.3b, respectively. $(P/Al)S_4$ tetrahedra are connected with LiS_x (x=4 and 6) polyhedra via edge sharing. The Li(1) is 4-fold coordinated by sulfur atoms and its site is fully occupied, the Li(2) (*8d*) site is split into two equally occupied positions 0.97(3) Å apart, and the partially occupied Li(3) has a 4-fold coordination sphere of sulfur atoms (**Tables** 7.1 and 7.3).

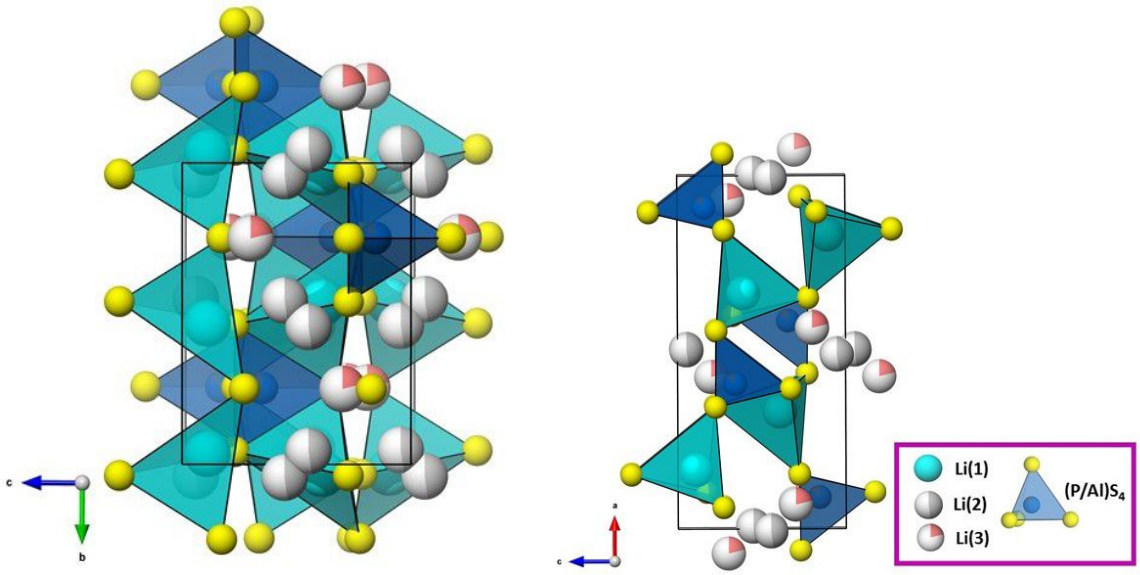

(a) [100] **(b)** [010]

Figure 7.3: View of the structure of $Li_{3.3}P_{0.85}Al_{0.15}S_4$ from single crystal data along **a.** [100]; **b.** [010]. Color code: Li(1), Li(2), and Li(3): light rose; S: yellow, P:blue; $(P/Al)S_4$ polyhedra are shown in blue. Using the model obtained by single crystal data.

The crystal structure of $Li_{3.3}P_{0.85}Al_{0.15}S_4$ was solved as follows: first, the P/Al and S atoms were located, and their ADPs were anisotropically refined. Then the Li sites were located in the remainder electron density. Subsequently, the Li occupancies were freely refined, and only the ADPs of Li(1) and L(2) were anisotropically refined (**Table** 7.2). The structure model converged to a residual factor of 1.245 and residual electron density of 1.194 e·Å^{-3}. The three Li sites account for a Li content of only 3.11(2) f.u.(Li), where its large ADP (0.15(6)) hampers its accurate localization (**Table** 7.1). Rietveld refinement of $Li_{3.3}P_{0.85}Al_{0.15}S_4$ against TOF neutron diffraction was thus performed using the model initially derived from single crystal diffraction (**Figure** 7.4a inset). All the atomic positions as well as the Li SOFs were refined freely, while the P/Si ratio and ADPs were fixed to the values obtained by single crystal data (**Table** 7.1). An increase on the SOF of the Li(3) (*4c*) site from SOF=0.21(7) to SOF=0.44(4) is observed, and thus a total Li content of 3.33(2) f.u. (Li) is obtained (**Table** 7.4). This model was used to refine against PXRD data of x=0.15 as exhibited in **Figure** 7.4a, and neutron TOF and PXRD data of x=0.2 and x=0.33 in $Li_{3+2x}P_{1-x}Al_xS_4$ as shown in **Figures** 7.4b and 7.4c, respectively. **Figure** 7.4d shows the final crystal structure of $Li_{3.3}P_{0.85}Al_{0.15}S_4$ obtained from TOF neutron diffraction

data.

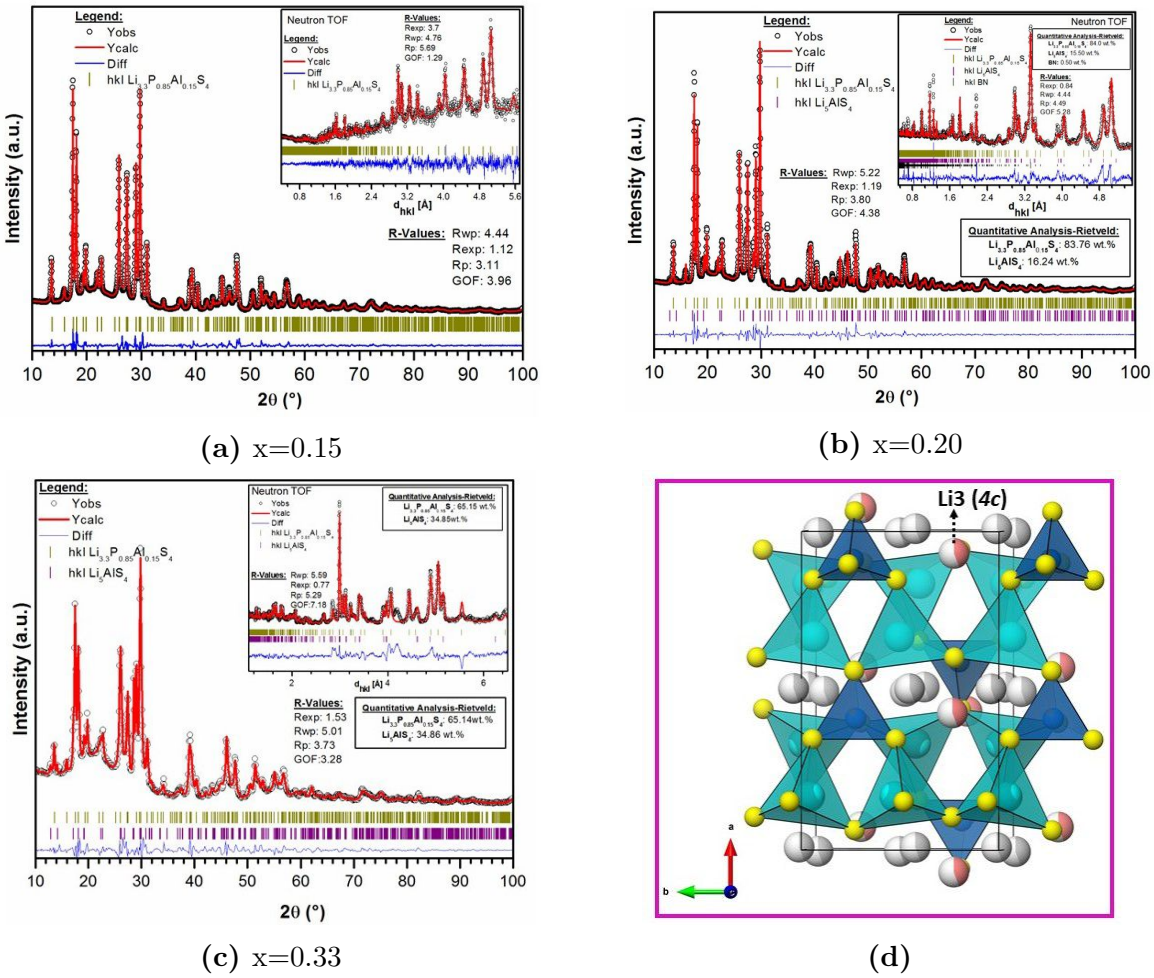

(a) x=0.15 **(b)** x=0.20

(c) x=0.33 **(d)**

Figure 7.4: Rietveld refinement fits of $Li_{3+2x}P_{1-x}Al_xS_4$ (Debye-Scherrer geometry) and TOF neutron diffraction pattern shown in the inset: **a.** x=0.15, olive vertical ticks correspond to $Li_{3.3}P_{0.85}Al_{0.15}S_4$ Bragg reflections; **b.** x=0.20, purple vertical ticks correspond to Li_5AlS_4, and black to BN impurity coming from the BN crucible; **c.** x=0.33. The black circles correspond to the data points, the red line denotes the calculated pattern and the difference map is shown in blue; **d.** View of the $Li_{3.3}P_{0.85}Al_{0.15}S_4$ structure along the [001] direction obtained from TOF neutron data.

Atom	Wyckoff site	x	y	z	SOF	U_{eq}/Å^2
P	*4c*	0.0881(5)	1/4	0.1616(10)	0.85	0.01454
Al	*4c*	0.0881(5)	1/4	0.1616(10)	0.15	0.01454
S1	*8d*	0.1555(7)	0.0399(10)	0.2656(17)	1	0.02484
S2	*4c*	0.4399(9)	1/4	0.236(2)	1	0.0191
S3	*4c*	0.0982(11)	1/4	0.828(2)	1	0.0250
Li1	*8d*	0.3360(14)	0.473(2)	0.383(3)	1	0.0452
Li2	*8d*	0.009(3)	0.062(4)	0.571(5)	0.44(3)	0.040
Li3	*4c*	0.383(7)	1/4	0.829(17)	0.45(4)	0.15

Table 7.4: Atomic coordinates, site occupation factors and equivalent isotropic displacement parameters of $Li_{3.33(2)}P_{0.85}Al_{0.15}S_4$ obtained from TOF neutron diffraction at 300°K. With lattice parameters a=12.9598(19) Å, b=8.0689(12) Å, c=6.1392(9) Å, and V=641.99(17) Å^3.

The attempted synthesis of the material with stoichiometry $Li_{11}AlP_2S_{12}$ or $Li_{3.67}P_{0.67}Al_{0.33}S_4$ resulted in a mixture of $Li_{3.3}P_{0.85}Al_{0.15}S_4$ (65.15 wt%), Li_5AlS_4 (34.8 wt%), and an unknown impurity (**Figure** 7.4c), indicating the greater thermodynamic stability of the $Li_{3.3}P_{0.85}Al_{0.15}S_4$ phase and the limited solubility of Al in this thio-LISICON structure. Indeed, the reported decomposition energy of $Li_{11}AlP_2S_{12}$ is relatively high, 60 meV/atm, whereas the $Li_{10}MP_2S_{12}$ with M= Ge, Sn and Si family have calculated decomposition energies of 25, 25 and 19 meV/atm, respectively [160].

$Li_{3.3}P_{0.85}Al_{0.15}S_4$ is found to be isostructural with the recently reported $Li_{3.15}Si_{0.15}P_{0.85}S_4$ material [155], and similar to that of the high-temperature phase β-Li_3PS_4 [148], but a different lithium environment as discussed below. In β-Li_3PS_4, the Li atoms occupy three distinct crystallographic Wyckoff sites *8d*, *4b* and *4c*. The *4b* position slightly shifts to form the octahedrally coordinated *8d* (Li(2)) site in the Al-substituted material, this *8d* (Li(2)) site is split into two positions due to symmetry with an equally fractional occupation of less than 50% -as reported for the $Li_{3.15}Si_{0.15}P_{0.85}S_4$ material [155]-. While the Li(3) (*4c*) position shifts from its original tetrahedral site in β-Li_3PS_4 to a distorted bipyramidal site in $Li_{3.15}Si_{0.15}P_{0.85}S_4$ material [155], it remains in the 4-fold coordination in $Li_{3.3}P_{0.85}Al_{0.15}S_4$ -albeit, with a large ADP (0.15(6))- (**Table** 7.1). A comparison between the unit cell parameters of $Li_{3.3}P_{0.85}Al_{0.15}S_4$ and β-Li_3PS_4 is shown in **Table** 7.5. The a and c parameters of the $Li_{3.3}P_{0.85}Al_{0.15}S_4$ increase while the b decreases significantly relative to the β-Li_3PS_4 phase; in accordance with the observed change in the Bragg reflections of the PXRD patterns shown in **Figure** 7.2a. Although, Al^{3+} is a larger cation than P^{5+} (0.39 Å versus 0.17 Å); the shrinkage in the b-axis results

in a smaller unit cell volume for the $Li_{3.3}P_{0.85}Al_{0.15}S_4$ structure.

Compound	a (Å)	b (Å)	c (Å)	V (Å^3)	Ref.
$Li_{3.3}P_{0.85}Al_{0.15}S_4$	12.9572(13)	8.0861(8)	6.1466(6)	644.00(11)	this work
β-Li_3PS_4	12.819(5)	8.2195(4)	6.1236(2)	645.23(5)	[148]

Table 7.5: Unit cell parameters of $Li_{3.3}P_{0.85}Al_{0.15}S_4$ obtained from single crystal XRD at 280 K and of β-Li_3PS_4 obtained at 364 K.

Table 7.6 shows the comparison of the volumes of the LiS_x (x=4 and 6) and $(P/Al)S_4$ polyhedra for $Li_{3.3}P_{0.85}Al_{0.15}S_4$ and β-Li_3PS_4 compounds [148]. A slightly larger volume of the $(P/Al)S_4$ tetrahedron for $Li_{3.3}P_{0.85}Al_{0.15}S_4$ phase is observed, providing evidence for Al incorporation into the unit cell. The volume of the fully occupied $Li(1)S_4$ tetrahedron is likewise larger in the Al-substituted material, whereas the volumes of $Li(2)S_6$ and $Li(3)S_4$ are smaller in both polyhedral. The split of the Li(2) (*8d*) position in $Li_{3.3}P_{0.85}Al_{0.15}S_4$ causes the reduction in the volume of the $Li(2)S_6$ polyhedra and a shorter Li(2)-Li(3) interatomic distance (2.14(9) Å versus 2.53(5) Å **Table** 7.3 and [148]), leading to the shrinkage in the *b*-axis of the unit cell (**Table** 7.5).

Compound	Li(1)S_4 (Å^3) Wyckoff site	Li(2)S_6 (Å^3) Wyckoff site	Li(3)S_4 (Å^3) Wyckoff site	(P/Al)S_4, PS_4(Å^3) Wyckoff site
$Li_{3.3}P_{0.85}Al_{0.15}S_4$	7.014 *8d*	26.146 *8d*	7.79 *4c*	4.37 *4c*
β-Li_3PS_4	6.86 *8d*	27.122 *4b*	8.35 *4c*	4.28 *4c*

Table 7.6: Volumes of the LiS_x (x=4 and 6) and $(P/Al)S_4$ polyhedra for $Li_{3.3}P_{0.85}Al_{0.15}S_4$ and β-Li_3PS_4 compounds. The values for x=0.15 were taken from the single crystal X-ray diffraction data using VESTA.

To further confirm the substitution of P for Al in the lattice, ^{31}P fast magic-angle spinning (MAS) Nuclear Magnetic Resonance (NMR) studies were performed by Dr. David Bazak on two different samples of $Li_{3.3}P_{0.85}Al_{0.15}S_4$. While ^{31}P MAS NMR spectra of Li_3PS_4 based materials typically exhibit signals at 86.5 ppm characteristic of isolated $[PS_4]^{3-}$ tetrahedra [161] [162], we observed a primary feature centered at ± 81.5 ppm in the spectrum of $Li_{3.3}P_{0.85}Al_{0.15}S_4$ (**Figure** D.1). We propose that the chemical shift (81.5 ppm versus 86.5 ppm) is a consequence of the observed unit cell shrinkage induced by the presence of the

Al-containing S_4 tetrahedra; confirming the substitution of P for Al in the lattice, in agreement with the obtained crystal structure solution. While a refinement of the P^{5+}/Al^{3+} fractional occupancies would unequivocally confirm the incorporation of Al^{3+} on the P^{5+} site, these two elements are indistinguishable *via* X-rays and a stable refinement of the occupancies and ADPs in the neutron diffraction data was not possible. However, the increasing polyhedral volume, lattice parameters, and the ^{31}P MAS NMR results suggest the successful site substitution.

Li_3PS_4 is the most thermodynamic form in the Li_2S-P_2S_5 system. When γ-Li_3PS_4 is heated to 195°C, it converts to the high-conductor phase β-Li_3PS_4. Since the latter is not stable at RT, its conductivity at 25°C was calculated by extrapolation of the Arrhenius plot from elevated temperature (8.93×10^{-4} mS·cm^{-1}) [60]. Attempts have been made by different groups to stabilize the β-Li_3PS_4 at RT [163] [164] [60], being successfully accomplished by the synthesis of a version of the β-Li_3PS_4, $Li_{3.15}Si_{0.15}P_{0.85}S_4$ [155]. Likewise, based on crystal structure solution of $Li_{3.3}P_{0.85}Al_{0.15}S_4$, Al substitution -0.15($2Li^+ + Al^{3+}$) for P^{5+}- has effectively stabilized a β-type phase at RT with a more disordered Li sublattice.

7.4 Ionic and electronic properties

The Nyquist plot of $Li_{3+2x}P_{1-x}Al_xS_4$ with x=0.15, 0.20 and 0.33 is presented in **Figure** 7.5 (fitted parameters are presented in **Table** 7.8). The obtained overall ionic conductivities of $Li_{3+2x}P_{1-x}Al_xS_4$ are very similar for all compositions as presented in **Table** 7.7 (**Table** D.2), with the highest ionic conductivity of 0.31±0.02 mS·cm^{-1} is achieved for x=0.33 -although showing a ∼34 wt% of the Li_5AlS_4 impurity phase (**Figure** 7.4c)-. A total conductivity of 0.22±0.17 mS·cm^{-1} was obtained for $Li_{3.3}P_{0.85}Al_{0.15}S_4$, which is significantly larger than those of $Li_{4.4}Al_{0.4}M_{0.6}S_4$ with M=Ge and Sn (0.043±0.09 mS·cm^{-1} and 0.0043±0.03 mS·cm^{-1}, respectively)[165], similar to that of the "nanoporous" β-Li_3PS_4 prepared by solution using tetrahydrofuran (0.16 mS·cm^{-1}) [60], but lower than that of $Li_{11}AlP_2S_{12}$ (0.8 mS·cm^{-1}) [149] and $Li_{3.15}Si_{0.15}P_{0.85}S_4$ (1.15 mS·cm^{-1}) [155]

Table 7.7: RT ionic conductivity values of $Li_{3+2x}P_{1-x}Al_xS_4$ with x=0.15, 0.20 and 0.33 taken from **Table** D.2.

Compound	σ mS· cm^{-1}
$\mathbf{Li_{3.3}P_{0.85}Al_{0.15}S_4}$	0.22±0.17
$\mathbf{Li_{3.4}P_{0.8}Al_{0.2}S_4}$	0.14±0.10
$\mathbf{Li_{3.67}P_{0.67}Al_{0.33}S_4}$	0.31±0.02

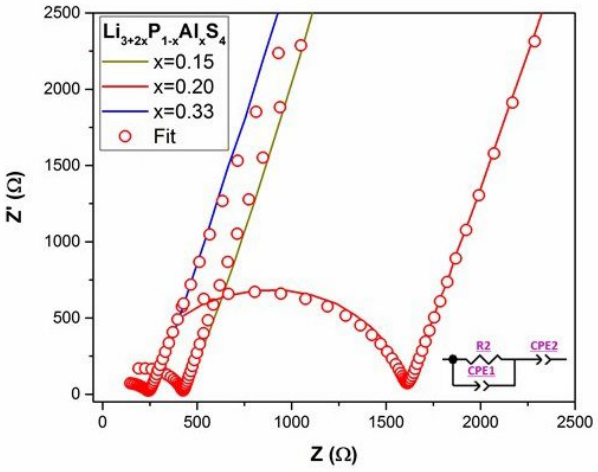

Figure 7.5: RT Nyquist impedance plot of $Li_{3+2x}P_{1-x}Al_xS_4$ with x=0.15, 0.20 and 0.33 with the respective equivalent circuit.

Compound	CPE_1 (F s^{a-1}) (10^{-9})	a_1	CPE_2 (F s^{a-1}) (10^{-6})	a_2	R_1 (Ω)
$\mathbf{Li_{3.3}P_{0.85}Al_{0.15}S_4}$	4.039	0.855	5.897	0.830	425.6
$\mathbf{Li_{3.4}P_{0.80}Al_{0.20}S_4}$	2.105	0.883	7.462	0.818	1609
$\mathbf{Li_{3.67}P_{0.67}Al_{0.33}S_4}$	0.138	0.657	7.947	0.812	249.4

Table 7.8: Parameters of the fit for the impedance data of $Li_{3+2x}P_{1-x}Al_xS_4$ with x=0.15, 0.20 and 0.33 at RT.

Figure 7.6a shows the linear dependence of the log$\sigma \cdot T$ versus $(1/T)$ following Arrhenius law for two different samples of $Li_{3.3}P_{0.85}Al_{0.15}S_4$. The activation barrier for Li^+-ion diffusion is 0.34±0.04 eV for x=0.15. A wide distribution in activation energy values is reported based on electrochemical experiments for β-Li_3PS_4: 0.16 eV [148], 0.32 eV [166], 0.36 eV [60], and 0.47 eV [167], while a lower activation energy for $Li_{11}AlP_2S_{12}$ was reported (0.25 eV) [149]. **Figure** 7.6b shows the DC polarization curve of $Li_{3.3}P_{0.85}Al_{0.15}S_4$ at three different voltages (0.25, 0.50 and 0.75 V). From a linear fit of DC voltage and stabilized current (**Figure** D.2), the DC electronic conductivity of $Li_{3.3}P_{0.85}Al_{0.15}S_4$ is estimated to be 2.26 x 10^{-5} mS·cm^{-1}, which are four orders of magnitude lower than its ionic conductivity.

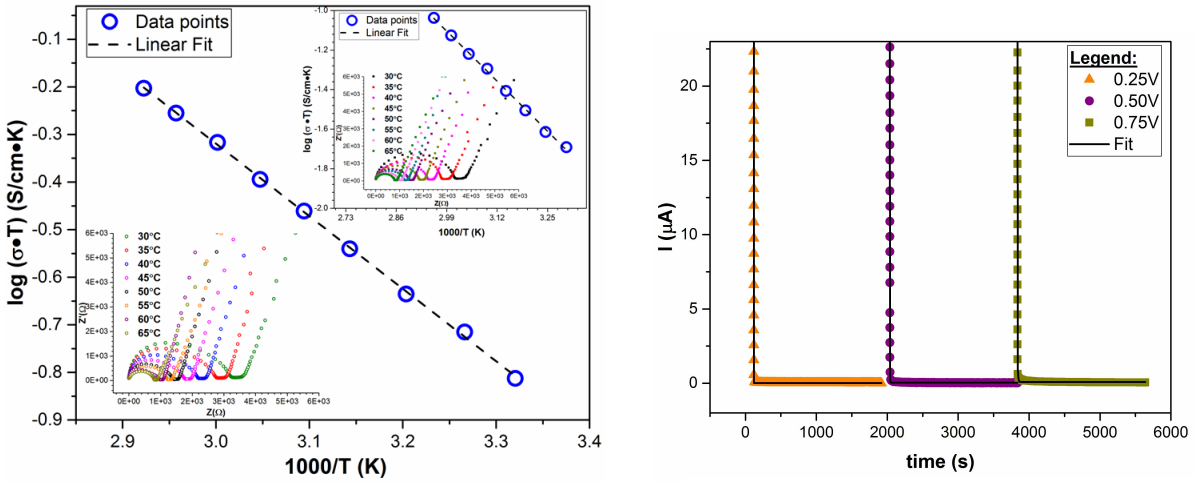

(a) (b)

Figure 7.6: a. Arrhenius conductivity plot of $Li_{3.3}P_{0.85}Al_{0.15}S_4$ from 30°C to 70°C. The top inset displays the Nyquist impedance plot from 30°C to 70°C. The low inset shows the Arrhenius conductivity plot of another sample for x=0.15 from 30°C to 65°C, with the inset showing the Nyquist impedance plot from 30°C to 65°C; **b.** DC polarization curves for electronic conductivity determination of $Li_{3.3}P_{0.85}Al_{0.15}S_4$ with an applied voltage of 0.25 (orange), 0.50 (purple), and 0.75 V (grey).

The conductivity of glass-ceramic materials strongly depends on the nature of the precipitated phases, their crystallinity and the heat-treatment conditions i.e. annealing.[168] [169]. The crystallization degree of $Li_{3.3}P_{0.85}Al_{0.15}S_4$ was estimated to be ∼91.7 wt%, using Si as an internal reference (**Figure** 7.7a and **Equation** 2.12), a SEM image of its morphology is shown in the inset of **Figure** 7.7a. In contrast, the targeted $Li_{3.67}P_{0.67}Al_{0.33}S_4$ ($Li_{11}P_2AlS_{12}$) exhibits a low crystallization degree with an amorphous content of ∼23.5 wt% (**Figure** 7.7b and **Equation** 2.12).

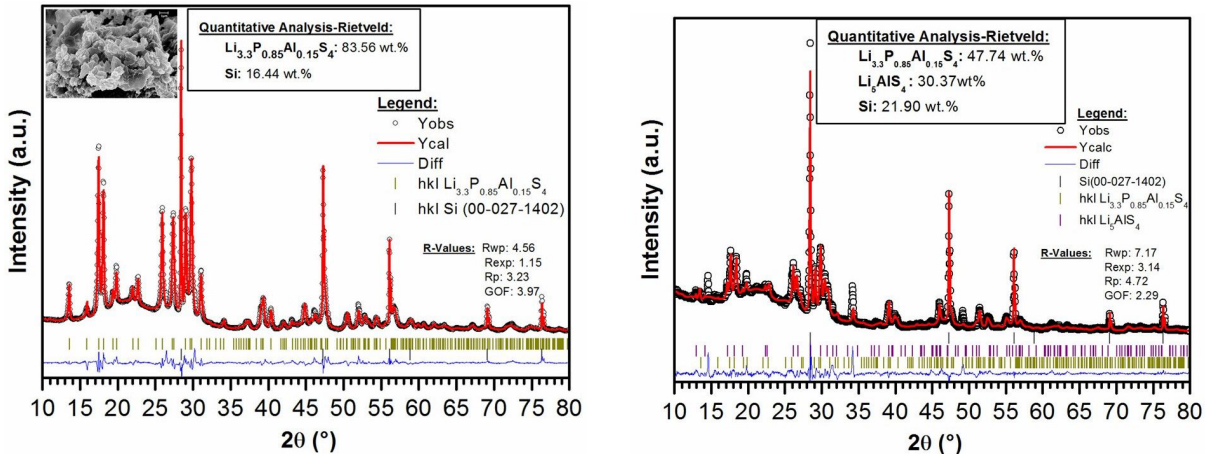

Figure 7.7: Rietveld refinement fits of **a.** $Li_{3.3}P_{0.85}Al_{0.15}S_4$ (8.3 wt% amorphous content) mixed with 12 - 13 wt% of Si, which was used as an internal standard; **b.** Targeted $Li_{3.67}P_{0.67}Al_{0.33}S_4$ mixed with 15 - 17 wt% of Si (Debye-Scherrer geometry).

The crystalline fraction varies within glass-ceramics and properties of these materials vary accordingly. Although, neither the percent crystallinity of $Li_{11}AlP_2S_{12}$ nor identification of the secondary phase, Li_5AlS_4, were reported by Jun Chen *at al.* [149]; the difference in $Li_{3.3}P_{0.85}Al_{0.15}S_4$ and $Li_{11}AlP_2S_{12}$ ionic conductivities, may be a result of the different fractions of crystalline, impurity and glassy phases due to the two distinct synthesis methods. The reported $Li_{11}AlP_2S_{12}$ was synthesized by mechanochemical route followed by a heat treatment at 500°C -when other temperatures were used (i.e., 400°C or 600°C) different phases were obtained (i.e., $Li_4P_2S_6$)- [149]; showing the sensitivity of $Li_{3.3}P_{0.85}Al_{0.15}S_4$ to sintering temperatures. In contrast, a high temperature solid-state approach was used for the $Li_{3.3}P_{0.85}Al_{0.15}S_4$ or $Li_{9.9}Al_{0.45}P_{2.55}S_{12}$ material.

The decrease in the ionic conductivity showed by the Al-substituted material vs Si-phase analogue (0.22 $mS{\cdot}cm^{-1}$ versus 1.15 $mS{\cdot}cm^{-1}$), may rely on the Li sublattice disorder observed in $Li_{3.15}Si_{0.15}P_{0.85}S_4$ [155]. The additional Li content in $Li_{3.3}P_{0.85}Al_{0.15}S_4$ ($0.15(2Li^+ + Al^{3+})$ versus $0.15(Li^+ + Si^{4+})$ for P^{5+}) increases the occupancy in the Li(1) (8d) site (SOF=97% (Si) versus SOF=100% (Al) and Li(3) (*4c*) site (SOF=28% (Si) versus SOF=44% (Al)) [155], reducing their Li vacancy populations. The inherent configurational disorder -partial site occupation or site disorder- and large number of lithium vacancies in the Li sublattice (∼35%) of $Li_{3.15}Si_{0.15}P_{0.85}S_4$ likely leads to its higher ionic conductivity.

Possible lithium pathways in $Li_{3.3}P_{0.85}Al_{0.15}S_4$ were examined using the BVSE approach.

Analysis of the [001] direction of the BVSE map reveals a lithium diffusion pathway in the form of a zigzag chain along the *b*-axis, which is formed by Li(2)-Li(2)-Li(3)-Li(2)-Li(2) sites or *8d*(O)-*8d*(O)-*4c*(T)-*8d*(O)-*8d*(O) Wyckoff sites (T(tetrahedral), (O(octahedral)) with a distance between Li(3)-Li(1) and Li(2)-Li(2) jumps of 2.14(9) Å and 0.97(3) Å (**Table** 7.3), respectively (**Figure** 7.8). Likewise, the Li-ion diffusion along the *b*-axis in β-Li_3PS_4 has been indicated by computational studies. The closest Li^+-Li^+ jump distance in β-Li_3PS_4 is 2.52(4) Å [148]; the shorter Li^+-Li^+ jump distance observed in $Li_{3.3}P_{0.85}Al_{0.15}S_4$ (0.97(3) Å) counts for its higher ionic conductivity when compared to bulk β-Li_3PS_4 (0.22 mS·cm^{-1} versus 8.93 x 10^{-4} mS·cm^{-1} [60]).

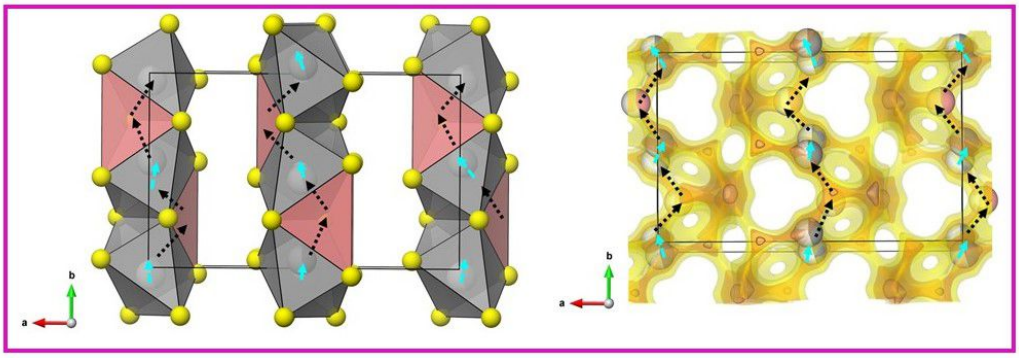

(a)

Figure 7.8: View of the structure of $Li_{3.3}P_{0.85}Al_{0.15}S_4$ along the [001] direction, and bond valence map of Li^+ ion migration pathways visualized as isosurfaces of constant bond valence site energy. The orange isosurface corresponds to a site energy characteristic of local hopping paths, while the yellow range isosurface corresponds to the long-range migration.

BVSE attempts to predict the energetic environment of Li^+-ions were carried out. **Figures** 2.13shows the BVSE models of migration barriers for Li-ion diffusion pathways along the *b* in $Li_{3.3}P_{0.85}Al_{0.15}S_4$, respectively. The average activation energy barrier for $Li_{3.3}P_{0.85}Al_{0.15}S_4$ along the *b*-axis formed by Li(2) - Li(2) - Li(3) sites is lower than the reported values for nanoporous β-Li_3PS_4 ($\sim$0.45 eV) [155], likely from the splitting of the Li(2) site in the Al-substituted material resulting in a change in the energy landscape, and similar for $Li_{3.25}Si_{0.25}P_{0.75}S_4$ ($\sim$0.375 eV) [155]. The BVSE calculations indicate that for Li-ion diffusion in $Li_{3.3}P_{0.85}Al_{0.15}S_4$ takes place along the *b*-axis, in contrast to $Li_{3.25}Si_{0.25}P_{0.75}S_4$ where Li-ion diffusion takes place both along the *b*-axis and in the

a,c-plane because not only Li(2) site is split, but also Li(1) and Li(3) sites, giving rise to a high conductivity of 1.22 mS·cm^{-1} [155].

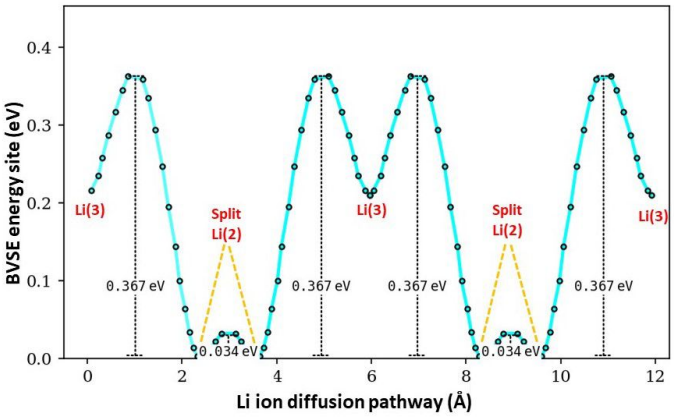

Figure 7.9: BVSE models of migration barriers of $Li_{3.3}P_{0.85}Al_{0.15}S_4$ along; **a.** b-axis. The Li(2) split site energies are referenced to zero as the lowest energy which is a relative, not absolute value.

7.5 Summary

The solid solution between Al and P in $Li_{3+2x}P_{1-x}Al_xS_4$ is formed within a narrow concentration range, where the limit of Al solubility is reached at about x=0.15. Al substitution -0.15($2Li^+ + Al^{3+}$) for P^{5+}- has effectively stabilized a version of the bulk β-Li_3PS_4 at RT.

$Li_{3.3}P_{0.85}Al_{0.15}S_4$ shows a higher RT ionic conductivity when compared to that of bulk β-Li_3PS_4 (0.22 mS·cm^{-1} vs 8.93 $\times$ 10^{-4} mS·cm^{-1}). The shorter Li^+-Li^+ jump distance observed in $Li_{3.3}P_{0.85}Al_{0.15}S_4$ (1.99(17) Å vs 2.52(4) Å) -caused by the splitting of the Li(2) site- counts for its higher ionic conductivity when compared to bulk β-Li_3PS_4.

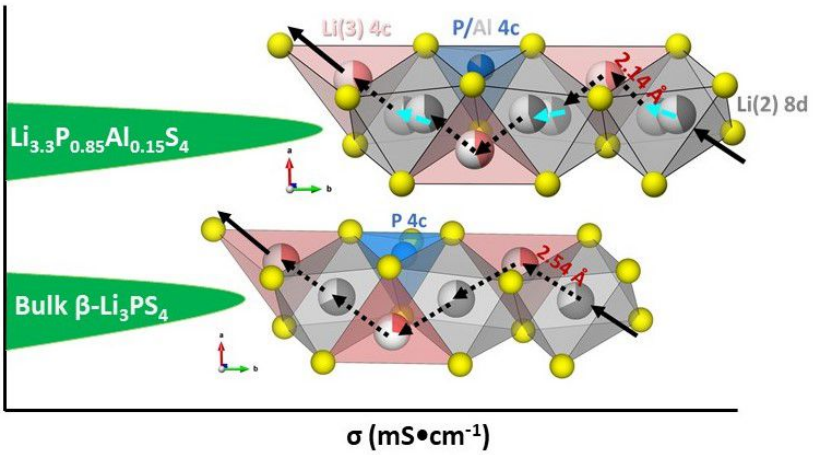

Figure 7.10: Schematic diagram showing the higher ionic conductivity of $Li_{3.3}P_{0.85}Al_{0.15}S_4$ vs. bulk β-Li_3PS_4. View of the Li^+-ion diffusion pathway along the b-axis for each phase.

Chapter 8

Final Thoughts

Research on battery materials has become the centre stage as one of the key technologies for the electrification of the transport sector and storage of intermittently produced energy. ASSB technology is a promising emerging alternative for next-generation energy storage; the main proposed benefit of their applicability is the increased safety, which stems from the absence of flammable liquid electrolytes normally used in LIBs [23]. Inorganic solid electrolytes are the most essential component for ASSBs, fundamental understanding of their properties is thus relevant to their integration in ASSBs.

The research presented throughout this thesis underlines the interplay of structure-property in new sodium and lithium conductors i.e., $Na_{11}Sn_2PnQ_{12}$ with Pn=Sb and S; Q=S and Se, $Li_{4.29}P_{0.71}Si_{0.29}S_4I$, and $Li_{3.3}P_{0.85}Al_{0.15}S_4$. The presented detailed structure analysis of these fast-ion conductors by a combination of single crystal and PXRD data contribute to a better understanding of the subtle factors governing ion transport mechanism in SEs. The findings obtained in the present work can be fruitful to guide new materials discovery as well as promising strategies towards enhancements in ion conductivity.

This work showed different synthesis methods and their associated processing conditions that yielded new SE materials with different properties such as composition, structure, purity and electrical conductivity. Although it is not straightforward to design synthesis protocols to find the most conducting compositions -most of the fastest SEs are often found by trial and error-, a long mixing time (40 min) and a fast cooling rate ($2°C{\cdot}min^{-1}$) were successful in enhancing the ionic conductivity of the $Na_{11}Sn_2PS_{12}$ phase. The former parameter was adopted to obtain a homogeneous mixture and smaller particle size; factors that can increase the reactivity of the powders, improving the reaction kinetics, and the later to avoid the formation of impurity phases (Na_3PS_4).

Even though Sb substitution in $Na_{11}Sn_2PnS_{12}$ with Pn=Sb and P led to a structure with a lager lattice volume and bottleneck size for Na-ion diffusion -qualitative descriptors that contribute to improve σ_i-, it exhibited lower ionic transport than the P-phase. The seemingly counterintuitive combination of a larger unit cell and a lower ionic conductivity is caused by different contributions of the two sublattices to the overall conductivity. The subtle interplay between stronger Coulombic attractions between Na^+-ions and the immobile framework, and the distribution of Na atoms in the mobile sublattice dictates ion conductivity in this new class of ion conductors. Therefore, the qualitative descriptor that a larger lattice and bottleneck size lead to higher ionic conductivites needs to be applied with caution among different structural families.

Structural tunning by isovalent substitution to increase the ionic conductivity of the Sb-phase in $Na_{11}Sn_2SbQ_{12}$ with Q=S and Se showed that the ion migration across the grain boundaries thus becomes the rate-determining step in the glass-ceramic $Na_{11}Sn_2SbSe_{12}$ material. The grain and grain boundary impedances showed that the later has a major contribution to its overall conductivity. Formation of low conductive impurity phases at the grain boundary causes a large resistive barrier hindering ion migration across interfaces.

The work conducted on $Li_{4+x}P_{1-x}Si_xS_4I$ with x=0, 0.12, 0.29 and 0.40 showed that aliovalent substitution (Si^{4+} for P^{5+}) can lead to structural changes and Li site configurational disorder, which can induce a lower activation energy for mobile Li ions. A similar number of mobile Li-ions and mobile vacancies in the framework is a condition for achieving maximal configurational entropy where the ionic conductivity is maximum, as observed in $Li_{4.29}P_{0.71}Si_{0.29}S_4I$. Aliovalent substitution can thus be a promising approach of highly disordered Li sublattices in the development of ionic conductivity enhancement strategies.

The full structure solution of $Li_{3.3}P_{0.85}Al_{0.15}S_4$ via single crystal methods that elucidate site occupancies and atomic displacement parameters with much greater reliability than powder methods, shed light on the predicted via first principle calculations and later synthesized, $Li_{11}AlP_2S_{12}$, by elucidating the greater thermodynamic stability of the $Li_{9.9}Al_{0.45}P_{2.55}S_{12}$ phase and the limited solubility of Al in this thio-LISICON structure.

Future work in this area must focus on enhancing ionic conductivity of the herein developed SEs by: (1) synthesizing more pure materials, (2) isovalent and/or aliovalent substitution, and (3) reducing grain boundary resistance by hot pressing approach. As it has been stated throughout this thesis, the aim of inorganic solid electrolyte studies is the successful integration of SEs in ASSBs; thus, Na/Li metal stability studies of the $Na_{11}Sn_2PnQ_{12}$ with Pn=Sb and S; Q=S and Se, $Li_{4.29}P_{0.71}Si_{0.29}S_4I$, and $Li_{3.3}P_{0.85}Al_{0.15}S_4$ ion conductors must be carried out in order to determine their applicability in ASSB technology.

References

[1] K. Bithas and P. Kalimeris. *Revisiting the Energy-Development Link: Evidence from the 20th Century for Knowledge-based and Developing Economies*. Springer, 2015.

[2] I. Bozkurt. Energy Resources and Their Effects on Environment. *Wseas transactions on Environment and development*, 6:8, 2010.

[3] Y. S. Mohammed, W. M. Mustafa, and B. Nouruddeen. Energy storage systems for renewable energy power sector integration and mitigation of intermittency. *Renewable and Sustainable Energy Reviews*, 35:499–514, 2014.

[4] S. Sorrell. Reducing energy demand: A review of issues, challenges and approaches. *Renewable and Sustainable Energy Reviews*, 47:74–82, 2015.

[5] P. A. Owusu and S. Asumadu-Sarkodie. A review of renewable energy sources, sustainability issues and climate change mitigation. *Cogent Engineering*, 3:1167990, 2016.

[6] A. K. Akella, R. P. Saini, and M. P. Sharma. Social, economical and environmental impacts of renewable energy systems. *Renewable Energy*, 34:390–396, 2009.

[7] I. Dincer. Renewable energy and sustainable development: a crucial review. *Renewable and Sustainable Energy Reviews*, 4:157–175, 2000.

[8] S. A. Kalogirou. Solar thermal collectors and applications. *Progress in Energy and Combustion Science*, 30:231–295, 2004.

[9] O. Ellabban, H. Abu-Rub, and F. Blaabjerg. Renewable energy resources: Current status, future prospects and their enabling technology. *Renewable and Sustainable Energy Reviews*, 39:748–764, 2014.

[10] T. Placke, R. Kloepsch, S. Dühnen, and M. Winter. Lithium ion, lithium metal, and alternative rechargeable battery technologies: The odyssey for high energy density. *Journal of Solid State Electrochemistry*, 21:1939–1964, 2017.

[11] International Electrotechnical Commission. Electrical energy storage. *IEC Market Strategy Board, Geneva, Switzerland*, 2011.

[12] *Advanced Energy Storage Technologies*. https://energystorage.org/why-energy-storage/technologies/.

[13] C. Gang. *Politics of Renewable Energy in China*. Edward Elgar Publishing, 2019.

[14] N. J. J. de Klerk and M. Wagemaker. Space-charge layers in all-solid-state batteries; important or negligible?. *ACS applied energy materials*, 1:5609–5618, 2018.

[15] A. Soret, M. Guevara, and J. M. Baldasano. The potential impacts of electric vehicles on air quality in the urban areas of Barcelona and Madrid (Spain). *Atmospheric Environment*, 99:51–63, 2014.

[16] A. L. Robinson and J. Janek. Solid-state batteries enter EV fray. *MRS Bulletin*, 39:1046–1047, 2014.

[17] K. Funke. Solid state ionics: from michael faraday to green energy—the european dimension. *Science and technology of advanced materials*, 14:043502, 2013.

[18] L. Pietronero and S. Strässler. *Toward a Theory of Superionic Conductors*. Springer US, 1978.

[19] D. Ouyang, M. Chen, Q. Huang, J. Weng, Z. Wang, and J. Wang. A review on the thermal hazards of the lithium-ion battery and the corresponding countermeasures. *Applied Sciences*, 9:2483, 2019.

[20] M. Agostini, Y. Aihara, T. Yamada, B. Scrosati, and J. Hassoun. A lithium-sulfur battery using a solid, glass-type P_2S_5—Li_2S electrolyte. *Solid State Ionics*, 244:48–51, 2013.

[21] J. Janek and W. G. Zeier. A solid future for battery development. *Nature Energy*, 1:4, 2016.

[22] S. Xin, Y. You, S. Wang, H. C. Gao, Y. X. Yin, and Y. G. Guo. Solid-state lithium metal batteries promoted by nanotechnology: progress and prospects. *ACS Energy Letters*, 2:1385–1394, 2017.

[23] T. Famprikis, P. Canepa, J. A. Dawson, I. M. Saiful, and C. Masquelier. Fundamentals of inorganic solid-state electrolytes for batteries. *Nature materials*, 18:1278–1291, 2019.

[24] M. Tatsumisago, M. Nagao, and A. Hayashi. Recent development of sulfide solid electrolytes and interfacial modification for all-solid-state rechargeable lithium batteries. *Journal of Asian Ceramic Societies*, 1:17–25, 2013.

[25] J. Kasemchainan and P. G. Bruce. All-Solid-State Batteries and their Remaining Challenges. *Johnson Matthey Technology Review*, 62:3, 2018.

[26] N. J. Taylor and J. Sakamoto. Unlocking lithium's potential with ceramic solid electrolytes. *American Ceramic Society Bulletin*, 98:6, 2019.

[27] Y. S. Hu. Batteries: getting solid. *Nature Energy*, 1:1–2, 2016.

[28] Y. Kato, R. Saito, M. Sakano, A. Mitsui, M. Hirayama, and R. Kanno. Synthesis, structure and lithium ionic conductivity of solid solutions of $Li_{10}(Ge_{1-x}M_x)P_2S_{12}$ (M = Si, Sn). *Journal of Power Sources*, 271:60–64, 2014.

[29] N. J. J. de Klerk and M. Wagemaker. Diffusion Mechanism of the Sodium-Ion Solid Electrolyte Na_3PS_4 and Potential Improvements of Halogen Doping. *Chemistry of Materials*, 28(9):3122–3130, 2016.

[30] C. Yu, S. Ganapathy, E. R. H. van Eck, H. Wang, S. Basak, Z. Li, and M. Wagemaker. Accessing the bottleneck in all-solid state batteries, lithium-ion transport over the solid-electrolyte-electrode interface. *Nature Communications*, 8:1–9, 2017.

[31] M. Du, K. Liao, Q. Lu, and Z. Shao. Recent advances in the interface engineering of solid-state Li-ion batteries with artificial buffer layers: Challenges, materials, construction, and characterization. *Energy & Environmental Science*, 12:1780–1804, 2019.

[32] C. Zhou, S. Bag, and V. Thangadurai. Engineering Materials for Progressive All-Solid-State Na Batteries. *ACS Energy Letters*, 3:2181–2198, 2018.

[33] F. P. McGrogan, T. Swamy, S. R. Bishop, E. Eggleton, L. Porz, X. Chen, Y. M. Chiang, and K. J. Van Vliet. Compliant yet brittle mechanical behavior of Li_2S-P_2S_5 lithium-ion-conducting solid electrolyte. *Advanced Energy Materials*, 7:1602011, 2017.

[34] Z. Jiang, Q. Han, S. Wang, and H. Wang. Reducing the interfacial resistance in all-solid-state lithium batteries based on oxide ceramic electrolytes. *ChemElectroChem*, 6:2970–2983, 2019.

[35] J. C. Bachman, S. Muy, A. Grimaud, H. H. Chang, N. Pour, S. F. Lux, O. Paschos, F. Maglia, S. Lupart, P. Lamp, L. Giordano, and Y. Shao-Horn. Inorganic Solid-State Electrolytes for Lithium Batteries: Mechanisms and Properties Governing Ion Conduction. *Chemical Reviews*, 116:140–162, 2015.

[36] E. Umeshbabu, B. Zheng, and Y. Yang. Recent progress in all-solid-state LithiumSulfur batteries using high li-ion conductive solid electrolytes. *Electrochemical Energy Reviews*, 2:31, 2019.

[37] J. J. Kim, K. Yoon, I. Park, and K. Kang. Progress in the Development of Sodium-Ion Solid Electrolytes. *Small Methods*, 1:1700219, 2017.

[38] P. Padma Kumar and S. Yashonath. Ionic conduction in the solid state. *Journal of Chemical Sciences*, 118(1):135–154, 2006.

[39] Y. Chuang, L. Yong, M. Willans, Z. Yang, K. R. Adair, Z. Feipeng, L. Weihan, D. Sixu, L. Jianwen, N. B. Mohammad, L. Ruying, H. Huan, Z. Li, Y. Rong, L. Shigang, H. Yining, and S. Xueliang. Superionic conductivity in lithium argyrodite solid-state electrolyte by controlled cl-doping. *Nano Energy*, 69:104396, 2020.

[40] M. Wu, B. Xu, and C. Ouyang. Physics of electron and lithium-ion transport in electrode materials for Li-ion batteries. *Chinese Physics B*, 25:018206, 2016.

[41] X. He, Y. Zhu, and Y. Mo. Origin of fast ion diffusion in super-ionic conductors. *Nature Communications*, 8:15893, 2017.

[42] W. D. Richards, T. Tsujimura, L. J. Miara, Y. Wang, J. C. Kim, S. P. Ong, I. Uechi, N. Suzuki, and G. Ceder. Design and synthesis of the superionic conductor $Na_{10}SnP_2S_{12}$. *Nature Communications*, 7:11009, 2016.

[43] A. Hayashi, A. Sakuda, and M. Tatsumisago. Development of sulfide solid electrolytes and interface formation processes for bulk-type all-solid-state li and na batteries. *Frontiers in Energy Research*, 4:25, 2016.

[44] T. Ohtomo, A. Hayashi, M. Tatsumisago, Y. Tsuchida, S. Hama, and K. Kawamoto. All-solid-state lithium secondary batteries using the $75Li_2S \cdot 25P_2S_5$ glass and the $70Li_2S \cdot 30P_2S_5$ glass–ceramic as solid electrolytes. *Journal of Power Sources*, 233:231–235, 2013.

[45] A. Hayashi, K. Noi, A. Sakuda, and M. Tatsumisago. Superionic glass-ceramic electrolytes for room-temperature rechargeable sodium batteries. *Nature Communications*, 3:856, 2012.

[46] T. Uemura, K. Goto, M. Ogawa, and K. Harada. All-solid secondary batteries with sulfide-based thin film electrolytes. *Journal of Power Sources*, 240:510–514, 2013.

[47] K. H. Park, Q. Bai, D. H. Kim, D. Y. Oh, Y. Zhu, M. Yifei, and Y. S. Jung. Design strategies, practical considerations, and new solution processes of sulfide solid electrolytes for all-solid-state batteries. *Advanced Energy Materials*, 8:1800035, 2018.

[48] C. Sun, J. Liu, Y. Gong, D. P. Wilkinson, and J. Zhang. Recent advances in all-solid-state rechargeable lithium batteries. *Nano Energy*, 33:363–386, 2017.

[49] J. A. S. Oh, L. He, A. Plewa, M. Morita, Y. Zhao, T. Sakamoto, X. Song, W. Zhai, K. Zeng, and L. Lu. Composite NASICON ($Na_3Zr_2Si_2PO_{12}$) solid-state electrolyte with enhanced na+ ionic conductivity: Effect of liquid phase sintering. *ACS applied materials & interfaces*, 11:40125–40133, 2019.

[50] M. Jansen and U. Henseler. Synthesis, structure determination, and ionic conductivity of sodium tetrathiophosphate. *Journal of Solid State Chemistry*, 99(1):110–119, 1992.

[51] N. Tanibata, K. Noi, A. Hayashi, and M. Tatsumisago. Preparation and characterization of highly sodium ion conducting Na_3PS_4—Na_4SiS_4 solid electrolytes. *RSC Advances*, 4:17120–17123, 2014.

[52] Z. Zhu, I.-H. Chu, Z. Deng, and S. P. Ong. Role of Na^+ Interstitials and Dopants in Enhancing the Na^+ Conductivity of the Cubic Na_3PS_4 Superionic Conductor. *Chemistry of Materials*, 27:8318–8325, 2015.

[53] Z. Yu, S. L. Shang, J. H. Seo, D. Wang, X. Luo, Q. Huang, S. Chen, J. Lu, X. Li, Z. K. Liu, and D. Wang. Exceptionally High Ionic Conductivity in $Na_3P_{0.62}As_{0.38}S_4$ with Improved Moisture Stability for Solid-State Sodium-Ion Batteries. *Advanced Materials*, 29(16):1605561, 2017.

[54] L. Zhang, K. Yang, J. Mi, L. Lu, L. Zhao, L. Wang, Y. Li, and H. Zeng. Na_3PSe_4: A Novel Chalcogenide Solid Electrolyte with High Ionic Conductivity. *Advanced Energy Materials*, 5:1501294, 2015.

[55] A. Banerjee, K. H. Park, J. W. Heo, Y. J. Nam, C. K. Moon, S. M. Oh, S. T. Hong, and Y. S. Jung. Na_3SbS_4 : A Solution Processable Sodium Superionic Conductor for All-Solid-State Sodium-Ion Batteries. *Angewandte Chemie*, 128:9786–9790, 2016.

[56] N. Wang, K. Yang, L. Zhang, X. Yan, L. Wang, and B. Xu. Improvement in ion transport in Na_3PSe_4—Na_3SbSe_4 by Sb substitution. *Journal of Materials Science*, 53:1987–1994, 2018.

[57] Z. Zhang, Y. Shao, B. Lotsch, Y. S. Hu, H. Li, J. Janek, L. F. Nazar, C. W. Nan, J. Maier, M. Armand, and L. Chen. New horizons for inorganic solid state ion conductors. *Energy & Environmental Science*, 11:1945–1976, 2018.

[58] R. Kanno, T. Hata, Y. Kawamoto, and M. Irie. Synthesis of a new lithium ionic conductor, thio-LISICON-Lithium germanium sulfide system. *Solid State Ionics*, 130:97–104, 2000.

[59] M. Murayama, R. Kanno, M. Irie, S. Ito, T. Hata, N. Sonoyama, and Y. Kawamoto. Synthesis of new lithium ionic conductor thio-lisicon—lithium silicon sulfides system. *Journal of Solid State Chemistry*, 168:140–148, 2002.

[60] W. Liu, Z.and Fu, E. A. Payzant, X. Yu, Z. Wu, N. J. Dudney, J. Kiggans, K. Hong, A. J. Rondinone, and C. Liang. Anomalous high ionic conductivity of nanoporous β-Li_3PS_4. *Journal of the American Chemical Society*, 135:975–978, 2013.

[61] M. Tachez, J. P. Malugani, R. Mercier, and G. Robert. Ionic conductivity of and phase transition in lithium thiophosphate Li_3PS_4. *Solid State Ionics*, 14:181–185, 1984.

[62] R. Kanno and M. Murayama. Lithium ionic conductor thio-LISICON: The Li_2S-GeS_2-P_2S_5 system. *Journal of the electrochemical society*, 148:A742–A746, 2001.

[63] Z. Liu, F. Huang, J. Yang, B. Wang, and J. Sun. New lithium ion conductor, thio-LISICON lithium zirconium sulfide system. *Solid State Ionics*, 179:1714–1716, 2008.

[64] B. T. Ahn and R. A. Huggins. Synthesis and lithium conductivities of Li_2SiS_3 and Li_4SiS_4. *Materials research bulletin*, 24:889–897, 1989.

[65] C. Dietrich, M. Sadowski, S. Sicolo, D. A. Weber, S. J. Sedlmaier, K. S. Weldert, S. Indris, K. Albe, J. Janek, and W. G. Zeier. Local structural investigations, defect formation, and ionic conductivity of the lithium ionic conductor $Li_4P_2S_6$. *Chemistry of Materials*, 28:8764–8773, 2016.

[66] H. Yamane, M. Shibata, Y. Shimane, T. Junke, Y. Seino, S. Adams, K. Minami, A. Hayashi, and M. Tatsumisago. Crystal structure of a superionic conductor, $Li_7P_3S_{11}$. *Solid State Ionics*, 178:1163–1167, 2007.

[67] T. Kaib, S. Haddadpour, M. Kapitein, P. Bron, A. Schroder, T. Eckert, B. Roling, and S. Dehnen. New lithium chalcogenidotetrelates, licht: synthesis and characterization of the Li^+-conducting tetralithium ortho-sulfidostannate Li_4SnS_4. *Chemistry of Materials*, 24:2211–2219, 2012.

[68] N. Kamaya, K. Homma, Y. Yamakawa, M. Hirayama, R. Kanno, M. Yonemura, T. Kamiyama, Y. Kato, S. Hama, K. Kawamoto, and M. Akio. A lithium superionic conductor. *Nature materials*, 10:682, 2011.

[69] P. Bron, S. Johansson, K. Zick, J. Schmedt auf der Günne, S. Dehnen, and B. Roling. $Li_{10}SnP_2S_{12}$: An Affordable Lithium Superionic Conductor. *Journal of the American Chemical Society*, 135:15694–15697, 2013.

[70] J. M. Whiteley, J. H. Woo, E. Hu, K.W. Nam, and S. H. Lee. Empowering the lithium metal battery through a silicon-based superionic conductor. *Journal of the Electrochemical Society*, 161:A1812–A1817, 2014.

[71] Y. Kato, S. Hori, T. Saito, K. Suzuki, M. Hirayama, A. Mitsui, M. Yonemura, H. Iba, and R. Kanno. High-power all-solid-state batteries using sulfide superionic conductors. *Nature Energy*, 1:16030, 2016.

[72] A. Kuhn, J. Köhler, and B. V. Lotsch. Single-crystal X-ray structure analysis of the superionic conductor $Li_{10}GeP_2S_{12}$. *Physical Chemistry Chemical Physics*, 15:11620–11622, 2013.

[73] Q. Pan, P. Guo, J. Duan, Q. Cheng, and H. Li. Comparative crystal structure determination of griseofulvin: Powder X-ray diffraction versus single-crystal X-ray diffraction. *Chinese Science Bulletin*, 57:3867–3871, 2012.

[74] K. M. Harris, M. Tremayne, and B. M. Kariuki. Contemporary advances in the use of powder x-ray diffraction for structure determination. *Angewandte Chemie International Edition*, 40:1626–1651, 2001.

[75] B. Fultz and J. M. Howe. *Diffraction and the X-Ray Powder Diffractometer*. Springer Berlin Heidelberg, Berlin, Heidelberg, 2001.

[76] Y. Liao. *Practical Electron Microscopy and Database*. Global Sino, 2006.

[77] A. R. West. *Solid state chemistry and its applications*. John Wiley & Sons, 2014.

[78] V. K. Pecharsky and P. Y. Zavalij. *Fundamentals of Powder Diffraction and Structural Characterization of Materials*. Springer, 2005.

[79] B. L. Dutrow and C. M. Clark. X-ray powder diffraction (XRD). *Geochemical Instrumentation and Analysis*, 2012.

[80] K. Hasegawa. Introduction to single crystal X-ray analysis. *The Rigaku Journal*, 28(1):14–18, 2012.

[81] S. Adams and R. P. Rao. *Understanding Ionic Conduction and Energy Storage Materials with Bond-Valence-Based Methods*. Springer Berlin Heidelberg, 2014.

[82] S. Adams and R. P. Rao. High power lithium ion battery materials by computational design. *physica status solidi (a)*, 208:1746–1753, 2011.

[83] D. Abou-Ras, T. Kirchartz, and U. Rau. *Advanced characterization techniques for thin film solar cells*. John Wiley & Sons, 2016.

[84] H. M. Rietveld. A profile refinement method for nuclear and magnetic structures. *Journal of Applied Crystallography*, 2(2):65–71, 1969.

[85] H. M. Rietveld. The crystal structure of some alkaline earth metal uranates of the type M3UO6. *Acta Crystallographica*, 20(4):508–513, 1966.

[86] R. E. Dinnebier and S. J. L. Billinge. *Powder Diffraction: Theory and Practice*. Royal Society of Chemistry, 2008.

[87] S. Kahraman and M. Alber. Electrical impedance spectroscopy measurements to estimate the uniaxial compressive strength of a fault breccia. *Bulletin of Materials Science*, 37:1543–1550, 2014.

[88] P. Vanysek. Introduction to electrochemical impedance. Technical report, Calgary Univ. Alberta, Dept. of Chemistry, 1994.

[89] D. C Sinclair. Characterization of Electro-materials using ac Impedance Spectroscopy. *Bol. Soc. Esp. Ceram. Vidrio*, 34:12, 1995.

[90] J. R. Macdonald and W. B. Johnson. *Fundamentals of Impedance Spectroscopy*. John Wiley & Sons, Ltd, 2018.

[91] J. R. Macdonald and E. Barsoukov. Impedance spectroscopy: theory, experiment, and applications. *History*, 1:1–13, 2005.

[92] J. R. Macdonald. Impedance spectroscopy and its use in analyzing the steady-state AC response of solid and liquid electrolytes. *Journal of Electroanalytical Chemistry and Interfacial Electrochemistry*, 223:25–50, 2010.

[93] S. Lunghammer, Q. Ma, D. Rettenwander, I. Hanzu, F. Tietz, and H. Wilkening. Bulk and grain-boundary ionic conductivity in sodium zirconophosphosilicate $Na_3Zr_2(SiO_4)_2PO_4$ (NASICON). *Chemical Physics Letters*, 701:147–150, 2018.

[94] H. Fricke. XXXIII. The theory of electrolytic polarization. *The London, Edinburgh, and Dublin Philosophical Magazine and Journal of Science*, 14:310–318, 1932.

[95] S. M. Haile, D. L. West, and J. Campbell. The role of microstructure and processing on the proton conducting properties of gadolinium-doped barium cerate. *Journal of Materials Research*, 13:1576–1595, 1998.

[96] S. Dhillon and R. Kant. Theory for electrochemical impedance spectroscopy of heterogeneous electrode with distributed capacitance and charge transfer resistance. *Journal of Chemical Sciences*, 129:1277–1292, 2017.

[97] M. E. Brown. *Introduction to thermal analysis: techniques and applications*, volume 1. Springer Science & Business Media, 2001.

[98] K. V. Kodre, S. R. Attarde, P. R. Yendhe, R. Y. Patil, and V. U. Barge. Differential scanning calorimetry: A review. *Research and Reviews: Journal of Pharmaceutical Analysis*, 3:11–22, 2014.

[99] S. Amaresh, K. Karthikeyan, K. J. Kim, Y. G. Lee, and Y. S. Lee. Aluminum based sulfide solid lithium ionic conductors for all solid state batteries. *Nanoscale*, 6:6661–6667, 2014.

[100] F. Lalere. *Développement de batteries céramiques tout-solide Li-et Na-ion à haute température: synthèses et mécanismes électrochimiques*. PhD thesis, Laboratoire de Réactivité et Chimie des Solides, 2015.

[101] D. Houtarde. *Synthesis of Sulfide-based Solid Electrolytes for Application to All-Solid-State Lithium Sulfur Batteries*. Master's thesis, Department of Chemical Engineering, University of Waterloo, 2015.

[102] V. S. Kandagal, M. D. Bharadwaj, and U. V. Waghmare. Theoretical prediction of a highly conducting solid electrolyte for sodium batteries: $Na_{10}GeP_2S_{12}$. *Journal of Materials Chemistry A*, 3(24):12992–12999, 2015.

[103] F. Tsuji, N. Tanibata, A. Sakuda, A. Hayashi, and M. Tatsumisago. Preparation of sodium ion conductive $Na_{10}GeP_2S_{12}$ glass-ceramic electrolytes. *Chemistry Letters*, 47:13–15, 2017.

[104] Z. Zhang, E. P. Ramos, F. Lalere, A. Assoud, K. Kaup, P. Hartman, and L. F. Nazar. $Na_{11}Sn_2PS_{12}$: a new solid state sodium superionic conductor. *Energy & Environmental Science*, 11(1):87–93, 2018.

[105] R. DeWees and H. Wang. Synthesis and properties of NASICON-type LATP and LAGP solid electrolytes. *ChemSusChem*, 12:3713–3725, 2019.

[106] A. Hayashi, K. Noi, N. Tanibata, M. Nagao, and M. Tatsumisago. High sodium ion conductivity of glass–ceramic electrolytes with cubic Na_3PS_4. *Journal of Power Sources*, 258:420–423, 2014.

[107] M. Tatsumisago and A. Hayashi. Superionic glasses and glass–ceramics in the Li_2S-P_2S_5 system for all-solid-state lithium secondary batteries. *Solid State Ionics*, 225:342–345, 2012.

[108] W. D. Richards, T. Tsujimura, L. J. Miara, Y. Wang, Y. C. Kim, S. Ping Ong, I. Uechi, and G. Ceder. Computational and Experimental Investigations of Na-Ion Conduction in Cubic Na_3PSe_4. *Chemistry of Materials*, 28:252–258, 2016.

[109] F. Mizuno, A. Hayashi, K. Tadanaga, and M. Tatsumisago. New, highly Ion-Conductive Crystals Precipitated from Li_2S-P_2S_5 Glasses. *Advanced Materials*, 17(7):918–921, 2005.

[110] G. Sahu, Z. Lin, J. Li, Z. Liu, N. Dudney, and C. Liang. Air-stable, high-conduction solid electrolytes of arsenic-substituted Li_4SnS_4. *Energy & Environmental Science*, 7:1053–1058, 2014.

[111] D. Zhang, X. Cao, D. Xu, N. Wang, C. Yu, W. Hu, X. Yan, J. Mi, B. Wen, L. Wang, and L. Zhang. Synthesis of cubic Na_3SbS_4 solid electrolyte with enhanced ion transport for all-solid-state sodium-ion batteries. *Electrochimica Acta*, 259:100–109, 2018.

[112] L. Zhang, D. Zhang, K. Yang, X. Yan, L. Wang, J. Mi, B. Xu, and Y. Li. Vacancy-Contained Tetragonal Na_3SbS_4 Superionic Conductor. *Advanced Science*, 3:1600089, 2016.

[113] T. W. Kim, K. H. Park, Y. E. Choi, J. Y. Lee, and Y. S. Jung. Aqueous-solution synthesis of Na_3SbS_4 solid electrolytes for all-solid-state na-ion batteries. *Journal of Materials Chemistry A*, 6:840–844, 2018.

[114] E. P. Ramos, Z. Zhang, A. Assoud, K. Kaup, F. Lalere, and L. F. Nazar. Correlating Ion Mobility and Single Crystal Structure in Sodium-Ion Chalcogenide-Based Solid State Fast Ion Conductors: $Na_{11}Sn_2PnS_{12}$ (Pn = Sb, P). *Chemistry of Materials*, 30:7413–7417, 2018.

[115] M. Duchardt, U. Ruschewitz, S. Adams, S. Dehnen, and B. Roling. Vacancy-Controlled Na^+ Superion Conduction in $Na_{11}Sn_2PS_{12}$. *Angewandte Chemie International Edition*, 57:1351–1355, 2018.

[116] T. Krauskopf, S. P. Culver, and W. G. Zeier. Bottleneck of Diffusion and Inductive Effects in $Li_{10}Ge_{1-x}Sn_xP_2S_{12}$. *Chemistry of Materials*, 30:1791–1798, 2018.

[117] P. Padma Kumar and S. Yashonath. Ionic conduction in the solid state. *Journal of Chemical Sciences*, 118(1):135–154, 2006.

[118] Z. Jinghuan, N. A. Raftery, and D. W. Field. X-ray diffraction powder data for schlippe's salt $Na_3SbS_4 \cdot 9H_2O$. *Powder Diffraction*, 8:61–64, 1993.

[119] F. Li, Z. Wei, A. Manthiram, Y. Feng, J. Ma, and L. Mai. Sodium-based batteries: from critical materials to battery systems. *Journal of Materials Chemistry A*, 7:9406–9431, 2019.

[120] S. Xin, Y. X. Yin, Y. G. Guo, and L. J. Wan. A high-energy room-temperature sodium-sulfur battery. *Advanced Materials*, 26:1261–1265, 2014.

[121] H. Wang, Y. Jiang, and A. Manthiram. Long cycle life, low self-discharge sodium–selenium batteries with high selenium loading and suppressed polyselenide shuttling. *Advanced Energy Materials*, 8:1701953, 2018.

[122] J. Ding, H. Zhou, H. Zhang, T. Stephenson, Z. Li, D. Karpuzov, and D. Mitlin. Exceptional energy and new insight with a sodium–selenium battery based on a carbon nanosheet cathode and a pseudographite anode. *Energy & Environmental Science*, 10:153–165, 2017.

[123] X. Li, J. Liang, J. Luo, C. Wang, X. Li, Q. Sun, R. Li, L. Zhang, R. Yang, and S. Lu. High-performance Li–SeS_x all-solid-state lithium batteries. *Advanced Materials*, 31:1808100, 2019.

[124] C. Luo, Y. Xu, Y. Zhu, Y. Liu, S. Zheng, Y. Liu, A. Langrock, and C. Wang. Selenium@Mesoporous carbon composite with superior lithium and sodium storage capacity. *ACS Nano*, 7:8003–8010, 2013.

[125] L. Wang, X. Zhang, L. Deng, J. Tang, H. Deng, W. Hu, and Z. Liu. Revealing the Reaction Mechanism of Sodium Selenide Confined within a Single-Walled Carbon Nanotube: Implications for Na-Se Batteries. *ACS applied materials & interfaces*, 11:4995–5002, 2019.

[126] Z. Yu, S. L. Shang, D. Wang, Y. C. Li, H. P. Yennawar, G. Li, H. T. Huang, Y. Gao, T. E. Mallouk, Z. K. Liu, and D. Wang. Synthesis and understanding of $Na_{11}Sn_2PSe_{12}$ with enhanced ionic conductivity for all-solid-state Na-ion battery. *Energy Storage Materials*, 17:70–77, 2019.

[127] M. Duchardt, S. Neuberger, U. Ruschewitz, T. Krauskopf, W. G. Zeier, G. Schmedt auf der, S. Adams, and S. Roling, B.and Dehnen. Superion conductor $Na_{11.1}Sn_{2.1}P_{0.9}Se_{12}$: Lowering the Activation Barrier of Na^+ Conduction in Quaternary 1–4–5–6 Electrolytes. *Chemistry of Materials*, 30:4134–4139, 2018.

[128] B. Eisenmann and R. Zagler. Selenoantimonate: Darstellung und Struktur von Na_3SbSe_4, K_3SbSe_4 und [Ba(en)4]2[Ba(en)3](SbSe$_4$)2/ Selenoantimonates(V): Preparation and Crystal Structure of Na_3SbSe_4, K_3SbSe_4 and [Ba(en)4]2[Ba(en)3](SbSe$_4$)2. *Zeitschrift für Naturforschung B*, 44:249–256, 2014.

[129] R. P. Rao, X. Zhang, K. C. Phuah, and S. Adams. Mechanochemical synthesis of fast sodium ion conductor $Na_{11}Sn_2PSe_{12}$ enables first sodium–selenium all-solid-state battery. *Journal of Materials Chemistry A*, 7:20790–20798, 2019.

[130] B. Krebs. Thio- and Seleno-Compounds of Main Group Elements—Novel Inorganic Oligomers and Polymers. *Angewandte Chemie International Edition in English*, 22(2):113–134, 1983.

[131] E. Rangasamy, J. Wolfenstine, and J. Sakamoto. The role of al and li concentration on the formation of cubic garnet solid electrolyte of nominal composition $Li_7La_3Zr_2O_{12}$. *Solid State Ionics*, 206:28–32, 2012.

[132] Y. T. Chen, A. Jena, W. K. Pang, V. K. Peterson, H. S. Sheu, H. Chang, and R. S. Liu. Voltammetric enhancement of li-ion conduction in al-doped $Li_{7-x}La_3Zr_2O_{12}$ solid electrolyte. *The Journal of Physical Chemistry C*, 121:15565–15573, 2017.

[133] K. Minami, F. Mizuno, A. Hayashi, and M. Tatsumisago. Lithium ion conductivity of the Li_2S-P_2S_5 glass-based electrolytes prepared by the melt quenching method. *Solid State Ionics*, 178:837–841, 2007.

[134] B. R. Shin, Y. J. Nam, D. Y. Oh, D. H. Kim, J. W. Kim, and Y. S. Jung. Comparative study of TiS_2/Li-In all-solid-state lithium batteries using glass-ceramic Li_3PS_4 and $Li_{10}GeP_2S_{12}$ solid electrolytes. *Electrochimica Acta*, 146:395–402, 2014.

[135] F. Han, A. S. Westover, J. Yue, X. Fan, F. Wang, M. Chi, D. N. Leonard, N. J. Dudney, H. Wang, and C. Wang. High electronic conductivity as the origin of lithium dendrite formation within solid electrolytes. *Nature Energy*, 4:187, 2019.

[136] H. K. Tian, B. Xu, and Y. Qi. Computational study of lithium nucleation tendency in $Li_7La_3Zr_2O_{12}$ (LLZO) and rational design of interlayer materials to prevent lithium dendrites. *Journal of Power Sources*, 392:79–86, 2018.

[137] H. Khlyap. *Physics and technology of semiconductor thin film-based active elements and devices*. Bentham Science Publishers, 2009.

[138] C. R. Mariappan, C. Yada, F. Rosciano, and B. Roling. Correlation between micro-structural properties and ionic conductivity of $Li_{1.5}Al_{0.5}Ge_{1.5}(PO_4)_3$ ceramics. *Journal of Power Sources*, 196:6456–6464, 2011.

[139] A. C. Sutorik, M. D. Green, C. Cooper, J. Wolfenstine, and G. Gilde. The comparative influences of structural ordering, grain size, li-content, and bulk density on the li^+-conductivity of $Li_{0.29}La_{0.57}TiO_3$. *Journal of Materials Science*, 47:6992–7002, 2012.

[140] R. Mercier, J. P. Malugani, B. Fahys, and R. Guy. Superionic conduction in Li_2S-P_2S_5-LiI-glasses. *Solid State Ionics*, 5:663–666, 1981.

[141] S. Ujiie, A. Hayashi, and M. Tatsumisago. Structure, ionic conductivity and electrochemical stability of Li_2S-P_2S_5-LiI glass and glass–ceramic electrolytes. *Solid State Ionics*, 211:42–45, 2012.

[142] R. P. Rao and S. Adams. Studies of lithium argyrodite solid electrolytes for all-solid-state batteries. *physica status solidi (a)*, 208(8):1804–1807, 2011.

[143] E. Rangasamy, Z. Liu, M. Gobet, K. Pilar, G. Sahu, W. Zhou, H. Wu, S. Greenbaum, and C. Liang. An iodide-based $Li_7P_2S_8I$ superionic conductor. *Journal of the American Chemical Society*, 137:1384–1387, 2015.

[144] S. J. Sedlmaier, S. Indris, C. Dietrich, M. Yavuz, C. Dräger, F. von Seggern, H. Sommer, and J. Janek. Li_4PS_4I: A Li^+ Superionic Conductor Synthesized by a Solvent-Based Soft Chemistry Approach. *Chemistry of Materials*, 29:1830–1835, 2017.

[145] H. J. Deiseroth, S. T. Kong, H. Eckert, J. Vannahme, C. Reiner, T. Zaiß, and M. Schlosser. Li_6PS_5X: A Class of Crystalline Li-Rich Solids With an Unusually High Li+ Mobility. *Angewandte Chemie International Edition*, 47:755–758, 2008.

[146] L. Zhou, K. H. Park, X. Sun, F. Lalere, P. Adermann, L. Hartmann, and L. F. Nazar. Solvent-engineered design of argyrodite Li_6PS_5X (X=Cl, Br, I) solid electrolytes with high ionic conductivity. *ACS Energy Letters*, 4:265–270, 2018.

[147] L. Zhou, A. Assoud, Q. Zhang, X. Wu, and L. F. Nazar. New family of argyrodite thioantimonate lithium superionic conductors. *Journal of the American Chemical Society*, 141:19002–19013, 2019.

[148] K. Homma, M. Yonemura, T. Kobayashi, M. Nagao, M. Hirayama, and R. Kanno. Crystal structure and phase transitions of the lithium ionic conductor Li_3PS_4. *Solid State Ionics*, 182:53–58, 2011.

[149] P. Zhou, J. Wang, F. Cheng, F. Li, and J. Chen. A solid lithium superionic conductor $Li_{11}AlP_2S_{12}$ with a thio-LISICON analogous structure. *Chemical Communications*, 52:6091–6094, 2016.

[150] Y. Aihara, S. Ito, R. Omoda, T. Yamada, S. Fujiki, T. Watanabe, Y. Park, and S. Doo. The electrochemical characteristics and applicability of an amorphous sulfide-based solid ion conductor for the next-generation solid-state lithium secondary batteries. *Frontiers in Energy Research*, 4:18, 2016.

[151] P. R. Rayavarapu, N. Sharma, V. K. Peterson, and S. Adams. Variation in structure and li+-ion migration in argyrodite-type Li_6PS_5X (X= Cl, Br, I) solid electrolytes. *Journal of Solid State Electrochemistry*, 16:1807–1813, 2012.

[152] M. A Kraft, S. Ohno, T. Zinkevich, R. Koerver, S. P. Culver, T. Fuchs, A. Senyshyn, S. Indris, B. J. Morgan, and W. G. Zeier. Inducing high ionic conductivity in the lithium superionic argyrodites $Li_{6+x}P_{1-x}Ge_xS_5I$ for all-solid-state batteries. *Journal of the American Chemical Society*, 140:16330–16339, 2018.

[153] V. R. Devi, N. A. Zabidi, and K. N. Shrivastava. Interpretation of the raman spectra of the glassy states of Si_xS_{1-x} and Si_xSe_{1-x}. *Materials Chemistry and Physics*, 141:651–656, 2013.

[154] D. E. Watson and S. W. Martin. Short range order characterization of the Na_2S + SiS_2 glass system using Raman, infrared and ^{29}Si magic angle spinning nuclear magnetic resonance spectroscopies. *Journal of Non-Crystalline Solids*, 471:39–50, 2017.

[155] L. Zhou, A. Assoud, A. Shyamsunder, A. Huq, Q. Zhang, P. Hartmann, J. Kulisch, and L. F. Nazar. An entropically stabilized fast-ion conductor: $Li_{3.25}[Si_{0.25}P_{0.75}]S_4$. *Chemistry of Materials*, 31:7801–7811, 2019.

[156] K. Momma, T. Ikeda, A. Belik, and F. Izumi. Dysnomia, a computer program for maximum-entropy method (mem) analysis and its performance in the mem-based pattern fitting. *Powder Diffraction*, 28:184–193, 2013.

[157] I. D. Brown and K. R. Poeppelmeier. *Bond valences*. Springer, 2014.

[158] D. Phani, K. Gopi, J. Balachandran, P. Kent, A. Rondinone, and P. Ganesh. Li-ion site disorder driven superionic conductivity in solid electrolytes: A first-principles investigation of β-Li_3PS_4. *Journal of Materials Chemistry A*, 5:1153–1159, 2016.

[159] Z. Xu, R. Chen, and H. Zhu. A Li_2CuPS_4 superionic conductor: a new sulfide-based solid-state electrolyte. *Journal of Materials Chemistry A*, 7:12645–12653, 2019.

[160] S. P. Ong, Y. Mo, W. D. Richards, L. Miara, H. S. Lee, and G. Ceder. Phase stability, electrochemical stability and ionic conductivity of the $Li_{10}\pm_1MP_2X_{12}$ (M= Ge, Si, Sn, Al or P, and X= O, S or Se) family of superionic conductors. *Energy & Environmental Science*, 6:148–156, 2013.

[161] M. Gobet, S. Greenbaum, G. Sahu, and C. Liang. Structural evolution and li dynamics in nanophase Li_3PS_4 by solid-state and pulsed-field gradient nmr. *Chemistry of Materials*, 26:3558–3564, 2014.

[162] H. Stöffler, T. Zinkevich, M. Yavuz, A. Senyshyn, J. Kulisch, P. Hartmann, T. Adermann, S. Randau, F. H. Richter, J. Janek, S. Indris, and H. Ehrenberg. Li^+-Ion Dynamics in β-Li_3PS_4 observed by NMR: Local Hopping and Long-Range Transport. *The Journal of Physical Chemistry C*, 122:15954–15965, 2018.

[163] K. Takada, M. Osada, N. Ohta, T. Inada, A. Kajiyama, H. Sasaki, S. Kondo, M. Watanabe, and T. Sasaki. Lithium ion conductive oxysulfide, Li_3PO_4-Li_3PS_4. *Solid State Ionics*, 176:2355–2359, 2005.

[164] N. Huu H. Phuc, K. Morikawa, M. Totani, H. Muto, and A. Matsuda. Chemical synthesis of Li_3PS_4 precursor suspension by liquid-phase shaking. *Solid State Ionics*, 285:2–5, 2016.

[165] B. T. Leube, K. K. Inglis, E. J. Carrington, P. M. Sharp, J. F. Shin, A. R. Neale, T. D. Manning, M. J. Pitcher, L. J. Hardwick, M. S. Dyer, F. BlancJohn, B. ClaridgeMatthew, and Rosseinsky J. Lithium transport in $Li_{4.4}M_{0.4}M'_{0.6}S_4$ (M = Al^{3+}, Ga^{3+}, and M' = Ge^{4+}, Sn^{4+}): Combined crystallographic, conductivity, solid state nmr, and computational studies. *Chemistry of Materials*, 30:7183–7200, 2018.

[166] N. H. H. Phuc, M. Totani, K. Morikawa, H. Muto, and A. Matsuda. Preparation of Li_3PS_4 solid electrolyte using ethyl acetate as synthetic medium. *Solid State Ionics*, 288:240–243, 2016.

[167] S. Teragawa, K. Aso, K. Tadanaga, A. Hayashi, and M. Tatsumisago. Liquid-phase synthesis of a Li_3PS_4 solid electrolyte using n-methylformamide for all-solid-state lithium batteries. *Journal of Materials Chemistry A*, 2:5095–5099, 2014.

[168] K. Minami, A. Hayashi, and M. Tatsumisago. Crystallization process for superionic $Li_7P_3S_{11}$ glass–ceramic electrolytes. *Journal of the American Ceramic Society*, 94:1779–1783, 2011.

[169] S. Wenzel, D. A. Weber, T. Leichtweiss, M. R. Busche, J. Sann, and J. Janek. Interphase formation and degradation of charge transfer kinetics between a lithium metal anode and highly crystalline $Li_7P_3S_{11}$ solid electrolyte. *Solid State Ionics*, 286:24–33, 2016.

[170] K. Oh, D. Chang, I. Park, K. Yoon, and K. Kang. First-principles investigations on sodium superionic conductor $Na_{11}Sn_2PS_{12}$. *Chemistry of Materials*, 31:6066–6075, 2019.

APPENDICES

Appendix A

In this appendix the single crystal XRD and impedance spectroscopy data of $Na_{11}Sn_2PnS_{12}$ with Pn=Sb and P materials are presented.

Crystal data	
Formula	$Na_{11.01(11)}Sn_2SbS_{12}$
Formula Weight	1001.27
Crystal System	Tetragonal
Space group	$I4_1/acd$:2 (No.142)
a= b, c (Å)	13.7681(10), 27.442(2)
V (Å^3)	5201.9(9)
Z	8
Calc. density (g/cm^3)	2.557
Abs. coef. μ(MoKσ) (/mm)	4.079
F(000)	3729
Crystal Size (mm)	0.130 x 0.090 x 0.040
Data Collection	
Temperature (K)	200
Radiation (Å)	MoKa 0.71073
Theta range for data collection (°)	2.565 to 27.986
Index ranges	-17<=h<=15, -7<=k<=15, -36<=l<=30
Reflections collected	8649
Independent reflections	1454 [R(int) = 0.0229]
Completeness to θ = 25.242°	100.0%
Absorption correction	Semi-empirical from equivalents
Max. and min. transmission	0.7460 and 0.6679
Refinement	
Refinement method	Full-matrix least-squares on F^2
Data/restraints/parameters	1454 / 0 / 75
Goodness-of-fit on F^2	1.036
Final R indices [I>2sigma(I)]	R1=0.0219, wR2=0.0487
R indices (all data)	R1=0.0256, wR2=0.0505
Extinction coefficient	0.000051(10)
Largest diff. peak and hole (e(Å^3))	1.405 and -1.223

Table A.1: Crystallographic data for $Na_{11.01(11)}Sn_2SbS_{12}$ obtained from single crystal XRD at 200 K.

Atom	Wyckoff site	x	y	z	SOF	U_{eq}/Å^2
Sn1	*16e*	0.28898(2)	0	1/4	1	0.01479(9)
Sb1	*8a*	0	1/4	3/8	1	0.01460(11)
S1	*32g*	0.14821(6)	0.36195(5)	0.05022(3)	1	0.02090(17)
S2	*32g*	0.15356(6)	0.06183(6)	0.05204(2)	1	0.01855(17)
S3	*32g*	0.10560(7)	0.15927(7)	0.32634(3)	1	0.0295(2)
Na1	*32g*	0.01954(15)	0.01500(14)	0.12717(6)	0.852(12)	0.0084(2)
Na2	*16d*	0	1/4	0.00721(10)	0.844(10)	0.0909(18)
Na3	*16e*	0.04027(16)	0	1/4	0.983(9)	0.0463(9)
Na4	*16c*	0	0	0	0.937(10)	0.0963(19)
Na5	*16f*	0.23034(14)	0.48034(14)	1/8	0.993(12)	0.0756(15)
Na6	*8b*	0	1/4	1/8	0.088(12)	0.031(12)

Table A.2: Atomic coordinates, site occupation factors and equivalent isotropic displacement parameters of $Na_{11.01(11)}Sn_2SbS_{12}$ obtained from single crystal XRD at 200 K.

Atom	U_{11}	U_{22}	U_{33}	U_{23}	U_{13}	U_{12}
Sn1	0.014(1)	0.014(1)	0.016(1)	0.001(1)	0	0
Sb1	0.014(1)	0.014(1)	0.016(1)	0	0	0
S1	0.021(1)	0.019(1)	0.023(1)	0.001(1)	0.003(1)	-0.004(1)
S2	0.016(1)	0.021(1)	0.018(1)	0.000(1)	0.005(1)	0.001(1)
S3	0.028(1)	0.027(1)	0.032(1)	-0.010(1)	0.009(1)	0.004(1)
Na1	0.061(1)	0.036(1)	0.044(1)	-0.006(1)	0.035(1)	-0.010(1)
Na2	0.056(3)	0.163(4)	0.032(2)	0	0	-0.072(3)
Na3	0.017(1)	0.061(2)	0.061(2)	0.031(1)	0	0
Na4	0.019(1)	0.213(4)	0.057(2)	-0.043(1)	-0.009(1)	-0.009(2)
Na5	0.102(2)	0.102(2)	0.024(1)	-0.018(1)	0.018(1)	-0.058(2)
Na6	0.036(16)	0.036(16)	0.020(14)	0	0	0.002(15)

Table A.3: Anisotropic displacement parameters (Å^2) of $Na_{11.01(11)}Sn_2SbS_{12}$ obtained from single crystal XRD at 200 K.

Atom1	Atom2	Bond distance (Å)
Sn1	**S1**	2.3924(8) × 2
Sn1	**S2**	2.3936(7) × 2
Sb1	**S3**	2.3362(8) × 4
Na1	**S1**	2.969(5)
Na1	**S1**	3.559(3)
Na1	**S2**	2.8408(17)
Na1	**S2**	3.228(2)
Na1	**S3**	2.965(2)
Na1	**S3**	3.011(2)
Na2	**S1**	2.8165(14) × 2
Na2	**S2**	3.5631(13) × 2
Na2	**S3**	2.989(2) × 2
Na3	**S1**	2.8733(19) × 2
Na3	**S2**	2.8195(18) × 2
Na3	**S3**	3.1633(11) × 2
Na4	**S1**	3.1105(8) × 2
Na4	**S2**	2.6896(8) × 2
Na4	**S3**	3.1468(9) × 2
Na5	**S1**	2.854(2) × 2
Na5	**S2**	2.797(2) × 2
Na5	**S3**	3.2526(10) × 2
Na6	**S1**	3.2789(8) × 4
Na6	**S2**	3.8975(8) × 4
Na1	**Na6**	3.2472(19) × 2
Na1	**Na3**	3.3891(17) × 2
Na1	**Na4**	3.5063(16) × 2
Na1	**Na5**	3.442(3), 3.477(3)
Na2	**Na6**	3.232(3) × 2
Na2	**Na3**	3.4920(5), 3.4920(5)
Na2	**Na4**	3.4477(3), 3.4477(3)

Table A.4: Interatomic distances of $Na_{11.01(11)}Sn_2SbS_{12}$ obtained from single crystal XRD at 200 K.

Crystal data	
Formula	$Na_{11.09(9)}Sn_2SbS_{12}$
Formula Weight	998.78
Crystal System	Tetragonal
Space group	$I4_1/acd$:2 (No.142)
a= b, c (Å)	13.7946(5), 27.4956(11)
V (Å^3)	5232.2(4)
Z	8
Calc. density (g/cm^3)	2.536
Abs. coef. μ(MoKσ) (/mm)	4.053
F(000)	3720
Crystal Size (mm)	0.130 x 0.090 x 0.040
Data Collection	
Temperature (K)	273
Radiation (Å)	MoKa 0.71073
Theta range for data collection (°)	2.560 to 29.990
Index ranges	-19<=h<=16, -17<=k<=18, -38<=l<=34
Reflections collected	13842
Independent reflections	1913 [R(int) = 0.0208]
Completeness to θ = 25.242°	100.0%
Absorption correction	Semi-empirical from equivalents
Max. and min. transmission	0.7460 and 0.6884
Refinement	
Refinement method	Full-matrix least-squares on F^2
Data/restraints/parameters	1913 / 0 / 75
Goodness-of-fit on F^2	1.048
Final R indices [I>2sigma(I)]	R1 = 0.0212, wR2 = 0.0479
R indices (all data)	R1 = 0.0246, wR2 = 0.0500
Extinction coefficient	0.000048(9)
Largest diff. peak and hole (e(Å^3))	1.375 and -1.249

Table A.5: Crystallographic data for $Na_{11.09(9)}Sn_2SbS_{12}$ obtained from single crystal XRD at 273 K.

Atom	Wyckoff site	x	y	z	SOF	U_{eq}/Å^2
Sn1	*16e*	0.2889(1)	0	1/4	1	0.01820(7)
Sb1	*8a*	0	1/4	3/8	1	0.01826 (8)
S1	*32g*	0.14843(5)	0.36218(5)	0.05011(2)	1	0.02531(13)
S2	*32g*	0.150364(4)	0.06165(5)	0.05192(2)	1	0.02236(13)
S3	*32g*	0.10533(6)	0.15946(6)	0.32646(3)	1	0.03501(16)
Na1	*32g*	0.01946(14)	0.01502(12)	0.12704(5)	0.895(6)	0.0559(7)
Na2	*16d*	0	1/4	0.00726(10)	0.844(10)	0.0909(18)
Na3	*16e*	0.04032(14)	0	1/4	0.977(8)	0.0521(8)
Na4	*16c*	0	0	0	0.924(16)	0.0966(16)
Na5	*16f*	0.23052(12)	0.48052(12)	1/8	0.972(10)	0.0776(13)
Na6	*8b*	0	1/4	1/8	0.074(9)	0.016(8)

Table A.6: Atomic coordinates, site occupation factors and equivalent isotropic displacement parameters of $Na_{11.09(9)}Sn_2SbS_{12}$ obtained from single crystal XRD at 273 K.

Atom	U_{11}	U_{22}	U_{33}	U_{23}	U_{13}	U_{12}
Sn1	0.018(1)	0.018(1)	0.019(1)	0.001(1)	0	0
Sb1	0.018(1)	0.018(1)	0.019(1)	0	0	0
S1	0.026(1)	0.023(1)	0.027(1)	0.001(1)	0.003(1)	-0.005(1)
S2	0.020(1)	0.026(1)	0.021(1)	0.000(1)	0.005(1)	0.001(1)
S3	0.034(1)	0.033(1)	0.038(1)	-0.011(1)	0.010(1)	0.004(1)
Na1	0.071(1)	0.045(1)	0.052(1)	-0.007(1)	0.035(1) -0.011(1)	
Na2	0.064(2)	0.169(4)	0.040(2)	0	0	-0.074(2)
Na3	0.021(1)	0.068(2)	0.067(2)	0.031(1)	0	0
Na4	0.024(1)	0.203(4)	0.062(2)	-0.040(1)	-0.011(1)	-0.008(2)
Na5	0.103(2)	0.103(2)	0.026(1)	-0.017(1)	0.017(1)	-0.059(2)
Na6	0.018(10)	0.018(10)	0.014(11)	0	0	0.002(10)

Table A.7: Anisotropic displacement parameters (Å^2) of $Na_{11.09(9)}Sn_2SbS_{12}$ obtained from single crystal XRD at 273 K.

Atom1	Atom2	Bond distance (Å)
Sn1	**S1**	2.3920(6) × 2
Sn1	**S2**	2.3939(6) × 2
Sb1	**S3**	2.3350(7) × 4
Na1	**S1**	2.969(5)
Na1	**S1**	2.9551(16)
Na1	**S2**	2.8467(15)
Na1	**S2**	3.240(2)
Na1	**S3**	2.973(2)
Na1	**S3**	3.0156(19)
Na2	**S1**	2.8240(13) × 2
Na2	**S2**	3.5708(12) × 2
Na2	**S3**	2.995(2) × 2
Na3	**S1**	2.8787(15) × 2
Na3	**S2**	2.8240(15) × 2
Na3	**S3**	3.1722(9) × 2
Na4	**S1**	3.1153(7) × 2
Na4	**S2**	2.6932(6) × 2
Na4	**S3**	3.1563(8) × 2
Na5	**S1**	2.8614(18) × 2
Na5	**S2**	2.8005(18) × 2
Na5	**S3**	3.2615(8) × 2
Na6	**S1**	3.2906(6) × 4
Na6	**S2**	3.9090(7) × 4
Na1	**Na6**	3.2517(17) × 2
Na1	**Na3**	3.3995(16) × 2
Na1	**Na4**	3.5095(15) × 2
Na1	**Na5**	3.449(2), 3.482(3)
Na2	**Na6**	3.237(3) × 2
Na2	**Na3**	3.4989(4) × 2
Na2	**Na4**	3.4544(2) × 2

Table A.8: Interatomic distances of $Na_{11.09(9)}Sn_2SbS_{12}$ obtained from single crystal XRD at 273 K.

Crystal data	
Formula	$Na_{11.08(8)}Sn_2SbS_{12}$
Formula Weight	998.55
Crystal System	Tetragonal
Space group	$I4_1/acd$:2 (No.142)
a= b, c (Å)	13.7973(8), 27.5026(19)
V (Å^3)	5235.5(7)
Z	8
Calc. density (g/cm^3)	2.534
Abs. coef. μ(MoKσ) (/mm)	4.051
F(000)	3719
Crystal Size (mm)	0.130 x 0.090 x 0.040
Data Collection	
Temperature (K)	280
Radiation (Å)	MoKa 0.71073
Theta range for data collection (°)	2.560 to 29.983
Index ranges	-16<=h<=19, -18<=k<=17, 38<=l<=34
Reflections collected	13838
Independent reflections	1913 [R(int) = 0.0215]
Completeness to θ = 25.242°	100.0%
Absorption correction	Semi-empirical from equivalents
Max. and min. transmission	0.7460 and 0.6884
Refinement	
Refinement method	Full-matrix least-squares on F^2
Data/restraints/parameters	1913 / 0 / 75
Goodness-of-fit on F^2	1.051
Final R indices [I>2sigma(I)]	R1=0.0221, wR2=0.0488
R indices (all data)	R1=0.0247, wR2=0.0507
Extinction coefficient	0. 000047(9)
Largest diff. peak and hole (e(Å^3))	1.263 and -1.289

Table A.9: Crystallographic data for $Na_{11.08(8)}Sn_2SbS_{12}$ obtained from single crystal XRD at 280 K.

Crystal data	
Formula	$Na_{11.08(10)}Sn_2PS_{12}$
Formula Weight	908.17
Crystal System	Tetragonal
Space group	$I4_1/acd$:2 (No.142)
a= b, c (Å)	13.6148(3), 27.2244(7)
V (Å^3)	5046.4(3)
Z	8
Calc. density (g/cm^3)	2.391
Abs. coef. μ(MoKσ) (/mm)	3.218
F(000)	3432
Crystal Size (mm)	0.070x0.020 x 0.018
Data Collection	
Temperature (°K)	280
Radiation (Å)	MoKa 0.71073
Theta range for data collection (°)	1.496 to 29.960
Index ranges	-18<=h<=19, -19<=k<=18, -36<=l<=29
Reflections collected	14755
Independent reflections	1820 [R(int) = 0.0382]
Completeness to θ = 25.242°	100.0%
Absorption correction	Semi-empirical from equivalents
Max. and min. transmission	0.7460 and 0.6468
Refinement	
Refinement method	Full-matrix least-squares on F^2
Data/restraints/parameters	1820 / 0 / 75
Goodness-of-fit on F^2	1.284
Final R indices [I>2sigma(I)]	R1=0.0392,wR2= 0.0880
R indices (all data)	R1 = 0.0521, wR2 = 0.0939
Extinction coefficient	n/a
Largest diff. peak and hole (e(Å^3))	1.182 and -0.883

Table A.10: Crystallographic data for $Na_{11.08(10)}Sn_2PS_{12}$ obtained from single crystal XRD at 280 K.

The relative density of $Na_{11}Sn_2PnS_{12}$ was calculated using the following equations:

$$\rho_{experimental} = \frac{m}{V}, \tag{A.1}$$

where m is the mass, V is the volume of the pellet (10-13 mm diameter).

$$\rho_{theoretical} = \frac{ZM}{VN_A}, \tag{A.2}$$

where Z is the formula unit of the unit cell, V is the volume of the unit cell and N_A is Avogadro's number.

Parameters/σ (mS·cm^{-1})	P	Sb
Thickness (mm)	1.22	1.4
R (Ω)	94.5	290
Total σ**(mS·cm**$^{-1}$**)**	1.64	0.61
Thickness (mm)	1.5	1.35
R (Ω)	144.5	300
Total σ **(mS·cm**$^{-1}$**)**	1.32	0.57
Thickness (mm)	1.6	1.5
R (Ω)	140.5	370
Total σ **(m S·cm**$^{-1}$**)**	1.45	0.52
Thickness (mm)	1.24	0.8
R (Ω)	140	161
Total σ **(mS·cm**$^{-1}$**)**	1.13	0.63
Thickness (mm)	—	0.6
R (Ω)	—	130
Total σ **(mS·cm**$^{-1}$**)**		0.59
Thickness (mm)	—	0.995
R (Ω)	—	263
Total σ **(mS·cm**$^{-1}$**)**		0.48
Thickness (mm)	—	1.3
R (Ω)	—	290
Total σ **(mS·cm**$^{-1}$**)**		0.57
Thickness (mm)	—	1.5
R (Ω)	—	370
Total σ **(mS·cm**$^{-1}$**)**		0.52
Average σ **(mS·cm**$^{-1}$**)**	1.39	0.57
SD(σ)	0.21	0.06
SE	0.11	0.03
Exp. density of Theor. (%)		84

Table A.11: Room temperature ionic conductivity values of $Na_{11}Sn_2PnS_{12}$ with Pn=Sb and P obtained by EIS of the pressed at 2 tons and 1.0 cm diameter pellets. The relative density of $Na_{11}Sn_2PnS_{12}$ was calculated using **Equations** A.1 and A.2. The SD and SE were calculated using **Equations** 2.29 and 2.30, respectively.

Appendix B

In this appendix the single crystal XRD and impedance spectroscopy data of $Na_{11}Sn_2SbS_{12-x}Se_x$ with x=1, 6 and 12 series are presented.

Crystal data	
Formula	$Na_{11.15(7)}Sn_2SbSe_{12}$
Formula Weight	1563.10
Crystal System	Tetragonal
Space group	$I4_1/acd$:2 (No.142)
a= b, c (Å)	14.3954(3), 28.6292(6)
V (Å^3)	5932.8(3)
Z	8
Calc. density (g/cm^3)	3.500
Abs. coef. μ(MoKσ) (/mm)	17.456
F(000)	5454
Crystal Size (mm)	0.130 x 0.090 x 0.030
Data Collection	
Temperature (K)	280
Radiation (Å)	MoKa 0.71073
Theta range for data collection (°)	2.455 to 29.999
Index ranges	-20<=h<=18, -19<=k<=9,-18<=l<=40
Reflections collected	21329
Independent reflections	2177 [R(int) = 0.0182]
Completeness to θ = 25.242°	100.0%
Absorption correction	Semi-empirical from equivalents
Max. and min. transmission	0.7460 and 0.5031
Refinement	
Refinement method	Full-matrix least-squares on F^2
Data/restraints/parameters	2177 / 0 / 75
Goodness-of-fit on F^2	1.038
Final R indices [I>2sigma(I)]	R1 = 0.0186, wR2 = 0.0411
R indices (all data)	R1 = 0.0226, wR2 = 0.0428
Extinction coefficient	n/a
Largest diff. peak and hole (e(Å^3))	1.207 and -0.870

Table B.1: Crystallographic data for $Na_{11.15(7}Sn_2SbSe_{12}$ obtained from single crystal XRD at 280 K.

Crystal data	
Formula	$Na_{11.09(10)}Sn_2SbS_{10.9(3)}Se_{1.1(3)}$
Formula Weight	1050.53
Crystal System	Tetragonal
Space group	$I4_1/acd$:2 (No.142)
a= b, c (Å)	13.8324(18), 27.597(4)
V (Å^3)	5280.2(15)
Z	8
Calc. density (g/cm^3)	2.643
Abs. coef. μ(MoKσ) (/mm)	5.453
F(000)	3879
Crystal Size (mm)	0.070 x 0.060 x 0.020
Data Collection	
Temperature (°K)	280
Radiation (Å)	MoKa 0.71073
Theta range for data collection (°)	2.552 to 29.997 2
Index ranges	-19<=h<=15,-17<=k<=19,-38<=l<=29
Reflections collected	13657
Independent reflections	1934 [R(int) = 0.0345]
Completeness to θ = 25.242°	100.0%
Absorption correction	Semi-empirical from equivalents
Max. and min. transmission	0.7460 and 0.6822
Refinement	
Refinement method	Full-matrix least-squares on F^2
Data/restraints/parameters	1934 / 0 / 78
Goodness-of-fit on F^2	1.043
Final R indices [I>2sigma(I)]	R1 = 0.0256, wR2 = 0.0530
R indices (all data)	R1 = 0.0359, wR2 = 0.0565
Extinction coefficient	0.000001(9)
Largest diff. peak and hole (e(Å^3)	1.139 and -0.982

Table B.2: Crystallographic data for $Na_{11.09(10)}Sn_2SbS_{10.9(3)}Se_{1.1(3)}$ obtained from single crystal XRD at 280 K.

Atom	Wyckoff site	x	y	z	SOF	U_{eq}/Å^2
Sn1	*16e*	0.2120(1)	1/2	1/4	1	0.019(1)
Sb1	*8a*	0	1/4	3/8	1	0.020(1)
S/Se1	*32g*	0.1125(1)	0.3966(1)	0.1992(1)	0.825(3) / 0.175(3)	0.028(1)
S/Se2	*32g*	0.3091(1)	0.4032(1)	0.3017(1)	0.966(3) / 0.034(3)	0.024(1)
S/Se3	*32g*	0.0912(1)	0.3549(1)	0.4235(1)	0.932(3) / 0.068(3)	0.038(1)
Na1	*32g*	0.2662(1)	0.2690(2)	0.3765(1)	0.888(7)	0.060(1)
Na2	*16d*	0	1/4	0.2425(1)	0.826(13)	0.102(2)
Na3	*6e*	-0.0395(2)	1/2	1/4	0.982(9)	0.056(1)
Na4	*16c*	1/4	1/4	1/4	0.927(11)	0.109(2)
Na5	*16f*	0.2317(1)	0.5183(1)	3/8	0.965(12)	0.081(2)
Na6	*8b*	0	1/4	1/8	0.133(12)	0.037(8)

Table B.3: Atomic coordinates, site occupation factors and equivalent isotropic displacement parameters of $Na_{11.09(10)}Sn_2SbS_{10.9(3)}Se_{1.1(3)}$ obtained from single crystal XRD at 280 K.

Atom	U_{11}	U_{22}	U_{33}	U_{23}	U_{13}	U_{12}
Sn1	0.019(1)	0.019(1)	0.020(1)	0.001(1)	0	0
Sb1	0.020(1)	0.020(1)	0.021(1)	0	0	0
S/Se1	0.025(1)	0.031(1)	0.028(1)	-0.001(1)	0.001(1)	-0.003(1)
S/Se2	0.028(1)	0.022(1)	0.022(1)	0.005(1)	0.001(1)	0.001(1)
S/Se3	0.036(1)	0.036(1)	0.041(1)	-0.010(1)	-0.011(1)	-0.005(1)
Na1	0.049(1)	0.074(2)	0.056(1)	0.036(1)	-0.007(1)	-0.011(1)
Na2	0.185(3)	0.073(3)	0.047(2)	0	0	-0.080(3)
Na3	0.024(1)	0.072(2)	0.072(2)	-0.034(1)	0	0
Na4	0.231(5)	0.027(2)	0.068(2)	-0.011(1)	-0.052(1)	-0.005(2)
Na5	0.109(2)	0.109(2)	0.026(1)	-0.016(1)	-0.016(1)	0.061(2)
Na6	0.046(10)	0.046(10)	0.019(10)	0	0	-0.015(10)

Table B.4: Anisotropic displacement parameters (Å^2) of $Na_{11.09(10)}Sn_2SbS_{10.9(3)}Se_{1.1(3)}$ obtained from single crystal XRD at 280 K.

Atom1	Atom2	Bond distance (Å)
Sn1	**S1/Se1**	2.4298(7) × 2
Sn1	**S2/Se2**	2.4016(8) × 2
Sb1	**Se3**	2.3426(8) × 4
Na1	**S1/Se1**	2.9650(19)
Na1	**S1/Se1**	3.525(3)
Na1	**S2/Se2**	2.8492(18)
Na1	**S2/Se2**	3.254(2)
Na1	**S3/Se3**	2.993(2)
Na1	**S3/Se3**	3.035(2)
Na2	**S1/Se1**	2.8212(17) × 2
Na2	**S2/Se2**	3.3635(15) × 2
Na2	**S3/Se3**	3.011(3) × 2
Na3	**S1/Se1**	2.9040(17) × 2
Na3	**S2/Se2**	2.8307(17) × 2
Na3	**S3/Se3**	3.1777(11) × 2
Na4	**S1/Se1**	3.1129(7) × 2
Na4	**S2/Se2**	2.6983(8) × 2
Na4	**S3/Se3**	3.1740(9) × 2
Na5	**S1/Se1**	2.881(2) × 2
Na5	**S2/Se2**	2.806(2) × 2
Na5	**S3/Se3**	3.2685(10) × 2
Na6	**S1/Se1**	3.2755(7) × 4
Na6	**S2/Se2**	3.9112(9) × 4
Na1	**Na6**	3.245(2) × 2
Na1	**Na3**	3.427(2) × 2
Na1	**Na4**	3.508(2), 3.508(2)
Na1	**Na5**	3.468(3), 3.482(3)
Na2	**Na6**	3.242(4) × 2
Na2	**Na3**	3.5072(6), 3.5072(6)
Na2	**Na4**	3.4643(5), 3.4643(5)

Table B.5: Interatomic distances of $Na_{11.09(10)}Sn_2SbS_{10.9(3)}Se_{1.1(3)}$ obtained from single crystal XRD at 280 K.

Crystal data	
Formula	$Na_{11.12(10)}Sn_2SbS_{6.25(3)}Se_{5.75(3)}$
Formula Weight	1268.86
Crystal System	Tetragonal
Space group	$I4_1/acd$:2 (No.142)
a=b, c (Å))	14.0842(7), 28.0585(14)
V (Å^3)	5565.8(6)
Z	8
Calc. density (g/cm^3)	3.028
Abs. coef. μ(MoKσ) (/mm)	10.894
F(000)	4550
Crystal Size (mm)	0.160 x 0.110 x 0.040
Data Collection	
Temperature (K)	280
Radiation (Å)	MoKa 0.71073
Theta range for data collection (°)	2.508 to 29.992
Index ranges	-18<=h<=19,-19<=k<=16,-39<=l<=39
Reflections collected	31864
Independent reflections	2033 [R(int) = 0.0243]
Completeness to θ = 25.242°	100.0%
Absorption correction	Semi-empirical from equivalents
Max. and min. transmission	0.7460 and 0.6411
Refinement	
Refinement method	Full-matrix least-squares on F^2
Data/restraints/parameters	2033 / 0 / 77
Goodness-of-fit on F^2	1.028
Final R indices [I>2sigma(I)]	R1 = 0.0204, wR2 = 0.0473
R indices (all data)	R1 = 0.0252, wR2 = 0.0491
Extinction coefficient	n/a
Largest diff. peak and hole (e(Å^3)	1.055 and -1.200

Table B.6: Crystallographic data for $Na_{11.12(10)}Sn_2SbS_{6.25(3)}Se_{5.75(3)}$ obtained from single crystal XRD at 280 K.

Atom	Wyckoff site	x	y	z	SOF	U_{eq}/Å^2
Sn1	*16e*	0.2093(1)	1/2	1/4	1	0.021(1)
Sb1	*8a*	0	1/4	3/8	1	0.021(1)
S/Se1	*32g*	0.1096(1)	0.3948(1)	0.1985(1)	0.281(3) / 0.719(3)	0.028(1)
S/Se2	*32g*	0.3113(1)	0.4026(1)	0.3018(1)	0.683(2) / 0.317(2)	0.026(1)
S/Se3	*32g*	0.0920(1)	0.3561(1)	0.4240(1)	0.599(3) / 0.401(3)	0.038(1)
Na1	*32g*	0.2620(1)	0.2697(2)	0.3759(1)	0.917(6)	0.062(1)
Na2	*16d*	0	1/4	0.2456(1)	0.839(10)	0.108(2)
Na3	*16e*	-0.0429(1)	1/2	1/4	0.984(7)	0.058(1)
Na4	*16c*	1/4	1/4	1/4	0.921(8)	0.106(2)
Na5	*16f*	0.2313(1)	0.5187(1)	3/8	0.959(9)	0.074(1)
Na6	*8b*	0	1/4	1/8	0.047(11)	0.050(20)

Table B.7: Atomic coordinates, occupation factor and equivalent isotropic displacement parameters of $Na_{11.12(10)}Sn_2SbS_{6.25(3)}Se_{5.75(3)}$ obtained from single crystal XRD at 280 K.

Atom	U_{11}	U_{22}	U_{33}	U_{23}	U_{13}	U_{12}
Sn1	00.020(1)	0.020(1)	0.023(1)	0.002(1)	0	0
Sb1	0.021(1)	0.021(1)	0.021(1)	0	0	0
S/Se1	0.025(1)	0.028(1)	0.029(1)	-0.001(1)	-0.001(1)	-0.004(1)
S/Se2	0.030(1)	0.024(1)	0.025(1)	0.005(1)	0.002(1)	0.001(1)
S/Se3	0.036(1)	0.036(1)	0.041(1)	-0.010(1)	-0.012(1)	-0.003(1)
Na1	0.046(1)	0.078(2)	0.062(1)	0.035(1)	-0.006(1)	-0.008(1)
Na2	0.206(5)	0.076(2)	0.042(2)	0	0	-0.083(3)
Na3	0.025(1)	0.079(2)	0.069(2)	-0.029(1)	0	0
Na4	0. 219(5)	0.028(2)	0.071(2)	-0.011(1)	-0.044(2)	-0.003(2)
Na5	0.095(2)	0.095(2)	0.031(1)	-0.016(1)	-0.016(1)	0.053(2)
Na6	0.060(30)	0.060(30)	0.020(30)	0	0	0

Table B.8: Anisotropic displacement parameters (Å^2) of $Na_{11.12(10)}Sn_2SbS_{6.25(3)}Se_{5.75(3)}$ obtained from single crystal XRD at 280 K.

Atom1	Atom2	Bond distance (Å)
Sn1	**S1/Se1**	2.5012(4) × 2
Sn1	**S2/Se2**	2.4610(5) × 2
Sb1	**S3/Se3**	2.4102(5) × 4
Na1	**S1/Se1**	3.0310(16)
Na1	**S1/Se1**	3.6050 (19)
Na1	**S2/Se2**	2.8820(16)
Na1	**S2/Se2**	3.350(2)
Na1	**S3/Se3**	3.007(2)
Na1	**S3/Se3**	3.0434(19)
Na2	**S1/Se1**	2.8802(14) × 2
Na2	**S2/Se2**	3.6682(13) × 2
Na2	**S3/Se3**	2.999(2) × 2
Na3	**S1/Se1**	2.9828(14) × 2
Na3	**S2/Se2**	2.8654(14) × 2
Na3	**S3/Se3**	3.2070(7) × 2
Na4	**S1/Se1**	3.1876(4) × 2
Na4	**S2/Se2**	2.7347(5) × 2
Na4	**S3/Se3**	3.2136(5) × 2
Na5	**S1/Se1**	2.9448(17) × 2
Na5	**S2/Se2**	2.8567(17) × 2
Na5	**S3/Se3**	3.3141(6) × 2
Na6	**S1/Se1**	3.2856(3) × 4
Na6	**S2/Se2**	3.9874(5) × 4
Na1	**Na6**	3.3631(17) × 2
Na1	**Na3**	3.5015(18) × 2
Na1	**Na4**	3.5474(17) × 2
Na1	**Na5**	3.533(3), 3.537(3)
Na2	**Na6**	3.385(3) × 2
Na2	**Na3**	3.5746(4), 3.5746(4)
Na2	**Na4**	3.5232(2), 3.5232(2)

Table B.9: Interatomic distances of $Na_{11.12(10)}Sn_2SbS_{6.25(3)}Se_{5.75(3)}$ obtained from single crystal XRD at 280 K.

Atom1	Atom2	Bond distance (Å)
Sn1	**Se1**	2.5273(3) × 2
Sn1	**Se2**	2.5310(3) × 2
Sb1	**Se3**	2.4946(3) × 4
Na1	**Se1**	3.1000(15)
Na1	**Se1**	3.8127(17)
Na1	**Se2**	2.9726(14)
Na1	**Se2**	3.3847(17)
Na1	**Se3**	3.0119(18)
Na1	**Se3**	3.0610(16)
Na2	**Se1**	2.9568(12) × 2
Na2	**Se2**	3.7938(11) × 2
Na2	**Se3**	3.0319(19) × 2
Na3	**Se1**	3.0126(14) × 2
Na3	**Se2**	2.9407(14) × 2
Na3	**Se3**	3.2852(6) × 2
Na4	**Se1**	3.2761(3) × 2
Na4	**Se2**	2.8179(3) × 2
Na4	**Se3**	3.2329(3) × 2
Na5	**Se1**	2.9790(15) × 2
Na5	**Se2**	2.9295(15) × 2
Na5	**Se3**	3.3762(4) × 2
Na6	**Se1**	3.3731(3) × 4
Na6	**Se2**	4.0753(4) × 4
Na1	**Na6**	3.5214(17) × 2
Na1	**Na3**	3.5111(15) × 2
Na1	**Na4**	3.6756(15) × 2
Na1	**Na5**	3.600(2), 3.630(2)
Na2	**Na6**	3.498(3) × 2
Na2	**Na3**	3.6532(3) × 2
Na2	**Na4**	3.59976(10) × 2

Table B.10: Interatomic distances of $Na_{11.12(10)}Sn_2SbS_{6.25(3)}Se_{5.75(3)}$ obtained from single crystal XRD at 280 K.

Parameters/σ (mS·cm^{-1})	**x=1**	**x=6**	**x=12**
Thickness (mm)	0.65	0.5	1.3
R (Ω)	268	482.9	1435
Total σ(mS·cm^{-1})	0.3	0.13	0.12
Thickness (mm)	0.84	0.3	1.44
R (Ω)	295	204.3	9372.2
Total σ (mS·cm^{-1})	0.36	0.19	0.2
Thickness (mm)	1.06	0.57	0.522
R (Ω)	382	430	499.3
Total σ (m S·cm^{-1})	0.33	0.17	0.13
Thickness (mm)	0.9	0.61	0.29
R (Ω)	321	365	9634
Total σ (mS·cm^{-1})	0.36	0.21	0.15
Average σ (mS·cm^{-1})	0.34	0.18	0.15
SD(σ)	0.03	0.03	0.04
SE	0.01	0.02	0.02
Exp. density of Theor. (%)		87.6	

Table B.11: Room temperature ionic conductivity values of $Na_{11}Sn_2SbS_{12-x}Se_x$ with x= 1, 6 and 12 obtained by EIS of the pressed at 2 tons and 1.0 cm diameter pellets. The SD and SE were calculated using **Equations** 2.29 and 2.30, respectively. The relative density of $Na_{11}Sn_2SbS_6Se_6$ was calculated using **Equations** A.1 and A.2.

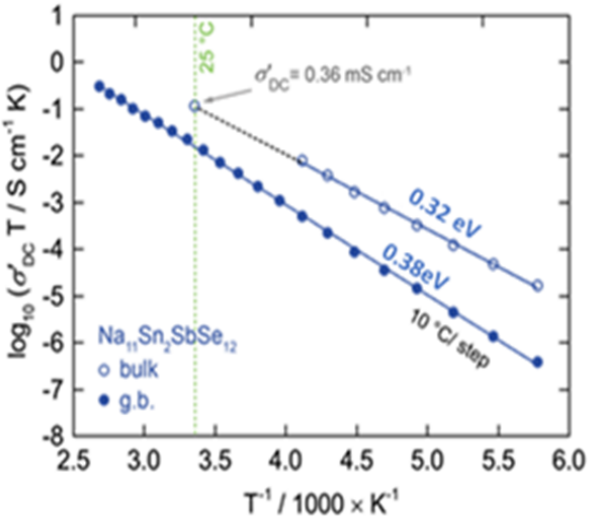

Figure B.1: Temperature dependence of the bulk and grain boundary conductivity of $Na_{11}Sn_2SbSe_{12}$.

Based on the structural model of $Na_{11}Sn_2SbSe_{12}$ obtained from single crystal diffraction, the Na channel volume was calculated from the following equation [170]:

$$Na_{channelvolume} = unitcellvolume - 16x(SnS_4volume) - 8x(SbS_4volume) \qquad \text{(B.1)}$$

Appendix C

In this appendix the single crystal XRD and impedance spectroscopy data of $Li_{4+x}P_{1-x}Si_xS_4I$ with x=0, 0.12 and 0.29 series are presented.

Crystal data	
Formula	$Li_{4.14(10)}P_{0.88(6)}Si_{0.12(6)}S_4I$
Formula Weight	314.53
Crystal System	Tetragonal
Space group	$P_4/\ nmm$ (No.129)
a= b, c (Å)	8.4813(6), 5.9270(4)
V (Å^3)	426.34(7)
Z	2
Calc. density (g/cm^3)	2.450
Abs. coef. μ(MoKσ) (/mm)	4.816
F(000)	289
Crystal Size (mm)	0.160 x 0.060 x 0.010
Data Collection	
Temperature (K)	280
Radiation (Å)	MoKa 0.71073
Theta range for data collection (°)	3.397 to 29.926
Index ranges	-11<=h<=11, -11<=k<=8, -7<=l<=8
Reflections collected	4313
Independent reflections	384 [R(int) = 0.0138]
Completeness to θ = 25.242°	100.0%
Absorption correction	Semi-empirical from equivalents
Max. and min. transmission	0.7460 and 0.6528
Refinement	
Refinement method	Full-matrix least-squares on F^2
Data/restraints/parameters	384 / 0 / 32
Goodness-of-fit on F^2	1.241
Final R indices [I>2sigma(I)]	R1 = 0.0088, wR2 = 0.0206
R indices (all data)	R1 = 0.0094, wR2 = 0.0207
Extinction coefficient	0.405 and -0.229

Table C.1: Crystallographic data for $Li_{4.14(10)}P_{0.88(6)}Si_{0.12(6)}S_4I$ obtained from single crystal XRD at 280 K.

Crystal data	
Formula	$Li_{4.31(3)}P_{0.71(11)}Si_{0.29(11)}S_4I$
Formula Weight	315.30
Crystal System	Tetragonal
Space group	$P_4/\ nmm$ (No.129)
a= b, c (Å)	8.5090(7), 5.9473(5)
V (Å^3)	430.60(8)
Z	2
Calc. density (g/cm^3)	2.432
Abs. coef. μ(MoKσ) (/mm)	4.760
F(000)	289
Crystal Size (mm)	0.050 x 0.040 x 0.020
Data Collection	
Temperature (K)	280
Radiation (Å)	MoKa 0.71073
Theta range for data collection (°)	3.386 to 29.817
Index ranges	-11<=h<=11, -10<=k<=10, -8<=l<=7
Reflections collected	3292
Independent reflections	384 [R(int) = 0.0324]
Completeness to θ = 25.242°	100.0%
Absorption correction	Semi-empirical from equivalents
Max. and min. transmission	
Refinement	
Refinement method	Full-matrix least-squares on F^2
Data/restraints/parameters	384 / 0 / 32
Goodness-of-fit on F^2	1.119
Final R indices [I>2sigma(I)]	R1 = 0.0193, wR2 = 0.0394
R indices (all data)	R1 = 0.0259, wR2 = 0.0417
Extinction coefficient	0.878 and -0.360

Table C.2: Crystallographic data for $Li_{4.31(3)}P_{0.71(11)}Si_{0.29(11)}S_4I$ obtained from single crystal XRD at 280 K.

Crystal data	
Formula	Li_4PS_4I
Formula Weight	313.87
Crystal System	Tetragonal
Space group	$P_4/\ nmm$ (No.129)
a= b, c (Å)	8.4789(4), 11.8499(6)
V (Å^3)	851.91(9)
Z	2
Calc. density (g/cm^3)	2.447
Abs. coef. μ(MoKσ) (/mm)	4.825
F(000)	576
Crystal Size (mm)	0.180 x 0.070 x 0.010
Data Collection	
Temperature (K)	280
Radiation (Å)	MoKa 0.71073
Theta range for data collection (°)	1.718 to 27.985
Index ranges	-7<=h<=11, -11<=k<=11, -15<=l<=15
Reflections collected	15222
Independent reflections	638 [R(int) = 0.0166]
Completeness to θ = 25.242°	100.0%
Absorption correction	Semi-empirical from equivalents
Max. and min. transmission	
Refinement	
Refinement method	Full-matrix least-squares on F^2
Data/restraints/parameters	638 / 0 / 39
Goodness-of-fit on F^2	1.246
Final R indices [I>2sigma(I)]	R1 = 0.0107, wR2 = 0.0240
R indices (all data)	R1 = 0.0132, wR2 = 0.0301
Extinction coefficient	Largest diff. peak and hole (e.Å-3) 0.308 and -0.379

Table C.3: Crystallographic data for Li_4PS_4I obtained from single crystal XRD at 280 K.

Atom	Wyckoff site	x	y	z	SOF	U(eq)(Å^2)
P	*2b*	3/4	1/4	1/2	0.71	0.01368(6)
Si	*2b*	3/4	1/4	1/2	0.29	0.01368(6)
S	*8i*	1/4	0.5558(4)	0.7064(6)	1	0.02178(6)
I	*2c*	1/4	1/4	0.1577(6)	1	0.02394(8)
Li1	*2c*	1/4	1/4	0.619(4)	0.45(6)	0.03293(6)
Li2	*2a*	3/4	1/4	0	0.63(3)	0.02280(4)
Li3	*8j*	0.0367(9)	0.0367(9)	0.4224(16)	0.579(10)	0.036723(2)
Li4	*4d*	0	0	0	0.45(2)	0.06839(7)

Table C.4: Atomic coordinates, site occupation factors and equivalent isotropic displacement parameters of $Li_{4.3(7)}P_{0.71}Si_{0.29}S_4I$ obtained from TOF neutron diffraction at 300 K. With lattice parameters a=8.5086(15) Å, c=5.9490(2) Å, Z=2 and V=430.69(2) Å^3. Due to the similar neutron scattering factors of Si and P (4.14 versus 5.13 fm), the Si/P ratio was fixed to the single crystal value, and the other parameters were freely refined except for a constrain on total Li occupancy for charge balance.

Atom	Wyckoff site	x	y	z	SOF	U(eq)(Å^2)
P	*4f*	3/4	1/4	0.23777(18)	1	0.01013(4)
S1	*8i*	1/4	0.5516(4)	0.8585(2)	1	0.01659(6)
S2	*8i*	1/4	0.5587(4)	0.3457(2)	1	0.01608(6)
I1	*2c*	1/4	1/4	0.0760(3)	1	0.02127(9)
I2	*2c*	1/4	1/4	0.57613(2)	1	0.02168(9)
Li1	*8j*	0.0440(4)	0.0440(4)	0.7123(4)	1	0.0271(10)
Li2	*4d*	0	0	0	1	0.02241(19)
Li3	*2c*	1/4	1/4	0.3060(7)	1	0.03799(3)
Li4	*2b*	3/4	1/4	1/2	1	0.04812(19)

Table C.5: Atomic coordinates, site occupation factors and equivalent isotropic displacement parameters of Li_4PS_4I obtained from TOF neutron diffraction at 300 K. With lattice parameters a=8.47019(5) Å, c=11.84157(15) Å, Z=4 and V=849.562(15)Å^3.

Parameters/σ (mS·cm^{-1})	**x=0**	**x=0.12**	**x=0.29**	**x=0.4**
Thickness (mm)	1.01(0.01)	0.77(0.03)	1.02(0.03)	0.932(0.008)
R (Ω)	3108	197.8	107	379
Total σ(mS·cm^{-1})	0.041	0.5	1.21	0.32
Thickness (mm)	0.95	0.3	1.48(0.02)	0.6
R (Ω)	2193	204.3	147.8	170.2
Total σ (mS·cm^{-1})	0.055	0.19	1.27	0.45
Thickness (mm)	0.59(0.01)	0.912(0.007)	1.8	—
R (Ω)	1910	204	136.6	—
Total σ (m S·cm^{-1})	0.039	0.56	1.67	—
Thickness (mm)	0.75		0.383(0.007)	
R (Ω)	200		35	
Total σ (mS·cm^{-1})	0.048		1.50	
Thickness (mm)			1.2	
R (Ω)			92.5	
Total σ (mS·cm^{-1})			1.65	
Average σ (mS·cm^{-1})	0.046	0.42	1.46	0.39
SD(σ)	0.007	0.20	0.21	0.09
SE	0.004	0.11	0.09	0.05
Exp. density of Theor. (%)			90	

Table C.6: Room temperature ionic conductivity values of $Li_{4+x}P_{1-x}Si_xS_4I$ with x=0, 0.12, 0.29 and 0.4 obtained by EIS of the pressed at 2 tons and 1.0 cm diameter pellets. The SD and SE were calculated using **Equations** 2.29 and 2.30, respectively. The relative density of $Li_{4.29}P_{0.71}Si_{0.29}S_4I$ was calculated using **Equations** A.1 and A.2.

Atom	Wyckoff site	x	y	z	SOF	U(eq)(Å^2)
P	*4f*	3/4	1/4	0.23898(4)	0.89(5)	0.0105(2)
Si	*4f*	3/4	1/4	0.23898(4)	0.11(5)	0.0105(2)
S1	*8i*	1/4	0.55044(4)	0.85741(3)	1	0.01437(8)
S2	*8i*	1/4	0.55886(4)	0.34624(3)	1	0.02100(6)
I1	*2c*	1/4	1/4	0.07741(2)	1	0.02508(9)
I2	*2c*	1/4	1/4	0.57852(2)	1	0.02168(9)
Li1	*8j*	0.0443(3)	0.0443(3)	0.7120(3)	1	0.0261(6)
Li2	*4d*	0	0	0	1	0.0498(14)
Li3	*2c*	1/4	1/4	0.3051(5)	1	0.0288(14)
Li4	*2b*	3/4	1/4	1/2	1	0.0238(12)
Li5	*2a*	3/4	1/4	0	0.185(16)	0.0238(12)

Table C.7: Atomic coordinates, site occupation factors and equivalent isotropic displacement parameters of $Li_{4.09(16)}P_{0.89(5)}Si_{0.11(5)}S_4I$ -$Li_{4.12}P_{0.88}Si_{0.12}S_4I$- obtained from single crystal XRD at 280 K using the highly ordered model.

Atom	U_{11}	U_{22}	U_{33}	U_{23}	U_{13}	U_{12}
P	0.0107(3)	0.0089(3)	0.0119(3)	0	0	0
Si	0.0107(3)	0.0089(3)	0.0119(3)	0	0	0
S1	0.01723(19)	0.01060(18)	0.01529(17)	0.00210(13)	0	0
S2	0.01558(18)	0.01072(18)	0.01537(17)	0.00090(13)	0	0
I1	0.02454(8)	0.02454(8)	0.01393(10)	0	0	0
I2	0.01799(7)	0.01799(7)	0.01353(10)	0	0	0
Li1	0.0235(9)	0.0235(9)	0.0311(16)	-0.0007(9)	-0.0007(9)	0.0066(12)
Li2	0.056(2)	0.056(2)	0.036(3)	0.0052(18)	0.0052(18)	-0.017(3)
Li3	0.033(2)	0.033(2)	0.021(3)	0	0	0
Li4	0.0275(18)	0.0275(18)	0.016(3)	0	0	0
Li5	0.0275(18)	0.0275(18)	0.016(3)	0	0	0

Table C.8: Anisotropic displacement parameters (Å^2) of $Li_{4.09(16)}P_{0.89(5)}Si_{0.11(5)}S_4I$ obtained from single crystal XRD at 280 K using the highly ordered model.

Atom1	Atom2	Bond distance (Å)
P/Si	**S1**	2.0419(5) × 2
	S2	2.0600(5) × 2
Li1	**S1**	2.581(4) × 2
	S2	2.592(3 × 2
	I2	2.931
Li2	**S1**	2.7449(3) × 4
	I1	3.1356(2) × 2
Li3	**S2**	2.6643(12) ×4
	I1	2.699(6)
	I2	3.241(6)
Li4	**S2**	2.4391(4) ×4
Li5	**S1**	2.3918(4) ×4
Li1	**Li2**	3.455(3)
Li1	**Li1**	3.489(5)
Li1	**Li3**	3.535(3)
Li1	**Li5**	2.9983(2)

Table C.9: Interatomic distances of $Li_{4.09(16)}P_{0.89(5)}Si_{0.11(5)}S_4I$ obtained from single crystal XRD at 280 K using the highly ordered model.

Atom	Wyckoff site	x	y	z	SOF	U(eq)(Å^2)
P	*4f*	3/4	1/4	0.24020(12)	0.71	0.0133(3)
Si	*4f*	3/4	1/4	0.24020(12)	0.29	0.0133(3)
S1	*8i*	1/4	0.55159(16)	0.85665(8)	1	0.0201(3)
S2	*8i*	1/4	0.55896(16)	0.34692(7)	1	0.0191(3)
I1	*2c*	1/4	1/4	0.07828(5)	1	0.0300(2)
I2	*2c*	1/4	1/4	0.57944(4)	1	0.02362(19)
Li1	*8j*	0.0432(8)	0.0432(8)	0.7109(7)	1	0.036(2)
Li2	*4d*	0	0	0	0.75(3)	0.042(6)
Li3	*2c*	1/4	1/4	0.3075(14)	1	0.036(4)
Li4	*2b*	3/4	1/4	1/2	1	0.033(5)
Li5	*2a*	3/4	1/4	0	0.11(5)	0.01(4)

Table C.10: Atomic coordinates, site occupation factors and equivalent isotropic displacement parameters of $Li_{3.81(1)}P_{0.71}Si_{0.29}S_4I$ -$Li_{4.29}P_{0.71}Si_{0.29}S_4I$- obtained from single crystal XRD at 280 K using the highly ordered model. An underestimation of Li content is observed (3.81 f.u.(Li) versus the targeted 4.29 f.u.(Li))

Atom	U_{11}	U_{22}	U_{33}	U_{23}	U_{13}	U_{12}
P	0.0143(10)	0.0107(10)	0.0150(6)	0	0	0
Si	0.0143(10)	0.0107(10)	0.0150(6)	0	0	0
S1	0.0249(8)	0.0140(7)	0.0214(5)	0.0026(4)	0	0
S2	0.0223(8)	0.0154(7)	0.0197(5)	0.0014(4)	0	0
I1	0.0352(3)	0.0352(3)	0.0195(3)	0	0	0
I2	0.0259(3)	0.0259(3)	0.0190(3)	0	0	0
Li1	0.029(3)	0.029(3)	0.051(5)	0.002(3)	0.002(3)	0.013(4)
Li2	0.048(8)	0.048(8)	0.031(8)	0.010(5)	0.010(5)	-0.012(9)
Li3	0.037(7)	0.037(7)	0.034(9)	0	0	0
Li4	0.040(8)	0.040(8)	0.019(7)	0	0	0
Li5	0.040(8)	0.040(8)	0.019(7)	0	0	0

Table C.11: Anisotropic displacement parameters (Å^2) of $Li_{3.81(1)}P_{0.71}Si_{0.29}S_4I$ obtained from single crystal XRD at 280 K using the highly ordered model.

Atom1	Atom2	Bond distance (Å)
P/Si	**S1**	2.0438(15) × 2
	S2	2.0624(15) × 2
Li1	**S1**	2.599(8) × 2
	S2	2.591(7) × 2
	I2	2.939(8)
Li2	**S1**	2.7613(7) × 4
	I1	3.1491(3) × 2
Li3	**S2**	2.670(4) ×4
	I1	2.726(17)
	I2	3.235(17)
Li4	**S2**	2.4408(12) ×4
Li5	**S**	2.3995(12) ×4
Li1	**Li2**	3.478(9)
Li1	**Li1**	3.518(14)
Li1	**Li3**	3.535(10)
Li	**Li5**	3.0083(2)

Table C.12: Interatomic distances of $Li_{3.81(1)}P_{0.71}Si_{0.29}S_4I$ obtained from single crystal XRD at 280 K using the highly ordered model.

Atom	Wyckoff site	x	y	z	SOF	U(eq)(Å^2)
P	*2b*	3/4	1/4	1/2	1	0.02038(17)
S	*8i*	1/4	0.55522(4)	0.70368(5)	1	0.01982(10)
I	*2c*	1/4	1/4	0.15250(3)	1	0.02306(9)
Li1	*2c*	1/4	1/4	0.607(2)	0.50(4)	0.035(5)
Li2	*2a*	3/4	1/4	0	0.52(3)	0.028(4)
Li3	*8j*	0.0461(6)	0.0461(6)	0.4260(11)	0.532(15)	0.034(2)
Li4	*4d*	0	0	0	0.47(2)	0.051(4)

Table C.13: Atomic coordinates, site occupation factors and equivalent isotropic displacement parameters of $Li_{4.08(9)}PS_4I$ -Li_4PS_4I- obtained from single crystal XRD at 280 K suing the small cell model.

Atom	U_{11}	U_{22}	U_{33}	U_{23}	U_{13}	U_{12}
P	0.0116(2)	0.0116(2)	0.0380(5)	0	0	0
Si	0.02051(18)	0.01447(17)	0.02449(19)	-0.00008(13)	0	0
I	0.02595(10)	0.02595(10)	0.01729(12)	0	0	0
Li1	0.042(6)	0.042(6)	0.021(7)	0	0	0
Li2	0.034(5)	0.034(5)	0.015(5)	0	0	0
Li3	0.030(2)	0.030(2)	0.042(4)	-0.0025(19)	-0.0025(19)	0.009(2)
Li4	0.055(6)	0.055(6)	0.043(7)	0.008(4)	0.008(4)	-0.013(6)

Table C.14: Anisotropic displacement parameters (Å^2) of $Li_{4.08(9)}PS_4I$ obtained from single crystal XRD at 280 K using the small cell model.

Atom1	Atom2	Bond distance (Å)
P	**S1**	2.0415(4) × 4
Li1	**S1**	2.649(3) × 4
	I	2.693(12), 3.232(12)
Li2	**S**	2.4150(4) × 4
Li3	**S1**	2.625(6) ×2, 2.532(6) ×2
	I	2.933(6) × 2
Li4	**S1**	2.7959(3) × 4
	I	3.13084(18) × 2
Li1	**Li3**	2.670(9)
Li2	**Li4**	2.99764(18)
Li3	**Li3**	1.411(14)
Li3	**Li4**	2.568(5), 3.445(7)

Table C.15: Interatomic distances of $Li_{4.08(9)}PS_4I$ obtained from single crystal XRD at 280 K using the small cell model.

Vacant site	Atom	Bond distance (Å)
i1	**I**	2.7720(3)
i1	**S1**	2.5345(6) × 2, 2.3450(7)
i1	**Li4**	2.28994(18), 2.797(10)
i1	**Li1**	3.963(18)
i1	**Li2**	1.61280(12)

Table C.16: Interatomic distances of the vacant site i1 at 0.75, 0.073, 0.903 in $Li_{4.29}P_{0.71}Si_{0.29}S_4I$ obtained from bond valence site calculations using the small cell model.

Appendix D

In this appendix the single crystal XRD, impedance spectroscopy and NMR data of $Li_{3+2x}P_{1-x}Al_xS_4$ with x=0.15 are presented.

Crystal data	
Formula	$Li_{3.11(9)}P_{0.85}Al_{0.15}S_4$
Formula Weight	180.21
Crystal System	Orthorhombic
Space group	$P_4/\ nma$ (No.62)
a, b, c (Å)	12.9572(13), 8.0861(8), 6.1466(6)
V (Å^3)	644.00(11)
Z	4
Calc. density (g/cm^3)	1.859
Abs. coef. μ(MoKσ) (/mm)	1.564
F(000)	352
Crystal Size (mm)	0.130 x 0.060 x 0.020
Data Collection	
Temperature (K)	280
Radiation (Å)	MoKa 0.71073
Theta range for data collection (°)	3.669 to 27.993
Index ranges	-17<=h<=17, -10<=k<=10, -8<=l<=8
Reflections collected	9773
Independent reflections	828 [R(int) = 0.0201]
Completeness to θ = 25.242°	97.7%
Absorption correction	Semi-empirical from equivalents
Max. and min. transmission	
Refinement	
Refinement method	Full-matrix least-squares on F^2
Data/restraints/parameters	828 / 0 / 52
Goodness-of-fit on F^2	1.245
Final R indices [I>2sigma(I)]	R1 = 0.0287, wR2 = 0.0761
R indices (all data)	R1 = 0.0287, wR2 = 0.0761
Extinction coefficient	1.194 and -0.347

Table D.1: Crystallographic data for $Li_{3.11(9)}P_{0.85}Al_{0.15}S_4$ obtained from single crystal X-ray diffraction at 280 K.

Parameters/σ (mS·cm^{-1})	**x=0.15**	**x=0.20**	**x=0.33**
Thickness (mm)	0.99(0.05)	0.612	0.6
R (Ω)	1175	1120	249.4
Total σ(mS·cm^{-1})	0.11	0.07	0.31
Thickness (mm)	0.6	1.34(0.02)	0.65
R (Ω)	781	660	313.2
Total σ (mS·cm^{-1})	0.31	0.25	0.27
Thickness (mm)	1.17	1.3	0.5
R (Ω)	291.3	1609	200
Total σ (m S·cm^{-1})	0.52	0.103	0.32
Thickness (mm)	0.37(0.02)	—	—
R (Ω)	425.6	—	—
Total σ (mS·cm^{-1})	0.11	—	—
Thickness (mm)	1.60(0.05)	—	—
R (Ω)	1500	—	—
Total σ (mS·cm^{-1})	0.13	—	—
Thickness (mm)	0.84(0.04)	—	—
R (Ω)	1000	—	—
Total σ (mS·cm^{-1})	0.11	—	—
Average σ (mS·cm^{-1})	0.22	0.14	0.31
SD(σ)	0.17	0.10	0.02
SE	0.07	0.06	0.02

Table D.2: Room temperature ionic conductivity values of $Li_{3+x}P_{1-x}Al_xS_4$ with x= 0.15, 0.20 and 0.33 obtained by EIS of the pressed at 2 tons and 1.0 cm diameter pellets. The SD and SE were calculated using **Equations** 2.29 and 2.30, respectively.

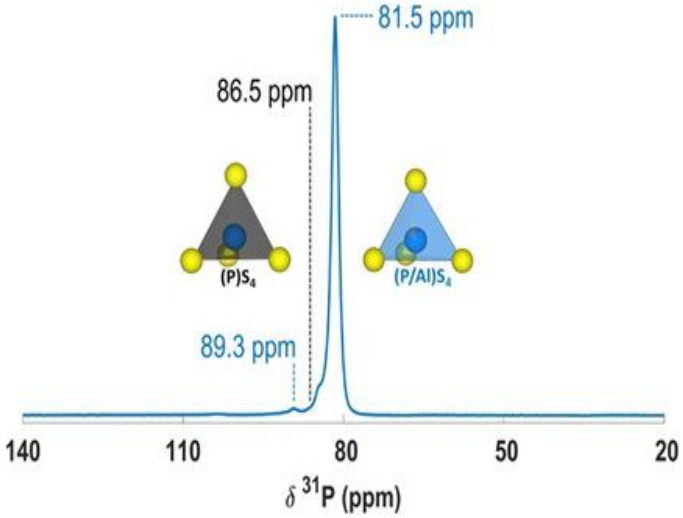

Figure D.1: ^{31}P MAS-NMR spectrum of crystalline $Li_{3.3}P_{0.85}Al_{0.15}S_4$ at 850 MHz and 30 kHz MAS rate. The primary signal is at 81.5 ppm, with a shoulder centred at 84 ppm and a secondary signal at 89.3 ppm.

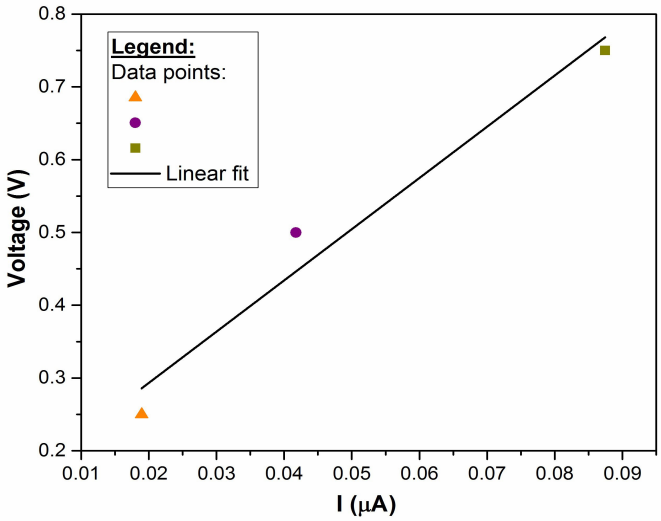

Figure D.2: Linear fit of the voltage vs current of $Li_{3.3}P_{0.85}Al_{0.15}S_4$.